Charles University in Prague
Faculty of Mathematics and Physics

DOCTORAL THESIS

František Dinnbier

Propagating star formation

Astronomical Institute of the Academy of Sciences
of the Czech Republic

Supervisor of the doctoral thesis:	Mgr. Richard Wünsch, Ph.D.
Study programme:	Physics
Study branch:	Theoretical Physics, Astronomy and Astrophysics

Prague 2017

I declare that I carried out this doctoral thesis independently, and only with the cited sources, literature and other professional sources.

I understand that my work relates to the rights and obligations under the Act No. 121/2000 Sb., the Copyright Act, as amended, in particular the fact that the Charles University in Prague has the right to conclude a license agreement on the use of this work as a school work pursuant to Section 60 subsection 1 of the Copyright Act.

In .... date .... signature of the author

Title: Propagating star formation

Author: František Dinnbier

Department: Astronomical Institute of the Academy of Sciences
of the Czech Republic

Supervisor: Mgr. Richard Wünsch, Ph.D., Astronomical Institute of
the Academy of Sciences of the Czech Republic

Abstract: Massive stars are powerful energetic sources shaping their surrounding interstellar medium (ISM), which is often swept up into a cold dense shell. If the shell fragments and forms a new generation of massive stars, the stars may form new shells, and this sequence repeats recursively leading to propagating star formation. Using three dimensional hydrodynamic simulations, we investigate fragmentation of the shell in order to estimate masses of stars formed in the shell. We develop a new numerical method to calculate the gravitational potential, which enables us to approximate a part of the shell with a plane–parallel layer. Our main results are as follows. Firstly, we compare our numerical calculations to several analytical theories for shell fragmentation, constrain the parameter space of their validity, and discuss the origin of their limitations. Secondly, we report a new qualitatively different mode of fragmentation - the coalescence driven collapse. While layers with low pressure confinement form monolithically collapsing fragments, layers with high pressure confinement firstly break into stable fragments, which subsequently coalesce. And thirdly, we study whether layers tend to self–organise and form regular patterns as was suggested in literature, and we find no evidence for this conjecture. Based on our simulations, we provide an analytic estimate for fragment properties, which in contrast to previous works, suggests that fragment masses are typically too low to form massive stars needed for self–propagating star formation.

Keywords: Stars: formation ISM: H II regions Physical processes: instabilities Physical processes: waves

I would like to thank to my supervisor, Richard Wünsch for his guidance, discussions and help. Next, I wish to express many thanks to Jim Dale and David Hubber for one productive month which I spent with them in Munich. I also appreciate their hospitality. I am thankful to Ant Whitworth for his stimulating discussions and pieces of advice which significantly improved my understanding of shell fragmentation. I thank Tereza Jeřábková for many inspiring discussions. I thank Jan Palouš for his useful comments on our paper about fragmenting layers. The analysis of presented simulations would not be possible without Raid and Virgo facilities maintained mainly by Michal Bursa. I would like to thank Michal Bílek, Soňa Ehlerová, Pavel Jáchym, Sergio Martínez–Gonzalez, Simonne Recchi, Rhys Taylor and Michal Zajaček (in alphabetical order) for useful discussions and friendly environment during my work on this project. I appreciate the working environment and hardware equipment (from the induction heater to my workstation) provided by The Astronomical Institute of the CAS.

Contents

Introduction

In the Thesis, I present the main body of work, which I did during my doctoral studies at the Astronomical Institute of the Academy of Sciences of the Czech Republic and at the Faculty of Mathematics and Physics of Charles University in Prague. The Thesis is organised in six chapters: Chapters 1 to 3 are introduction to the subject, while Chapters 4 to 6 describe my work and results.

Chapter 1 provides a brief overview of the star forming process with an emphasis on the current theories for massive star formation, and kinds of their feedback. This Chapter also presents mechanisms how massive stars can trigger new star forming event, and lists several examples of observed star forming regions with signposts of triggering. Particular attention is paid on so called Collect and collapse mechanism where massive stars compress their surrounding interstellar medium into a cold dense shell.

Chapter 2 describes three analytical estimates used for accessing properties of fragments formed in the wall of the swept up shell. The estimates generally differ in their predictions for the fragmenting timescale and masses of fragments.

Chapter 3 provides a brief introduction to hydrodynamical code Flash, which is used to perform simulations presented in the Thesis.

Chapter 4 describes my modification to the Ewald method, which enables to calculate gravitational field in a configuration with mixed boundary conditions for self–gravity, and thus to perform the simulations presented in Chapter 5. Results presented in Chapter 4 are part of the work describing the tree gravity solver (Wünsch et al. in preparation).

In Chapter 5, a small area in the shell surface is approximated by a layer, and its fragmentation is investigated by three dimensional simulations using hydrodynamical code Flash. The simulations are calculated by supercomputers Anselm and Salomon at the National Supercomputing Center IT4Innovations. The parameter space covers layers with various degree of confinement by the external pressure. The study pertains to several aspects of the fragmenting process. I study the dispersion relation in the linear regime of fragmentation (when the amplitudes of perturbations are smaller than the unperturbed quantities), and the course of fragmentation in the non–linear regime for layers confined by thermal pressure from both surfaces. I also investigate fragmentation of layers accreting onto one surface, and the possible tendency of layers to self–organise and form regular patterns during their evolution in the non–linear regime.

In Chapter 6, I use the simulations of fragmenting layers to construct a semi–analytical model for fragmentation of an expanding shell powered by an H II region. I compare our results with that of previous works, and discuss the results in the context of propagating star formation. Results presented in Chapters 5 and 6 are published in Dinnbier et al. [2017].

Appendix A is the reprint of Dinnbier et al. [2017]. Appendix B lists formulae, which can be useful for implementation of the standard or modified Ewald method in a numerical scheme.

1. Concept of propagating star formation

To describe the idea of propagating star formation, we firstly adumbrate the characteristic conditions and the most important implications of the star forming process (Section 1.1). The purpose of the section is to sketch an evolutionary line pointing from molecular gas to massive stars, so we omit an in–depth description which can be found in a standard textbook (e.g. Stahler and Palla [2005], Draine [2011], Ward-Thompson and Whitworth [2011]). The relevant properties of massive stars and their influence on the surrounding interstellar medium are described in Section 1.2. In Section 1.3, we review three candidate processes how massive stars can trigger another star formation event with an emphasis on collect and collapse scenario where the surrounding medium is swept up into a shell. In Section 1.4, we provide observational examples of triggered and propagating star formation.

1.1 Star formation overview

In current Galaxy, star formation occurs exclusively within molecular clouds (MCs). Typical sizes of MCs range from ~ 0.5pc to ~ 50pc and masses from $\sim 10^2\mathrm{M}_\odot$ to $\sim 6 \times 10^6\mathrm{M}_\odot$ [McKee and Williams, 1997, Roman-Duval et al., 2010]. Mass of MCs is dominated by molecular hydrogen H_2 and atomic helium He (constituting $\sim 26\%$ of mass) with a small contribution of heavier elements. MCs are the densest and coldest parts of the interstellar medium (ISM). MCs are highly inhomogeneous and clumpy so the density typically spans many orders of magnitude: From dense cores of particle density $n \sim 10^6\,\mathrm{cm}^{-3}$ to outer parts where n is below $10^2\,\mathrm{cm}^{-3}$ with mean over the whole cloud $n = 10^{2.6\pm0.3}\,\mathrm{cm}^{-3}$ [Solomon et al., 1987, Roman-Duval et al., 2010]. Characteristic temperature inside non–star forming MCs is approximately 8 - 15 K (i.e. sound speed $c_s \simeq 0.2\mathrm{km\,s}^{-1}$), but rises to $\gtrsim 50$K in the vicinity of star forming sites [Cernicharo, 1991, Blitz, 1991]. The molecular phase of clouds is enveloped in cold H I gas.

The majority of MCs is situated very close to the galactic midplane at vertical scaleheight up to ~ 60pc Scoville and Sanders [1987] where MCs concentrate in spiral arms. Smaller fraction (around 30% in mass) of MCs lies in the interarm regions [Foyle et al., 2010]. The total mass of galactic H_2 is approximately $0.9 \times 10^9\mathrm{M}_\odot$ comprising $\simeq 17$ percent of total galactic gaseous content (the dominant part is in the form of H I $\simeq 3 \times 10^9\mathrm{M}_\odot$ and H II $\simeq 1.1 \times 10^9\mathrm{M}_\odot$). Number of clouds $\mathrm{d}N$ in mass interval $\mathrm{d}M$ can be approximated as $\mathrm{d}N/\mathrm{d}M \propto M^\alpha$ where $\alpha = -1.5$ [McKee and Williams, 1997]. When considering a power law mass distribution, the slope α immediately tells us the relative contribution of low and high mass objects to the total mass and to the total number of objects. In given logarithmic mass bin, there are more low mass than high mass objects if $\alpha < -1$ and there is more total mass in low mass than high mass objects if $\alpha < -2$. Thus, the majority of MCs are of lower mass while the molecular gas mass budget is dominated by higher mass MCs.

The observed motions inside MCs (up to $\sim 10\mathrm{km\,s}^{-1}$) significantly exceeding sound velocity are apparently of a non–thermal origin. Larson [1981] finds correlations between non–thermal velocity dispersion σ inside MCs as a function of cloud size R or mass M. Notably, the correlation $\sigma \propto R^{0.38}$ may suggest turbulence as the relation is not significantly different from Kolmogorov law $\sigma \propto R^{1/3}$ [Landau and Lifshitz, 1959]. Further, for a particular MC, the correlations also hold for its subclouds indicating self–similarity, which is another property of turbulent flows. Larson [1981] also proposes that the scale where turbulence becomes subsonic ($\sigma \simeq c_s$) corresponds to a break in the distribution function for newly formed stars (see IMF below). He estimates the break to be near $0.1\mathrm{M}_{\odot}$. The correlations are revisited and corrected by Solomon et al. [1987] and Heyer et al. [2009].

Despite continuing research, many important questions regarding the dynamics of MCs remain unanswered and it is even difficult to exactly define a molecular cloud as an entity [Dobbs and Pringle, 2013, Dobbs et al., 2014]. One of the open questions is the value of the virial parameter $\alpha_G = M_{virial}/M$, where $M_{virial} = 5\sigma^2 R/G$. The observing errors prevent from distinguishing between state of virial equilibrium ($\alpha_G = 1$) from a cloud in a free fall collapse characterised by $\alpha_G = 2$ (assuming spherically symmetric model) [Dobbs et al., 2014]. Another question is the process responsible for driving turbulence, since the turbulence would dissipate on timescale comparable to one cloud free–fall time and it is supposed to be maintained for longer. The candidate processes for turbulence driving are gravitational collapse in colliding flows Vázquez-Semadeni et al. [2007], hydrodynamic instabilities in colliding flows Hunter et al. [1986], Vishniac [1994], Koyama and Inutsuka [2002], shear near spiral arms Dobbs and Pringle [2013], or photoionising and radiation pressure feedback from young stars Walch et al. [2012], Krumholz and Matzner [2009].

Further support against gravity is provided by magnetic fields. However, it is difficult to assess the strength of the field since usually only its component along the line of sight can be obtained. Although the magnetic field can substantially influence the collapse of a MC and induce interesting morphological structures (e.g. hourglass shape observed by Girart et al. [2006]), the magnetic field alone probably cannot overcome the selfgravity and prevent the collapse Crutcher [2012].

Star formation begins in the densest parts of the cloud (above density $n \gtrsim 10^4\mathrm{cm}^{-3}$) when the cloud is still being assembled so the cloud is never static. Only small volume of the whole cloud is above this density and thus star forming. Observations have revealed that the vast majority ($\sim 90\%$) of young stellar objects is clustered Lada et al. [1991]; Evans et al. [2009]. Since the star formation is ongoing, the clusters are still embedded in their natal gas and invisible in visual wavelengths. Hierarchically clustered star formation is also found in simulations as a result of gravitational collapse of a turbulent cloud Bonnell et al. [2003].

The distribution of stars formed in one star forming event as a function of their mass is called the initial mass function (IMF). The range of stellar masses spans from $0.08\mathrm{M}_{\odot}$ (the lowest mass of an object able to fuse hydrogen in the centre) to the upper limit $\sim 150\mathrm{M}_{\odot}$ Zinnecker and Yorke [2007]. The upper limit is not firmly set because the observed most massive stars may be in fact unresolved binaries. Star forming regions also contain objects with mass below

$0.08\mathrm{M}_\odot$ (Brown dwarfs).

After the pioneering work of Salpeter [1955], more recent approximations to IMF are provided by Scalo [1998];Kroupa [2001];Chabrier [2003]. The approximations are either piecewiese power law functions Scalo [1998], Kroupa [2001] or their combination with the lognormal distribution [Chabrier, 2003]. The remarkable property of the IMF is its universality regardless of cloud density or metallicity Kroupa [2002];Massey [1998];Bastian et al. [2010]. Possible deviations from the IMF are in exotic environments (e.g. Galactic centre, starbursting galaxies) Kroupa et al. [2013]. Note that inferring the IMF is not a straightforward task and cannot be obtained from one single system due to mainly stellar evolution, unresolved binaries and star cluster dynamics. This leaves substantial uncertainties in determining the power law indices and may obscure their finer variations.

The origin of the form of the IMF and the changes in its power law indices presumably contain an essential piece of information about the star forming process. It serves as a check which any reliable theory of star formation must reproduce. An interesting clue to constraining the origin of the IMF was obtained by Alves et al. [2007]. They found that dense molecular cores observed in the Pipe nebula already have mass function with the same power law indices as the universal stellar IMF (they recovered two parts of power law above their sensitivity limit). This suggests that whatever process is responsible for the shape of the IMF, its action is finished in the early stage of core evolution. They also recovered the characteristic mass where the slope of the IMF changes. However, the core mass function is shifted by factor ~ 3 towards higher mass. The shift is by the same factor for both low and high mass cores. The independency of the shift on mass indicates that during transformation into a star, every dense molecular core losses a comparable amount of gas (around 2/3) regardless of its mass. The mapping from a core to a star is presumably more complicated than this simple picture since each core may fragment into several protostars. Goodwin et al. [2008] find more closer relationship between the core mass function and the IMF assuming that each core spawns two or three protostars and losses around 2/3 in of its mass in the course of the process.

The formation process for massive stars (mass above $\sim 8\mathrm{M}_\odot$) is different and significantly less understood than that of lower mass stars. Massive stars reach the main sequence (and commence hydrogen burning in their cores) on much shorter timescale ($\lesssim 0.1$Myr) than their lower mass counterparts (~ 30Myr for a star with $1\mathrm{M}_\odot$). Unlike low mass stars, massive stars continue accreting large amounts of gas after they reached the main sequence. Their high temperatures (above 20000 K) and radii ($\sim 4 - 15\mathrm{R}_\odot$) imply significantly higher luminosities. The high luminosity means that radiation pressure acting on dust grains dominates the gravitational attraction making spherical accretion impossible.

Three possible scenarios for massive star formation have been proposed: Core accretion, competitive accretion and protostellar collisions [Zinnecker and Yorke, 2007, Tan et al., 2014]. In the *core accretion* model, one or a few massive stars are formed from a monolithic collapse of a massive ($\sim 100\mathrm{M}_\odot$) starless core. The protostar(s) are surrounded by a disc which supplies them with gas. In this geometry, the radiation pressure is anisotropic; it is significantly higher near the rotation axis than in the equatorial plane. While radiation pressure carves cavities near the rotation axis and leads to "flashlight" [Yorke and Sonnhalter, 2002], it is unable to prevent accretion from the dense disc in the equatorial plane. Moreover, the innermost part of the disc is heated at such a high temperature that dust grains evaporate, which further reduces the effect of the radiation pressure.

Bonnell et al. [1997] and Bonnell et al. [2001] find in their simulations an interesting mechanism which they call *competitive accretion*. To illustrate this idea, consider a model of an embedded star cluster, which consists of a gaseous and protostellar component. At the beginning, the gaseous component comprises 90% of the system mass. The gaseous component is initially static and homogeneous, and it starts collapsing. The protostars are initially of the same mass. They move and accrete the gas. The position of a protostar inside the cluster strongly influences its accreting rate and thus the final mass. The more isolated protostars have larger gaseous reservoirs to accrete than protostars with a closer neighbour. Thus the former accrete at higher rate than the latter. The more a protostar accretes, the more its kinetic energy per unit mass decreases and the accreting protostar sinks towards the cluster centre. In addition, a gaseous wake forms behind the protostar further decreasing its kinetic energy per unit mass. As the protostar reaches the central parts of the cluster, its accretion rate increases due to higher density of gas near the centre. Therefore a protostar which happens to be at a suitable location ends up with a significantly higher final mass than a protostar starting at less favourable location. This process leads to a variation in stellar masses. The majority of the massive stars is also located near the cluster centre. Indeed, in many young clusters, the most massive stars are situated near the centres (*mass segregation*), which competitive accretion may naturally explain.

Massive stars can be also formed in *protostellar collisions* of low mass stars in the centres of dense star clusters [Bonnell et al., 1998]. Note that the stars are still in their pre–main–sequence stage, so they have by factor ~ 5 to 20 larger radius than at the main sequence. They are also surrounded by accretion discs. Such large cross section enables the collisions. This mechanism circumvents the necessity of forming stars with $\gtrsim 10\mathrm{M}_\odot$ via accretion and might be an alternative to the core accretion mechanism. The stars produced in collisions retain the angular momentum of the progenitor stars, which would make them rapidly rotate. This is also in adherence with observations since most massive stars are fast rotators.

Massive stars are the dominant source of feedback disrupting the rest of their natal cloud. When on the main sequence, their feedback is mostly in the form of hydrogen ionising photons and mechanical luminosity due to stellar winds. In addition, massive stars eventually explode as supernovae. Feedback from lower mass stars is mainly in the form of protostellar outflows and infrared radiation and has only a minor impact on the cloud relative to the feedback from massive stars [Ossenkopf and Mac Low, 2002]. Nevertheless, even in the absence of massive stars, lower mass stars are able to disperse the cloud on timescale of several Myr.

Star formation efficiency (SFE) is a mass fraction of a gaseous system which turns into stars during the star formation process. Taking a MC as a whole, observations show that star formation is not efficient, typically only 3% to 6% of the total cloud mass is transformed to stars [Evans et al., 2009]. However, within a MC, local SFE spatially varies and is higher for embedded clusters ($\sim 10\% - 30\%$;

Lada and Lada [2003]).

The change of gravitational potential during gas expulsion has a profound impact on the dynamics of the stars. Whether the cluster remains bound after gas expulsion depends mainly on its duration τ and the SFE. The characteristic timescale on which the stars can react to evolving potential is of the order their crossing time t_{cr}, $t_{cr} = 2R/\sigma$ where R is cluster radius and σ velocity dispersion. When the gas is removed adiabatically ($\tau \gg t_{cr}$), the cluster gradually expands to radius R/SFE [Elmegreen, 1983]. To remain bound, the cluster must remain inside its tidal radius confined by the Galaxy after gas expulsion is completed. Observed densities of molecular clouds and the condition on tidal radius constrain the lower SFE for formation of bound clusters to be about 30% [Lada et al., 1984]. When the gas is removed explosively ($\tau \ll t_{cr}$), the cluster is disrupted for SFE below $\sim 30\%$ [Geyer and Burkert, 2001]. For higher SFE, the cluster expands, but it revirialises and remains bound [Kroupa et al., 2001]. The number of stars which remains bound increases with increasing SFE. Note that SFE $\sim 1/3$ is exactly the expected value assuming that 1/3 of mass in dense cores is converted into stars as indicated by [Alves et al., 2007]. The upper value of SFE is observationally constrained to be $\sim 50\%$ [Lada and Lada, 2003].

Observations show that only 10% of embedded clusters survive to the age 10Myr as bound open star clusters [Lada and Lada, 2003]. The rest of embedded clusters becomes unbound due to gas expulsion and is observed as *OB associations*. OB associations are slowly expanding (typical velocity a few km/sec) small groups (memberships ranges from several to tens) of massive stars (earlier than spectral type B2) Blaauw [1964]. In addition to luminous massive stars, OB associations contain lower mass stars with mass distributed in good approximation with standard model for the IMF Preibisch et al. [2002].

Apart from proposed origin of OB associations in disrupted embedded clusters with initial sizes $\sim$ 1pc, there is another model for their origin in significantly more extended configurations $\sim 20-40$pc. The value is based on tracing members of OB associations back in time [Blaauw, 1991]. In this model, an OB association is composed of stars formed in small clusters scattered over the whole MC and the MC consequently destroyed by stellar feedback. This model was simulated by [Clark et al., 2005]. In contrast to the formation in embedded clusters where the velocity of escaping stars is given by initial velocity dispersion of the cluster, in the other model, the velocity of escaping stars is given by initial turbulent motions of the cloud.

There is no general concensus on lifetime of MCs. Assuming that protostellar cores cannot collapse until the magnetic flux is removed by ambipolar diffusion, Shu et al. [1987] estimate lifetime to be $\sim$ 10Myr. Comparing the number of MCs without high mass star formation, with incipient high mass star formation and in the process of disruption, Kawamura et al. [2009] estimate typical cloud lifetime in the Large Magellanic Cloud to be $\sim$ 25Myr. Koda et al. [2009] argue that presence of interarm clouds in galaxy M 51 suggests even longer age $\sim$ 100Myr as the clouds are rather remainings of more massive clouds swept up by spiral arms than formed in situ. Based on numerical simulations, Dobbs and Pringle [2013] find cloud lifetimes to be in the range from 4 to 25Myr, but they stress the difficulty of the molecular cloud definition since the clouds often fragment or coalesce.

On the other hand, stars in star forming regions are usually very young and there is no evidence for older stars to be present in star forming regions suggesting that MCs are disrupted soon after star formation began Hartmann et al. [2001]; Ballesteros-Paredes and Hartmann [2007]; Elmegreen [2007]. Taking into account that the majority of MCs are already star forming, Ballesteros-Paredes and Hartmann [2007] conclude that lifetimes of MCs can hardly be longer than a few Myr. It is also not clear how MCs could avoid rapid destruction by feedback from massive stars if they are supposed to survive for several tens of Myr. Another method for estimating the duration of a star forming event is based on age spreads among stars in young star clusters Lada and Lada [2003] and references therein. The clusters already expelled most if not all of their natal gas. Although several studies indicate rather narrow $\lesssim$ 3Myr age spreads implying early cloud disruption, the result is not decisive due to uncertainty in premain sequence evolutionary tracks and accretion effects onto protostars. For example, NGC 2264 contains both young stars with broader age spread $\sim$ 5Myr and large quantities of molecular gas apparently turning into stars Dahm [2008].

Note that the evidence for longer and shorter cloud lifetimes are not necessarily mutually exclusive. The longer timescales are derived for very massive MCs ($M \gtrsim 10^5 \mathrm{M}_\odot$), while the shorter timescales are based on data for nearby ($M \lesssim 10^4 \mathrm{M}_\odot$) MCs. Thus a possible explanation may rest in different lifetime for clouds of different mass.

We illustrate some of the properties of molecular clouds described above on molecular cloud W3 (Westerhout 3) Rivera-Ingraham et al. [2013] (figure 1.1). W3 is a nearby ($\sim$ 2kpc) high mass star forming cloud of total mass $\sim 4 \times 10^5 \mathrm{M}_\odot$. The cloud is highly inhomogeneous and hierarchical with many substructures, filaments and shells. Cluster IC 1795 containing OB stars is $3 - -5$Myr old and probably triggered star formation in W3 (OH) region. Massive star formation is ongoing in W3 Main and W3 (OH) and is probably incipient in AFGL 333, so the majority of the cloud is still quiescent.

1.2 Forms of stellar feedback

We focus on the forms of feedback which are suggested to be the most destructive for the ISM: photoionisation, stellar winds and supernovae. We also mention another forms of feedback which can be important. We stress that the relative importance of various feedback forms is a subject of intensive research and has not been definitely established yet.

1.2.1 Main sequence stars

In this section, we quantify the photoionising rates and stellar winds as a function of the stellar mass and compute total yields from a coeval stellar population. We then review simple models for interaction of a photoionising source and stellar winds with their surrounding medium. These two forms of feedback probably dominate for the majority of stellar populations; however, it is possible that the dominant main sequence feedback mechanism for the most massive and compact star clusters is radiation pressure (see section 1.2.3).

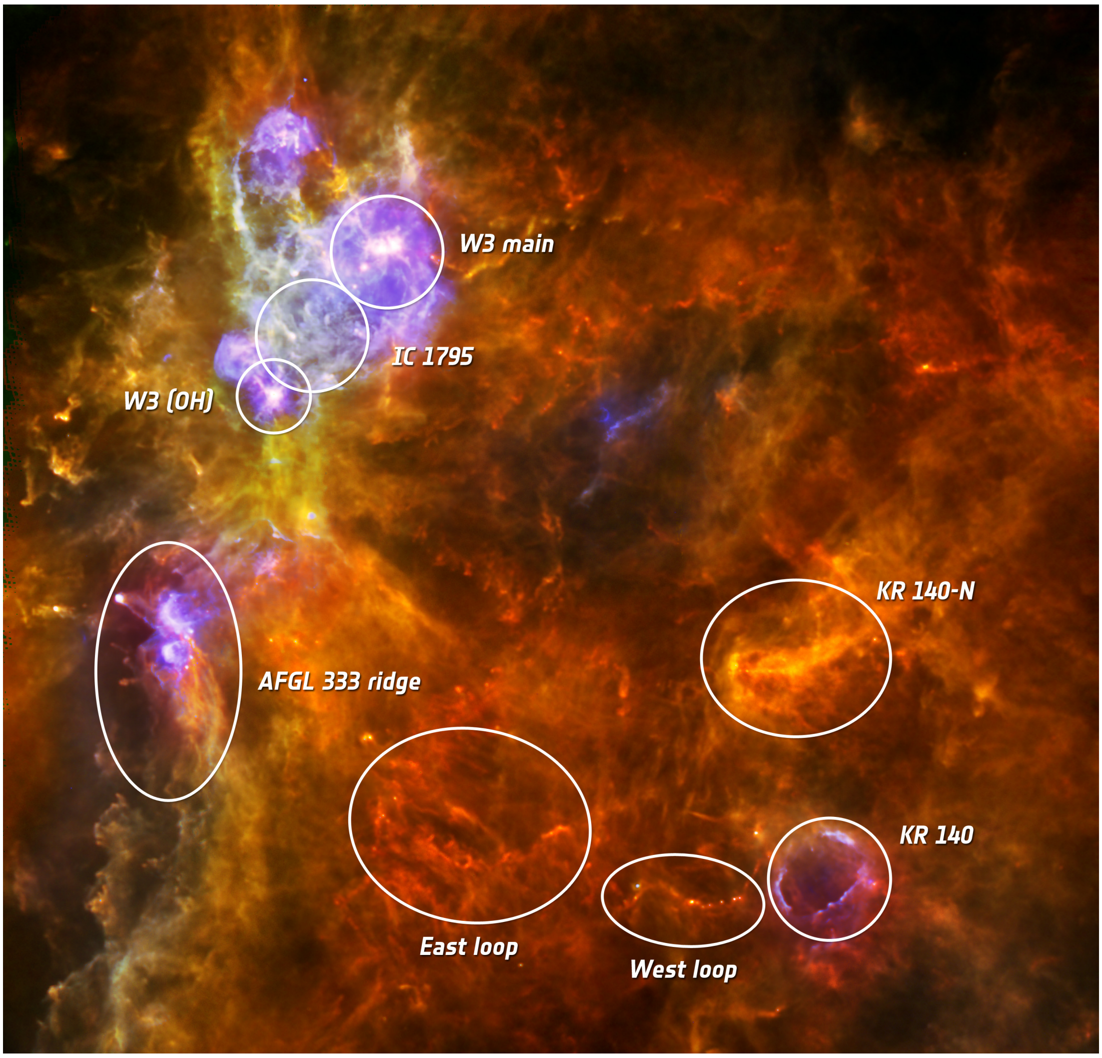

Figure 1.1: W3 star forming cloud (Rivera-Ingraham et al. [2013]). The colorscale corresponds to Herschel filters at 70 μm (blue), 160 μm (green) and 250 μm (red). Dust emits at higher temperature (shorter wavelengths) due to heating by nearby massive stars.

Spectral type	M $[\mathrm{M}_\odot]$	$\log_{10} S$ $[\mathrm{s}^{-1}]$	$\dot{M}$ $[10^{-6}\mathrm{M}_\odot \mathrm{yr}^{-1}]$	v_∞ $[\mathrm{km\,s}^{-1}]$	$\log_{10} L_w$ $[\mathrm{erg\,s}^{-1}]$
O3	58.34	49.63	3.10	3160	36.99
O4	46.16	49.47	2.00	2990	36.75
O5	37.28	49.26	1.30	2760	36.49
O5.5	34.17	49.11	1.00	2650	36.35
O6	31.73	48.96	0.80	2560	36.22
O6.5	29.02	48.80	0.60	2460	36.06
O7	26.52	48.63	0.40	2320	35.83
O7.5	24.15	48.44	0.35	2210	35.73
O8	21.95	48.29	0.26	2100	35.56
O8.5	19.82	48.10	0.22	1960	35.43
O9	18.03	47.90	0.18	1820	35.27
O9.5	16.46	47.56	0.15	1660	35.11
B1	10.4	45.11			
B2	8.8	44.45			
B3	7.1	43.36			
B5	5.8	42.22			

Table 1.1: Logarithms of number of hydrogen ionising photons per second S and mechanical luminosity L_w produced by a main sequence star of mass M. Stars have mass loss rate $\dot{M}$ and terminal wind velocity v_∞. The models have solar metallicity. Data for O stars are based on atmospheric models calculated by Martins et al. [2005]; Smith [2006], data for B stars are based on Thompson [1984] and Diaz-Miller et al. [1998] (properties of stellar winds for B stars are not provided).

Photoionising rate and mechanical luminosity

Table 1.1 lists ionising radiation and stellar winds as a function of stellar mass M. Number of hydrogen ionising photons (i.e. photons more energetic than 13.6 eV) emitted per second is denoted S, and mechanical luminosity L_w of stellar winds with terminal velocity v_∞ and mass loss rate $\dot{M}$ is

$$L_w = \frac{\dot{M} {v_\infty}^2}{2}. \tag{1.1}$$

Thus, both ionising photon flux and mechanical luminosity are strongly increasing functions of the stellar mass.

In the previous section, we mentioned that inside MCs, stars are formed exclusively in groups either as gravitationally bound star clusters Lada and Lada [2003] or unbound OB associations Blaauw [1991]. In both cases, the distribution of stellar mass produced in one star forming event can be well approximated by the standard model for the IMF. The number of ionising photons S^{pop} and mechanical luminosity L_w^{pop} produced by a coeval stellar population in mass interval $m, m + \mathrm{d}m$ (number of stars in the mass interval is $\mathrm{d}n$) is $S(m)\,\mathrm{d}n(m)$ and $L_w(m)\,\mathrm{d}n(m)$, respectively. Functions S^{pop} and L_w^{pop} for data from table 1.1 and the IMF model from Kroupa [2001] are plotted in the left panel of figure 1.2. Both S^{pop} and L_w^{pop} are normalised to unit mass of $1\mathrm{M}_\odot$ for the coeval population.

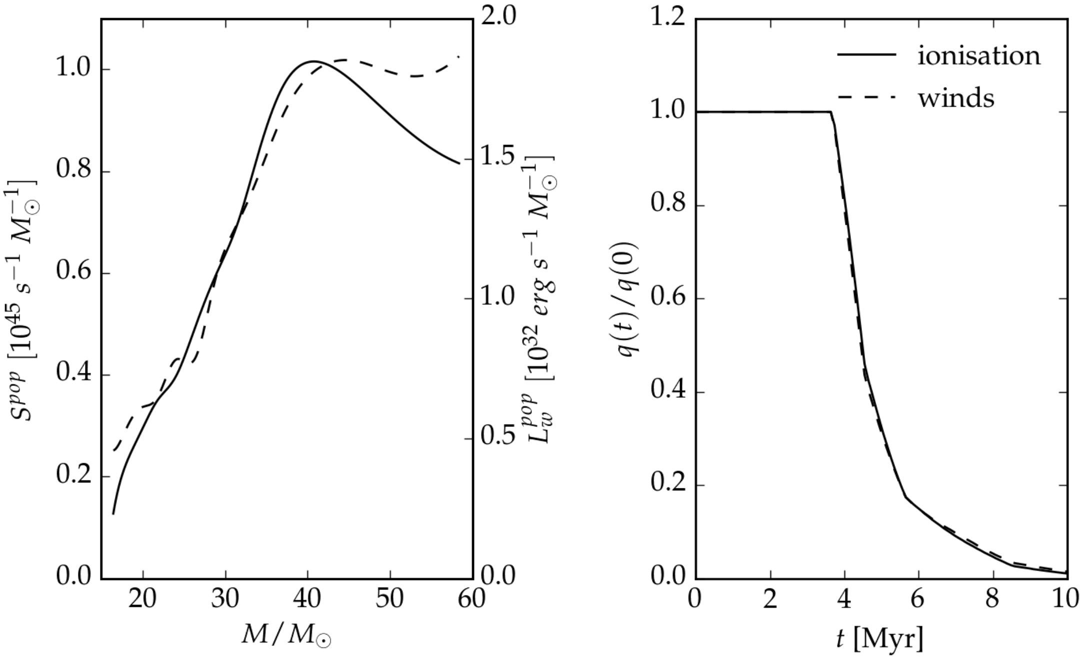

Figure 1.2: Feedback from a coeval stellar population with the standard IMF. Left panel: Mass dependence of functions S^{pop} (solid line) and L_w^{pop} (dashed) per $1\mathrm{M}_\odot$ of the population at age zero. Righ panel: Time dependence of total number of ionising photons (solid) and total mechanical luminosity (dashed) produced by the population. q denotes either form of feedback. The data are plotted relative to the value at the age zero.

According to the standard IMF, a coeval stellar population contains substantially less number of massive stars relative to lower mass stars. Let the population contains objects in mass interval $(0.01\mathrm{M}_\odot, 50\mathrm{M}_\odot)$. Although massive stars (mass above $\sim 8\mathrm{M}_\odot$) exclusively dominate the feedback, these stars make up only 0.37% of the total number of stars and contain 17% of the total mass. Integrating functions S^{pop} and L_w^{pop} in interval $(0.01\mathrm{M}_\odot, 50\mathrm{M}_\odot)$, we obtain the total production of ionising photons and mechanical luminosity for the coeval stellar population. Normalised to $1\mathrm{M}_\odot$ of the population, the numbers are $2.3 \times 10^{46}\mathrm{s}^{-1}$ and $4.3 \times 10^{33}\mathrm{erg\,s}^{-1}$, respectively.

The more massive a star is, the earlier it explodes as a supernova. After the explosion, the ionising or mechanical luminosity budget of the population decreases by the contribution of the exploding star. Evolution of ionising and mechanical luminosity feedback from a coeval stellar population is shown in the righ panel of figure 1.2. Stellar lifetimes from stellar evolutionary models with solar metallicity from [Bressan et al., 1993] were used to make the figure. For the plot, changes in luminosity due to stellar evolution beyond the main sequence are neglected.

After quantifying the photoionisation and stellar winds for a star or stellar population, we focus on its influence on the ambient interstellar medium. For this purpose, we review simplified models where analytic or semi–analytic solutions can be found.

Photoionising feedback

Massive stars start emitting ionising photons usually when still embedded in relatively dense and cold molecular gas. Spitzer [1978] adopt a simplified model to illustrate their feedback. There is one source emitting S hydrogen ionising photons per second into an initially cold homogeneous medium. Density, temperature and sound speed in the cold medium is n_0, T_0 and c_{s0}, respectively. Self–gravity and the role of dust are neglected.

The evolution can be divided into two phases: Very short ($\sim 10^{-3}$Myr) initial static phase when the surrounding medium is suddenly ionised and the following dynamical phase when a shell is being swept up around the expanding ionised cavity.

When the source switches on, an ionisation front propagates into the surrounding medium. The gas is abruptly heated from temperature $T_0 \sim 10$K to $T_i \sim 1.0 \times 10^4$K which according to the state equation for ideal gas leads to a rapid pressure increase by a factor of 10^3. Another additional factor of 4 comes from the reduction of the mean particle mass due to dissociation and ionisation. Since the propagation speed v of the ionisation front is substantially higher than the sound speed c_{si} in the ionised hydrogen, the ionised gas does not have enough time to expand and its motions are unimportant in this evolutionary phase.

As the radiative source is approximately black body, characteristic photon energy is proportional to the temperature of the source. Typical temperature of stars igniting H II regions ranges from 2.0×10^4K to 5.0×10^4K. Although the typical temperature of stars igniting H II regions ranges from 2.0×10^4K to 5.0×10^4K, there is an efficient thermostat keeping the temperature T_i of the ionised hydrogen around 1.0×10^4 K. The narrow range of T_i is controlled by cooling via collisional excitation of ionts of heavier elements (mainly oxygen with smaller contribution from nitrogen and neon). Despite their significantly smaller abundance, the heavier elements are the most important cooling mechanism and dominate the total energy budget emitted from the H II region.

Ionised hydrogen recombine at a rate $\beta(T_i)n_i^2$ per unit volume, where $\beta(T_i)$ is the recombination coefficient and n_i the density of ionised hydrogen. Approximately one third of all recombinations goes immediately into the groud state and as a result another hydrogen ionising photon is emitted. The assumption that the reemitted photon ionises an hydrogen atom in the same area where it was emitted is called *on the spot approximation.* The rest (2/3) of recombinations goes into an excited state and subsequently cascades into the ground state emitting photons unable to ionise another neutral hydrogen atom and these recombinations can be viewed as absorbers for ionising photons. Assuming on the spot approximation, the recombination rate per unit volume is $\beta^*(T_i)n_i^2$, where $\beta^*(T_i) = 2\times 10^{-10} T_i^{-3/4}\mathrm{cm}^3\mathrm{s}^{-1}$ is the recombination coefficient into excited states.

As the ionisation front propagates, the mass of the ionised gas increases and the photons are consumed to ionise already recombined atoms, so less photons remain to ionise neutral gas and the front propagating velocity v slows down. The radius R_{st} of a sphere which a source can ionise is set from a balance between the recombination rate in the sphere and the number of photons available for ionisations, $4\pi R_{st}^3 \beta^*(T_i) n_0^2/3 = S$, i.e.

$$R_{str} = \left(\frac{3S}{4\pi\beta^*(T_i)n_0^2} \right)^{\frac{1}{3}} = 0.74 \mathrm{pc} S_{49}^{\frac{1}{3}} n_3^{-\frac{2}{3}}, \tag{1.2}$$

where $S_{49} = [S/10^{49}\mathrm{s}^{-1}]$ and $n_3 = [n/10^3\mathrm{cm}^{-3}]$. The radius R_{str} is called the Strömgren radius. Note that in the static ionisation phase the density in the ionised and neutral medium is the same, so we use n_0 instead of n_i in eq. (1.2). Since S is a strong function of the stellar mass M (Table 1.1), only the most massive stars (earlier than type ∼ B2) are able to form significant H II regions. In a smaller star clusters containing only a handful of such stars, usually the most massive star dominates the total contribution to S. When the majority of photons is used up to counteract ionisations, the ionisation front stops and the strongly overpressured H II region starts expanding into the surrounding medium.

More rigorous view on the transition between the ionising and expanding phase can be obtained from the Rankine–Hugoniot conditions. Since the sound speeds c_{s0} and c_{si} are given from thermodynamic considerations, from the Rankine–Hugoniot conditions it follows, that an ionisation front can separate the neutral and ionised medium as long as $v > 2c_{si}$. After that the media cannot be in a contact and a shock front preceding the ionisation front evolves.

During the expanding phase, the highly overpressured H II region expands and sweeps up the ambient medium into a shell, a sketch illustrating this phase is shown in the left panel of Figure 1.3. In the early stage of the expansion, the thermal pressure in the ambient gas is negligible relative to its ram pressure. At time t, the radius R of the shell is given by

$$R = R_{str} \left(1 + \frac{7c_{si}t}{4R_{str}} \right)^{\frac{4}{7}}. \tag{1.3}$$

Since the sound crossing time through the ionised cavity is shorter than its lifetime t, the ionised gas is approximately isobaric. The gas is of constant density, because it is also isothermal. The gas inside the H II region is almost fully ionised, the change between ionised and neutral gas occurs abruptly at the ionisation front, there are no ionisations in the shell. However, photons less energetic than 13.6eV are present and they penetrate to some depth of the shell, forming a photodissociation region.

As the expansion proceeds, the density and pressure of the ionised gas decrease. At some instant, the pressure of the ionised gas equals to the pressure in the ambient medium, the shock front disappeares, and the expansion halts. The expansion stopping hardly occurs in nature as the massive stars responsible for the ionisation had escaped the main sequence at that time.

The assumption of homogeneous ambient medium is unlikely to be fulfilled in the real world since the ISM is highly inhomogeneous and massive stars are usually formed in the densest parts of MCs. As they form an H II region and it expands, we expect that it will reach places with decreasing density. The density gradient has a strong influence on the evolution: the classical expanding phase with a shock front preceding the IF is possible when $n_0(R)$ decreases slower than $\sim R^{-3/2}$; for steeper density gradients, the IF propagates without a shock front ahead, so the cloud is continually ionised without formation of a dense shell Franco et al. [1990].

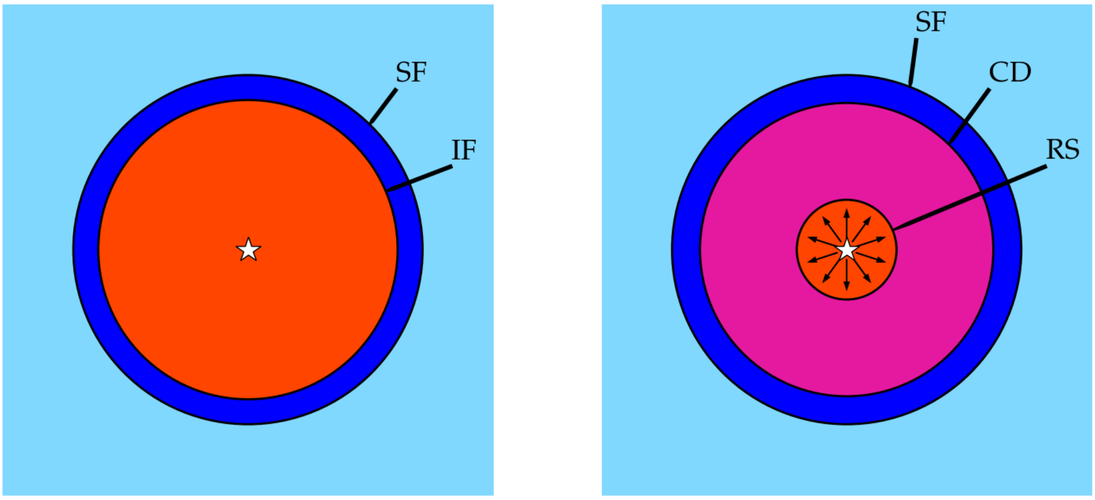

Figure 1.3: Left panel: Structure of the ISM around a photoionising source. The ionisation front (IF) separates an H II region from a cold swept up shell. As the shell expands, it accretes the ambient medium and is confined by a shock front (SF) on its outer surface. Right panel: Structure of a wind blown bubble. The free wind region is situated around the star. Stellar wind passes through the reverse shock (RS) and thermalises in shocked stellar wind region. The ambient medium is swept up by the expanding shell and passes through a shock front (SF). A contact discontinuity (CD) separates shocked stellar wind and shock interstellar gas regions. Note that the figures are not drawn to scale.

Another interesting deviation from the simple model described above occurs when an ionising star is located near a surface of a cloud (this model was propounded by Tenorio-Tagle [1979] and Whitworth [1979]). Although the ionisation front into dense gas in the direction towards the cloud centre proceeds relatively slowly, the ionisation front proceeds fast into the rarefied gas in the opposite direction with a following blow out. In consequence, the overpressured ionised gas is streaming out of the cloud and the density of recombining hydrogen in the direction of cloud centre decreases allowing high ionising photon flux to impinge the cloud. The cloud is photoionised at substantially higher rate than it would be if the source were located in its centre. This process can erode the whole cloud and quench star formation in it.

Stellar wind feedback

Wind blown bubbles around main sequence stars expand into already photoionised gas with density ρ_i. We follow the models proposed by Castor et al. [1975] and Weaver et al. [1977], who assume that the gas is homogeneous, the star is at rest relative to the gas, and that the stellar mass loss $\dot{M}$ and terminal velocity v_∞ are time independent.

The structure of a wind blown bubble is shown in the right panel of Figure 1.3. The innermost region is highly supersonic free stellar wind. The wind is shocked at the reverse shock. The postshock temperature is given by the Rankine-

Hugoniot conditions from which it follows for a gas with $\gamma = 5/3$,

$$T = \frac{3\mu u_0^2}{16R_g}, \tag{1.4}$$

where γ, μ, R_g and u_0 are the ratio of specific heats, mean molecular weight, the ideal gas constant and preshock velocity, respectively. Equation (1.4) holds for strong shocks (i.e. where the pressure of the preshock material is negligible relative to the postshock pressure) which is fulfilled at the reverse shock. According to eq. (1.4) and wind velocities from Table 1.1, the shocked stellar wind is at temperature $\gtrsim 10^7$K. Although stellar wind enters the shock at very high speed, the velocity of the shock front relative to the star is much smaller, typically a few $\mathrm{km\,s^{-1}}$.

The outer surface of the expanding bubble sweeps up the interstellar medium and as a result a shock is formed. Due to high postshock temperature, sound crossing time in both shocked interstellar gas and wind regions is significantly smaller than evolutionary timescale, so the regions are isobaric. They are separated by a contact discontinuity.

The early expansion phase is adiabatic (i.e. the sum of internal and kinetic energy is equal to the energy input $L_w t$) because radiative losses are negligible at this stage. The inserted energy is distributed between shocked wind and shocked interstellar gas region so as the total energy of the former is $5L_w t/11$ and that of the latter $6L_w t/11$. The vast majority of energy in the shocked wind region is in the form of internal energy. In the shocked interstellar gas region, $\sim 60\%$ of energy is in the form of internal energy with the rest in kinetic energy. Radius of the bubble expands as $R \propto (L_w/\rho_i)^{1/5} t^{3/5}$.

Cooling is more important in the shocked interstellar gas region than in the shocked wind region for two reasons: Its density is higher due to higher density of preshock gas and its temperature is lower (eq. (1.4)) since the upstream velocity at the outer shock is smaller than that at the reverse shock. The shocked interstellar gas region cools down when its cooling time becomes comparable to the age of the bubble. This typically occurs after a few 10^3yr. The temperature of the swept up shell drops to $\sim 10^4$K since it is still photoionised by the star.

Shell collapse does not change the slope of the expanding law $R \propto t^{3/5}$ because the expansion is powered by shocked wind region unaffected by the cooling in the shell. In Section 1.2.2, we will see that this behaviour is different from that of supernovae, where expansion slows down after the shell cools.

Shocked interstellar medium diffuses via the contact discontinuity to the shocked wind region. Diffusion is the dominant source of mass coming to the shocked wind region, but has a negligible influence on the total mass of the shocked interstellar gas region.

In the swept up shell, the number of recombinations increases as time proceeds, and at some time, the shell becomes able to absorb all ionising photons. After that, the ionisation front enters the shell from outside, the outer parts of the shell recombine and cools to low temperature $T \lesssim 10^4$K.

1.2.2 Supernovae

Stars more massive than $\simeq 8\mathrm{M}_\odot$ terminate their existence as supernovae. A supernova suddenly releases energy $E_s \sim 10^{51}$erg and mass of a few $\mathrm{M}_\odot$ into the ambient medium. The medium is already influenced by previous action of stellar winds, so its density ρ_0 is lower than the density of the natal cloud. The star could also be ejected from the cluster and it explodes in a low density phase of the ISM.

After the explosion, the supernova ejecta travel at velocity $\sim 1.0 \times 10^4 \mathrm{km\,s^{-1}}$ and sweep up the ambient gas. This phase (*free–expansion*) transforms to the *Sedov–Taylor phase* when the total mass of swept–up material is comparable to the mass of the ejecta. The radius and time when the transition occurs depend on the density in the ambient medium; in the Galaxy, typical values are of order $\sim$ 3pc and $\sim$ 500yr.

In the Sedov–Taylor phase, the sum of the thermal and kinetic energy of the bubble conserves. The bubble radius R obeys power–law expansion $R = \xi_0 (E_s/\rho_0)^{1/5} t^{2/5}$ [Sedov, 1959], where ξ_0 is a dimensionless constant of the order of unity depending only on the ratio of specific heats γ. Supernova bubbles have an inner structure. Density ρ, velocity v and pressure P at radius r inside the bubble at any instant t are given by the similarity solution,

$$\rho(t,r) = \frac{\gamma+1}{\gamma-1}\rho'(\xi) \tag{1.5a}$$

$$v(t,r) = \frac{4r}{5t(\gamma+1)}v'(\xi) \tag{1.5b}$$

$$P(t,r) = \frac{8\rho_0 r^2}{25t^2(\gamma+1)}P'(\xi) \tag{1.5c}$$

where the dimensionless parameter ξ is defined as $\xi \equiv \xi_0 r/R$. The numerical constants on the right hand side of eq. (1.5) follows from the Rankine–Hugoniot conditions at the strong shock. Dimensionless functions $\rho'(\xi)$, $v'(\xi)$ and $P'(\xi)$ for two values of γ are shown in figure 1.4. The majority of the swept up gas is concentrated near the bubble surface. The bubble interior is almost isobaric and at very high temperature $T \gtrsim 10^6$K.

The temperature immediately behind the shock front is given by eq. (1.4), where the upstream velocity u_0 equals the shock velocity $\dot{R} = \mathrm{d}R/\mathrm{d}t$ in our frame of reference. The temperature decreases as the bubble slows down. For the relevant temperatures, the cooling rate increases as the temperature decreases. At some instant, the shell becomes radiative, cools down and pressure inside it drops. Consequently, the hot interior compresses the shell and the elevated density further enhances cooling, so the shell cools down rapidly. After that, the shell enters *Snowplow phase* where its momentum is conserved, and the expansion proceeds at a slower pace $R \propto t^{1/4}$. Typical radii and age of shells when the transition occurs are $\sim$ 20pc and $\sim 4.10^4$yr, respectively.

1.2.3 Other forms of feedback

Feedback starts already during the protostellar stage. As a result of gravitational contraction, protostars emit infrared radiation. Infrared radiation heats the densest regions and increases the local minimum mass which can fragment. Although it influences gas dynamics at only small scales of the order 0.05pc, it makes formation of brown dwarfs more difficult and formation of high mass stars easier [Offner et al., 2009]. It may be responsible for some of the features found

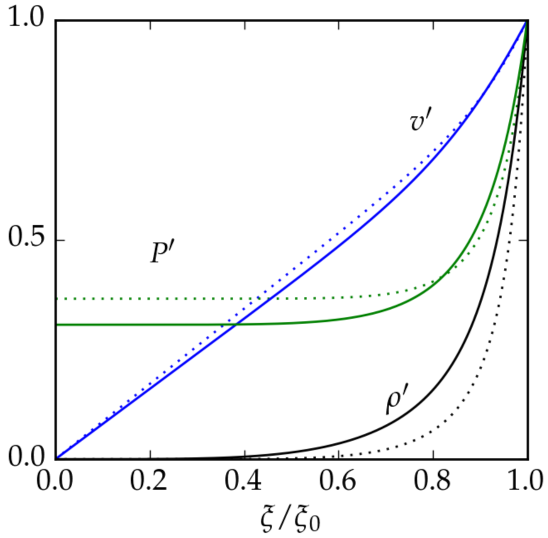

Figure 1.4: Dimensionless functions $\rho'(\xi/\xi_0)$, $v'(\xi/\xi_0)$ and $P'(\xi/\xi_0)$ for monatomic ($\gamma = 5/3$; solid line) and molecular ($\gamma = 7/5$; dotted line) gas.

in the shape of the IMF. Another pre–main sequence feedback are jets adding momentum to their surrounding medium.

Next we mention *radiation feedback*, which is relevant mainly to main sequence stars. Photons produced by main sequence stars carry momentum, which may have an important impact on their ambient medium. Total momentum of photons produced by a star of bolometric luminosity L is L/c, the radiation pressure at a distance R from the star is then $L/(4\pi R^2)$. However, there is no consensus on importance of radiation feedback because it is difficult to calculate interaction of photons with the ambient medium. In one extreme case of optically thin medium with no role of gas, its importance is negligible. In the other extreme, the visible part of radiation can be absorbed by dust in a shell around a star, reradiated in infrared and become trapped in the shell with many interactions. Thus, it is more convenient to express radiation pressure in the form

$$P_{rad} = \frac{f_{trap} L}{4\pi R^2}, \tag{1.6}$$

where coefficient f_{trap} is zero if all photons freely escape, but $f_{trap} \gg 1$ if photons are trapped.

In Section 1.2.1, we briefly described main sequence stellar wind feedback. However, stellar winds also operate when a massive star becomes a red supergiant and then a Wolf–Rayer (WR) star. Particularly important are winds during the WR stage, since mass loss is approximately of two orders of magnitude higher than at the main sequence and the wind velocity is comparable to the main sequence wind velocity. At their beginning, WR winds expand into medium already influenced by previous main sequence and RSG winds, whose density profile decreases as $\sim R^{-2}$. The WR shell then accelerates into the medium of decreased density and breaks into fragments as a result of Rayleigh–Taylor instability. An introduction to winds blown by both main and post–main sequence massive stars is described in Arthur [2007].

1.2.4 Relative importance of the feedback mechanisms and their interplay

Which form of feedback is the most important for shaping the ISM, eventual gas expulsion or sweeping up a dense shell? The situation is more complicated than the simple models described in Sections 1.2.1 and 1.2.2 since real ambient medium is highly inhomogeneous and the action of feedback mechanisms overlap. The models also neglect any influence of gravitational attraction. The importance of feedback mechanisms cannot be simply estimated by comparing their energetic yields. For example, energy released in the form of photoionising photons is typically two orders of magnitude higher than kinetic energy carried by winds. However, the vast majority of energy due to photoionisations is reemited in forbidden lines and escapes, and only a small fraction (typically smaller than 1%) is transferred to kinetic energy. On the other hand, stellar winds can transform $\sim 20\%$ of their kinetic energy into kinetic energy of the shell [Dyson and Williams, 1980].

Simulations are needed to tackle the task; however, the simulations rely on approximations, and no one simulation has incorporated all forms of feedback which may be important. Simulations performed to date typically include up to two different forms of feedback. Achievements as well as questions in understanding feedback and triggering are summarised in [Dale, 2015].

Dale et al. [2012] simulate collapsing MCs with star formation, and self–consistently follow photoionising feedback from the stars. Their simulations are terminated when the age of massive stars reaches 3Myr, i.e. before occurrence of the first supernova. Mass of the clouds is in the range $10^4 - 10^6 \mathrm{M}_\odot$ and their radii are comparable to radii of MCs observed in the Galaxy. Massive stars are formed in the densest filaments and at junctions of dense filaments. The flows feeding the emerging star clusters are highly inhomogeneous. The ability of stars to disrupt the cloud by photoionisation depends on the escape velocity from the H II regions. Since photoionised gas in a closed H II region cannot accelerate at velocity greater than sound speed in ionised gas $c_{si} \sim 10 \mathrm{km\,s^{-1}}$, the H II region cannot expand if escape speed is higher than $\sim 10 \mathrm{km\,s^{-1}}$, and it is swamped by a gas inflow instead. Photoionisation has very little influence on clouds with escape speed above this value.

The same set of MCs studied by Dale et al. [2012] is recalculated with stellar winds only and with photoionisation and winds combined [Dale et al., 2013] and [Dale et al., 2014], respectively. They find that the photoionisation dominates stellar winds in the ability to disrupt clouds. Analytic study done by Matzner [2002] suggests that photoionising feedback dominates combined effects of winds and supernovae.

However, the winds have an influence on morphology of the clouds. Firstly they expel the ionised gas from vicinity of massive stars forming a hole around them. Second, they disperse dense gas in the close vicinity of ionising sources, which influences the shape of the region which can be photoionised; without the action of winds, the close clouds cast sharp shadows, a feature which is not observed Wood and Churchwell [1989]. The morphology of simulated H II regions more resembles than that of observed H II regions after winds are included.

Although Dale et al. [2012] do not model supernova explosions directly, they estimate their disruptive effect by adding momentum carried by supernova ejecta to the cloud and then calculate the fraction of the cloud which becomes unbound. According to this study, only the least massive clusters ($10^4 M_\odot$) lose a significant amount of their gas ($\sim 20\%$), while this effect is negligible for the most massive clusters in their sample $10^6 M_\odot$. At least some fraction of supernova ejecta escapes the least massive clusters, but almost all mass in supernova ejecta is retained in the most massive clusters.

Iffrig and Hennebelle [2015] study the action of supernova feedback on a $10^4 M_\odot$ cloud. A supernova exploding inside the cloud has a strong influence on its dynamics rendering $\sim 50\%$ of its dense gas gravitationally unbound. On the contrary, a supernova exploding outside the cloud has only a minor influence on dynamics of the dense gas. Walch and Naab [2015] investigate supernova explosions inside clouds. If the supernova progenitor already photoionised its surrounding and then explodes, it deposits by factor $1.5\times$ more momentum and energy into the cloud than if it explodes without previous photoionisation.

Combined effect of stellar winds and supernovae on a stratified cloud is investigated by Rogers and Pittard [2013]. The effect of winds is very different than that on a homogeneous cloud (Section 1.2.1). At the beginning, the winds carve rather narrow channels in the directions of lower density. In the followings evolution, the winds stream through these channels, leaving the denser parts of the cloud almost unaffected. Similarly, supernova blast waves pass through the channels, so a significant fraction of molecular gas survives. In their simulations, stellar winds cause more damage to molecular gas than supernovae.

The simulations suggest that the dominant form of feedback is due to photoionisation. Yet, photoionising feedback is unable to accelerate ionised gas above the escape speed for more massive clusters. It implies that another form of feedback is necessary unless massive clusters are formed with SFE almost 100%. Observations of massive star clusters in NGC 4038/39 indicate that many of the clusters are dissolved at young age presumably due to gas expulsion [Whitmore et al., 2007]: radiation feedback seems to be a promising candidate process.

Radiation pressure P_{rad} can dominate thermal pressure P_{phot} caused by photoionisation only for massive star clusters. It is a consequence of different radial dependence of P_{rad} and P_{phot}. Since a balance between ionisations and recombinations is fulfilled during expansion of an H II region, eq. (1.2) holds for any radius R and density of the ionised gas n_i, i.e. P_{phot} is then

$$P_{phot} = n_i k_b T = k_b T \left(\frac{3S}{4\pi\beta^* R^3} \right)^{1/2} . \tag{1.7}$$

There is apparently a characteristic radius R_{ch} which separates regions dominated by one or the other pressure mechanism; $R < R_{ch}$ is dominated by radiation pressure, and $R > R_{ch}$ is dominated by thermal pressure. Assuming $f_{trap} = 2$, Krumholz and Matzner [2009] compare R_{ch} with the Strömgren radius R_{str} and find that $R_{ch}/R_{str} \simeq 0.27(n_3 S_{49})^{2/3}$. Thus, R_{ch} is located inside R_{str} for clusters with $S_{49} \lesssim 7/n_3$ (corresponding cluster mass for $n_3 = 0.1$ is a few $10^4 M_\odot$), and the contribution from radiation pressure is subordinate to the influence of photoionisation. Note that uncertainity in determining factor f_{trap} propagates into uncertainity of numerical factors in the estimates above, so significant deviations may be expected.

Apart from simulations, observations provide another source to estimate the relative importance of various forms of feedback. For a giant H II region 30 Doradus, Lopez et al. [2011] find that its expansion is currently driven by photoionisation. The role of stellar winds and radiation feedback is significantly smaller. The role of radiation feedback was likely dominant in the past, and then decreased as the H II region aged. In a subsequent study of 32 H II regions in the Magellanic Clouds, Lopez et al. [2014] find that 30 of them are dominated by photoionising feedback, and that for 2 of them, the role of photoionisation and trapped radiation is comparable. Thus both simulations and observations suggest that the most important form of feedback is due to photoionisations.

1.3 Triggering caused by stellar feedback

In this section, we introduce three different triggering mechanisms: Collect and Collapse, Globule squeezing and Edge effect due to a change in gravitational potential. We focus on mechanisms which can occur recursively, when a star forming event is triggered by another. For this reason, we do not discuss another triggering mechanisms (e.g. collisions between MCs), even though they are likely of comparable importance. We emphasize Collect and Collapse mechanism because it is the most important feedback process considered in this work.

1.3.1 Collect and Collapse

This model is proposed by Elmegreen and Lada [1977]. During expansion of an H II region, ambient gas accumulates between the shock front and ionisation front (left panel of Figure 1.3). After passing the shock front, the ambient gas is heated, but quickly cools down. Alternatively, an H II region is located near borders of a cloud and part of the cloud is compressed in a layer (Figure 1.5).

Since the layer is dense and cold, it is a suitable site where star formation can take place. It was suggested (e.g. Elmegreen and Lada [1977], Whitworth et al. [1994b]) that a fragmenting layer forms preferentially massive stars. The new generation of massive stars create new H II region, it again sweeps up the ambient gas in a layer, the layer fragments and forms another stellar generation. By this process, star formation can propagate, and several generations of OB associations are formed until the cloud is exhausted or star formation quenched. The necessary condition for star formation to propage is that the layer forms sufficiently massive stars which are able to ignite new H II region. The critical stellar mass is $\sim 8\mathrm{M}_{\odot}$, i.e. spectral type earlier than B2; stars with lower mass would not provide enough ionising photons to create a significant H II region (see strong dependence of the number of ionising photons on spectral type for B stars in Table 1.1).

Various approaches have been applied to estimate the maximum stellar mass which can be formed in a shell or layer. Several estimates have been made and there is no general consensus on the results. Since this issue is one of the main aims of this work, we defer a more in–depth overview to Sections 2.1 and 2.2.

The pattern of Collect and Collapse mechanism can occur under more general circumstances. For example, the shell driving mechanism can be stellar winds or supernovae instead of ionising radiation in case of supershells [McCray and

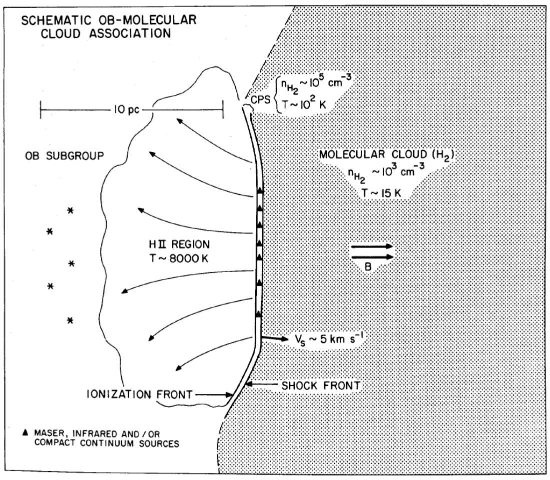

Figure 1.5: An illustration of the Collect and Collapse mechanisms. Massive OB stars ionise an H II region which drives a shock front towards a dense cloud. A cooled post-shock (CPS) layer is collected at the interface between the cloud and H II region. New generation of stars can be formed inside the CPS layer. The figure is adopted from Elmegreen and Lada [1977].

Kafatos, 1987]. Different nature of the driving source modifies the dispersion relation (and the ability to form massive fragments) for the shell via a different expanding law. In another case, the passing shock sweeps an inhomogeneous cloud. Star formation is triggered only in directions where the passing shock swept up significant overdensities, so the wall of the shell consists of several distinct clumps instead of being smooth. Dating of the clumps can potentially prove triggering since almost coeval clumps would be arranged in a shell–like configuration. The clumps are distributed over a structure significantly larger than to be influenced one another, indicating an external source of triggering [Hartmann et al., 2001]. An example is the Taurus molecular cloud.

1.3.2 Globule squeezing

Consider a shock propagating through an inhomogeneous cloud. The shock is driven by an H II region. Assume that the density enhancements (*globules*) already present in the cloud are stable against gravitational collapse. As the shock overruns a globule, the globule is squeezed due to the increase in ambient pressure by a factor of a few thousand and may become gravitationally unstable, collapse and form stars [Elmegreen, 1998].

An exposed globule is also irradiated by the stars which photoionise the H II region (this triggering mechanism is also known as *Radiation driven implosion* or *Cloud–crushing*) [Lefloch and Lazareff, 1994];[Bisbas et al., 2009]. This leads to compression and evaporation of the globule; each process acts in the opposite direction to trigger star formation. While compression promotes star formation, evaporation can disperse the globule before it is able to form stars. Simulating irradiated globules, Bisbas et al. [2011] find that the flux of ionising radiation is a critical factor for triggering. The globule has plenty of time to form stars for small ionising fluxes before being photoevaporated, whereas the globule forms only small number of lower mass stars and is quickly destroyed for higher ionising fluxes.

As the ionised gas streams out of the globule in direction to ionising stars, the globule is accelerated in the opposite direction in an analogy to the rocket propulsion [Oort and Spitzer, 1955]. Consequently, the globule recedes from ionising stars and dissolves later than it would be if it were located at a fixed distance [Bisbas et al., 2009].

1.3.3 Triggered edge effect

Unlike widely discussed *Collect and Collapse* mechanism and *Globule squeezing*, we emphasise that this triggering mechanism is not firmly established in theory of triggering (and not mentioned in any review about triggering we know about). This triggering mechanism does not have a widely recognised name. For the purpose of this work, we refer to it as *Triggered edge effect*.

To illustrate the idea, firstly proposed by Fukuda and Hanawa [2000], consider an infinite long self–gravitating isothermal cylinder (left panel of Figure 1.6). The cylinder is in vertical hydrostatic equilibrium, and its axis is identified with z axis. The equilibrium can be achieved if the mass $M_{CYL.CRIT}$ per unit length fulfills $M_{CYL.CRIT} \leq 2c_s^2/G$, where c_s and G are sound speed inside the cylinder and the gravitational constant, respectively Ostriker [1964]. If there are no perturbations, the cylinder does not fragment, and equipotential curves are cylindrical surfaces alighned with the z axis. The cylinder can be an approximation to an interstellar filament. Consider that feedback from a massive star formed inside the filament at $z = 0$ disperses surrounding parts of the filament from $z = -L/2$ to $z = L/2$. The model cylinder is now divided into two semi–infinite cylinders with a gap between them, which changes the gravitational field the cylinders generate. In analog to electrostatics, where intensity of electric field generated by an charged object is highest where the object is pointed, the gravitational attraction due to the cylinders is highest near their edges (right panel of Fig. 1.6). In context of gravity, this effect is described by Burkert and Hartmann [2004] and further investigated by Pon et al. [2012]. Consequently, the edge of the cylinder located at $z > 0$ accelerates in direction $+z$ and the edge of the other cylinder in direction $-z$, so a clump is assembled near the edge.

This process can repeat recursively, but once triggered, without the necessity of stellar feedback. A clump formed at the edge of a filament distorts gravitational field deeper into the filament, so the fragmentation of the filament gradually propagates inside. The same effect as we described for cylinders occurs at edges of finite sheets.

1.4 Observational evidence for propagating star formation

In this section, we present several observational examples of the collect and collapse mechanism (Section 1.4.1), and one example of the triggered edge effect (Section 1.4.2).

1.4.1 Candidates for collect and collapse mechanism

Since there are many candidates for this mechanism, we select only their very small subset; however, we try to illustrate on this subset the variety of the star forming events, and thus universality of the mechanism. Recall that there is a time delay during which the shock front sweeps up the ambient medium and collects a layer, and the time delay for the layer to collapse and form stars. Thus, we expect to observe two groups of stars of different age, but each of them to be almost coeval. There must be also the correct timing between these two groups.

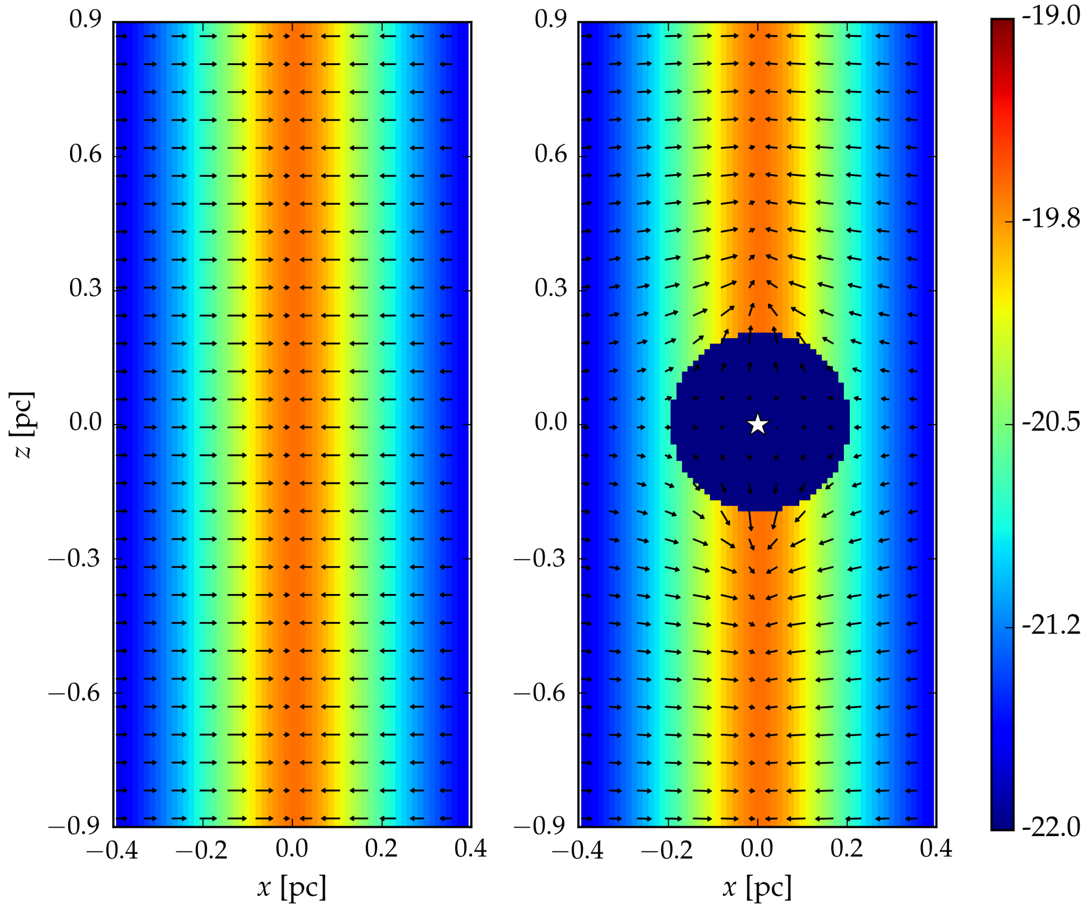

Figure 1.6: An illustration of the triggered edge effect in the case of a cylindrical cloud. The colorscheme represents logarithm of density, and the arrows the gravitational acceleration. Left: The intact cylinder; gravitational acceleration points radially inwards. Right: We mimick feedback of a massive star located at the axis of the cylinder by substituting a part of the cylinder by a sphere with low density. Real H II region would preferentially blow up in the radial direction, but it would have only minor influence on the gravitational field. The decrease in density leads to a change in gravitational acceleration, which has a significant z components near the tips of the cylinders. This would form fragments at the tips. The gravitational acceleration is almost undisturbed by the change at higher distances ($\|z\| \gtrsim 0.6$pc). The gravitational acceleration was calculated by Flash code using mixed boundary conditions.

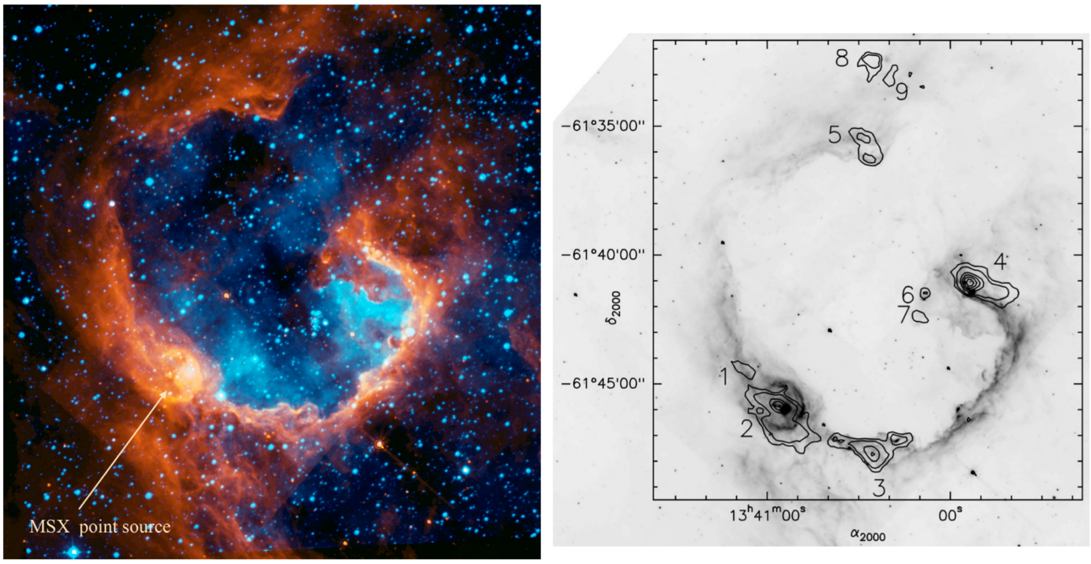

Figure 1.7: Infrared bubble RCW 79. Left panel: The photodissociation region is conspicuous in Spitzer 8 μm filter (orange). The emission is mainly from polycyclyc aromatic hydrocarbons excited by near UV photons leaking out of the H II region. Blue is Hαoriginating from ionised gas from H II region. MSX points source is located in the most massive fragment. Right panel: Millimetre continuum emission (contours) reveal several distinct clumps (numbered 1 to 9) located around its rim. Mass of the most massive clump (clump 2) is approximately $1000\,\mathrm{M}_\odot$. The image on the background is from Spitzer at 8 μm . The figure is adopted from Deharveng et al. [2005].

Since the swept up layer carries momentum, it is reasonable to expect that the groups are moving away from each other.

To prove that a particular star forming region was triggered is not straightforward for following reasons. In many cases, particularly for embedded objects, it is difficult to constrain the age of star forming events with the desired accuracy. In addition, many star forming regions have a complicated morphology making it difficult to determine their formation histories, and to distinguish triggered star formation from the spontaneous one. Thus, it is almost impossible to rule out the scenario in which the two star forming events are a merely coincidence without any causal connection.

Another insight can be obtained from hydrodynamic simulations. Unlike an observer, a simulator can (in the approximation enabled by the code) compare star forming histories between two models; one including stellar feedback self–consistently with the other without stellar feedback. The simulations indicate the difficulty with distinguishing triggered and spontaneous star formation in simulated observations. Despite considerable effort starting with the pioneering work Elmegreen and Lada [1977], there is no widely accepted concensus about the importance of triggering and propagating star formation for star formation in the Galaxy.

Triggering at the borders of H ii regions

Detection of triggered star formation is presumably easiest in H ii regions with simple morphology, where a young cluster is ionising previously quiet and almost homogeneous medium. The swept up medium would be seen at projection as a closed or partial ring with ongoing star formation. When interpreting observations in this Section, we assume that the observed structure is a projection of approximately spherical object. This is also the view presented in works whose results we review. An alternative scenario is introduced in Section 1.4.2.

For this purpose, Deharveng et al. [2005] selected 17 H ii regions with simple morphology containing massive fragments at their borders, which have been studied in–depth in following works. Zavagno et al. [2006] perform a multiwavelength study of bubble RCW 79 (cf. Fig. 1.7). The bubble is located at distance ~ 4.3kpc, and its diameter is 6.4pc. It is ionised by a small cluster of O stars producing in total $S = 10^{49.8}\mathrm{s}^{-1}$ hydrogen ionising photons [Martins et al., 2010]. The shell is probably broken at its north–western edge, and ionised gas is streaming away through this hole. Several massive condensations are observed around its perimeter (cf. right panel of Fig. 1.7), three of them (fragments 2, 3 and 4) contain young massive objects, which could form new H ii regions and propagate star formation in the future.

Sh 217 (cf. Fig. 1.8) is another candidate for triggering [Brand et al., 2011]. The bubble is at distance 4.2kpc and of size $\sim$ 11pc × 9pc. Its ionising source is significantly less luminous than that of RCW 79, it is an O9.5V star ($S = 10^{47.6}\mathrm{s}^{-1}$). The H ii region compressed and swept up a significant amount of dense material westward, where a very young embedded cluster is observed. It is possible that the cluster was formed due to triggering. The cluster is compact, with radius 1.3pc and of mass several hundreads solar masses. Feedback from massive stars in the cluster formed a ultracompact H ii region of radius 0.9pc. Age of the putative older H ii region and the cluster, both necessary to discuss their causal connection, can be obtained only approximately. Brand et al. [2011] provides rough estimates based on current radius, luminosity of ionising sources and assuming an expansion into an initially homogeneous medium according to eq. (1.2) and eq. (1.3). Moreover, there is significant uncertainty of the density of the undisturbed medium n_3 in eq. (1.2). They conclude that the H ii region is $\sim 4\,\mathrm{Myr}$ old, and the cluster is younger than $1.5\,\mathrm{Myr}$, so the cluster could be triggered. For a shell blown by an H ii region, Whitworth et al. [1994a] estimate the time when it fragments, and also fragment masses and radii as a function of luminosity of shell powering stars, initial density of the ambient medium and temperature in the shell. These estimates are in agreement with the estimated ages and the total mass of material associated with the cluster.

Deharveng et al. [2003a] investigate triggering in bubble Sh 104 (cf. Fig. 1.9). The bubble, powered by an O6V star ($S = 10^{49}\mathrm{s}^{-1}$) lies at distance $\sim$ 4kpc and is of radius 4pc. The H ii region is surrounded by a complete ring of dust. Molecular observations reveal four regularly spaced fragments at its rim. Their regular spacing may indicate a collapse of the swept up shell rather than spontaneous formation or compression of independent preexisting clumps, which would be unlikely arranged regularly. The fragments are massive ($\sim 700\,\mathrm{M}_\odot$), and at least one of them contains a ultracompact H ii region, which must have been formed by a massive star. This suggests that star formation will propagate in this shell.

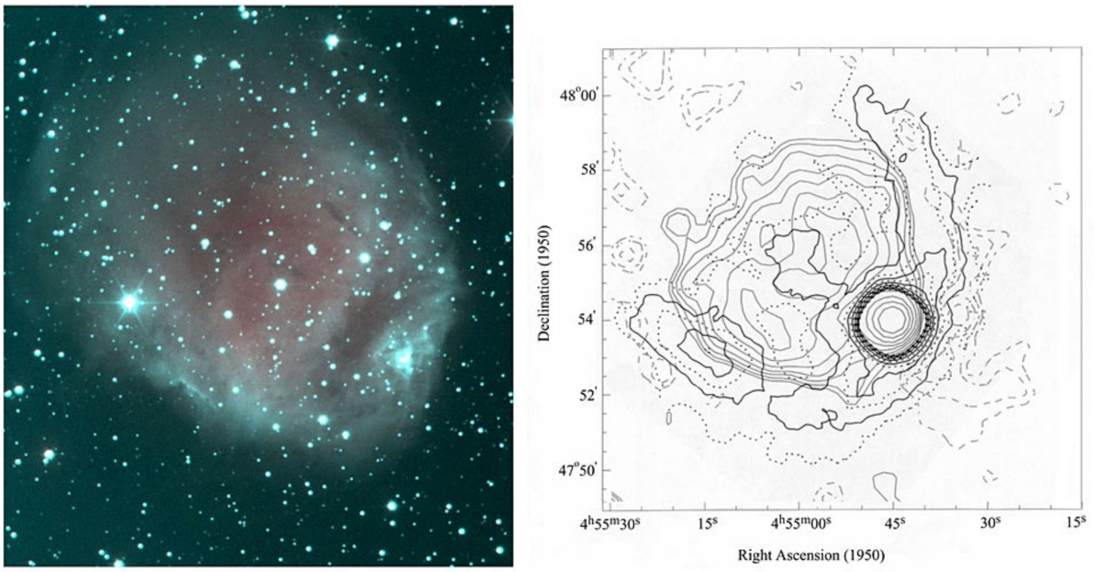

Figure 1.8: Infrared bubble Sh 217. Left panel: Hα(pink) and [S II] emission (turquoise). The latter traces the vicinity of the ionisation front since the ionisation potential of [S II] is lower than that of hydrogen. The embedded cluster is in the western edge of the H ii region. Right panel: Emission in MSX band A (around 8 μm ; solid and dotted contours) superimposed on the radio continuum (grey contours). The former originates from photodissociation region while the latter from ionised gas. Note the radio continuum emission tracing the ultracompact H ii region around the embedded cluster. The figure is adopted from Deharveng et al. [2003b].

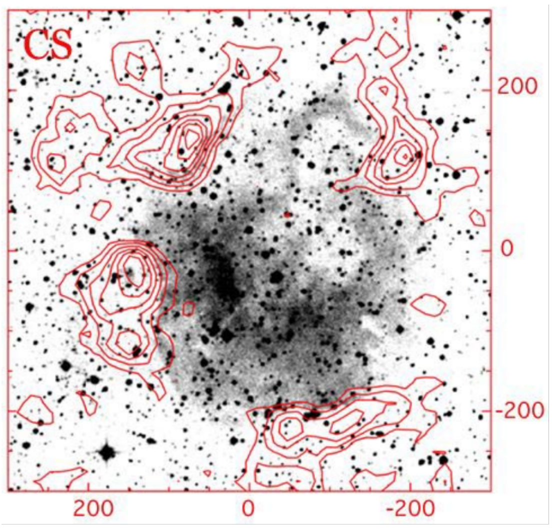

Figure 1.9: Bubble Sh 104 in CS line (contours) superimposed on DSS2 red frame. Four fragments seen in CS are regularly spaced around the rim of the H II region. The figure is adopted from Deharveng et al. [2003a].

Since temperature of the shell is known, one can use the estimate by Whitworth et al. [1994a], to determine initial density n_3. As a consistency check, we can calculate shell radius R (from eq. (5) in Whitworth et al. [1994a]); however, this formula provides $R \simeq 30$pc which is in a sharp contrast with the observed radius 4pc. This discrepancy can be explained either by another formation mechanism of the shell (e.g. geometry), or that formula for shell fragmentation proposed by Whitworth et al. [1994a] is not correct.

Inspecting Spitzer GLIMPSE survey, Churchwell et al. [2006] and Churchwell et al. [2007] identify 322 and 269 infrared shells, respectively. Even more shells (> 5000) have been identified in online citizen science project "The Milky Way Project" [Simpson et al., 2012]. These works constitute a significant amount of information, which provides us with some statistics about triggered star formation. Deharveng et al. [2010] study 102 shells from Churchwell et al. [2006], and they find that at least 86% of them surround H II regions formed by stars earlier than B2. Around 25% of the shells have ultracompact H II regions and/or methanol masers in their walls; both are indicators of massive star formation, which was probably triggered by the H II regions.

Thompson et al. [2012] investigate the correlation of massive young stellar objects with all shells cataloqued by [Churchwell et al., 2006]. The massive young stellar objects are not distributed randomly in field, but are concentrated around rims of the shells. This suggests that the objects were triggered by the action of the shells. The fraction of shells with signposts of triggering, 20% – 25% is in agreement with the result of [Deharveng et al., 2010].

Scorpius–Centaurus OB association

This OB association (hereafter Sco–Cen) is an intensively studied target due to its proximity ~ 140pc to the Sun. The association consists of three subgroups; Upper Scorpius (US), Upper Centaurus–Lupus (UC–L), and Lower Centaurus–Crux (LC–C) (their relative position is shown in Figure 1.10). The projected diameter of each of them is of the order of 50pc, the total mass of US and UC–L is $\sim 2200\mathrm{M}_\odot$, LC–C is less massive with total mass $\sim 1300\mathrm{M}_\odot$ [Blaauw, 1991];[de Geus, 1992]. They contained presumably several O type stars which are already gone as the association aged. Currently, any of the subgroups contains from 16

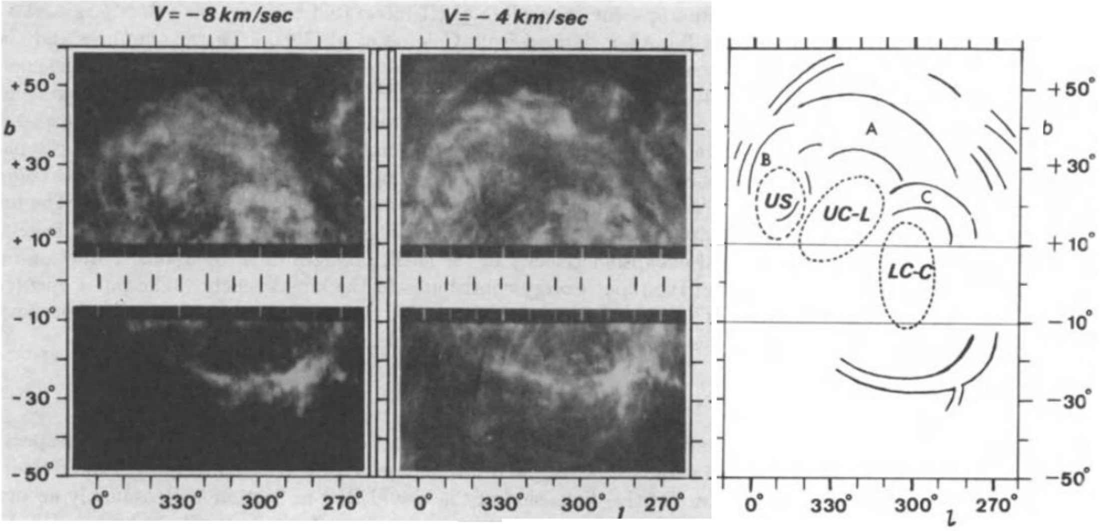

Figure 1.10: Scorpius–Centaurus OB association with its H i arcs and shells. Left and middle panels: H i at velocity $-8 \mathrm{km\,s^{-1}}$ and $-4 \mathrm{km\,s^{-1}}$, respectively. Coordinates are galactic longitude l and latitude b. Right panel: Position of H i arcs and shells relative to three subgroups US, UC–L and LC–C in Scorpius–Centaurus OB association. The figure is adopted from Blaauw [1991].

to 23 stars earlier than type B5. There are possibly more subgroups related to Sco–Cen (e.g. Pipe Nebula or Chamaeleon; [Preibisch and Mamajek, 2008]), but in this work we focus on UC and UC–L since their history is understood better.

The current picture of propagating star formation in Sco–Cen is as follows [Preibisch and Zinnecker, 2007]; [Preibisch and Mamajek, 2008] (Figure 1.11). Star formation began in U–CL around 16 Myr ago. Massive stars dispersed their natal cloud, and their stellar winds and supernova explosions have swept up and have driven a shell (shell A in Fig. 1.10). Comparing the amount of energy released from observed stars and stars which already exploded (their number is estimated from the total mass of the subgroup and the model of IMF) with the kinetic energy of the shell, de Geus [1992] concludes that the shell was likely formed by stars from U–CL.

At the age of ~ 5 Myr, US is significantly younger. Considering current 1D velocity dispersion $1.3 \mathrm{\,km\,s^{-1}}$, and the projected radius 28 pc, US could not begin as a compact embedded cluster with a radius of the order of 1 pc. Instead, the characteristic size of the subgroup was $\sim$ 25 pc at the time of its formation. Taking into account that this subgroup was formed in a single burst at timescale $\sim$ 3 Myr [Slesnick et al., 2008], indicates that an external process coordinated star formation in a cloud of size $\sim$ 25pc during several Myr. Supernova and stellar wind driven shock from UC–L could have been such a triggering mechanism. Indeed, the shell blown by UC–L (shell A in Fig. 1.10) passed through the region of US $4-5$ Myr ago, being a strong candidate for triggering. US also recedes from UC–L, as expected if it was formed due to a shock wave originated in UC–L.

Once formed, massive stars in US started to disperse the cloud, and ~ 1.5 Myr ago, the most massive star exploded as a supernova. This event probably formed shell B shown in Fig. 1.10. The shell encountred and compressed another molecular cloud, ρ Oph approximately 1 Myr ago. Since ρ Oph cloud is a site of recent

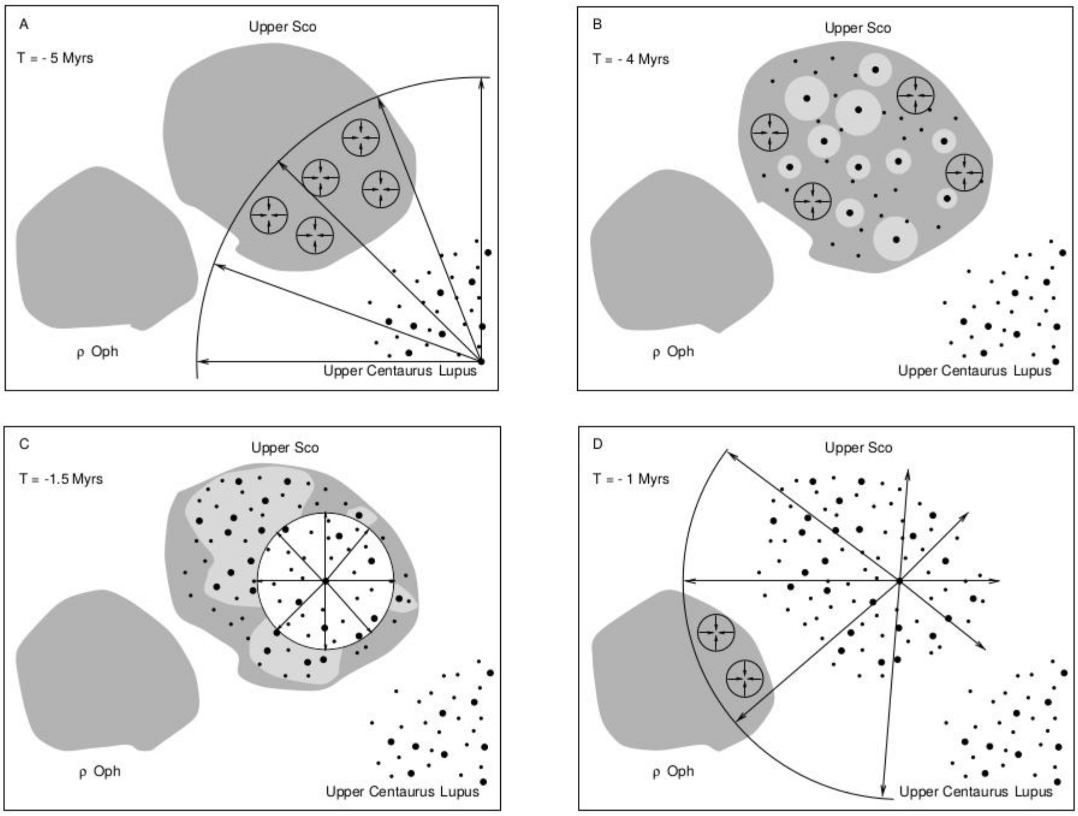

Figure 1.11: Propagating star formation in Scorpius–Centaurus OB association. Shock wave driven by massive stars from UC–L interacts with a MC at the position of US (Panel A), and triggers star formation there (Panel B). The most massive star in US explodes as a supernova and cleares the remaining gas from US (Panel C). The shock from US encounters the ρ Oph cloud and triggers star formation in it (Panel D). The figure is adopted from Preibisch and Zinnecker [1999].

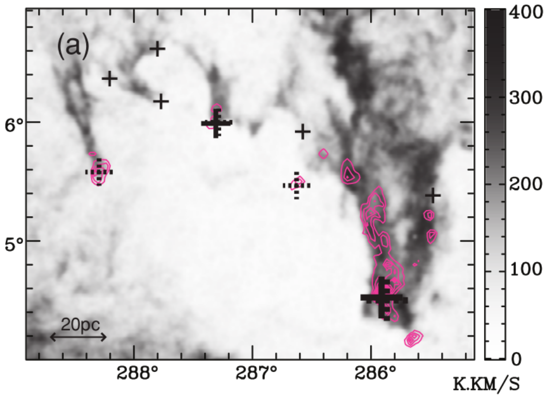

Figure 1.12: Star forming regions in a part of the wall of Carina flare supershell. H I emission is plotted by grayscale, ^{12}CO($J = 1 - 0$) by pink contours, both are integrated over the entire shell velocity range. IRAS young stellar objects candidates are plotted as crosses with radius corresponding to their bolometric luminosity. The young stellar objects are located in the dense CO gas near the edge of the drips indicating their triggering by the passage of the shell. The figure is adopted from Dawson et al. [2011b].

star formation, it is likely that it was triggered by the passing shell.

These findings suggest that star formation has propagated from UC–L to US and then to ρ Oph . Apart from this sequence, star formation history of UC–L and LC–C is more complicated and none of these groups was probably formed in a single short star forming event.

Carina flare supershell

This supershell, located in Sagittarius–Carina arm at the distance 2.6 ± 0.4kpc, is with size 230×360pc and total mass $\sim 1.3 \times 10^6\,\mathrm{M}_\odot$ [Dawson et al., 2008b] an example of triggering at much larger scale than the previous cases. There are vigorous star forming regions and young stellar clusters (e.g. Carina Nebula, Trumpler 14 and 16) near the galactic midplane close to the supershell. The supershell is assymetric in respect to the galactic plane since it has expanded only in one hemisphere (the one with positive galactic altitude b) with no signs of expansion in the other. The assymetry is probably due to a slight displacement of the progenitor massive stars in the direction of positive b. It is not clear whether the supershell will eventually blow out of the disc and become an open chimney feeding the hot interior gas into the galactic halo. The cluster or OB association which has powered the supershell is not observable because it is situated near the midplane where extinction is high. However, its stellar content can be roughly estimated from the energy which the stars imparted to the shell during its age $\sim 10\,$Myr; the source corresponds to ~ 30 stars more massive than $8\mathrm{M}_\odot$ which corresponds to a progenitor cluster of mass $\sim 5 \times 10^3\,\mathrm{M}_\odot$.

Dawson et al. [2011b] and Dawson et al. [2011a] investigate signs of ongoing star formation and the possibility of triggering in the walls of the supershell. The fraction of molecular gas in its wall is 3× higher than in its neighbourhood suggesting its elevated ability to form stars. The wall contains several drips with molecular gas near their tips (Fig. 1.12). Moreover, several tips are coincident with young stellar source candidates indicating incipient star formation. Since the shock wave of the expanding shell passed through these objects in the last a few Myr, star formation in them is probably triggered.

An especially promising target from the point of view of the collect and collapse mechanism is the cloud at $(l, b) = (285.9, 4.5)$ in Fig. 1.12 (cloud 16 in [Dawson et al., 2008a]). Total mass of the cloud is $\sim 5 \times 10^3\,\mathrm{M}_\odot$. From its kinematics, the cloud lies in the shell. The cloud is apparently connected to the shell by filamentary structures which probably feed fresh gas into it, so the cloud forms in situ from the collected material. Moreover, the cloud itself is a site of massive star formation as indicated by an H II region around a young cluster DBSB 49 [Dutra et al., 2003]. The H II region is powered by at least one B0V star and there is evidence for at least two bright embedded massive young stellar objects. The young cluster was very likely triggered by the shell since spontaneous formation of massive stars at $z \simeq 200$pc above galactic midplane is rare.

Triggering in simulations

Taking advantage of the knowledge of star formation history of simulated star forming regions, Dale et al. [2015] seek their simulations for signposts indicating triggering. They run two different models with identical initial conditions: one of them includes photoionising feedback self–consistently, the other is without feedback (control run). Some stars are triggered by photoionisation as they are absent in the control run. On the other hand, photoionisation inhibits formation of some stars which are present in the control run. Overall, photoionisation feedback always decreases the final SFE and star formation rate. The decrease is not crucial, typically it is $\lesssim 20$ % [Dale et al., 2014] for SFE.

Although triggering in simulations is detected by tracing the history of SPH particles which are progenitors for stars, it is hardly possible to decide which stars are triggered from one snapshot of the simulation since the expanding shell sweeps up and redistributes gaseous overdensities which would form stars even in absence of feedback. Consequently, the triggered and spontaneously formed stars are spatially interspersed. The ratio of triggered to spontaneously formed stars increases towards ionisation fronts by factor of ~ 2, however there is still a significant number of spontaneously formed stars near ionisation fronts and in the walls of shells. Likewise, simulated pillar–like structures protruding inside H II regions contain both triggered and spontaneously formed stars. Another possible check, comparison of stellar velocities relative to ionising stars, also do not clearly separate triggered from spontaneously formed stars because the latter are entrained in the expanding shell and acquire shell kinematics.

Simulations of Walch et al. [2015b] present another cautionary tale against oversimplifying the role of feedback and thus the interpretation of triggering events. They model an H II region powered by a single O7V star situated in a highly inhomogeneous medium with dense clumps. The ionisation front reaches larger distances in directions of lower density. Preexisting clumps are exposed inside the H II region and overrun by the ionisation front from sides, whereupon the clumps are laterally compressed. This compression can speed up or trigger star formation in preexisting clumps. The mass of clumps is increased by the medium swept into them and also they collect medium from outwards as they accelerate. This triggering mechanism combines some aspects of both collect and collapse and radiative driven implosion.

The exposed clumps simulated by Walch et al. [2015b] are apparently not the result of the collect and collapse mechanism. If these clumps were observed,

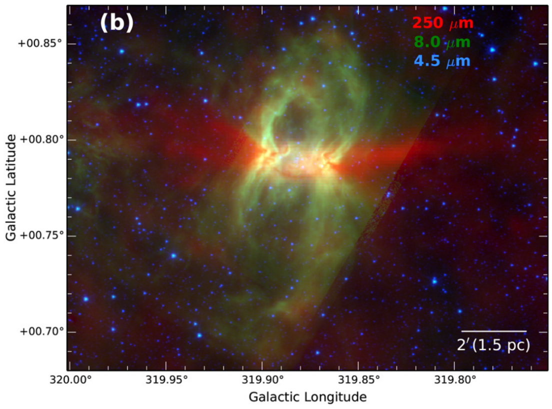

Figure 1.13: G319.88+00.79: A bipolar H II region with signposts of triggering. Red colour shows emission at 250 μm tracing cold natal sheet like cloud seen almost edge on, while green shows emission at 8 μm tracing PAHs emission from the photodissociation region. Note the waist around the ionising stars indicating that the natal cloud was rather sheet like than cylindrical. The figure is taken from Deharveng et al. [2015].

would they be wrongly classified as a triggering due to collect and collapse? To answer this question, Walch et al. [2015b] perform a synthetic observation of their simulation and compare it with star forming region RCW 120, which is by many authors considered as a prototypical example of triggering by the collect and collapse mechanism. The comparison shows close resemblance suggesting that the simulated cloud could be wrongly interpreted as an evidence for triggering due to collect and collapse.

We conclude that triggering probably occurs in nature, but its extent and unambiguous interpretation of morphology of star forming regions in the context of triggering remains unclear.

1.4.2 A candidate for triggered edge effect

Bipolar H II region G319.88+00.79 (Fig. 1.13; Deharveng et al. [2015]) comprises two bubbles identified by Churchwell et al. [2006], S 97 and S 98. The bubbles are part of one structure rather than two colliding independent bubbles driven by two massive stars since the radio continuum emission tracing ionised hydrogen has a distinct peak near the interface between the bubbles and fades smoothly towards the centres of the bubbles. The ionising star is identified and it is of spectral type O8V – O9V ($S = 2 \times 10^{48}\mathrm{s}^{-1}$). There are two simple models for formation of a bipolar H II region; the star forming event takes place either in a cylindrical or sheet like cloud and carves two holes down the density gradient forming two lobes in two opposite directions. The presence of a ring around the ionising star (Fig. 1.13) indicates that the natal cloud was rather sheet like than cylindrical.

Deharveng et al. [2015] identify three clumps located in the ring. Each of them is of mass of a few hundreds of $\mathrm{M}_\odot$ and particle density $10^4\,\mathrm{cm}^{-3}$ to $10^5\,\mathrm{cm}^{-3}$. There are two young stellar objects located in the clumps indicating incipient triggered star formation, and six more objects (probably untriggered) in the surrounding layer.

Since no simulation of photoionising feedback in a sheet like cloud has been performed so far, there is no model with which the observation can be compared. It prevents us from a quantitative discussion of the star formation history in this region. We are left only with qualitative scenarios. Apart from the possibility that the clouds are primordial, they might have been triggered by two different ways. In first scenario, the H ii region swept the material near the midplane into a ring which subsequently fragmented; it is an analog to the collect and collapse mechanism. Alternatively, and more interestingly, as the ionised gas streamed to the lobes effectively punching a hole into the sheet, the change in gravitational attraction induced a pull on the ring sweeping material outwards the ionising star and collecting cold neutral material into the expanding ring. It is a planar analog to cylindrical case of triggered edge effect as illustrated in Figure 1.6.

2. Gravitational fragmentation of shells and layers

In this chapter, we review analytical and semi–analytical estimates of gravitational fragmentation of shells and layers. Their fragmentation is typically described by a dispersion relation. A dispersion relation provides important properties of the fragments, i.e. their mass, radii as well as the characteric time when fragmentation occurs. However, in most cases, several simplifying assumptions are necessary to be adopted in order to find an analytic formula. Consequently, these estimates predict different dispersion relations, each implying different properties of fragments. This is worrying in context of propagating star formation since for the same shell (or a layer) one estimate of the dispersion relation may predict massive fragments enabling massive star formation, so star formation can propagate, while another estimate predicts low mass fragments unable to form sufficiently massive stars, implying quenching of star formation.

In Section 2.1, we review two different analytical estimates of the dispersion relation for an expanding shell. In order to simplify the comparison between the estimates, we express them for a layer by taking the limit of a shell with an infinite radius. In Section 2.2, we compare these estimates with a semi–analytic dispersion relation for a stratified layer. Each of the dispersion relations is different. Since testing the dispersion relations by numerical simulations is one of the goals of this thesis, we find the appropriate dispersion relation in 5.3.2. Then, it is natural to ask which unjustified assumptions lead to incorrect behaviour of two of the estimates. To answer this question (Section 5.3.3), we briefly review the derivations of these dispersion relations.

Apart from gravitational instability, expanding shells can be prone to many other instabilities. We briefly mention some examples in Section 2.3.

Since dispersion relations are an important subject of this work, it is necessary to adopt one convention and use it consistently. We always assume that perturbation quantities have time dependence $\sim \exp(i\omega t)$. Oscillating modes have purely real ω, stable decreasing modes have $\mathrm{Im}(\omega) > 0$. Modes with $\mathrm{Im}(\omega) < 0$ are unstable. For the unstable modes, we distinguish between ones with monotonically increasing amplitude which have purely imaginary ω, and overstable ones (oscillations with growing amplitude) which have ω with non–zero real part.

2.1 Gravitational fragmentation of shells

We review the derivation of two analytical estimates for the dispersion relation of an expanding shell. They are called *Thin shell dispersion relation* and *Pressure assisted gravitational instability* (PAGI).

2.1.1 Thin shell dispersion relation

This approximation is derived by Vishniac [1983] to investigate a spherical shock expanding in the early universe. His work has also been widely adopted to shocks due to stellar feedback (e.g. [Elmegreen, 1994];[Mac Low and Norman, 1993];[Whitworth et al., 1994b]). Vishniac proposes two different instabilities arising in the shell, both of them are derived under the thin shell approximation. Here, we describe the one including self–gravity of the shell. The other, purely hydrodynamic instability due to surface corrugations, is described in Section 2.3.3. Since the derivation of relevant equations, eq. (2.4), can be found in Vishniac [1983], here we point out only the most important ideas and assumptions.

The shell is expanding into an ambient medium of density ρ_{amb}. A shock at radius R_s confines the shell from outside. The shell is confined by a contact discontinuity from inside at radius R_i, so its thickness $h = R_s - R_i$. The pressure acting at the inner surface is P_i.

Next, we define the thin shell approximation,

$$h/R_s < kh \ll 1, \tag{2.1a}$$

$$\frac{\partial}{\partial t} \sim \frac{1}{\tau_p} \ll \frac{c_s}{h} \sim \frac{1}{\tau_{sc}}, \tag{2.1b}$$

which we apply to simplify the problem. In eq. (2.1), k and c_s denote the wavenumber of a perturbation and the sound speed in the shell, respectively. Equation (2.1a) states that wavelengths of perturbations are significantly longer than thickness of the shell. Equation (2.1b) states that the evolution timescale τ_p for any perturbed quantity is significantly longer than the vertical sound crossing time τ_{sc} through the shell, so the shell reacts quasi–statically.

Surface density of the shell is

$$\Sigma(\theta, \phi) = \frac{1}{R_s^2} \int_{R_i}^{R_s} \rho r^2 \mathrm{d}r, \tag{2.2}$$

where r is the radial distance from its centre. Velocity of the shock front is $V_s = \dot{R}_s$, average shell radius is R_0, and shell–averaged transversal velocity $\mathbf{V}_t$

$$\mathbf{V}_t(\theta, \phi) = \frac{1}{\Sigma R_s^2} \int_{R_i}^{R_s} \rho \mathbf{v}_t r^2 \mathrm{d}r, \tag{2.3}$$

where $\mathbf{v}_t$ is the transversal component of velocity inside the shell wall.

Further approximation is to calculate the shell–average of the equation of continuity and momentum,

$$\frac{\partial \Sigma}{\partial t} = -\frac{2V_s\Sigma}{R_s} + \rho_{amb}V_s - \Sigma\nabla_T.\mathbf{V}_t, \tag{2.4a}$$

$$\frac{\partial V_s}{\partial t} = -\frac{1}{\Sigma}(\rho_{amb}V_s^2 - P_i) - \left.\frac{\partial \Phi}{\partial r}\right|_{r=R_s}, \tag{2.4b}$$

$$\frac{\partial \mathbf{V}_t}{\partial t} = -\frac{\rho_{amb}V_s\mathbf{V}_t}{\Sigma} - \frac{V_s\mathbf{V}_t}{R_s} - \left.\nabla_T\Phi\right|_{r=R_s} - \frac{c_s^2\nabla_T\Sigma}{\Sigma} - \frac{P_i\nabla_T R_s}{\Sigma}, \tag{2.4c}$$

where Φ is the gravitational potential and ∇_T are partial derivatives in the transversal directions.

Individual terms on the right–hand side in equations eq. (2.4) have the following meaning. The first to the third terms in eq. (2.4a) represent changes in the surface density due to stretching as the shell expands, accretion of the ambient medium and transversal flows, respectively. The first term in eq. (2.4b) is acceleration due to the difference between the ram pressure from outside and thermal pressure from inside, and the second term is gravitational attraction of the shell. The first to the fifth terms in eq. (2.4c) are due to increase of inertia due to accreted mass, due to stretching, gravitational attraction of inhomogeneities in the shell, the pressure gradient caused by the inhomogeneities and different angle between ram and thermal pressure acting on a corrugated part of the surface, respectively.

Various approximations in general equations eq. (2.4) can be made in order to address particular question. Let suppose for simplicity the expansion velocity V_s to be a constant, so equation eq. (2.4b) is zero. To simplify the equations further, we assume that the surface of the shell is not corrugated, i.e. the position of shock front R_s is independent on coordinates (θ, ϕ) since surface corrugations result in another kind of instability (discussed in Section 2.3.3). Thus we neglect the fifth term on the right–hand side of eq. (2.4c). This simplification is adopted and discussed in Elmegreen [1994].

We seek a solution for a linear perturbation, i.e. any quantity q is a sum of unperturbed q_0 and perturbed $\tilde{q}_1$ part where $\|\tilde{q}_1\| \ll q_0$. The unperturbed part of Σ is non–zero, while the unperturbed part of $\mathbf{V}_t$ is zero. Perturbation equations are

$$\frac{\partial \tilde{\Sigma}_1}{\partial t} = -\frac{2V_s\tilde{\Sigma}_1}{R_s} - \Sigma_0 \nabla_T . \tilde{\mathbf{V}}_{t_1}, \tag{2.5a}$$

$$\frac{\partial \tilde{\mathbf{V}}_{t_1}}{\partial t} = -\frac{\rho_{amb} V_s \tilde{\mathbf{V}}_{t_1}}{\Sigma_0} - \frac{V_s \tilde{\mathbf{V}}_{t_1}}{R_s} - \nabla_T \tilde{\Phi}_1 \bigg|_{r=R_s} - \frac{c_s^2 \nabla_T \tilde{\Sigma}_1}{\Sigma_0}. \tag{2.5b}$$

To analyse linear perturbations of a shell, we seek the perturbation solution in the form $\tilde{q}_1 = q_1 \exp(i\omega t) Y_{lm}$, where Y_{lm} is a spherical harmonics with angular wavenumber l. Note that spherical harmonics are angular eigenfunctions of the Laplace operator, $\Delta Y_{lm} = -l(l+1)Y_{lm}/R_s^2$, a useful identity to handle with eq. (2.5) to get the dispersion relation. Poisson's equation for a non–corrugated shell is then

$$\Delta \Phi_1 = -\frac{2}{2l+1} 2\pi G \Sigma_1 R_s \Delta Y_{lm}. \tag{2.6}$$

From eq. (2.5) and eq. (2.6), and substituting $\rho_{amb} = 3\Sigma_0/R_s$ in eq. (2.5b), we obtain the dispersion relation for a shell expanding into a homogeneous medium

$$\omega = \frac{3V_s i}{R_s} \pm i\sqrt{\frac{V_s^2}{R_s^2} + \frac{4\pi l(l+1)G\Sigma_0}{(2l+1)R_s} - \frac{l(l+1)c_s^2}{R_0^2}}. \tag{2.7}$$

The limit of this equation for high wavenumbers $l \gg 1$ is found by Elmegreen [1994].

For a shell expanding into a vacuum, the only difference in equations eq. (2.5) is that the first term on the right hand side in eq. (2.5b) equals zero. By the same process, we arrive at the dispersion relation

$$\omega = \frac{3V_s i}{2R_s} \pm i\sqrt{\frac{V_s^2}{4R_s^2} + \frac{4\pi l(l+1)G\Sigma_0}{(2l+1)R_s} - \frac{l(l+1)c_s^2}{R_0^2}}, \tag{2.8}$$

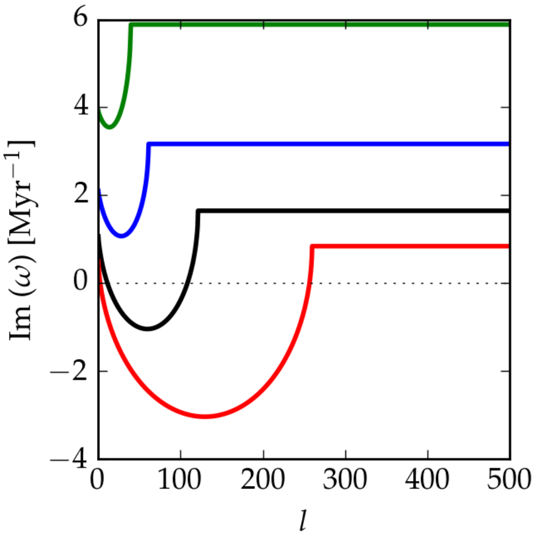

Figure 2.1: Thin shell dispersion relation for expansion into an homogeneous medium, eq. (2.7). The imaginary part of the dispersion relation is plotted at 0.25Myr (green line), 0.5Myr (blue line), 1.0Myr (black line) and 2.0Myr (red line). The transition between stable and unstable modes is shown by a dashed horizontal line.

which is derived in Wünsch et al. [2010].

We use a shell driven by an H II region to illustrate the qualitative behaviour of the dispersion relation in eq. (2.7), see Figure 2.1. The nature of the source enters this simple analysis only via the expanding law; supernova or wind blown bubbles would not qualitatively change the result. The example shell is powered by a massive star emitting 10^{49} ionising photons per second, has sound speed $c_s = 0.2\mathrm{km\,s}^{-1}$, and the shell expands into an ambient medium of particle density $n = 10^3\mathrm{cm}^{-3}$. The range of unstable wavenumbers is given by the relative importance of self–gravity on one hand, and stretching and thermal pressure trying to stabilise a fragment on the other. At the early stage of expansion (time 0.25Myr and 0.5Myr), all wavenumbers are stabilised by stretching. As the shell expands and slows down, the role of stretching decreases and self–gravity starts to be important. Consequently, a range of unstable wavenumbers appears (the line at 1.0Myr). Stretching still dominates self–gravity for the largest wavelengths (smallest l), while small wavelengths (large l) are supported by the thermal pressure; both confining the range of unstable wavenumbers. As the shell slows down further, the growth rate of unstable modes increases. The range of unstable wavenumbers also shifts towards higher l because during the expansion, Σ increases making self–gravity more important, and the wavelength corresponding to particular l increases making pressure gradients less important.

2.1.2 Pressure assisted gravitational instability (PAGI)

Dale et al. [2009] study the dispersion relation of a shell expanding into very dense and hot ambient medium. The medium has a negligible dynamical influence on the shell, but it confines the shell with thermal pressure P_{ext}. They find that the numerical dispersion relation (i.e. the one measured in simulations) depends on P_{ext}. Since the thin shell dispersion relation does not include the role of the external pressure, the thin shell dispersion relation is not the exact description for fragmentation of a pressure confined shell. Moreover, they find that the numerical dispersion relation differs from the thin shell dispersion relation even when P_{ext} is negligible. In a subsequent paper, Wünsch et al. [2010] propose a correction to the thin shell dispersion relation and include there the role of the external pressure P_{ext}.

Wünsch et al. [2010] investigate the stability of a fragment located inside the wall of a shell (see Figure 2.2). The instantaneous radius and velocity of the shell are R_s and V_s, respectively. The fragment is modelled as a homogeneous oblate spheroid of total mass M, and with semi–major axis r and semi–minor axis z. The spheroid is isothermal with sound speed c_s. The spheroid is embedded in gas of pressure P_{ext}, but with no dynamical influence on the spheroid. To simplify the analysis, they neglect the effects of shell curvature, so the results can be applied only to fragments with $r \ll R_s$; this approximation is reasonable because the most unstable fragments we are interested in obey this inequality. The acceleration acting on an element at the equator of the spheroid is then [Boyd and Whitworth, 2005]

$$\begin{aligned} \ddot{r} &= -\frac{3GM}{2r^2}\left\{\frac{\cos^{-1}(z/r)}{(1-(z/r)^2)^{3/2}} - \frac{z/r}{1-(z/r)^2}\right\} \\ &\quad -\frac{20\pi r z P_{ext}}{3M} + \frac{5c_s^2}{r}. \end{aligned} \tag{2.9}$$

Since the spheroid is a part of the shell, it stretches as the shell expands. Stretching velocity at the equator is

$$\dot{r} = rV_s/R_s. \tag{2.10}$$

Wünsch et al. [2010] estimate the instability growth rate from the initial collapse rate of the spheroid. Evolution of the radius r obeys $r(t) = r_0 + \dot{r}_0 t + \ddot{r}_0 t^2/2$, where subscript 0 denotes radius at time zero. After time t_ϵ,

$$(\epsilon - 1)r_0 = \dot{r}_0 t_\epsilon + \frac{1}{2}\ddot{r}_0 t_\epsilon^2, \tag{2.11}$$

the initial radius r_0 shrinks by a factor ϵ to radius $r = r_0(1-\epsilon)$. The spheroid of radius r_0 approximates a perturbation of angular wavenumber $l = \pi R_s/r_0$. Instability growth rate is approximately $\omega = -i/t_\epsilon$. Expressing time from eq. (2.11) and using eq. (2.9) and eq. (2.10), setting the spheroid semi–minor axis z to the shell half–thickness H, they found

$$\begin{aligned} \omega_\epsilon(l) &= i\frac{\dot{r}_0}{2\epsilon r_0} - i\sqrt{\left(\frac{\dot{r}_0}{2\epsilon r_0}\right)^2 - \frac{\ddot{r}_0}{2\epsilon r_0}} \\ &= \frac{iV_s}{2\epsilon R_s} - \frac{i}{\sqrt{\epsilon}}\left\{\frac{1}{\epsilon}\left(\frac{V_s}{2R_s}\right)^2\right. \\ &\quad + \frac{3G\Sigma_0 l}{4R_s}\left(\frac{\cos^{-1}(Hl/R_s\pi) - \sqrt{l^2H^2/(\pi R_s)^2 - 1}}{(1 - l^2H^2/(R_s\pi)^2)^{3/2}}\right) \\ &\quad - \frac{5c_s^2 l^2}{2R_s^2\pi^2} \\ &\quad \left. + \frac{10P_{ext}c_s^2 l^2}{3R_s^2\pi^2(2P_{ext} + \pi G\Sigma_0^2)}\right\}^{\frac{1}{2}}. \end{aligned} \tag{2.12}$$

Equation 2.12 is the PAGI dispersion relation. Its structure is similar to that of the thin shell dispersion relation. The meaning of the terms after the second

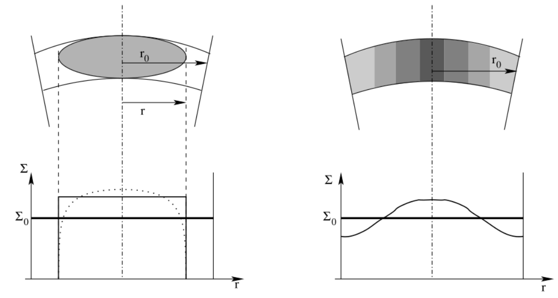

Figure 2.2: Comparison between models of a perturbation in PAGI (left) and in the thin shell dispersion relation (right). In the case of PAGI, the perturbation is modelled by an oblate spheroid, while in the case of thin shell dispersion relation, the perturbation is modelled by a sine function. The figure is adopted from Wünsch et al. [2010].

equal sign is as follows. The first two terms are due to stretching, the third term represents self–gravity and the fourth term the support of the thermal pressure. The fifth term is due to the external pressure.

All but the fifth term have an analog in the thin shell approximation 2.8. However, the exact numerical value of the terms is different from that of the thin shell (see for example the coefficient in the pressure support term $\sim c_s^2 l^2/R_s^2$). The comparison between PAGI and the thin shell dispersion relation is deferred to Section 2.2.2. We discuss the role of parameter ϵ in Section 2.2.2.

2.2 Gravitational fragmentation of layers

We firstly review the properties of the hydrostatic equilibrium for a vertically stratified isothermal layer (Section 2.2.1). Then, in Section 2.2.1, we review the derivation of the dispersion relation for this layer. In Section 2.2.2, we compare this dispersion relation with the thin shell dispersion relation and PAGI. We discuss differences between these dispersion relations as well as their implications for mass of resulting fragments. In Section 2.2.3, we illustrate that the knowledge of the correct approximation to the dispersion relation is crutial to discuss whether star formation can propagate. In Section 2.2.4, we review the results of second order perturbation theory of fragmenting layers.

2.2.1 Dispersion relation of a vertically stratified layer

To study the dispersion relation, we shall first known the unperturbed state. For simplicity, we assume that the layer is isothermal with sound speed c_s, although modifications for polytropic layers were found [Kim et al., 2012], and references therein. Except for its self–gravity, no other force acts on the layer. Both surfaces of the layer are confined by external pressure P_{ext}.

The dispersion relation for a layer with zero confining pressure is found by Simon [1965]. On the other hand, the dispersion relation in the limit of very high P_{ext} is found by Goldreich and Lynden-Bell [1965]. Elmegreen and Elmegreen [1978] find a general dispersion relation for any value of P_{ext}. The nature of individual modes is investigated by Kim et al. [2012], whose approach we follow in this work.

We set our coordinate system so as the normal to the layer points in the direction z, and that the layer is semi–infinite in the directions x and y. We search for the solution to first order in the perturbed quantities, i.e. $q = q_0 +$

$\tilde{q}_1$ where q_0 and $\tilde{q}_1$ are the unperturbed and perturbed part of any quantity q, respectively. The quantities in question are density ρ, velocity $\mathbf{u}$, pressure P and gravitational potential Φ. Note that the unperturbed part of velocity $\mathbf{u}_0$ is zero. The unperturbed part of any quantity is a function of z only. The equation of continuity, the momentum equation and Poisson's equation

$$\begin{aligned} \frac{\partial \rho}{\partial t} + \nabla.(\rho \mathbf{u}) &= 0 && (2.13)\\ \frac{\partial \mathbf{u}}{\partial t} + \mathbf{u}.\nabla \mathbf{u} &= -\frac{\nabla P}{\rho} - \nabla \Phi && (2.14)\\ \Delta \Phi &= 4\pi G \rho && (2.15) \end{aligned}$$

are split into the unperturbed part

$$\begin{aligned} 0 &= -\frac{1}{\rho_0(z)}\frac{\partial P_0}{\partial z} - \frac{\partial \Phi_0}{\partial z} && (2.16)\\ \Delta \Phi_0 &= 4\pi G \rho_0(z) && (2.17) \end{aligned}$$

and the perturbed part

$$\begin{aligned} \frac{\partial \tilde{\rho}_1}{\partial t} + \nabla.(\rho_0 \tilde{\mathbf{u}}_1) &= 0 && (2.18)\\ \frac{\partial \tilde{\mathbf{u}}_1}{\partial t} &= \frac{\tilde{\rho}_1}{\rho_0^2}\nabla P_0 - \frac{1}{\rho_0}\nabla \tilde{P}_1 - \nabla \tilde{\Phi}_1, && (2.19)\\ \Delta \tilde{\Phi}_1 &= 4\pi G \tilde{\rho}_1(z). && (2.20) \end{aligned}$$

The hydrostatic equilibrium

The solution to eq. (2.16) and eq. (2.17) was found by [Spitzer, 1942]; The density $\rho_0(z)$ and potential $\Phi_0(z)$ of the layer are

$$\begin{aligned} \rho_0(z) &= \frac{\rho_{00}}{\cosh^2(z/H_0)}, && (2.21)\\ \Phi_0(z) &= 2c_s^2 \ln\left(\cosh(z/H_0)\right), && (2.22) \end{aligned}$$

where ρ_{00} is the midplane density, and

$$H_0 = \frac{c_s}{\sqrt{2\pi G \rho_{00}}} \qquad (2.23)$$

is the vertical scale height.

Surface density of the layer Σ_0 is defined

$$\Sigma_0 = \int_{-z_{max}}^{+z_{max}} \rho_0(z) \mathrm{d}z, \qquad (2.24)$$

where $\pm z_{max}$ is the boundary of the layer. From the condition that the thermal pressure $c_s^2 \rho(z)$ equals the external pressure P_{ext} at $\pm z_{max}$ and eq. (2.21), we yield

$$z_{max} = H_0 \,\mathrm{acosh}\left(\sqrt{\frac{\rho_{00} c_s^2}{P_{ext}}}\right), \qquad (2.25)$$

which for strongly pressure confined layers ($P_{ext} \gg \pi G \Sigma^2$) takes the form

$$z_{max} \doteq \frac{c_s^2 \Sigma_0}{\sqrt{2} P_{ext}}. \tag{2.26}$$

Integrating eq. (2.24), and using eq. (2.23) and eq. (2.25), one finds the relation between midplane density ρ_{00} and surface density Σ_0,

$$\rho_{00} = \frac{\pi G \Sigma_0^2}{2 c_s^2} \left(1 + \frac{2 P_{ext}}{\pi G \Sigma_0^2} \right) \tag{2.27}$$

To study the dispersion relation, it is very convenient to use dimensionless parameter

$$A = \frac{1}{\sqrt{1 + \frac{2 P_{ext}}{\pi G \Sigma_0^2}}}. \tag{2.28}$$

Parameter A measures the relative importance of external pressure to self–gravity for a given layer. Expressed by A, the density contrast between surface $\rho_0(z_{max})$ and the midplane ρ_{00} of the layer is $\rho_0(z_{max})/\rho_{00} = 1 - A^2$.

Consider a layer with fixed Σ_0, and let external pressure P_{ext} be variable. In the limit of negligible P_{ext}, $A \to 1^-$. Layers with A close to 1 are self–gravity dominated. These layers are significantly stratified with a strong density contrast. As P_{ext} increases, A monotonically decreases and $A \to 0$ in the limit of $P_{ext} \gg \pi G \Sigma_0^2$. Layers with A close to 0 are pressure dominated. These layers are truncated by external pressure at $z_{max} \ll H_0$, so they are of almost uniform density.

Another useful quantity is the half thickness of the layer

$$H = \frac{\Sigma_0}{2 \rho_{00}} = A H_0 = \frac{A^2 c_s^2}{\pi G \Sigma_0} = \frac{c_s^2 \Sigma_0}{2 P_{ext} + \pi G \Sigma_0^2}, \tag{2.29}$$

where the alternative expressions were obtained with the help of eq. (2.23), eq. (2.27) and eq. (2.28). Vertical acceleration is

$$g_0(z) = -\frac{\mathrm{d}\Phi_0}{\mathrm{d}z} = -\frac{2 c_s^2}{H_0} \tanh(z/H_0). \tag{2.30}$$

At the layer boundary $\pm z_{max}$, eq. (2.30) with eq. (2.25) recovers the result which also follows from the Gauss's theorem,

$$g_0(z_{max}) = -2\pi G \Sigma_0. \tag{2.31}$$

We note that the major focus of this work is on another than spherically symmetric systems. Some properties of layers have no analogs in spherical clouds, and may seem counterintuitive on the first sight. The most relevant features to this work are the questions of hydrostatic equilibrium and the form of the dispersion relation. We discuss the former here, while the latter is discussed in Section 2.2.1.

Assume that c_s is fixed. An interesting property of the layers is that for any Σ_0, even arbitrarily large, there exists an equilibrium configuration. In other words, we cannot make the layer gravitationally collapse in direction z by adding matter into it (e.g. by accretion). Likewise, the collapse cannot by achieved by any increase in P_{ext}.

This is a unique property of the geometry, and it is absent in spherical symmetry. Hydrostatic equilibrium of an isothermal cloud is a Bonnor–Ebert sphere [Ebert, 1955];[Bonnor, 1956]. For given P_{ext}, there is a mass threshold above which no equilibrium exists and the sphere collapses. Likewise, for a given mass, there is a pressure threshold with the same property.

Systems with cylindrical symmetry (e.g. filaments) also have characteristic features regarding their stability, in some sense combining properties of layers and spherical clouds. For given P_{ext}, an isothermal cylinder can be gravitationally unstable if its mass per unit length exceeds a threshold [Ostriker, 1964];[Inutsuka and Miyama, 1992]. On the other hand, if the mass is below the threshold, an isothermal cylinder is stable to any increase in P_{ext} [Ebert, 1955].

How does a layer adjust to increasing Σ_0 so as to find the hydrostatic equilibrium? Let c_s and P_{ext} be fixed, and we increase Σ_0. Starting from pressure dominated layer, the thickness of the layer increases with increasing Σ_0 (see eq. (2.29)). As the role of self–gravity increases with Σ_0, the thickenning slows down, and the layer attains maximum thickness for $A = 1/\sqrt{2}$ [1]. Increasing Σ_0 further, the layer is pulled towards its midplane and its thickness decreases.

The dispersion relation

In the previous Section, we see that we cannot make the layer collapse by increasing Σ_0 nor increasing P_{ext}. However, the layer can be unstable in respect to small perturbations in transversal directions x and y. The layer is always stable to perturbations in the direction z as was found by [Goldreich and Lynden-Bell, 1965]. Thus, it is natural to seek for a solution in the form $\tilde{q}_1 = q_1(z)\exp(i(\omega t + kx))$. Substituting this into the perturbation equations eq. (2.18), eq. (2.19) and eq. (2.20), using ideal gas law for isothermal gas $P = c_s^2\rho$, define Lagrangian displacement $\tilde{\mathbf{u}} = \partial\tilde{\boldsymbol{\xi}}/\partial t$ and perturbed enthalpy $h_1 = P_1/\rho_0$, one yields

$$\frac{\mathrm{d}\xi_{1z}}{\mathrm{d}z} = \frac{k^2}{\omega^2}(\Phi_1 + h_1) - \frac{1}{c_s^2}(h_1 + g_0(z)\xi_{1z}), \tag{2.32}$$

$$\frac{\mathrm{d}h_1}{\mathrm{d}z} = \omega^2\xi_{1z} - \Phi_1', \tag{2.33}$$

$$\frac{\mathrm{d}\Phi_1}{\mathrm{d}z} = \Phi_1', \tag{2.34}$$

$$\frac{\mathrm{d}\Phi_1'}{\mathrm{d}z} = k^2\Phi_1 + \frac{4\pi G\rho_0(z)h_1}{c_s^2}. \tag{2.35}$$

These equations must be supplied with boundary conditions. Following Kim et al. [2012], we study only even symmetry modes because odd symmetry modes are always stable. Even symmetry modes satisfy $\xi_{1z}(z) = -\xi_{1z}(-z)$, $h_1(z) = h_1(-z)$ and $\Phi_1(z) = \Phi_1(-z)$. Thus we get two boundary conditions, which are

---

[1] This is not a general result and serves only as an illustration. In this example, we vary Σ_0 and keep P_{ext} fixed. For a general expanding shell, both Σ_0 and P_{ext} vary and the highest layer thickness is attained for different A.

evaluated at the midplane

$$\begin{aligned}\xi_{1z}(0) &= 0, \qquad (2.36)\\ \Phi_1'(0) &= 0. \qquad (2.37)\end{aligned}$$

Two other boundary conditions are evaluated at the upper surface z_{max}. From Poisson's equation, it follows

$$-k_x \Phi_1(z_{max}) - \frac{\mathrm{d}\Phi_1}{\mathrm{d}z}(z_{max}) = 4\pi G \rho_0(z_{max}) \xi_{1z}(z_{max}). \qquad (2.38)$$

We distinguish between two kinds of boundary conditions; First one has surface at fixed position (rigid boundary), the other has surface, which can freely move (free boundary). The former, and the latter are

$$\xi_{1z}(z_{max}) = 0, \qquad (2.39a)$$

$$h_1(z_{max}) = -g_0(z_{max}) \xi_{1z}(z_{max}). \qquad (2.39b)$$

Equations from (2.32) to (2.35) do not constitute a set of equations with constant coefficients as is highlighted by writing explicit dependence of functions $\rho_0(z)$ and $g_0(z)$. No general analytical solution to these equations is known.

However, for the limitting cases $A \to 0$ and $A \to 1$ either exact solutions or good approximations can be found. Firstly, we review the solutions for layers with free boundary conditions. There is an exact solution in the limit $A \to 0$ (pressure dominated layers) [Goldreich and Lynden-Bell, 1965];[Doroshkevich, 1980],

$$\frac{\omega^2}{2\pi G \rho_{00}} = 2kH \tanh(kH) - (1 - \exp(-2kH)). \qquad (2.40)$$

There is an approximate solution for self–gravity dominated layers (when $A \to 1$),

$$\frac{\omega^2}{2\pi G \rho_{00}} = (kH)^2 - \frac{2kH}{1 + kH}. \qquad (2.41)$$

The dispersion relation for layers with rigid boundary conditions in the limit $A \to 0$ reads

$$\frac{\omega^2}{2\pi G \rho_{00}} = (kH)^2 - 2kH. \qquad (2.42)$$

In Section 2.2.2, we will see that eq. (2.42) is exactly the thin shell dispersion relation for an infinite slab. In the limit $A \to 1$, the dispersion relation is the same as that of a layer with free boundaries, i.e. eq. (2.41).

2.2.2 Comparison between the dispersion relations

We introduce the following notation to clarify the comparison of dispersion relations for layers. Instead of their full names, we refer to the thin shell dispersion relation and PAGI as V83 and W10, respectively. We refer to the dispersion relation of a stratifiad layer (i.e. the one obtained by numerical integration from

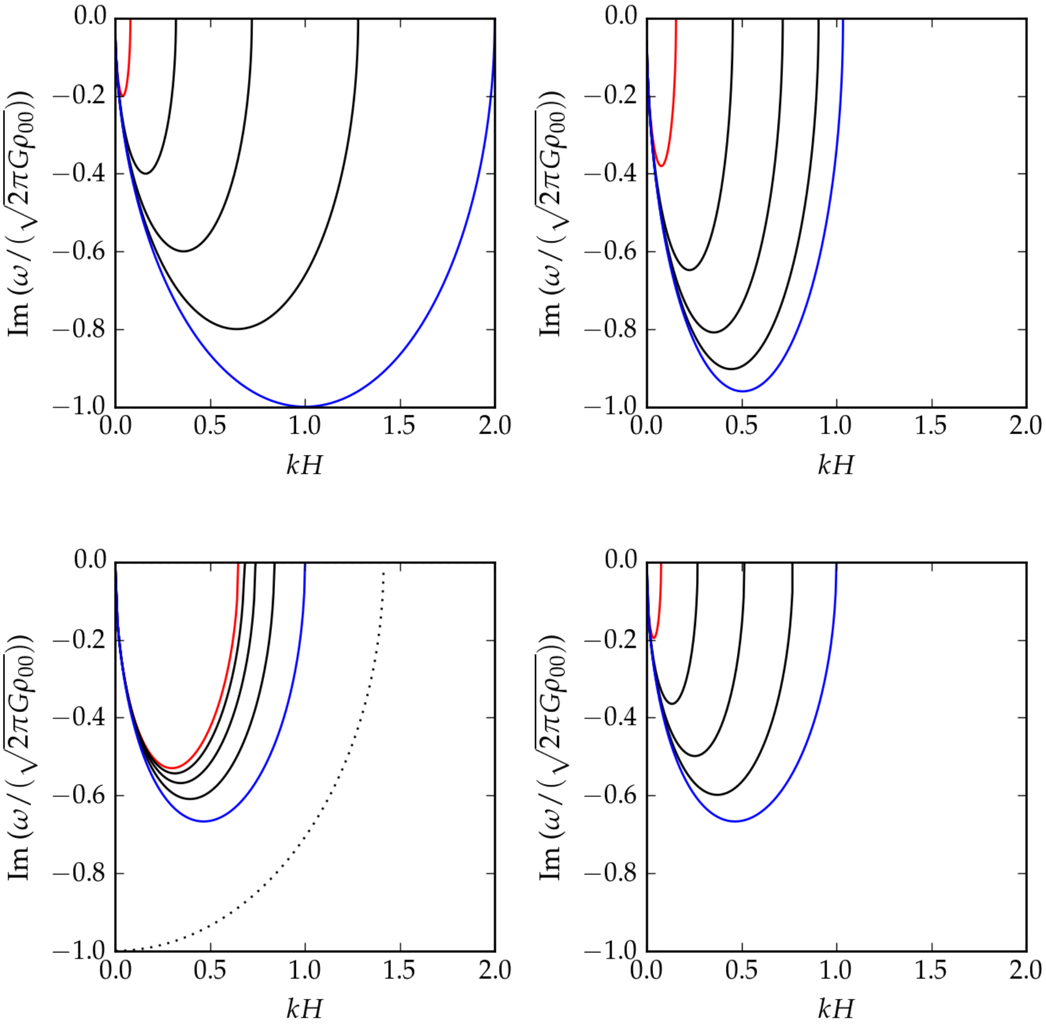

Figure 2.3: Comparison of dispersion relations of layers. Top row: Thin shell dispersion relation (left panel) and PAGI with $\epsilon = 0.1$ (right panel). Bottom row: Dispersion relation of vertically stratified layers with free (left panel) and rigid (right panel) boundary conditions. The bottom left panel shows the Jeans dispersion relation (dotted line) with $\omega^2/2$. Each dispersion relation is plotted for $A = 0.2$, $A = 0.4$, $A = 0.6$, $A = 0.8$ and $A = 0.9999$. Two extreme values of A, $A = 0.2$ and $A = 0.9999$ are plotted with red and blue lines, respectively; the ordering of curves between the extreme values changes smoothly with parameter A.

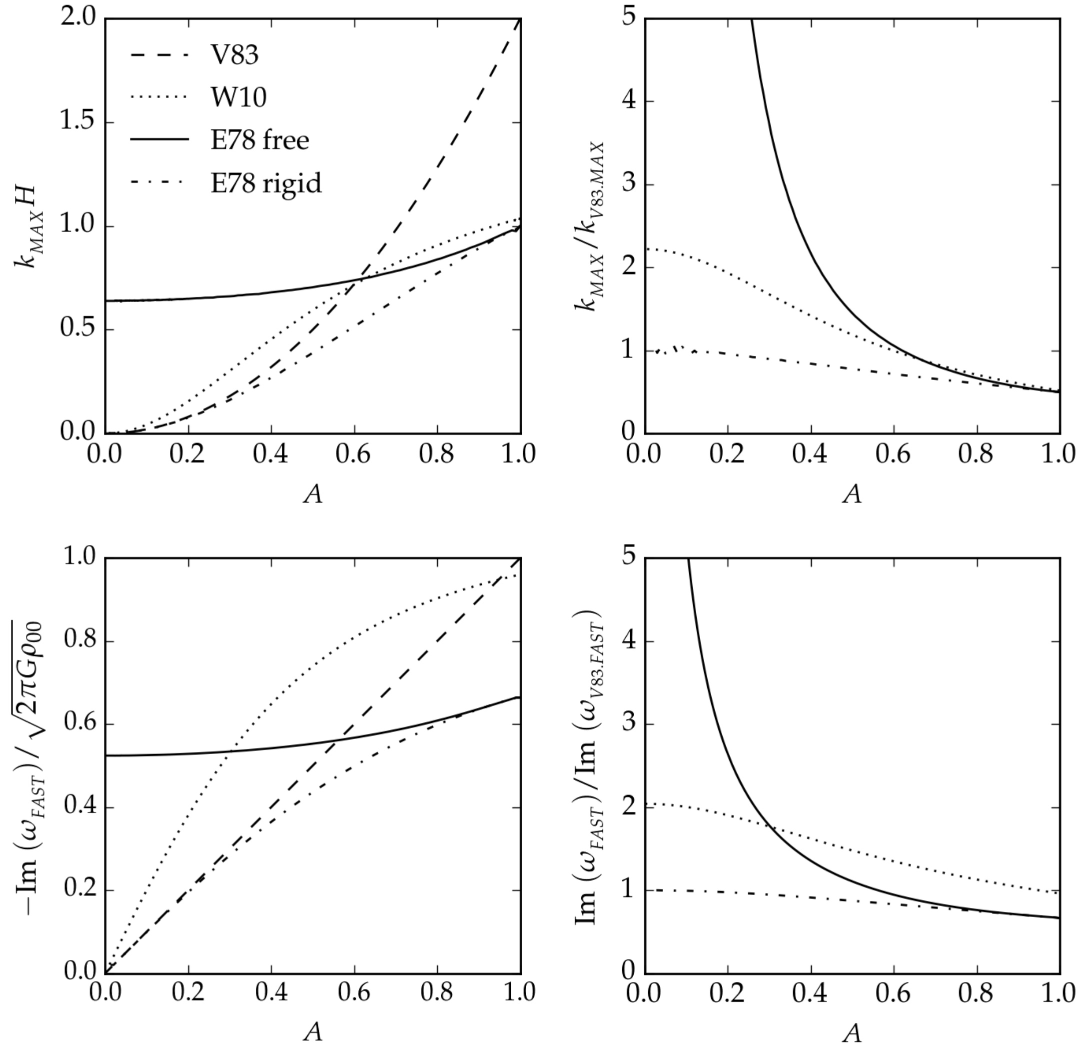

Figure 2.4: Important properties of the dispersion relations for layers as a function of parameter A. TOP ROW: The highest unstable wavenumber k_{MAX} normalised to layer half–thickness H (left panel) and to the highest unstable wavenumber for the thin shell dispersion relation $k_{\mathrm{V83.MAX}}$ (right panel). BOTTOM ROW: Instability growth rate $-\mathrm{Im}(\omega_{\mathrm{FAST}})$ normalised to $\sqrt{2\pi G\rho_{00}}$ (left panel) and to the instability growth rate of V83, $-\mathrm{Im}(\omega_{\mathrm{V83.FAST}})$ (right panel).

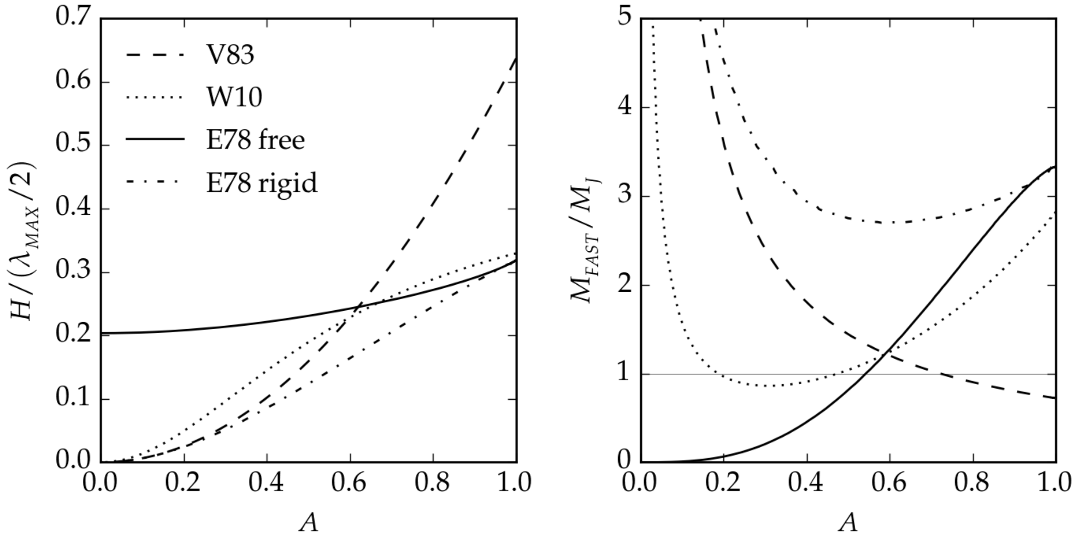

Figure 2.5: Left panel: Axis ratio of the marginally unstable fragment as predicted by the dispersion relations. Its semi minor and semi major axis are approximated by H and $\lambda_{\mathrm{MAX}}/2$, respectively. Right panel: Mass M_{FAST} of the fragment with the highest growth rate normalised to the midplane Jeans mass M_J. Thin horizontal line is an order of magnitude estimate separating gravitationally stable ($M_{\mathrm{FAST}} < M_J$) and unstable ($M_{\mathrm{FAST}} > M_J$) fragments.

eq. (2.32) to eq. (2.35) with boundary conditions from eq. (2.36) to eq. (2.39)) as E78. Their abbreviations are derived from the papers when they appeared for the first time. The abbreviations are used as subscripts of their properties (e.g. characteristic wavenumbers, growth rate).

Throughout the thesis, we decide to plot the dispersion relations for layers in the form that wavevector k is normalised by the inverse of the layer half–thickness $1/H$ and instability growth rate ω is normalised by $\sqrt{2\pi G\rho_{00}}$. Thus, from the plot, we can immediately compare the perturbation wavelength $\lambda = 2\pi/k$ with layer thickness as well as the e–folding time $t_{efold} = 1/\omega$ with the free–fall time $\simeq 1/\sqrt{2\pi G\rho_{00}}$ of a homogeneous medium of midplane density ρ_{00}. When reading the plots, it is important to remember that both H and ρ_{00} depends on A (see eq. (2.27) and eq. (2.29)). We note that the plotted dispersion relations hold for any layer with given A regardless of its c_s or ρ_{00} (or equivalently Σ_0).

The thin shell dispersion relation and PAGI were derived on a surface of an expanding shell. This adds two extra terms into the dispersion relation as well as the effects of curvature for perturbations with small l in the case of the thin shell dispersion relation. To focus on the interplay between self–gravity and the thermal pressure in the modes, we neglect the influence of stretching, so $V_s = 0$. As we see from figure 2.1, the modes with the highest growth rate have $l \gg 1$, so their curvature is negligible. We select a small part on the surface of the shell, neglect its curvature, and approximate it as a part of a layer. The angular wavenumbers l are related to planar wavevectors k by $k = l/R_s$. The thin shell dispersion relation eq. (2.7) for a layer then reads,

$$\frac{\omega_{\mathrm{V83}}^2}{2\pi G\rho_{00}} = \frac{1}{A^2}(kH)^2 - 2kH, \tag{2.43}$$

which is a parabola in kH. PAGI eq. (2.12) becomes

$$\frac{\omega^2_{\rm W10}}{2\pi G\rho_{00}} = \frac{1}{\epsilon}\Bigg\{ -\frac{3}{4}\left(\frac{\pi^2 kH \arccos(kH/\pi)}{(\pi^2-(kH)^2)^{\frac{3}{2}}} - \frac{(kH)^2}{\pi^2-(kH)^2)}\right) + \frac{5(kH)^2}{6\pi^2 A^2}\left(1+2A^2\right)\Bigg\}. \qquad (2.44)$$

Although ϵ is a free parameter, it does not influence the range of k where the dispersion relation is unstable. It influences only the numerical value of $\omega^2_{\rm W10}$. In this section, we set $\epsilon = 0.1$ as was found by Wünsch et al. [2010] based on comparison of PAGI with the thin shell dispersion relation.

In previous section, we mention that there exists the hydrostatic equlibrium for layers regardless of their Σ_0 or P_{ext}; a situation qualitatively different from that of spherical symmetry. Here we mention another qualitative difference, the form of the dispersion relations. The dispersion relations in question are shown in Figure 2.3 for several values of parameter A. For comparison, we plot the Jeans dispersion relation ($\omega^2 = -c_s^2k^2 + 4\pi G\rho_{00}$) calculated for the midplane density ρ_{00} in the upper left panel. We divide its ω^2 by a factor of 2 to fit the frame, but it has influence only on its particular numerical value. According to Jeans dispersion relation, the wavenumber with the highest growth rate is zero, and the longer the wavelength the higher the instability growth rate. On the contrary, each of the dispersion relations for layers has a peak in its growth rate at non–zero $k_{\rm FAST}$ defining characteristic wavelength $\lambda_{\rm FAST}$. For $k < k_{\rm FAST}$, the growth rate decreases and tends to zero as $k \to 0$.

The different limit for $k \to 0$ between Jeans dispersion relation and the dispersion relations for layers is caused by different dependence of gravitational force on radius. To illustrate this, we neglect the term containing c_s since thermal pressure is unimportant for modes with $k/k_{\rm FAST} \ll 1$; these modes are in a good aproximation in their free fall. For a spherically symmetric cloud with overdensity ρ_1, the free–fall time t_{ff} is independent on radius, $t_{ff} \sim 1/\sqrt{G\rho_1}$, so $\omega \sim -i/t_{ff} \sim -i\sqrt{G\rho_1}$. For a layer with surface overdensity Σ_1, the free–fall time $t_{ff} \sim \sqrt{R/(G\Sigma_1)}$ depends on radius, taking $k \sim 1/R$, we get $\omega \sim -i\sqrt{G\Sigma_1/R} \sim -i\sqrt{kG\Sigma_1}$. Thus we recover the correct scaling of the dispersion relations for small k.

We begin our comparison of dispersion relations of layers with V83. Dispersion relations for several values of parameter A are plotted in the upper left panel of Figure 2.3. As the external pressure P_{ext} increases, the range of unstable wavenumbers decreases from $k_{\rm V83.MAX}H = 2$ for $A \to 1$ to zero for $A \to 0$ (see also the upper left panel of Fig. 2.4). The wavenumber with the highest growth rate $k_{\rm V83.FAST}$ is in the middle of the range of the unstable wavenumbers, $k_{\rm V83.FAST} = k_{\rm V83.MAX}/2$. According to eq. (2.43), $k_{\rm V83.MAX}$ is independent on A. It implies that the radius of the marginally unstable fragment $\simeq \lambda_{\rm V83.MAX}/2$ is independent on A, while its half thickness H decreases with decreasing A. Thus the marginally unstable fragments become very flattened with semi major axis significantly higher than semi minor axis (left panel of Fig. 2.5). As midplane density ρ_{00} increases with decreasing A, the Jeans mass decreases, and the marginally unstable fragment contains many Jeans masses when A is small (right panel of Fig. 2.5; the mass $M_{\rm FAST}$ of the most unstable fragment is

$M_{\text{FAST}} = \pi\Sigma_1(\lambda_{\text{FAST}}/2)^2$). It means that fragments smaller than $\simeq \lambda_{\text{V83.MAX}}/2$ are according to this dispersion relation gravitationally stable, even though they are significantly more massive than the Jeans mass. The highest instability growth rate, $\omega_{\text{V83.FAST}} = \omega_{\text{V83}}(k_{\text{V83.FAST}})$ normalised by $\sqrt{2\pi G\rho_{00}}$ decreases from 1 to 0 with decreasing A (lower left panel of Fig. 2.4).

The range of unstable wavenumbers for W10 is by a factor $\simeq$ 2 narrower than that of V83 if $A = 1$ (upper right panel of Fig. 2.3). With decreasing A, the range shrinks and it is infinitesimaly small as $A \to 0$ (upper left panel of Fig. 2.4). With comparison to V83, marginally unstable fragments are by factor $\simeq 2$ more elongated if $A = 1$, but become by approximately the same factor less elongated when $A \to 0$ (left panel of Fig. 2.5). As for any of the dispersion relations for layers investigated in this thesis, here again $k_{\text{W10.FAST}} \simeq k_{\text{W10.MAX}}/2$. Thus, in comparison to V83, the mass of the most unstable fragment $M_{\text{W10.FAST}}$ is approximately 4 times higher if $A \to 1$ and by the same factor smaller if $A \to 0$, Similarly to V83, the normalised instability growth rate $\omega_{\text{W10.FAST}}/\sqrt{2\pi G\rho_{00}}$ decreases from $\simeq 1$ to 0.

Next, we describe E78 with free boundary conditions (bottom left panel of Fig. 2.3). The range of unstable wavenumbers kH decreases from $(0, 1)$ for $A \to 1$ (where the dispersion relation is close to W10) to $(0, 0.639)$ for $A \to 0$. The wavenumber with the highest growth rate $k_{\text{E78.FAST}}$ decreases from $k_{\text{E78.FAST}}H = 0.466$ for $A \to 1$ to $k_{\text{E78.FAST}}H = 0.294$ for $A \to 0$. Both $k_{\text{E78.FAST}}$ and $k_{\text{E78.MAX}}$ have a different asymptotic behaviour for A around 0 than V83 or W10. It brings interesting consequences. Since H decreases with decreasing A, $k_{\text{E78.MAX}}$ grows and $\lambda_{\text{E78.MAX}}$ decreases without limit. Any wavelength can become gravitationally unstable if the layer is sufficiently compressed. The axis ratio of the marginally unstable fragment is finite, and it depends only weakly on parameter A. The small fragments are of smaller than the Jeans mass and once formed, they are stable to further collapse (right panel of Fig. 2.5). The highest instability growth rate $-\text{Im}(\omega_{\text{E78.FAST}})/\sqrt{2\pi G\rho_{00}}$ changes only slightly from 0.647 ($A \to 1$) to 0.526 ($A \to 0$) (bottom left panel of Fig. 2.4), so the e–folding time is always of the order of the free–fall time; this asymptotic behaviour is also different from that of V83 and W10.

E78 with rigid boundary conditions is shown in the bottom right panel of Fig. 2.3. For layers with A near unity, the role of boundary conditions is not very important and the dispersion relations are close to each other with the same limit $A \to 1$. It is the reason why eq. (2.41) is identical for layers both with free and rigid boundary conditions. However, for $A < 1$, the dispersion relations are different with different asymptotic behaviour of $k_{\text{E78.FAST}}$ and $\omega_{\text{E78.FAST}}$ for A near 0. E78 for rigid boundaries tends to V83 as $A \to 0$ (Figs. 2.4 and 2.5). The range of unstable wavenumbers $k_{\text{MAX}}H$ shrinks to an infinitesimally small interval around the origin.

The different behaviour of E78 with free and rigid boundary conditions is the consequence of different nature of modes arising under different circumstances [Kim et al., 2012]. In layers with rigid boundary conditions, gravitationally unstable modes correspond to acoustic waves modified with their self–gravity (*Jeans modes*). These waves propagate inside the layer. In layers with free boundary conditions, there are two different kinds of gravitationally unstable modes. The first kind of modes are Jeans modes, the same as in layers with rigid boundary conditions. The second kind of modes are *surface–gravity modes*, arising due to surface corrugations and propagate near the surface. These modes again have a non–self–gravitating analog in terrestrial environment; waves on the surface of water (see e.g. chapters 12 and 13 in Landau and Lifshitz [1959] for a detailed description). The relative importance of either kind of modes depends on the parameter A. While Jeans modes dominate for layers with A near unity, their relative importance decreases with decreasing A, and surface–gravity modes dominate for layers with A near 0.

We discussed E78 with rigid boundary conditions mainly to illustrate the influence of the boundary conditions and to compare it with V83 during discussion in Section 5.3.3. E78 with free boundary conditions is more appropriate for layers investigated in this Thesis. Thus, in the following text, when referencing to E78, we always mean E78 with free boundary conditions.

2.2.3 The necessity to know the correct approximation to discuss propagating star formation

After we described the dispersion relations, we should quantify their implications to propagating star formation. The characteristic wavelength λ_{FAST} defines the characteristic mass of fragments which are formed first. Assuming that no other process substantially changes the fragment mass during its collapse, one can estimate the maximum mass of newly formed stars [Elmegreen and Elmegreen, 1978];[Whitworth et al., 1994b];[Ehlerova et al., 1997];[Dale et al., 2009]. As we see from the right panel of Fig. 2.5, the mass of fragments depends on the adopted approximation in the derivation of the dispersion relation.

We illustrate the importance of the issue on the following example. Consider a spherical shock sweeping a homogeneous medium of preshock particle density $n = 250\,\text{cm}^{-3}$ and forming a shell of radius 6pc. The surface density of the shell is $0.0025\,\text{g.cm}^{-2}$. Assuming that the shell is near its vertical hydrostatic equilibrium and taking $A = 0.2$, M_{FAST} is $28.5\,\text{M}_\odot$ for V83, $7.7\,\text{M}_\odot$ for W10, and $0.5\,\text{M}_\odot$ for E78. We mention that only stars with mass above $\sim 8\text{M}_\odot$ can lead to propagating star formation. In this particular case, star formation can propagate easily according to V83, it may propagate according to W10 if there are high enough statistical fluctuations in fragment masses, but it cannot propagate according to E78. Thus the knowledge of the dispersion relation is crutial to decide whether star formation can propagate and we dedicate Section 5.3 to this issue.

2.2.4 Sedond order perturbations

Assuming that the amplitudes of the initial perturbations are small relative to the unperturbed state, the initial fragmentation is well described by appropriate dispersion relation. Dispersion relations are based on first order perturbation analysis. When the perturbations become large, first order terms become subordinate to higher order terms and first order analysis cannot be applied. We call the evolutionary stage *linear regime* if the first order analysis is a good approximation, and we call it *non–linear regime* after that.

Miyama et al. [1987a,b] calculate second order perturbations for a vertically stratified layer. They consider density eigenfunctions in the form $\sim \cos(k_x x)\cos(k_y y)$; this leads in first order perturbations to E78 dispersion relation. Note that the growth rate for E78 depends on $\|k\|$. However, in the second order analysis, the growth rate depends also on the ratio k_x/k_y, and more elongated modes have higher growth rate. It implies, that in the non–linear regime, the fragments become more and more elongated, transforming to slender filaments. It is a nice theory how a layer breaks into a net of filaments.

However, another prediction for a fragmeting layer in the non–linear regime was obtained by Fuchs [1996]. He proposes that the layer has tendency to self–organise and form a regular hexagonal pattern in its surface density. Similar result was obtained by Wünsch and Palouš [2001] for a surface of an expanding shell.

2.3 Purely hydrodynamical instabilities

We briefly mention several other instabilities which may arise in shells formed by stellar feedback. For most of them, we do not reproduce their derivation, because it can be either found in a textbook or is too complicated to fall into the scope of the thesis.

2.3.1 Rayleigh–Taylor instability

Consider two static fluid layers one lying above the other. Density of the upper and bottom fluid is ρ_1 and ρ_2, respectively. They are in homogeneous gravitational field g acting towards bottom. The dispersion relation for a wave of wavenumber k propagating accross the interface between the layers is

$$\omega^2 = -kg\frac{\rho_1 - \rho_2}{\rho_1 + \rho_2}. \tag{2.45}$$

The configuration is stable when the denser fluid lies at the bottom ($\rho_1 < \rho_2$), and is unstable otherwise. Note that the higher k, the higher the instability growth rate; unlike the dispersion relations describing the gravitational instability we encountered in Section 2.2, there is no upper limit for $-\mathrm{Im}(\omega)$. It is viscosity what is not contained in eq. (2.45), and which prevents very high k from very high growth rate.

Equivalently to the gravitational force, this instability can by caused by acceleration. This is relevant for supernovae during the transition from Sedov–Taylor to momentum conserving phase when rarefied very hot interior gas pushes (accelerates) the denser shell. This is equivalent to a denser layer lying above a hot rarefied layer in a homogeneous gravitational field.

2.3.2 Kelvin–Helmholtz instability

Consider the same fluid layers as in the previous section. Now, the configuration is Rayleigh–Taylor stable, $\rho_1 < \rho_2$. If one of the layers moves horizontally, the interface become unstable. The highest unstable wavenumber is again set from viscosity.

2.3.3 Vishniac instability

In Section 2.1, we focus on gravitational instability of an expanding shell. There is another, purely hydrodynamic instability of the shell. The instability is described in the same paper as the gravitational instability, Vishniac [1983]. To illustrate the mechanism driving this instability, we adopt a simple example of a planar layer. This example was also propounded by Vishniac [1983].

The equations of continuity and momentum for a shell expanding into homogeneous medium are eq. (2.4). Now we assume that the position of the shock front R_s can freely ripple to first order perturbations, so $R_s = R_{s0} + R_1(\theta, \phi)$, where R_{s0} is the average shock radius. We define $V_0 = \mathrm{d}R_{s0}/\mathrm{d}t$. Neglecting the gravitational potential, and the shell curvature ($R_{s0} \to \infty$), the first order perturbation equations are

$$\frac{\partial \Sigma_1}{\partial t} = \rho_{amb}\frac{\partial R_1}{\partial t} - \Sigma_0 \nabla_T . \mathbf{V}_{t_1}, \tag{2.46a}$$

$$\frac{\partial^2 R_1}{\partial t^2} = -\frac{2\rho_{amb}V_0}{\Sigma_0}\frac{\partial R_1}{\partial t} - \frac{\Sigma_1 V_0}{\Sigma_0}, \tag{2.46b}$$

$$\frac{\partial \mathbf{V}_{t_1}}{\partial t} = -\frac{\rho_{amb}V_0\mathbf{V}_{t_1}}{\Sigma_0} - \frac{c_s^2}{\Sigma_0}\nabla_T\Sigma_1 - \frac{P_i}{\Sigma_0}\nabla_T R_1. \tag{2.46c}$$

Assuming that the increase in surface density due to accretion is negligible relative to the characteristic growth time of the perturbation τ_p, i.e. $\rho_{amb}V_0/\Sigma_0 \ll 1/\tau_p$, the first term on the right hand side of eq. (2.46a), eq. (2.46b) and eq. (2.46c) can be neglected. Further, in eq. (2.46c), the second term in the right hand side is negligible relative to the third term (it follows from eq. (2.1b)). Then, one can find the dispersion relation

$$\omega^4 = \frac{P_i V_0 k^2}{\Sigma_0}. \tag{2.47}$$

The perturbations are overstable if the layer decelerates ($V_0 < 0$).

A more intuitive insight into the nature of the instability is provided in Figure 2.6. There are two pressures acting on the layer; thermal pressure P_i acting from the inside and the ram pressure $\rho_{amb}V_0^2$ acting from the outside. The instability arises from the different nature of the pressures. While the thermal pressure acts always perpendicular to the surface, the ram pressure acts from the direction of the motion. When the layer is not corrugated (Panel (a) in Fig. 2.6), there is a balance between the pressures. When the layer is corrugated, the angle between the presurres is different, which results in transversal acceleration (eq. (2.46c); Panel (b)). The transversal flows assemble gas into the lagging parts of the layer, where the surface density Σ_1 increases. The layer is decelerated by the ram pressure. The deceleration is the smallest in the lagging parts due to their increased inertia. Consequently, the lagging parts accelerate in the direction z and overtake the layer (Panel (d)). The transversal velocity feeding the overdensity is the highest when the overdensity passes through the midplane of the layer eq. (2.46c). As the overdensity moves outwards, it becomes eroded by the same process and slows down. The oscillations repeat with growing amplitudes.

According to the dispersion relation, eq. (2.47), the growth rate increases with increasing wavenumber without an upper limit. Actually, the upper limit cannot

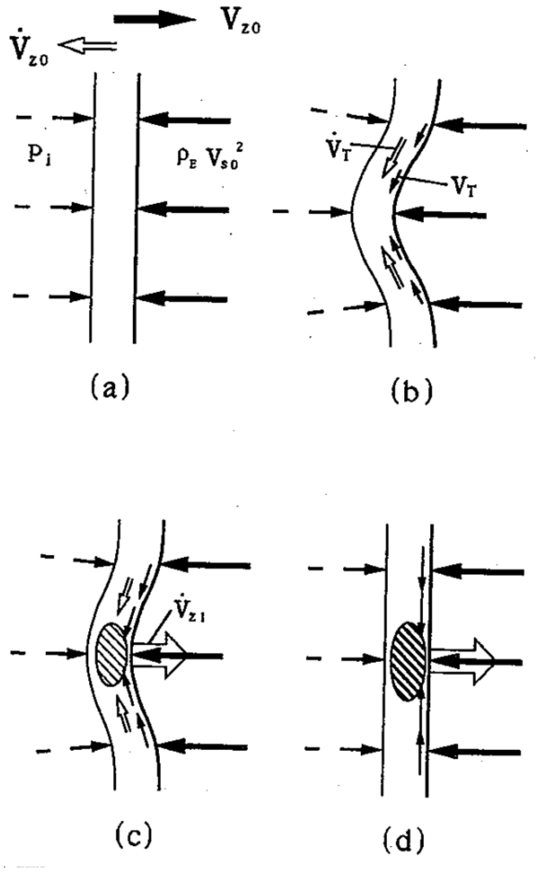

Figure 2.6: An illustration of the Vishniac instability. Velocity and acceleration of the layer is denoted V_{z0} and $\dot{V}_{z0}$ on the figure. PANEL (A): The configuration of the layer before it becomes rippled. PANEL (B): When the layer is rippled, the different angle of incidence between the ram pressure and thermal pressure induces tangential flows. PANEL (C): The flows assemble material into the lagging part of the layer. Since the layer decelerates, the assembled material has higher inertia and overtakes the layer (PANEL (D)). The figure is adopted from Nishi [1992].

be obtained from this form of the dispersion relation since it was derived under the thin shell approximation eq. (2.1). Equation (2.47) holds only for wavelengths significantly longer than the shell thickness. An improved model able to resolve the shell thickness is proposed in subsequent work Ryu and Vishniac [1987] and Vishniac and Ryu [1989], where it was demonstrated that the shortest unstable wavelength is comparable to the shell thickness.

More careful considerations indicate that there are further complexities to this simplified model. There should be a significant density contrast accross the shock front for this instability to develop. From the Rankine–Hugoniot conditions it follows that the density contrast is $(\gamma + 1)/(\gamma - 1)$, so it increases as the ratio of specific heats γ decreases. Ryu and Vishniac [1987] find that a shell is susceptible to the overstability if $\gamma \lesssim 1.2$. It explains why the overstability was not reported in intensively studied terrestrial blast waves where $\gamma \simeq 1.4$.

Mac Low and Norman [1993] detect the overstability in their simulations confirming the previous analytical results. Mac Low and Norman [1993] follow the growth of the instability to the stage when the perturbed quantities are of the same order as the unperturbed ones. They find that the growth of the overstability saturates when the transversal velocity V_t exceeds the sound speed c_s inside the layer, which forms weak transversal shocks. The perturbed surface density Σ_1 is then a few times Σ_0. As the overstability saturates and transforms to stable oscillations, this overstability does not break the shell into pieces.

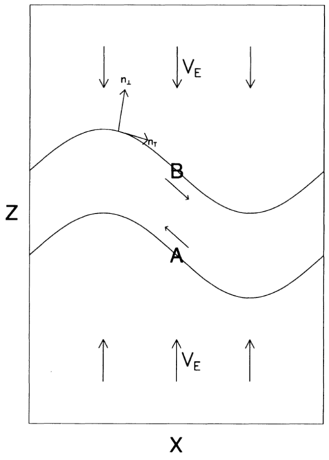

Figure 2.7: Momentum transport inducing nonlinear thin shell instability. The layer is accreting gas supersonically at velocity V_E from both surfaces. Momentum transfer in the direction z by transversal flows A and B results in growth of the ripples. The figure is adopted from Vishniac [1994].

2.3.4 Nonlinear thin shell instability

Without derivation and exact description, we briefly mention the mechanism responsible for the instability proposed by Vishniac [1994]. Vishniac considers a layer bounded with shock fronts from both surfaces (Figure 2.7). The velocity and density of the gas inflowing from above are equal to the velocity and density of the gas inflowing from below, so the ram pressures acting on both surfaces are equal and the layer as a whole is not accelerated.

If the layer is displaced as shown in Fig. 2.7, the different direction between the force due to the ram pressure and the thermal pressure of the gas inside the layer causes tangential flows (arrows A and B). It is the same mechanism which is responsible for the Vishniac instability described in Section 2.3.3. The net mass transport is zero because the amount of mass transported at the upper part of the layer is compensated by the same amount transported in the bottom part in the opposite direction. However, the flow at B transports the zth component of momentum in the direction $+x$, and the flow at A transports the same amount of zth component of momentum, but of opposite sign in the direction $-x$. Consequently, the zth component of momentum at the parts of the layer displaced above increases and these parts accelerate in the direction $+z$. The parts of the layer displaced below accelerate in the direction $-z$, and the amplitude of the ripples increases. Note that this effect is nonlinear since the momentum transport is quadratic in transversal velocity.

3. Overview of Flash code

Flash code, developed since 1997 at the University of Chicago is a state-of-the-art tool for modelling astrophysical fluid phenomena. The code is MPI–parallelised with input/output facility handled by HDF5 library. For the purpose of the Thesis, we provide only a very brief description of the overall code (in Section 3.1), and refer an interested reader to Fryxell et al. [2000] and Dubey et al. [2008]. However, in section 3.2, we describe selected features of the code and numerical methods which are either closely related to the Ewald method (Tree gravity, particles) or which were modified to accomplish some of the presented simulations (TreeRay).

3.1 Introduction

The code contains many units for modelling various physical processes. Particular unit often contains several different options for a given phenomenon. For example, Gravity unit offers multipole, multigrid, or octal tree based algorithm. The selected option is specified before compilation. To model desired processes, the user can easily put together chosen implementation of many units.

Each unit is hierarchically organised according to firm nomenclature to increase clarity of the code. The unit always contains directory `"Unit"Main` (”Unit” is the unit name), which contains available implementations. Since a routine from one unit often calls routines from another unit without any information which particular implementation of the latter unit was invoked, it may happen that the latter routine is not necessary (available) for given implementation. In this case, a *stub routine* (routine doing anything) is linked. The usage of stub routines greatly enhances the modularity of the code as routines from one unit can be called without a priori knowledge of the particular implementation of the unit.

Each unit contains three mandatory routines. `"Unit"_init` reads the input parameters and initialises constants for the given unit. The routine is called before the first hydrodynamical step. Global variables for the given unit are stored in routine `"Unit"_data` during the simulation. At the end of the simulation, routine `"Unit"_finalize` deallocates arrays. If variables of a given unit are needed by another unit, they are accessed via routines in directory `localAPI` located in the top level unit directory.

In the Flash code, each fluid variable: density ρ, velocity $\mathbf{v}$, pressure P and the sum of internal ϵ and kinetic energy per unit mass $E = \epsilon + \mathbf{v}^2/2$ is stored in a grid of cell–centered data. Fluid variables are evolved by the hydrodynamics equations

$$\frac{\partial \rho}{\partial t} + \nabla \cdot (\rho \mathbf{v}) = 0, \tag{3.1}$$

$$\frac{\partial \rho \mathbf{v}}{\partial t} + \nabla \cdot (\rho \mathbf{v}\mathbf{v}) + \nabla P = \rho \mathbf{g}, \tag{3.2}$$

$$\frac{\partial \rho E}{\partial t} + \nabla \cdot ((\rho E + P)\mathbf{v}) = \rho \mathbf{v}.\mathbf{g}, \tag{3.3}$$

where $P = (\gamma - 1)\rho\epsilon$ for the ideal gas. γ is the barotropic exponent. Optionally, the fluid can comprise several chemical or nuclear species. Species j is represented

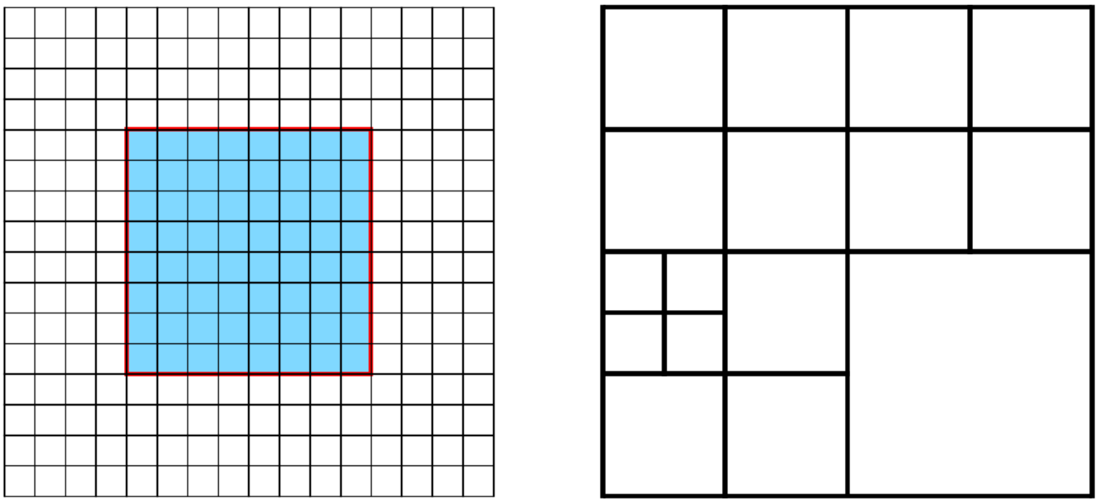

Figure 3.1: LEFT PANEL: Structure of a cartesian block. The block contains 8 interior cells in each direction (blue square). The block is surrounded by four rows of guard cells (white). BOTTOM ROW: A small computational domain with blocks of three refinement levels. Cells are not shown in this plot.

by its mass fraction X_j. Individual species are evolved by the advection equation

$$\frac{\partial \rho X_j}{\partial t} + \nabla \cdot (\rho X_j \mathbf{v}) = 0. \tag{3.4}$$

Obviously, mass conservation $\Sigma_j X_j = 1$ must be fulfilled.

The variables are discretized in grid and stored in cell-centered data. The grid is cartesian in all the presented simulations, but spherical or cylindrical grid is also available. The grid cells are organised in blocks (see left panel of Figure 3.1), and blocks fill the whole computational domain. The blocks does not overlap, but a block shares its boundary with other blocks, or with the boundary of the computational domain (right panel of Fig. 3.1). Each block has the same number of cells in directions x, y and z. In addition, to the interior cells, each face of a block is surrounded by four rows of guard cells, which provide boundary conditions. The guard cells are filled from cells in the surrounding blocks. After the guard cells are filled, the block can be taken as an entity isolated from the rest of the universe (if long–range forces are neglected), and the interior cells can be advanced by one time step by solving equations eq. (3.1) to eq. (3.4).

We solve the hydrodynamics equations by piecewise parabolic method (PPM) [Woodward and Colella, 1984, Colella and Woodward, 1984]. The solution is split into two steps. In the first step (*reconstruction step*), the values of flow variables at cell interfaces are reconstructed from the known cell average values. It is done by fitting cubic polynomial with the proper cell average values. In addition, there is special treatment of contact discontinuities and shock fronts. In order to prevent contact discontinuities from spreading through many cells, they are detected and steepened. To prevent artificial postshock oscillations shock fronts are flattened. In the second step (*solution step*), flow variables are updated according to equations eq. (3.1) to eq. (3.4).

The above described solution is realised along one coordinate axis. To access two– and three–dimensional problems, the directions x, y, (z) are traversed in a permuting order [Strang, 1968].

To capture the huge spans of densities encountered in the modelled interstellar medium, it is useful to increase the spatial resolution of the mesh at the denser parts of the computational domain. To handle adaptive mesh refinement, we select PARAMESH library MacNeice et al. [2000]. Two conditions for mesh refinement are widely adopted: according to the second derivative of a given variable, or to resolve one Jeans length by minimum number of grid cells. For either of these condition, to preserve the nested structure of the blocks inside the computational domain, another three criteria must be fulfilled:

- The side length of a child block is equal to one half of the side length of the parent block, so the parent block is split into eight child block of the same size.
- The children blocks cannot overlap one another, they must fill the whole volume of their parent block.
- Two blocks sharing the same boundary can differ by at most one refinement level.

Right panel of Fig. 3.1 shows a computational domain with blocks at three refinement levels.

If a block is marked for refinement, the values of flow variables in the child block are interpolated from that of the parent block. In the case of derefinement, the flow variables of the parent block are spatially averaged from the child blocks. After refinement is done, blocks are redistributed among processors so that each processor has a comparable amount of work. The blocks are redistributed according to their Morton numbers.

Courant–Friedrichs–Lewy condition must be fulfilled in order to maintain stability. This condition states that the timestep Δt cannot be longer than time needed for information to travel across the grid cell size $min(\Delta \mathbf{r})$. In a static fluid disturbance propagates at sound velocity c_s, and bulk motions of fluid are of velocity $\mathbf{v}$, thus the condition for one cell can be written as

$$\Delta t = \frac{C_0 min(\Delta \mathbf{r})}{|\mathbf{v}| + c_s}, \tag{3.5}$$

where C_0 is smaller than 1. The code has one global time step for all blocks, which is minimum from eq. (3.5) taken across the whole computational domain.

3.2 Selected features of the code

3.2.1 Octal tree based algorithms for self–gravity

To calculate gravitational field for each cell directly, $\sim N^2$ interactions need to be calculated, where N is the number of cells in the computational domain. Tree algorithms enable us to perform the same task in $\sim N\log(N)$ interactions. Where high accuracy is not needed, tree algorithms are usually used.

Current implementation of tree algorithms in Flash uses octal tree, and it is connected to PARAMESH library. The implementation was done mainly by Richard Wünsch (Wünsch et al. in preparation).

Note that the computational domain in PARAMESH consists of hierarchically nested blocks at different refinement levels. The AMR blocks at the top level have refinement level $l = 1$, and we call them *root blocks*. These blocks are hierarchically structured down to *leaf blocks* at the bottom level $l = l_{lb}$. Leaf blocks contain no other blocks, they are the basic units (blue square in left panel of Fig 3.1) containing only cells. The blocks for calculating self–gravity are calculated from AMR blocks, but their structure is different. To clarify terminology, we call them block nodes.

We can look at the gravitational field generated by a distant block node of mass M as the field from a point mass M located at the block node mass center plus higher order terms of multipole expansion. Since the higher order terms decrease more rapidly than the lower order terms, the lower order terms (and especially the monopole term) dominate above certain distance d. The basic idea behind tree codes is to set a criterion on distance d for a block node so that we believe that the contribution of multipole terms higher than of order p to the gravitational field of the block node is negligible. If the criterion is met, the gravitational field due to the block node is approximated up to term p in its multipole expansion. Otherwise, the block node is split into 8 child block nodes, and the criterion tested on each of the child block node. This algorithm starts at root blocks and proceeds recursively until it decomposes the whole computational domain into a hierarchy of block nodes and grid cells. This hierarchy is called *gravity tree*. To illustrate the difference between block and block nodes, distant blocks are generally grouped in larger block nodes, while close blocks are split into smaller block nodes. Note that each cell in the computational domain ends up with a generally different structure of accepted nodes of the gravity tree.

The criterion for node acceptance has a strong influence on speed and accuracy. In current Flash, following criteria are available.

(i) Barnes and Hut [1986] propose an algorithm accepting block nodes if

$$\frac{h}{d} < \theta_{lim}, \tag{3.6}$$

where h is the length of the block node, d is the distance between block node mass center and the cell where self–gravity is calculated (*target cell*), and θ_{lim} the limiting angle. Angle θ_{lim} is a user defined constant for the whole simulation. Obviously, smaller θ_{lim} provides higher accuracy at the cost of speed.

This algorithm is purely geometric, it does not take into account neither the spatial distribution of mass inside the block nor the total mass. These features can lead to serious problems. For larger limiting angles, $\theta_{lim} > 1/\sqrt{3}$, the former can lead to spurious explosions for certain configurations as was discovered by Salmon and Warren [1994]. We refer an interested reader to the appendix A of the paper for details. The latter feature may imply that a lot of time is spent by calculating contributions of many close block nodes containing rarefied gas of negligible importance for gravity, while significant error may arise from a relatively distant and very massive node.

(ii) An algorithm controlling the worst possible absolute error to gravitational acceleration due to one block node [Salmon and Warren, 1994]. The maximum error $\Delta a_{(0)}$ can be expressed analytically from the multipole expansion. For a block node approximated to the order p in its multipole expansion, and the distance between its center of mass and the most distant part of the block b_{max}, it follows

$$\Delta a_{(p)} \leq \frac{1}{d^2(1-b_{max}/d)^2}\left((p+2)\frac{B_{(p+1)}}{d^{p+1}} - (p+1)\frac{B_{(p+2)}}{d^{p+2}}\right), \tag{3.7}$$

where $B_{(p)}$ is the multipole moment of order p,

$$B_{(p)} = \Sigma_j m_j |\mathbf{r}_j - \mathbf{r}_0|^p. \tag{3.8}$$

The sum runs over all cells in the block node; jth cell is of mass m_j and is at position $\mathbf{r}_j$. Block mass center is at $\mathbf{r}_0$. This choice is invoked by setting `gr_bhPhysMACTW = .true.`, `grv_bhUseRelAccErr = .false.` and `grv_bhMAC = "MaxPartialErr"`.

(iii) Alternatively to eq. (3.7) and eq. (3.9), the contribution to the maximum error of higher order terms to the multipole expansion is estimated by a simpler formula [Springel, 2005]

$$\Delta a_{(p)} \simeq \frac{GM}{d^2}\left(\frac{h}{d}\right)^{(p+1)}. \tag{3.9}$$

This option is invoked by `gr_bhPhysMACTW = .true.`, `grv_bhUseRelAccErr = .false.` and `grv_bhMAC = "ApproxPartialErr"`.

(iv) Control on relative error of gravitational acceleration caused by interaction with one block node [Salmon and Warren, 1994]. The formula for node acceptance is

$$\Delta a_{(p)}/|a_{(0)}| \leq \frac{1}{B_{(0)}(1-b_{max}/d)^2}\left((p+2)\frac{B_{(p+1)}}{d^{p+1}} - (p+1)\frac{B_{(p+2)}}{d^{p+2}}\right). \tag{3.10}$$

It appears that this approach is not as efficient as the criteria for absolute errors. Since the acceleration is typically dominated by a small number of nodes, setting $\Delta a_{(p)}/|a_{(0)}|$ larger may cause a significant error due to these important nodes. In contrast, setting $\Delta a_{(p)}/|a_{(0)}|$ small gives a reasonable accuracy, but most of the time is spent computing many nodes with negligible absolute value of $\Delta a_{(0)}$. This acceptance criterion can be switched on by `gr_bhPhysMACTW = .true.`, `grv_bhUseRelAccErr = .true.` and `grv_bhMAC = "ApproxPartialErr"`.

(v) Although criteria ii - iv take into account distribution of mass inside blocks, they treat blocks independently, leaving the total error unknown. These criteria would be sufficient if errors from different blocks would act in opposite directions and cancel. However, Salmon and Warren [1994] caution against this assumption and point out that errors usually tend to accumulate. They propose a criterion constraining the maximum total error Δ_{tot} from all nodes by

$$\Sigma_k \Delta a_{(p)\,k}^2 \leq \Delta_{tot}^2, \tag{3.11}$$

where $\Delta a_{(p)\,k}$ is the upper bound of the error of node k. This condition is invoked by `gr_bhPhysMACTW = .true.` and `grv_bhMAC = "SumSquare"`

During an MPI–parallel simulation, blocks in the computational domain are located at different processors. To construct the gravity tree for a cell, we need to evaluate the acceptance criterion, and thus to know mass distribution in the whole computational domain. Communication of the mass distribution in the computational domain to each processor would be costly and would consume an enormous amount of memory. For this reason, the gravity tree is constructed in two steps.

In the first step, positions $\mathbf{r}_0$ and masses M of all AMR blocks from levels $l = 1$ to $l = l_{lb}$ are sent to each processor. Then the chosen acceptance criterion is applied to these blocks, so the gravity tree is constructed from levels $l = 1$ to $l = l_{lb}$. Obviously, not all leaf blocks (refinement level $l = l_{lb}$) fulfill the acceptance criterion, so these blocks must be resolved further. A list of leaf blocks to be resolved is constructed for each processor. In the second step, each processor finds the ranks of the processors where desired leaf blocks are located and asks them for the complete mass content of the leaf blocks. After the processor gathers this information, the acceptance criterion is applied to the leaf blocks which were not previously accepted, so the whole gravity tree is constructed. When the gravity tree is known, it is straightforward to calculate the gravitational force.

Since gravity is a long–range force, the gravitational acceleration typically evolves slowly with time at given location in space. Motivated by this, the code can be used with an option (`gr_bhAcceptAccurateOld = .true.` and `gr_bhLoadBalancing = .true.`), which calculates the gravitational force only if it changed from the previous value by more than by a user controlled factor. This leads to a significant speed up as for the check, the acceleration is evaluated only at the eight edges of each block instead of its 512 grid cells (if blocks with 8 grid cells are used).

So far, we have described calculation of gravitational field for a computational domain with no source of gravitational field outside its boundary (*isolated boundary conditions*). For some models, it is more appropriate to surround the computational domain by its periodic copies in all three spatial directions and include their contribution to the field in the computational domain (*periodic boundary conditions*). Alternatively, the periodic copies are present in one or two directions, while the computational domain is isolated in the other direction(s) (*mixed boundary conditions*). These options are invoked by setting parameter `grav_boundary_type` to `"periodic"` or `"mixed"`, and specifying desired boundary conditions (BCs) in particular directions (i.e. `grav_boundary_type_x = "periodic"` for periodic BCs in the direction x).

In comparison to an isolated computational domain, the cost for calculating contributions from neighbouring domains directly (i.e. summation of M/d^2 terms) in the case of periodic or mixed boundary conditions would make these

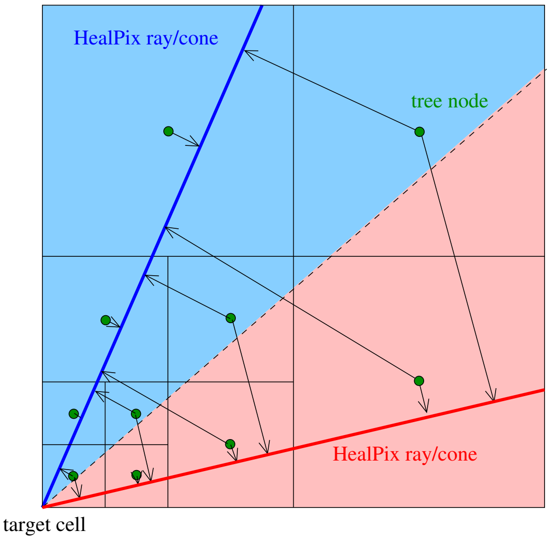

Figure 3.2: Mapping blocks to rays in TreeRay. Gaseous parcel of one block is mapped on several neighbouring rays with weights proportional to the angular distance from the block. The figure is adopted from Wünsch et al. in preparation.

simulations prohibitively time consuming. However, this obstacle can be circumvented by Ewald method, which is described in Chapter 4

3.2.2 TreeRay

This module is used for modelling ionising radiation in on the spot approximation (implementation `OnTheSpot`), or for calculating the column density (implementation `OpticalDepth`). In the future, it is planned to extend the module and use it for modelling general radiative transfer.

Both `OnTheSpot` and `OpticalDepth` implementations use inverse ray tracing, so to calculate the desired physical quantity (i.e. ionising photon flux F or column density σ) at the given cell (target point), rays are cast from the target point instead of the source. The rays are calculated by Healpix algorithm Górski et al. [2005] splitting the surface of a sphere in 3×4^N (N is an integer number; typically $N = 1, 2, 3$) parts with equal area. Then the gas is mapped on the rays (see Figure 3.2). The code is simplified considerably using the same tree as for self–gravity for mapping gas on rays since no extra communication is needed. Gaseous parcel of one block is mapped on several neighbouring rays with weights proportional to the angular distance from the block. If higher resolution is needed, it is necessary not only to increase the number of rays, but also to decrease acceptance angle accordingly. For example, increasing number of rays by factor of 4 implies 2× higher angular resolution and thus to decrease acceptance angle for blocks by factor of 2. In the case of `OpticalDepth`, column density is calculated by integration along rays.

In the case of `OnTheSpot`, sources of ionising radiation are mapped on rays in the analogical way as blocks were mapped. Then the equation of radiative transfer is solved along each ray, and the energy of ionising photons per unit volume ϵ_{rad} at the target cell is calculated. Since ionising photons can propagate only through the ionised medium, the ionisation state along the ray is crucial to the radiative transfer. Each cell or block along the ray are generally not updated at the time step when the particular target cell is evaluated, so the ionisation state at gas along the ray may change during the step. Therefore, TreeRay iterates the whole computational domain until the maximum difference between the values of

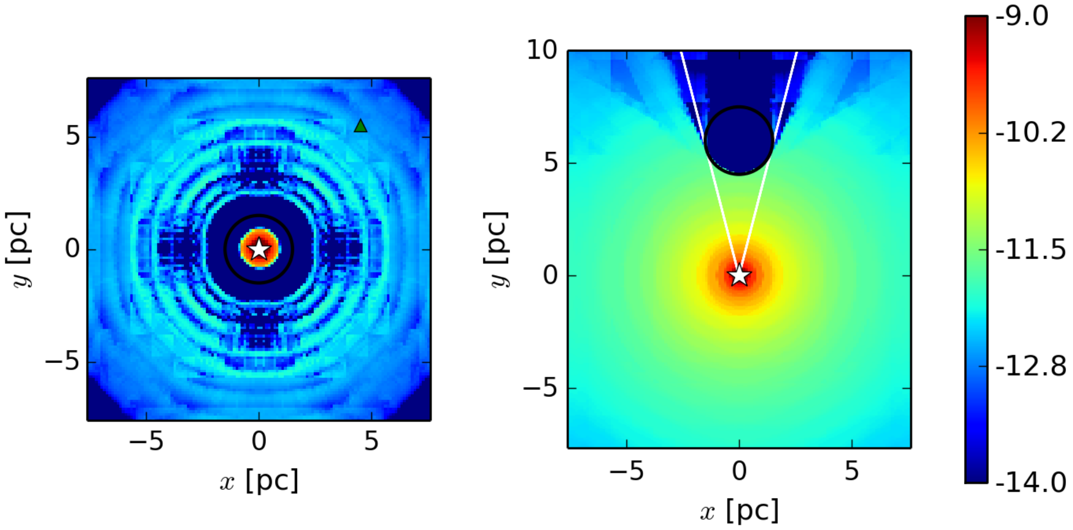

Figure 3.3: Known limitations of TreeRay module. Ionising source is located at the origin of the coordinate axes (white asterisk), and the colorscheme represents $\log_{10}(\epsilon_{rad})$ in erg s^{-1}; cm^{-3}. Left panel: The cloud (its outer boundary is the black circle) contains the source in its centre. At this evolutionary stage, the source ionises only the central part of the cloud leaving the outer envelopes neutral so that all ionising photons are absorbed inside the cloud. While the algorithm reproduces shielding correctly at the close vicinity of the cloud ($\lesssim$ 2.5pc), it produces spurious ionising photons at larger distances. Position of the target cell discussed in the text is shown by the green triangle. Right panel: The cloud is irradiated by an external source. TreeRay overestimates the angle cast by the shadow behind the cloud.

ϵ_{rad} in the current and previous time step is smaller than a specified constant.

Although TreeRay appears to reasonably model H II regions in on the spot approximation (for example it reproduces the expanding law eq. (1.3) for combined output of many ionising sources), we should mention two known non–trivial problems of the algorithm. We adopt highly idealised configurations to illustrate these features qualitatively. The same features arise in more realistic simulations, where they are more difficult to disentangle.

The left panel of Figure 3.3 shows an ionising source located inside a homogeneous spherical cloud (black circle) of neutral hydrogen. The cloud contains more mass than the source is able to ionise, so only the inner part of the cloud is ionised. The outer part of the cloud is neutral and there should be no ionising photons outside. However, the algorithm artificially inserts ionising photons at higher distance from the cloud.

To understand the cause of this spurious behaviour, consider the tree structure when ϵ_{rad} is calculated for the cell marked by the green triangle. The large distance between the target cell and the ionising source implies that the whole cloud, which is the only object in the computational domain of non–negligible density, would be put with its wide surroundings in one block. The mean particle density of the block $\langle n \rangle$ is substantially lower than the particle density n of the cloud. Since the number of recombinations per unit volume equals n^2, the averaging underestimates the recombination rate significantly, so some photons artificially leak.

In the example on the righ panel of Figure 3.3, the source irradiates the cloud from outside. The irradiated cloud cast a conical shadow. However, the algorithm overestimates the angle subtended by the shadow, the correct angle is indicated by the white bars. This feature arises in cells inside the cone surface where the ray closest to the source and bringing the highest amount of photons passes close to the shielding cloud, so a significant fraction of the cloud is mapped on this ray absorbing all ionising photons. Note that the irradiated rectangles in the shadow are due to the artificial photon leakage.

These features are not bugs in code, but inherent properties of the adopted algorithm. Their magnitude can be partially suppressed, but not eliminated, by using higher number of rays.

3.2.3 Particles

Current version of Flash code has implementation of two kinds of particles: active and passive. Active particles interact with the matter in the cells and/or with themselves. For the purpose of this work, we describe only gravitationally interacting sink particles, but more options are available. Passive particles are lagrangian tracers of gaseous flows with no influence on the medium or themselves.

As the central density increases during the gravitational collapse, more refinement levels are needed, and the calculation would become prohibitively expensive at some stage. Further complication comes from free–fall timescale t_{ff} decreasing like $\propto 1/\sqrt{G\rho}$, which would necessitate extremely short timesteps. These issues can be treated by *sink particle method* which was originally developed for SPH numerical schemes Bate et al. [1995], and later adopted to AMR techniques Krumholz et al. [2004]. Below we briefly describe current implementation to Flash code, which is due to [Federrath et al., 2010].

Sink particles are an approximation for the densest parts of the gas. They are spheres characterised only by their accretion radius r_{acc}, mass, momentum, and angular momentum. Sink particles enable us to model the molecular cloud outside them, but we resign at resolving their inner structure. For typical simulations, they represent significantly larger volume than sole protostars.

Several conditions must be met to model sink particle formation reasonably well (i.e. to avoid artificial formation of many sink particles in one collapsing object, or formation a sink particle in dense but gravitationally unbound compressed postshock layer). It is natural to require that the dense gaseous condensation prior sink particle formation is well resolved. Following Truelove et al. [1997], one Jeans length $\lambda_J = c_s\sqrt{\pi/(G\rho)}$ must be resolved by at least 4 grid cell sizes Δx. Since Δx is fixed for a particular simulation, we get the density threshold for formation of sink particles,

$$\rho_{thr} = \frac{\pi c_s^2}{n_{cells}^2 r_{acc}^2}, \tag{3.12}$$

where n_{cells} is the number of cells per r_{acc}. Federrath et al. [2010] suggest that the reasonable value of $n_{cells} = 2.5$.

Sink particles can be formed only in cells which are at the highest refinement level, and which are above the density threshold ρ_{thr}. In addition, all the following criteria must be fulfilled inside the volume of a candidate sink particle:

- The flow inside is converging.
- The gas is gravitationally bound and Jeans unstable
- The volume contains the gravitational potential minimum.
- The candidate particle does not overlap with an existing sink particle.

Once formed, a sink particle can further gain mass by accretion.

The gravitational interaction between sink particles and gas is implemented self–consistently: sink particles are subject to the gravitational force from the gaseous potential and themselves, and gas is attracted by grav. force both due to gas and sink particles. Sink particles can freely move across cells. They are integrated by leap–frog algorithm. Numerical difficulties arising at their close encounters are treated by spline softening. Sink particles can be used with isolated, mixed or periodic BCs for self–gravity.

4. Ewald method and its modifications

Ewald method provides an efficient formula for calculating gravitational field in computational domains with periodic boundary conditions. We describe the method in section 4.1. Since some astrophysical systems are layer or filamentary like with periodic boundary conditions in only one or two directions, and with isolated BCs in the other direction(s), it is natural to seek for a modification of the Ewald method for these configurations. We derive the formulae for gravitational potential for these systems in Section 4.2 (periodic BCs in two directions and isolated BCs in the third direction; hereafter 2P1I) and Section 4.3 (periodic BCs in one direction and isolated in the other two directions; hereafter 1P2I). We implement standard Ewald method and our modifications of the Ewald method to codes Flash and Gandalf. We test the implementation on systems with known analytic solution (Section 4.4). For possible future implementation in another code, we provide the formulae for acceleration and its spatial derivatives in Appendix B. The derivation of the formulae for potential in the case of computational domains with mixed BCs and test simulations will be published in (Wuñsch et al. in preparation).

4.1 Standard Ewald method

This method is invented by Ewald [1921] to calculate the electrostatic potential on a regularly spaced crystal lattice. Since the gravitational potential decreases with distance in the same way as the electrostatic potential, it is straightforward to use this method for gravitational problems with periodic boundary conditions [Hernquist et al., 1991, Klessen, 1997]. The whole computational domain of an astrophysical simulation is an analog to one unit cell in the crystal lattice.

For the purpose of the thesis we do not provide the precise derivation of the desired formula, but only sketch the basic idea behind. Consider a cuboidal computational domain with side lengths L_x, L_y and L_z along coordinate axes x, y and z, respectively. The domain contains N point masses located at $\mathbf{r}_a$ and of mass m_a, and the domain is surrounded by its periodic copies in directions x, y and z (we refer to this configuration as 3P). To speed up the calculation of the contribution to potential at $\mathbf{r}$ from a point mass at $\mathbf{r}_a$ and its periodic copies, Ewald splits the potential in two parts $1/(\|\mathbf{r}-\mathbf{r}_a\|) = \mathrm{erfc}(\alpha\|\mathbf{r}-\mathbf{r}_a\|)/\|\mathbf{r}-\mathbf{r}_a\| + \mathrm{erf}(\alpha\|\mathbf{r}-\mathbf{r}_a\|)/\|\mathbf{r}-\mathbf{r}_a\|$, where α is an arbitrary constant. The first term converges rapidly in the physical space, while the second term converges rapidly in the Fourier space using the Poisson summation formula. Summing over all particles in the computational domain, the potential becomes

$$\begin{aligned}
\phi(\mathbf{r}) &= -G\sum_{a=1}^{N} m_a \left(P_S(\mathbf{r},\mathbf{r_a}) + P_L(\mathbf{r},\mathbf{r_a})\right) && (4.1)\\
&= -G\sum_{a=1}^{N} m_a \Big\{ \sum_{i_1,i_2,i_3} \frac{\mathrm{erfc}(\alpha\|\mathbf{r}-\mathbf{r_a}-i_1\mathbf{e_x}L_x - i_2\mathbf{e_y}L_y - i_3\mathbf{e_z}L_z\|)}{(\|\mathbf{r}-\mathbf{r_a}-i_1\mathbf{e_x}L_x - i_2\mathbf{e_y}L_y - i_3\mathbf{e_z}L_z\|)}\\
&\quad -\frac{1}{L_xL_yL_z}\sum_{k_1,k_2,k_3,\|k\|\neq 0} \frac{4\pi}{k^2}\exp(-\frac{k^2}{4\alpha^2})\cos(\mathbf{k}.(\mathbf{r}-\mathbf{r_a}))\Big\}. && (4.2)
\end{aligned}$$

To simplify the notation, we explicitly denote the short– and long–range contributions to the potential as $P_S(\mathbf{r},\mathbf{r_a})$ and $P_L(\mathbf{r},\mathbf{r_a})$; These terms are then expressed in the following two lines. Indices i_1, i_2, i_3 are integers, $\mathbf{e_x}, \mathbf{e_y}, \mathbf{e_z}$ unit vectors in directions of coordinate axes, and $\mathbf{k}$ is the wavevector with components k_1, k_2, k_3 given by

$$k_1 = \frac{2\pi l_1}{L_x}, \tag{4.3a}$$

$$k_2 = \frac{2\pi l_2}{L_y}, \tag{4.3b}$$

$$k_3 = \frac{2\pi l_3}{L_z}, \tag{4.3c}$$

where l_1, l_2, l_3 are integers.

The rapid convergence of both terms in eq. (4.2) enables us to reach high accuracy with taking into account only small number of terms in the sequence, which is valuable for numerical reasons. The value of the parameter α controls the speed of the convergence. Higher α leads to more rapid convergence of the short–range terms and to the slower convergence of the long–range terms. Following Klessen [1997], for cubical computational domains ($L_x = L_y = L_z$), the optimal convergence rate is reached when

$$\|i\|^2 \leq 16, \tag{4.4}$$

$$\|l\|^2 \leq 10. \tag{4.5}$$

and $\alpha = 2/L_x$.

4.2 Ewald method for 2P1I boundary conditions

In this section, we present our modification to the standard Ewald method, eq. (4.2) for computational domains with periodic BCs in directions $\mathbf{e_x}$ and $\mathbf{e_y}$, and with isolated BCs in the direction $\mathbf{e_z}$.

At the beginning of the process of modification, our configuration is a computational domain with periodic BCs in all three spatial directions, so the potential is given by eq. (4.2). For convenience, we express the side lengths of the computational domain in multiples of L_x, i.e. $L_y = bL_x$ and $L_z = cL_x$. To undertake the modification, it is useful to look at the whole space filled with periodically

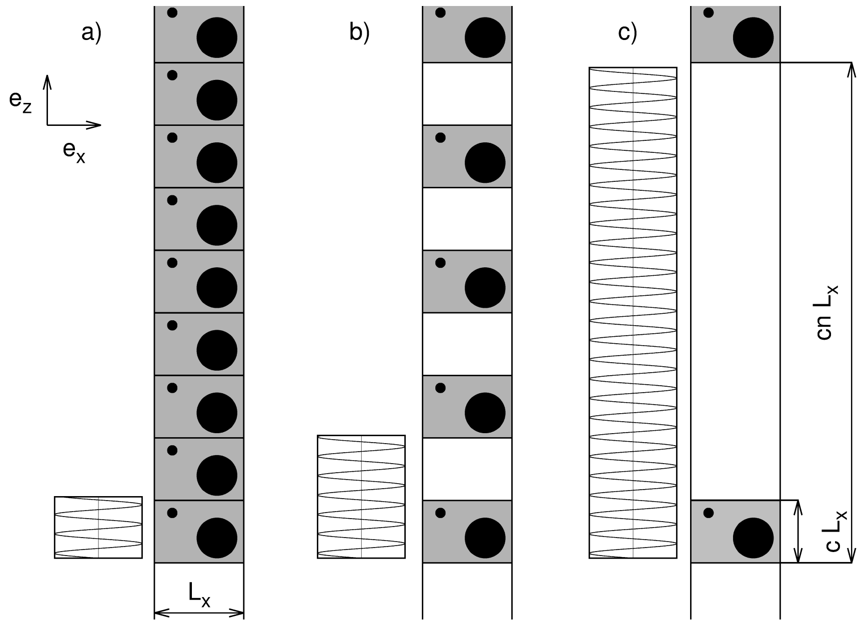

Figure 4.1: Illustration of the limiting process which transforms BCs periodic in directions $\mathbf{e_x}$ and $\mathbf{e_z}$ to BCs periodic in direction $\mathbf{e_x}$ and isolated in direction $\mathbf{e_z}$. One computational domain is the grey rectangle containing two idealised clouds (black circles). We show periodic copies only in direction $\mathbf{e_z}$. PANEL A: Configuration before the limiting process starts ($n = 1$). PANEL B: Computational domain is stretched by one layer thickness cL_x, i.e. $n = 2$. PANEL C: Computational domain is stretched by eight layer thicknesses cL_x, i.e. $n = 8$. The box to the left of the computational domain illustrates eq. (4.8): to maintain the same sampling frequency and thus spatial resolution for the Fourier transformation to calculate the long–range term $P_L(\mathbf{r}, \mathbf{r_a})$, the highest wavenumber l_3 (proportional to the zeros of the sine function) must increase with n.

repeating computational domains as that the periodic copies are organised in layers, where one layer is selected (we call the layer *fundamental layer*) and the other layers are its periodic copies. We choose the layers so that their normals point in direction z, so each layer stretches vertically from kcL_x to $(k+1)cL_x$ where k is an integer. Let extend the fundamental layer in the direction z by a factor n, but keep the mass distribution from $z = 0$ to $z = cL_x$ intact, and the space from cL_x to ncL_x to be empty. This also stretches all layers which are periodic copies (see Figure 4.1). Increasing $n \to \infty$, we displace all periodic copies of the fundamental layer to infinity, and all material in the whole space is located in the fundamental layer. This is the configuration for which we want to evaluate the gravitational potential; the fundamental layer has periodic BCs in two directions (here $\mathbf{e_x}$ and $\mathbf{e_y}$), and isolated BCs in the third direction (here $\mathbf{e_z}$). Since eq. (4.2) holds as n increases, the formula for gravitational potential in the configuration with 2P1I BCs is the limit of eq. (4.2) when $n \to \infty$. A cartoon illustrating the limiting process is shown in Figure 4.1.

We evaluate the potential eq. (4.2) in the limit $n \to \infty$. The short–range term has the form

$$P_S(\mathbf{r}, \mathbf{r_a}) = \sum_{i_1, i_2, i_3} \frac{\operatorname{erfc}(\alpha \|\mathbf{r} - \mathbf{r_a} - i_1 \mathbf{e_x} - i_2 b \mathbf{e_y} L_x - i_3 c n \mathbf{e_z} L_x\|)}{(\|\mathbf{r} - \mathbf{r_a} - i_1 \mathbf{e_x} L_x - i_2 b \mathbf{e_y} L_x - i_3 c n \mathbf{e_z} L_x\|)}. \tag{4.6}$$

According to condition eq. (4.5), any contribution to the sum with $i_3 \neq 0$ becomes negligible already when $n > 4/c$, vanishing as $n \to \infty$. The only non–negligible contributions are those with $i_3 = 0$. We show the limit of the short range term in eq. (4.16) below (it is the first term on the right hand side).

The long–range term becomes

$$
\begin{aligned}
P_L(\mathbf{r}, \mathbf{r_a}) \;=\; & -\frac{1}{\pi L_x b} \sum_{l_1, l_2} \exp\left(-\frac{\pi^2}{\alpha^2 L_x^2}\left(l_1^2 + \left(\frac{l_2}{b}\right)^2\right)\right) \times \\
& \lim_{n\to\infty} \frac{1}{n} \sum_{l_3} \frac{\exp(-\frac{\pi^2 l_3^2}{\alpha^2 c^2 L_x^2 n^2})}{c\ (l_1^2 + (l_2/b)^2 + (l_3/cn)^2)} \\
& \cos\left(\frac{2\pi l_1(x - x_a)}{L_x} + \frac{2\pi l_2(y - y_a)}{bL_x} + \frac{2\pi l_3(z - z_a)}{cnL_x}\right).
\end{aligned} \tag{4.7}
$$

From eq. (4.5), we obtain the condition for the minimum range of indices to be taken into account as

$$
l_1^2 + (l_2/b)^2 + (l_3/cn)^2 \leq 10. \tag{4.8}
$$

The range for index l_3 increases with increasing n while the ranges for indices l_1 and l_2 are independent on n. This behaviour is intuitive because with lengthening the computational domain in direction $\mathbf{e}_z$, one must cover higher number of wavelengths in this direction in the Fourier space to get the same spatial resolution as in directions $\mathbf{e}_x$ and $\mathbf{e}_y$, where the size of the domain is fixed.

With this condition in mind, the term on the second and third line in eq. (4.7) is a Riemann sum over interval $(-\sqrt{10}, \sqrt{10})$ with bins of size $1/cn$. The limit over index l_3 becomes

$$
\begin{aligned}
& -\sin\left(\frac{2\pi l_1(x - x_a)}{L_x} + \frac{2\pi l_2(y - y_a)}{L_x b}\right) \int_{-\infty}^{\infty} \frac{\exp(-\frac{\pi^2 t^2}{\alpha^2 c^2 L_x^2})}{c\ (l_1^2 + (l_2/b)^2 + (t/c)^2)} \sin\left(\frac{2\pi t(z - z_a)}{cL_x}\right) \mathrm{dt} + \\
& \quad \cos\left(\frac{2\pi l_1(x - x_a)}{L_x} + \frac{2\pi l_2(y - y_a)}{L_x b}\right) \int_{-\infty}^{\infty} \frac{\exp(-\frac{\pi^2 t^2}{\alpha^2 c^2 L_x^2})}{c\ (l_1^2 + (l_2/b)^2 + (t/c)^2)} \cos\left(\frac{2\pi t(z - z_a)}{cL_x}\right) \mathrm{dt}
\end{aligned} \tag{4.9}
$$

where we extend the interval $(-\sqrt{10}, \sqrt{10})$ to infinity to facilitate the following integration. The integral on the first line is zero because the integrand is an even function calculated over an interval centered at zero. To simplify the notation, we introduce

$$
\gamma \;=\; \frac{2\pi(z - z_a)}{L_x}, \tag{4.10}
$$

$$
\zeta \;=\; \frac{\pi^2}{\alpha^2 L_x^2}. \tag{4.11}
$$

With substitution $u = t/c$, the integral on the second line of eq. (4.9) is

$$
I(l_1, l_2, z - z_a) = 2\int_0^{\infty} \frac{\exp(-\zeta u^2)\cos(\gamma u)}{(l_1)^2 + (l_2/b)^2 + u^2} \mathrm{du}. \tag{4.12}
$$

The solution to eq. (4.12) can be found in the closed form. For $|l_1|+|l_2|\neq 0$, integration yields

$$\begin{aligned} I(l_1,l_2,z-z_a) &= \frac{\pi}{2\sqrt{l_1^2+(l_2/b)^2}}\exp\left(-\sqrt{l_1^2+(l_2/b)^2}\gamma+\zeta\left(l_1^2+(l_2/b)^2\right)\right)\times \\ &\quad \left\{\exp\left(2\sqrt{l_1^2+(l_2/b)^2}\gamma\right)\operatorname{erfc}\left(\frac{\zeta\sqrt{l_1^2+(l_2/b)^2}+\gamma/2}{\sqrt{\zeta}}\right)\right. \\ &\quad \left.+\operatorname{erfc}\left(\frac{\zeta\sqrt{l_1^2+(l_2/b)^2}-\gamma/2}{\sqrt{\zeta}}\right)\right\}. \end{aligned} \tag{4.13}$$

For $l_1 = l_2 = 0$, integral 4.12 diverges. However, with the help of identity $\cos(x) = 1-2\sin^2(x/2)$, we express the integral as

$$I(0,0,z-z_a) = 2\int_0^\infty \frac{\exp(-\zeta u^2)}{u^2}\mathrm{dt} - 4\int_0^\infty \frac{\exp(-\zeta u^2)\sin^2(\gamma u/2)}{u^2}\mathrm{dt}. \tag{4.14}$$

We can omit the divergent first term on the right hand side because its value does not depend on coordinates, so it has no influence on acceleration. The independence on coordinates follows from the independence of formula (4.9) for $l_1 = l_2 = 0$ on x and y, and from the independence of this term on z. The second term on the right hand side of eq. (4.14) is easy to integrate, and we find

$$I(0,0,z-z_a) = \pi\left\{\gamma\operatorname{erf}\left(\frac{\gamma}{2\sqrt{\zeta}}\right)+2\sqrt{\frac{\zeta}{\pi}}\exp(-\gamma^2/4\zeta)\right\}-2\sqrt{\pi\zeta}. \tag{4.15}$$

Substituting these results for the long–range term in eq. (4.7), the formula for the potential eq. (4.2) for a computational domain with periodic BCs in directions $\mathbf{e}_x$ and $\mathbf{e}_y$, and with isolated BCs in the direction $\mathbf{e}_z$ reads

$$\begin{aligned} \phi(\mathbf{r}) &= -G\sum_{a=1}^{N} m_a\Big\{\sum_{i_1,i_2,i_1^2+(bi_2)^2\le 10}\frac{\operatorname{erfc}(\alpha\|\mathbf{r}-\mathbf{r_a}-i_1\mathbf{e_x}L_x-i_2\mathbf{e_y}bL_x\|)}{(\|\mathbf{r}-\mathbf{r_a}-i_1\mathbf{e_x}L_x-i_2\mathbf{e_y}bL_x\|)} \\ &\quad -\frac{1}{\pi L_x b}\sum_{l_1,l_2,l_1^2+(l_2/b)^2\le 10}\exp(-\zeta(l_1^2+(l_2/b)^2))\times \\ &\quad \cos\left(\frac{2\pi l_1(x-x_a)}{L_x}+\frac{2\pi l_2(y-y_a)}{L_x b}\right)I(l_1,l_2,z-z_a)\Big\}. \end{aligned} \tag{4.16}$$

4.3 Ewald method for 1P2I boundary conditions

We modify the Ewald method for computational domains with periodic BCs in direction $\mathbf{e}_x$, and with isolated BCs in directions $\mathbf{e}_y$ and $\mathbf{e}_z$. We arrive at the desired formula for potential by an analogous limiting process to that in the case 2P1I.

The starting configuration is one layer of computational domains with isolated BCs in direction $\mathbf{e}_z$, whose potential is already known. In analogy to the limit in case 2P1I, where it was useful to work with periodic copies of the fundamental

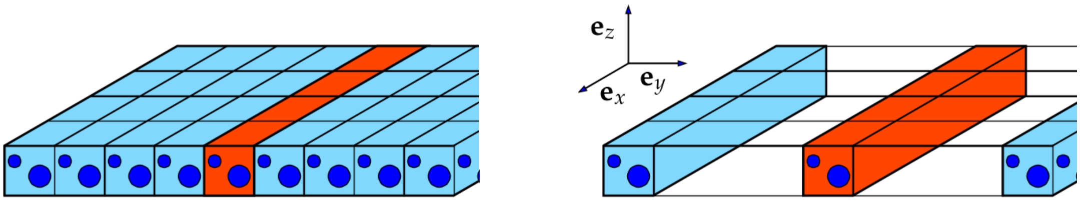

Figure 4.2: Illustration of the limiting process leading to the potential formula in configuration 1P2I. The fundamental cuboid is coloured red. One computational domain is a blue cube with two idealised clouds. LEFT PANEL: Configuration before the limiting process starts ($n = 1$). RIGHT PANEL: The computational domain is stretched by four layer thicknesses bL_x, i.e. $n = 4$.

layer, we look at the fundamental layer as it consists of parallel cuboids of infinite length (Figure 4.2). One cuboid is selected *fundamental cuboid*, and the other cuboids are its periodic copies. The longest axis of the fundamental cuboid points in the direction $\mathbf{e}_x$.

The extent of the fundamental cuboid in the direction $\mathbf{e}_y$ is from 0 to bL_y. The cuboid is surrounded by two periodic copies at $y < 0$ and $y > bL_y$. Let increase the distance to the periodic copies by stretching the side length bL_y by factor n so that the mass distribution inside the cuboid from 0 to bL_y is unaltered, and only empty space is added from bL_y to bnL_y (right panel of Fig. 4.2). This displacement is applied to all cuboids because from definition they copy the fundamental cuboid. In the limit of $n \to \infty$, all periodic copies of the fundamental cuboid are displaced to infinity and we end up with empty space filled only by the fundamental cuboid. Note that a computational domain in the fundamental cuboid has periodic BCs in direction $\mathbf{e}_x$, and isolated BCs in directions $\mathbf{e}_y$ and $\mathbf{e}_z$; it is the configuration for which we search the formula for the potential. Since eq. (4.16) describes the potential for any n, the potential in case 1P2I is the limit of eq. (4.16) for $n \to \infty$.

The limit to the short–range term $P_S(\mathbf{r}, \mathbf{r_a})$ is calculated easily using the same idea as in the case of 2P1I configuration, and the result is written as the first term on the right hand side of eq. (4.28) below.

To write the limit of the long–range term, we substitute $b \to bn$ to eq. (4.16), which yields

$$P_L(\mathbf{r}, \mathbf{r_a}) = -\frac{1}{\pi L_x nb} \sum_{l_1} \exp(-\zeta l_1^2) \sum_{l_2} \exp\left(-\zeta (l_2/(bn))^2\right) \times \cos\left(\frac{2\pi l_1 (x - x_a)}{L_x} + \frac{2\pi l_2 (y - y_a)}{bnL_x}\right) \int_{-\infty}^{\infty} \frac{\exp(-\zeta t^2)\cos(\gamma t)}{(l_1)^2 + (l_2/bn)^2 + t^2} \tag{4.17}$$

The minimum range of index l_2 follows from condition eq. (4.8), which now reads

$$l_1^2 + (l_2/bn)^2 \leq 10. \tag{4.18}$$

In an analog to γ (see eq. (4.10)), we introduce δ

$$\delta = \frac{2\pi(y - y_a)}{L_x}, \tag{4.19}$$

to make following formulae more compact. Applying identity $\cos(x+y) = \cos(x)\cos(y) - \sin(x)\sin(y)$ on the term $\cos\left(\frac{2\pi l_1(x-x_a)}{L_x} + \frac{2\pi l_2(y-y_a)}{bnL_x}\right)$ in eq. (4.17), we see that the sine terms cancel because of their oddity. Then the limit of eq. (4.17) is

$$\begin{aligned} P_L(\mathbf{r},\mathbf{r_a}) &= -\frac{1}{\pi L_x}\sum_{l_1, l_1^2\leq 10} \exp\left(-\zeta l_1^2\right)\cos\left(\frac{2\pi l_1(x-x_a)}{L_x}\right)\times \\ & \int_{-\infty}^{\infty}\int_{-\infty}^{\infty}\frac{\exp(-\zeta(t^2+w^2))\cos(\gamma t)\cos(\delta w)}{l_1^2+t^2+w^2}\mathrm{dtdw}. \qquad (4.20) \end{aligned}$$

Although we did not find the value of the integral in eq. (4.20),

$$K(l_1, y-y_a, z-z_a) \equiv \frac{1}{2\pi}\int_{-\infty}^{\infty}\int_{-\infty}^{\infty}\frac{\exp(-\zeta(t^2+w^2))\cos(\gamma t)\cos(\delta w)}{l_1^2+t^2+w^2}\mathrm{dtdw} \quad (4.21)$$

in the closed form, we simplified it to one dimensional integral, which facilitates its numerical evaluation. Applying $\cos(\gamma t)\cos(\delta w) = \cos(\gamma t + \delta w) + \sin(\gamma t)\sin(\delta w)$ to eq. (4.21), we get two integrals, where one of them, the sine integral is zero due to its oddity, and we get

$$K(l_1, y-y_a, z-z_a) = \frac{1}{2\pi}\int_{-\infty}^{\infty}\int_{-\infty}^{\infty}\frac{\exp(-\zeta(t^2+w^2))\cos(\gamma t+\delta w)}{l_1^2+t^2+w^2}\mathrm{dtdw}. \quad (4.22)$$

Since the isocontours of the exponential term and the term in denominator are constants on circles with centre at the origin, and the cosine term is constant on lines $\gamma t + \delta w = const.$, a simplification can be gained by rotating the coordinate frame so as the lines of $\gamma t + \delta w = const.$ are aligned with one of the coordinate axis. Substitution

$$\begin{aligned} t &= \frac{1}{\sqrt{\gamma^2+\delta^2}}(-\delta u + \gamma v) \qquad (4.23) \\ w &= \frac{1}{\sqrt{\gamma^2+\delta^2}}(\gamma u + \delta v) \qquad (4.24) \end{aligned}$$

aligns these lines parallel to $\mathbf{e}_v$, and we obtain

$$K(l_1, y-y_a, z-z_a) = \frac{1}{2\pi}\int_{-\infty}^{\infty}\int_{-\infty}^{\infty}\frac{\exp(-\zeta(u^2+v^2))\cos(v\sqrt{\gamma^2+\delta^2})}{l_1^2+u^2+v^2}\mathrm{dudv}. \quad (4.25)$$

We can simplify this formula to one dimensional integration by substitution to polar coordinates ($u = q\cos\phi$ and $v = q\sin\phi$), after which, we yield

$$\begin{aligned} K(l_1, y-y_a, z-z_a) &= \frac{2}{2\pi}\int_0^{\infty}\int_0^{\pi}\frac{\exp(-\zeta q^2)\cos(\eta\, q\sin\phi)}{l_1^2+q^2}\mathrm{d\phi dq} \\ &= \int_0^{\infty}\frac{J_0(\eta q)\exp(-\zeta q^2)}{l_1^2+q^2}q\mathrm{dq}, \qquad (4.26) \end{aligned}$$

where J_0 is the Bessel function of the first kind and zero order, and the distances in isolated directions γ and δ are symmetrised by $\eta = \sqrt{\gamma^2+\delta^2}$. Unfortunately, we did not find a way how to evaluate eq. (4.26) in the closed form. Function K diverges for $l_1 = 0$, an analogous behaviour to that we encountered with function

$I(0,0,z-z_a)$ in eq. (4.12) for 2P1I boundary conditions. We circumvent the issue in the same spirit. In the analog to eq. (4.14), we insert trivial identity $J_0 = J_0 - 1 + 1$ to eq. (4.26) for $l_1 = 0$, and omit the diverging integral $\int_0^\infty \exp(-\zeta q^2)/q dq$ since it does not depend on coordinates and has no influence on acceleration. After that, we obtain,

$$K(0, y - y_a, z - z_a) = \int_0^\infty \frac{(J_0(\eta q) - 1)\exp(-\zeta q^2)}{q} dq. \tag{4.27}$$

Now, we can write the potential for a computational domain with periodic BCs in direction $\mathbf{e}_x$ and isolated BCs in directions $\mathbf{e}_y$ and $\mathbf{e}_z$ as,

$$\begin{aligned}\phi(\mathbf{r}) \;=\; & -G\sum_{a=1}^{N} m_a \Big\{ \sum_{i_1, i_1^2 \le 10} \frac{\operatorname{erfc}(\alpha\|\mathbf{r} - \mathbf{r_a} - i_1 \mathbf{e_x} L_x\|)}{(\|\mathbf{r} - \mathbf{r_a} - i_1 \mathbf{e_x} L_x\|)} \\ & -\frac{2}{L_x} \sum_{l_1, l_1^2 \le 10} \exp(-\zeta l_1^2) \cos\left(\frac{2\pi l_1 (x - x_a)}{L_x}\right) K(l_1, y - y_a, z - z_a) \Big\},\end{aligned} \tag{4.28}$$

where the function $K(l_1, y - y_a, z - z_a)$ is given by eq. (4.26) for $l_1 = 0$, and by eq. (4.27) otherwise.

4.4 Implementation to hydrodynamical codes Gandalf and Flash

Although Ewald method or its modifications greatly facilitate the calculation of gravitational field, it would be still prohibitively time consuming to directly calculate potential from eq. (4.2), eq. (4.16), or eq. (4.28) for each cell–node interaction at every time step. Moreover, such a high accuracy would be unnecessary because the uncertainty or adopted approximations in another important physical processes (i.e. chemistry, radiation) has a stronger influence on model evolution. Instead, the values of $P^{Ewald}(\mathbf{r} - \mathbf{r_a}) = P_S(\mathbf{r} - \mathbf{r_a}) + P_L(\mathbf{r} - \mathbf{r_a})$ (or their higher derivatives if desired) are precalculated on a grid (hereafter *Ewald array*) covering the computational domain before the simulation starts. This can be done a priori since the function P^{Ewald} is independent on mass distribution in the computational domain. Then, during the simulation, the potential for a grid cell at $\mathbf{r}$ is obtained by summing over all accepted block nodes, each of mass m_a, i.e.

$$\phi(\mathbf{r}) = -G\sum_{a=1}^{N} m_a P^{Ewald}(\mathbf{r} - \mathbf{r_a}), \tag{4.29}$$

(cf. eq. (4.1)), and the value of $P^{Ewald}(\mathbf{r} - \mathbf{r_a})$ is obtained (by interpolation or Taylor expansion) from the Ewald array. Likewise, acceleration is calculated as

$$\mathbf{a}(\mathbf{r}) = G\sum_{a=1}^{N} m_a \mathbf{A}^{Ewald}(\mathbf{r} - \mathbf{r_a}), \tag{4.30}$$

where

$$\mathbf{A}^{Ewald} = -\nabla P^{Ewald} \tag{4.31}$$

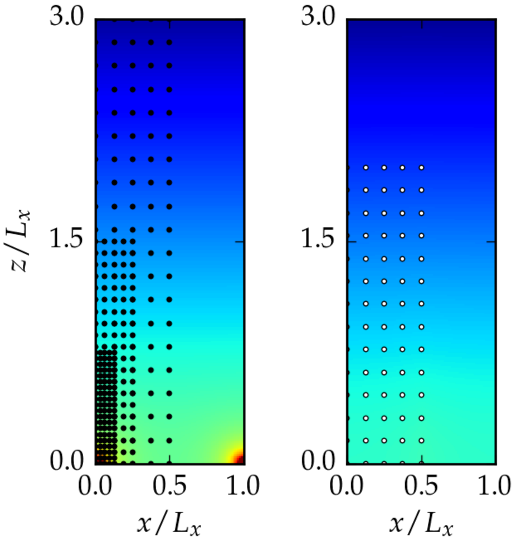

Figure 4.3: Coverage of the computational domain by the Ewald array (points). The domain has periodic BCs in direction $\mathbf{e}_x$, and isolated BCs in direction $\mathbf{e}_z$. LEFT PANEL: Ewald array on a three level nested grid with $n_{x.Ewald} = 4$ (first approach to construction of the Ewald array). Colourscale represents the value of P^{Ewald}. RIGHT PANEL: Ewald array in the second approach. Colourscale represents the value of $P^{Ewald} - 1/(\|(\mathbf{r}-\mathbf{r_a})\|)$

is again evaluated from the Ewald array. To avoid numerical problems with calculating derivatives, we always use a formula for $\mathbf{A}^{Ewald}$ (see Appendix B); $\mathbf{A}^{Ewald}$ is never calculated by taking numerical differences of P^{Ewald}. This is the basic idea. Below we describe construction of the grid and approximations done during evaluation of the Ewald array.

In code Flash, we experimented with two kinds of construction of the Ewald array. In the first approach, we evaluate functions P^{Ewald} and $\mathbf{A}^{Ewald}$ on several levels of nested grid (left panel of Figure 4.3) centered at the origin. The value of P^{Ewald} and $\mathbf{A}^{Ewald}$ at a desired location is then estimated by a trilinear interpolation on appropriate grid level. Since these functions are symmetric in a periodic direction (e.g. $P^{Ewald}(L_x - (\mathbf{r}-\mathbf{r_a})) = P^{Ewald}(\mathbf{r}-\mathbf{r_a})$ for periodic BCs in direction $\mathbf{e}_x$), it is sufficient to cover only part of the computational domain by the Ewald array, which saves some memory. Thus, the first level of the Ewald array occupies volume $L_x/2 \times L_y/2 \times L_z/2$ for configuration 3P, it occupies $L_x/2 \times L_y/2 \times L_z$ for configuration 2P1I, and $L_x/2 \times L_y \times L_z$ for configuration 1P2I. The next level of the grid has the same number of grid points in direction $\mathbf{e}_x$ ($n_{x.Ewald}$), $\mathbf{e}_y$ ($n_{y.Ewald}$) and $\mathbf{e}_z$ ($n_{z.Ewald}$) as the previous level, but is of half the spatial extent of the previous level, so its resolution is two times higher. This enables to interpolate rapidly increasing P^{Ewald} and $\mathbf{A}^{Ewald}$ near the origin.

In the second approach, we subtract terms $1/\|(\mathbf{r}-\mathbf{r_a})\|$ and $(\mathbf{r}-\mathbf{r_a})/\|(\mathbf{r}-\mathbf{r_a})\|^3$ from functions P^{Ewald} and $\mathbf{A}^{Ewald}$, which removes their singular behaviour near the origin, and enables us to use grid of only one level (right panel of Fig. 4.3). Another memory saving can be achieved by shortening the physical extent of the Ewald array in the isolated direction(s), and to use the analytic approximation to the Ewald array in the rest of the computational domain. For example, in configuration 2P1I, we can look at functions P^{Ewald} and $\mathbf{A}^{Ewald}$ as they are proportional (with constant $1/(Gm_a)$) to the gravitational potential and acceleration generated by identical point masses in two dimensional lattice of rectangular cells. The lattice lies in plane (x, y) with normal pointing in the direction $\mathbf{e}_z$. With increasing height z above the plane, the inhomogeneities of the gravitational field due to the discrete point masses decrease, and the field converges to that of a homogeneous plane (eq. (2.31)). Comparing this equation with eq. (4.30), one

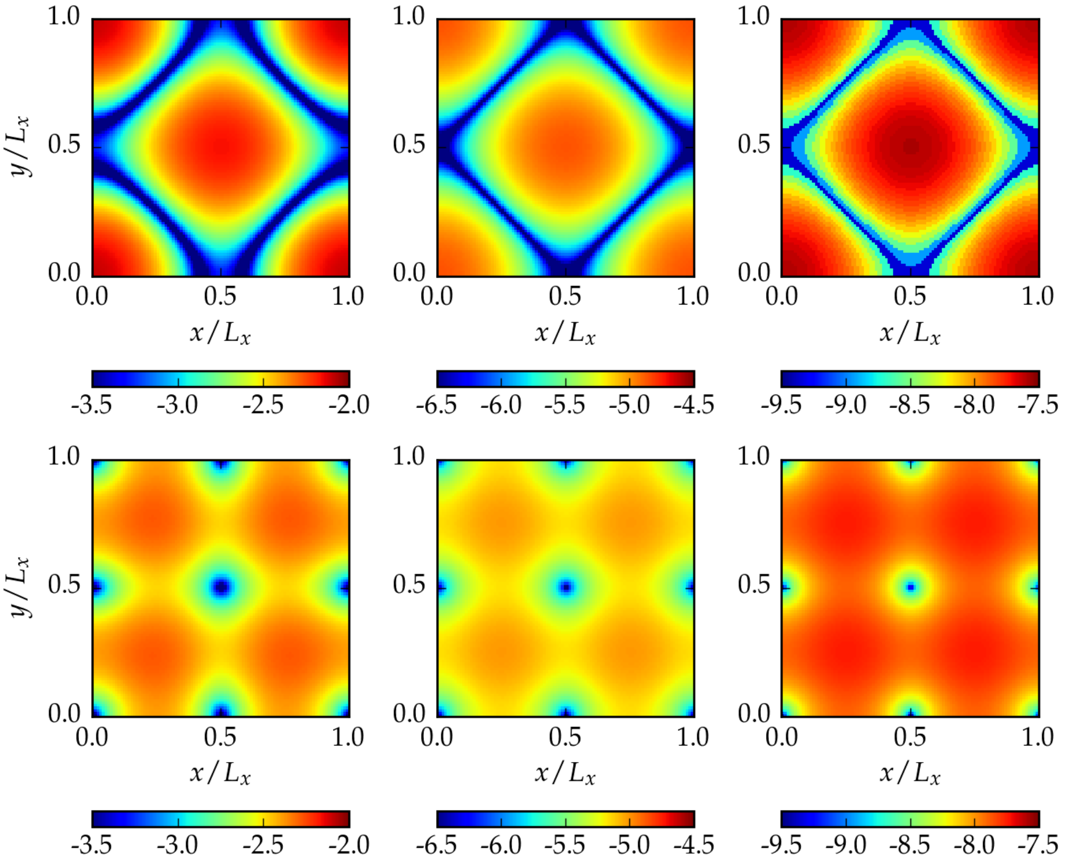

Figure 4.4: Convergence rate of function $\mathbf{A}^{Ewald}$ to its analytical estimate $\mathbf{A}_{anl}$ for configuration 2P1I for $L_x = L_y$. The functions are compared on slices $z = L_x$ (left panel), $z = 2L_x$ (middle panel) and $z = 3L_x$ (right panel). TOP ROW: Logarithm of the relative error in acceleration in the normal direction ($\log_{10}(|A_z^{Ewald} - A_{z.anl}|/|A_z^{Ewald}|)$). BOTTOM ROW: Logarithm of the ratio between acceleration in the tangential to normal direction ($\log_{10}(|\sqrt{(A_x^{Ewald})^2 + (A_y^{Ewald})^2}|/|A_z^{Ewald}|)$).

finds the analytical approximation to $\mathbf{A}^{Ewald}$ for $z \gg \max(L_x, L_y)$

$$\mathbf{A}_{anl} = -2\pi\,\mathrm{sign}(z)/(L_x L_y). \tag{4.32}$$

In Figure 4.4, we compare function $\mathbf{A}^{Ewald}$ for configuration 2P1I with its approximation $\mathbf{A}_{anl}$ of a homogeneous plane at slices of constant height above the plane $z = 0$ (from left to right $z = L_x$, $z = 2L_x$ and $z = 3L_x$). The top row shows the relative error between the zth component of $\mathbf{A}^{Ewald}$ and $\mathbf{A}_{anl}$, demonstrating fast convergence of $\mathbf{A}^{Ewald}$ to $\mathbf{A}_{anl}$; the relative error in acceleration is of the order 10^{-5} for $z > 2L_x$. The bottom row compares the magnitude of the acceleration in the tangential $\sqrt{(A_x^{Ewald})^2 + (A_y^{Ewald})^2}$ to normal direction $|A_z^{Ewald}|$. The acceleration in the tangential direction decreases rapidly, becoming soon smaller by several orders of magnitude than the acceleration in the normal direction. In both cases, the decrease is exponential $\simeq \exp(-2\pi z/L_x)$ as can be seen from eq. (B.24), eq. (B.25) and eq. (B.26).

Likewise, in configuration 1P2I, the gravitational field due to regularly–separated discrete point masses arranged on axis $\mathbf{e}_x$ converges with increasing

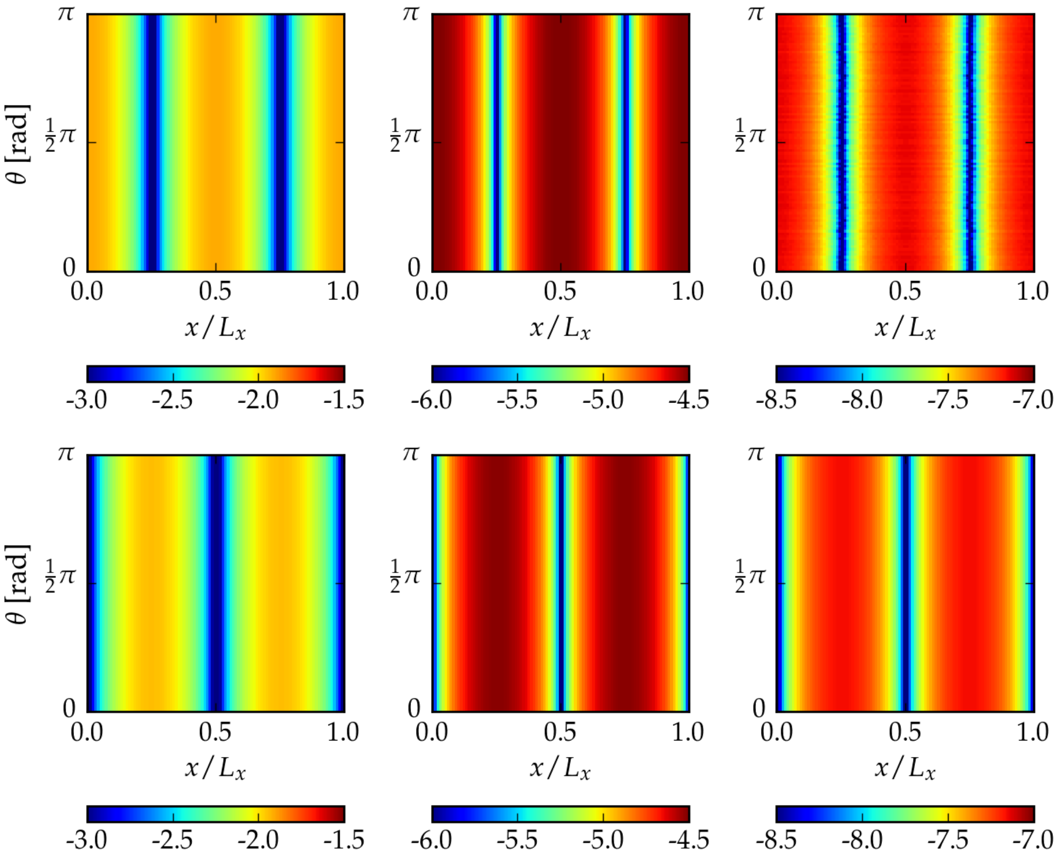

Figure 4.5: Convergence rate of function $\mathbf{A}^{Ewald}$ to its analytical estimate $\mathbf{A}_{anl}$ for configuration 1P2I. The functions are compared on cylindrical surfaces $R = L_x$ (left panel), $R = 2L_x$ (middle panel) and $R = 3L_x$ (right panel). The surfaces are coaxial with axis $\mathbf{e}_x$. TOP ROW: Logarithm of the relative error in acceleration in radial direction ($\log_{10}(|A_R^{Ewald} - A_{R.anl}|/|A_R^{Ewald}|)$). BOTTOM ROW: Logarithm of the ratio between acceleration in the tangential to radial direction ($\log_{10}(|A_x^{Ewald}|/|A_R^{Ewald}|)$)).

radial distance $R = \sqrt{y^2 + z^2}$ of the axis to the field generated by a homogeneous cylinder of the same mass per unit length. From the Gauss's theorem it follows that the radial component of gravitational acceleration generated by the cylinder is

$$\mathbf{A}_{anl} = -2\mathbf{e}_R/(RL_x), \tag{4.33}$$

where $\mathbf{e}_R$ is a unit vector in the radial direction. The comparison between the smooth solution $\mathbf{A}_{anl}$ and function $\mathbf{A}^{Ewald}$ on cylindrical surfaces with radii $R = L_x$, $R = 2L_x$ and $R = 3L_x$ is shown in Figure 4.5. The top row shows the relative error between the radial component of $\mathbf{A}^{Ewald}$ and $\mathbf{A}_{anl}$. Again, the relative error decreases very fast with increasing radius and it is smaller than 10^{-4} for $R > 2L_x$. The bottom row represents the ratio between the tangential and radial component of function $\mathbf{A}^{Ewald}$. The tangential component decreases rapidly with increasing R.

Thus, in the second approach, for configuration 2P1I, we cover the computational domain by the Ewald array only in volume $(0, L_x/2) \times$

$(0, L_y/2) \times (0, \min(L_z, 2\max(L_x, L_y)))$ (right panel of Fig. 4.3), and for $z > \min(L_z, 2\max(L_x, L_y))$, we use the analytic approximation to P^{Ewald} and $\mathbf{A}^{Ewald}$. For configuration 1P2I, the Ewald array occupies volume $(0, L_x/2) \times (0, 2L_x) \times (0, 2L_x)$, and the analytic approximation is used for $\sqrt{y^2 + z^2} > 2L_x$. This assures that the analytic approximation does not cause relative error in the magnitude of acceleration larger than 10^{-5} and 10^{-4} for configurations 2P1I and 1P2I, respectively.

Unlike the first approach where the value of P^{Ewald} and $\mathbf{A}^{Ewald}$ is obtained by trilinear interpolation on a grid, in the second approach, the value of these functions is estimated by the Taylor expansion to the first order,

$$\begin{aligned}
P^{Ewald}(\mathbf{r}) &\doteq P^{Ewald}(\mathbf{r_0}) - \Sigma_j A_j^{Ewald}(\mathbf{r_0})(r_j - r_{0j}) \\
&= \widetilde{P}(\mathbf{r_0}) - \Sigma_j A_j^{Ewald}(\mathbf{r_0}) r_j, \qquad (4.34)\\
A_i^{Ewald}(\mathbf{r}) &\doteq A_i^{Ewald}(\mathbf{r_0}) + \Sigma_j C_{ij}^{Ewald}(\mathbf{r_0})(r_j - r_{0j}) \\
&= \widetilde{A_i}(\mathbf{r_0}) + \Sigma_j C_{ij}^{Ewald}(\mathbf{r_0}) r_j. \qquad (4.35)
\end{aligned}$$

Functions $\mathbf{A}^{Ewald}$ and C_{ij}^{Ewald}, $C_{ij}^{Ewald} \equiv \partial A_i^{Ewald}/\partial r_j$ for given configuration are listed in the Appendix B. Note that only six components of C_{ij}^{Ewald} are independent since $C_{ij}^{Ewald} = C_{ji}^{Ewald}$ because of $C_{ij}^{Ewald} = -\frac{\partial}{\partial r_i}\left(\frac{\partial P^{Ewald}}{\partial r_j}\right) = -\frac{\partial}{\partial r_j}\left(\frac{\partial P^{Ewald}}{\partial r_i}\right)$. Thus in the Ewald array we store variables $\widetilde{P}(\mathbf{r_0}) = P^{Ewald}(\mathbf{r_0}) - \Sigma_j A_j^{Ewald}(\mathbf{r_0})$, $\widetilde{A_i}(\mathbf{r_0}) = A_i^{Ewald}(\mathbf{r_0}) + \Sigma_j C_{ij}^{Ewald}(\mathbf{r_0}) r_j$ (for $i = \{1, 2, 3\}$), derivatives of potential $A_i^{Ewald}(\mathbf{r_0})$ (for $i = \{1, 2, 3\}$), and six components of C_{ij}^{Ewald}.

Using the Taylor expansion to evaluate P^{Ewald} by eq. (4.34) or any component of $\mathbf{A}^{Ewald}$ by eq. (4.35) reduces the number of float point operations considerably in comparison to the trilinear interpolation. Whereas the former case needs 6 multiplications and 7 additions (some operations are needed to find the grid points), the latter needs 30 multiplications and 22 additions for the same task. From test simulations, we find that using Taylor polynomials (eq. (4.34) and eq. (4.35)) to evaluate P^{Ewald} or $\mathbf{A}^{Ewald}$ speeds simulations up by factor $\simeq 1.4$ to $\simeq 1.9$ (depending on the configuration and the shape of the computational domain) in comparison to the first approach with trilinear interpolation. The main cost to use Taylor polynomials is laborious implementation of functions C_{ij}^{Ewald}.

We decide to implement the second approach as a default to Flash code due to its speed. This can be valuable for simulations where self–gravity consumes the most of time. The first, simpler approach can be invoked by defining setup variable `bhtreeEwaldV42` at code configuration.

We implement all three configurations, 3P, 2P1I and 1P2I also to code Gandalf. In Gandalf, there is only one approach to evaluate P^{Ewald} and $\mathbf{A}^{Ewald}$ from the Ewald array. The functions are precalculated on a grid of one level, and term $1/\|(\mathbf{r}-\mathbf{r_a})\|$ subtracted from P^{Ewald}, and $(\mathbf{r}-\mathbf{r_a})/\|(\mathbf{r}-\mathbf{r_a})\|^3$ from $\mathbf{A}^{Ewald}$. Using SPH code with isolated BCs for self–gravity at least in one direction necessitates an analytic approximation to P^{Ewald} and $\mathbf{A}^{Ewald}$ beyond certain distance since we apriori do not know the extent of volume to which particles can move, and which must be covered by the Ewald array. In this case, we cover the same volume as in the second approach in Flash. The value of P^{Ewald} and $\mathbf{A}^{Ewald}$ is approximated by trilinear interpolation in Ewald array.

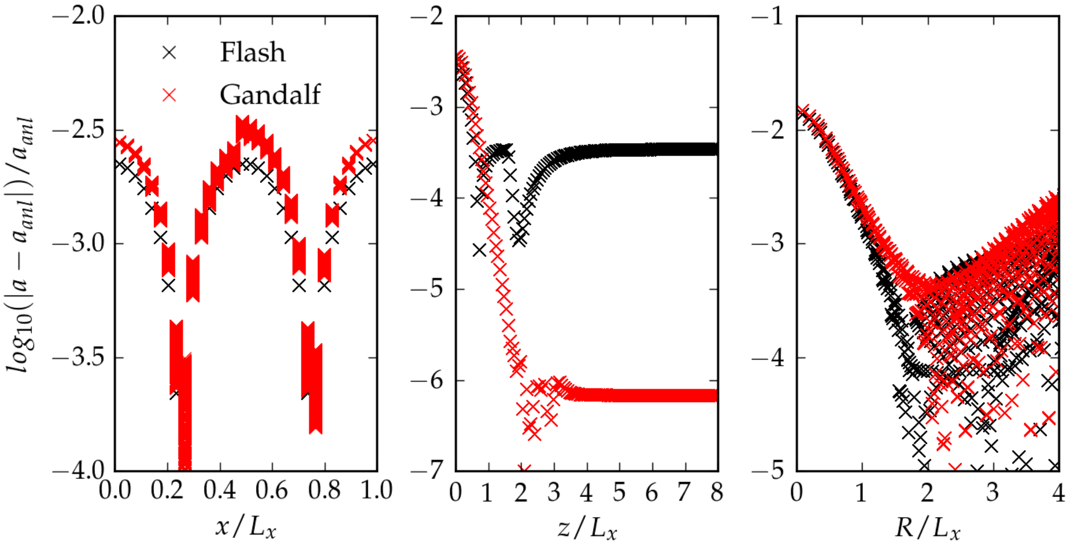

Figure 4.6: Tests of the implementation of the Ewald method and its modifications to hydrodynamic codes Flash (black crosses) and Gandalf (red crosses). We plot the logarithm of the relative error in acceleration between the value calculated by the code and the analytic formula for each grid cell or SPH particle in the computational domain. LEFT PANEL: Configuration 3P with density distribution in the form of a sine wave (eq. (4.36b)). MIDDLE PANEL: Configuration 2P1I with density distribution for the isothermal layer (eq. (2.21)). RIGHT PANEL: Configuration 1P2I with density distribution for the isothermal cylinder (eq. (4.37b)).

Parameter α can be used to test the implementation of functions P^{Ewald} and $\mathbf{A}^{Ewald}$ for each configuration. While the short–range term and the long–range term for both P^{Ewald} and $\mathbf{A}^{Ewald}$ changes significantly with a change of α, their sum must be independent on α.

Further, we test our implementation on simple models where potential–density pairs can be found in the closed form. For this purpose, we calculate the gravitational force with all block nodes open to increase the accuracy of a tree algorithm.

For configuration 3P, we use

$$\rho(x) = \rho_0 + \rho_1 \sin(2\pi x/L_x), \tag{4.36a}$$

$$\Phi(x) = \Phi_0 - \frac{G\rho_1 L_x^2}{4\pi} \sin(2\pi x/L_x), \tag{4.36b}$$

$$\mathbf{a}(x) = \mathbf{e}_x \frac{G L_x \rho_1}{2} \cos(2\pi x/L_x), \tag{4.36c}$$

where ρ_0 and ρ_1 (we adopt $\rho_1/\rho_0 = 0.2$ for the test) are constants for density, and Φ_0 a constant which shifts the potential. We are not interested in particular value of Φ_0 because it has no influence on dynamics. The relative error in acceleration as calculated by code Flash (black crosses) and Gandalf (red crosses) using the Ewald method is always smaller than 1%, which demonstrates very good agreement with the analytical value (left panel of Figure 4.6). Note that the neglect of the long–range contribution to the Ewald array would result in relative errors at least 10%.

For configuration 2P1I, the test model is the isothermal layer (cf. Section

2.2.1) where density, potential and acceleration are given by eq. (2.21), eq. (2.22) and eq. (2.30), respectively. We use a highly stratified layer (the density contrast between the midplane and surface is $\simeq 10^3$, so $A = 0.999$) because it constitutes stronger test than a layer with low density contrast where the vertical acceleration deviates only slightly from a piecewise linear function (see eq. (2.30), eq. (2.31) and eq. (2.25)). The test layer has vertical scale–height $H_0 = 0.4L_x$, and it is truncated by warm gas of negligible density above its surface at $z_{max} = 1.6$. The computational domain is significantly extended in the direction $\mathbf{e}_z$, $L_z/L_x = 16$. The relative error between acceleration calculated by code Flash or Gandalf and the analytic formula eq. (2.30) is shown in the middle panel of Fig. 4.6. The plot demonstrates very good agreement between the numerical and analytical solution.

For configuration 1P2I, the test model is the isothermal cylinder with analytical solution found by [Ostriker, 1964],

$$\rho(R) = \frac{\rho_0}{(1 + (R/R_0)^2)^2}, \tag{4.37a}$$

$$\Phi(R) = 2c_s^2 \ln\left(1 + (R/R_0)^2\right), \tag{4.37b}$$

$$\mathbf{a}(R) = -\mathbf{e}_R \frac{4R}{R_0^2} \frac{c_s^2}{(1 + (R/R_0)^2)}, \tag{4.37c}$$

where c_s is the sound speed in the cylinder, ρ_0 density on the axis $R = 0$, and

$$R_0 = \sqrt{\frac{2c_s^2}{\pi G \rho_0}}. \tag{4.38}$$

We set $R_0 = 0.8L_x$ in the test calculation, so the density continuously decreases by a few orders from $R = 0$ to the boundary at $R = 4L_x$. The relative error in acceleration between numerical and analytical values for this model is shown in the right panel of Fig. 4.6 indicating very good behaviour of the numerical scheme.

Throughout this section, we describe for the sake of clarity that the isolated direction in configuration 2P1I points in the direction $\mathbf{e}_z$, and the periodic direction in configuration 1P2I points in the direction $\mathbf{e}_x$. In Flash and Gandalf, the orientation of these directions can be set generally by the user.

5. Simulations of fragmenting layers

Assuming that shells swept up around H II regions can cool to the temperature of tens of Kelvin, the shells become thin (i.e. the ratio between their thickness and radius is very small). To simulate the gravitational instability, one needs to resolve the shell thickness. Especially near the beginning of the expansion, when the confining pressure is very high, and the shell is very thin, the simulation would need to have many levels of adaptive mesh refinement to resolve the shell thickness and also to accommodate the whole shell at later times when it significantly expanded. It would make the simulation prohibitively time consuming.

In Section 2.2.3, we show that the adopted approximation to the dispersion relation has a strong influence on the mass of fragments. However, considering typical parameters in the interstellar medium, any of the approximations predicts the longest unstable wavelength, λ_{MAX} to be significantly smaller than the shell radius R. It enables us to take a small area on the shell surface as a representative sample for the whole shell. Neglecting shell curvature, we apply periodic boundary conditions in the two directions tangential to the shell surface and instead of investigating fragmentation of a shell, we focus on layers (Figure 5.1). This transformation significantly reduces the dimension of the parameter space.

The purpose of this chapter is twofold. Firstly, we study and discuss several aspects of the fragmenting process of layers. These layers have a wide range of pressure confinement; from negligible to strongly pressure confined. Secondly, we obtain estimates of fragmenting time, fragment sizes and masses as a function of the layer properties. These results are then used in the following chapter in a model for shell fragmentation, and for discussion of propagating star formation. We defer the discussion of the most important approximations adopted in these models to the following chapter.

In Sections 5.1 and 5.2, we describe the numerical approach and the initial conditions common to all models. Special settings for individual models is described at the beginning of following sections. We start with the simplest models to understand basic properties of fragmenting layers and proceed towards more complicated and perhaps more realistic ones. In Section 5.3, we measure the dispersion relation for layers confined by thermal pressure from both sides, and compare it with its analytical estimates presented in Chapter 2. In Section 5.4, we investigate the course of fragmentation deep into the non–linear regime for layers with various degree of pressure confinement. In Section 5.5, we study the possibility that at later stages of fragmentation, the layer self–organises, forming a regular pattern in its surface density. In Section 5.6, we investigate fragmentation of layers accreting onto one surface and backed by thermal pressure from the other surface.

5.1 Numerical approach

We use MPI-parallel code Flash4.0 to calculate all the simulations presented in this chapter. In addition to the standard Flash code, we benefit from modules

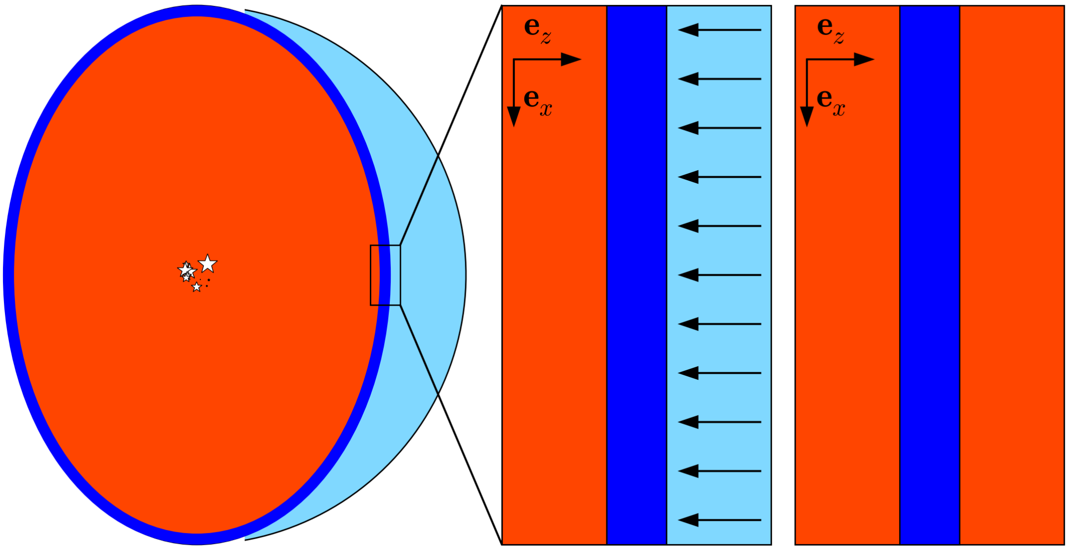

Figure 5.1: Approximation of a small area on the shell wall by a layer. Red colour represents the H II region caused by massive stars in the centre, dark blue is the cold dense shell, and light blue the rest of the cloud. We model a part of the shell of neglected curvature approximated by a layer. The external material is inflowing from the right in the frame of the layer (middle panel; we study these configurations in Section 5.6). We also simulate simpler models of non–accreting layers confined by thermal pressure from both surfaces (right panel; Sections 2 to 5.5). The orientation of coordinate axes is indicated by arrows.

TreeRay, Particles and BHTree for self–gravity, which have been developed or significantly extended by members of SILCC project [Walch et al., 2015a]. These modules are described in Section 3.2. Apart from these modules, we use standard Flash modules, which are well documented, so we refer only to relevant works without providing further details.

The grid is always cartesian with cubic cells. We use adaptive mesh refinement based on the Jeans condition. The layer half–thickness H_0 is resolved by at least four grid cells, so the simulations satisfy the criterion proposed by [Truelove et al., 1997] to avoid artificial gravitational fragmentation. Hydrodynamic equations are solved by piecewise parabolic method [Woodward and Colella, 1984, Colella and Woodward, 1984].

Self–gravity is calculated by the octal tree algorithm which accepts nodes according to the approximative acceleration criterion (the criterion described in iii of Section 3.2.1). Based on tests between accuracy and speed for several values of the error tolerance $\Delta a_{(0)}$, we set $\Delta a_{(0)} = 1.0 \times 10^{-12}$cm.s^{-2}. Note that the vertical acceleration at the layer boundary (which we take as the proxy for the characteristic acceleration) depends only at the surface density (eq. (2.31)). Since our models have the same surface density, we use this value of $\Delta a_{(0)}$ for all the models.

To follow the collapse deep into the non–linear regime, we allow for the formation of sink particles if all the conditions for their formation described in Section 3.2.3 are fulfilled. Once a sink particle is formed, we set its accreting radius to be 2.5 grid cell size at the lowest refinement level according to [Federrath et al., 2010].

The BCs for self–gravity are mixed (i.e. periodic in directions $\mathbf{e}_x$ and $\mathbf{e}_y$, and isolated in the direction $\mathbf{e}_z$), so the gravitational potential and accleration is calculated by modified Ewald method for configuration 2P1I (eq. (4.16) and eq. (B.24), eq. (B.25) and eq. (B.26)).

The hydrodynamic boundary conditions (BCs) are periodic in directions $\mathbf{e}_x$ and $\mathbf{e}_y$. In direction $\mathbf{e}_z$, we use different BCs for non–accreting and accreting models. The BCs are reflect for non–accreting models, while the BCs are inflow from the top and outflow from the bottom of the computational domain for accreting models.

For accreting simulations (see Section 5.2.2 for details), we need to determine the optical depth for cooling. This is calculated by module `TreeRay/OpticalDepth`.

After all the modules were included, we perform resolution tests for models with extreme values of pressure confinement. The tests show very good convergence with increasing resolution.

5.2 Initial conditions

At the beginning of a simulation, each model layer is truncated by the external medium at the height $\pm z_{max}$ above its midplane, which lies at $z = 0$. Below, we describe the properties of the layer and the external medium.

5.2.1 The layer

The model layer is a superposition of an unperturbed layer and a perturbation of initially small amplitude. Since we use three kinds of perturbations to explore various aspects of layer fragmentation, we describe the initial conditions for a particular perturbation type at the beginning of the relevant section, and here describe the unperturbed state. The unperturbed layer is isothermal and in its vertical hydrostatic equilibrium with density profile given by eq. (2.21).

The surface density corresponds to the surface density of a shell driven by a $41\mathrm{M}_\odot$ star into a homogeneous cloud of density $n = 10^3\mathrm{cm}^{-3}$ (This model is studied by [Iwasaki et al., 2011]) at time $t = 0.8$Myr when the role of stretching is comparable to that of self–gravity. At this time, the shell reaches radius $R = 3.86$pc, so the surface density is $\Sigma_0 = 0.0068\mathrm{g.cm}^{-2}$. We use this value of surface density for all the simulations presented in this Chapter. The relative importance of the external pressure to self–gravity as expressed by parameter A (see eq. (2.28)) is regulated only by change of the external pressure P_{ext}.

The sound speed c_s is given by the ideal gas law

$$c_s = \sqrt{\gamma R_{gas} T/\mu}, \tag{5.1}$$

where γ, R_{gas}, T and μ is the effective barotropic exponent, the ideal gas constant, temperature and the mean molecular weight. We set $\gamma = 1.0001$ since $\gamma = 1.0$ is excluded from numerical reasons. Inside the layer, we use $T = 10$K and $\mu = 2$ (pure molecular hydrogen). Although we adopt these particular values for physical quantities, we note that the non–accreting models are sufficiently simple so that the results can be rescaled for any layer with given A.

5.2.2 The external medium

We use two kinds of the external medium confining the layer. The first kind is a rarefied isothermal warm gas of temperature $T_{\rm AMB}$ imposing its thermal pressure on the layer surface, so the layer–external medium interface is a contact discontinuity (the warm gas is in pressure equilibrium with the layer surface). Since the gravitational acceleration outside the layer is a constant (eq. (2.31)), the hydrostatic equilibrium of the warm external medium is the isothermal atmosphere

$$\rho_{\rm AMB}(z) = \rho_{\rm AMB}(z_{max}) \exp(-\frac{2\pi G\Sigma_0\mu_{\rm AMB}(|z| - z_{max})}{R_{gas}T_{\rm AMB}}), \tag{5.2}$$

where $\mu_{\rm AMB}$ is the mean molecular weight in the ambient medium. We set the density of the ambient medium according to eq. (5.3) to prevent it from vertical motions, which would have induced spurious ram pressure on the layer.

We aim to compare the numerical dispersion relation with the analytic estimates. Since the derivation of any of them neglects any other role of the ambient medium than that the medium imposes the thermal pressure, we must assure that the bulk motions in the ambient medium have negligible influence on layer dynamics. Using convergence tests, we find that this requirement is met for $\rho_{\rm AMB}(z_{max}) \lesssim 10^{-2}\rho_0$. Taking into account this requirement and the condition for pressure balance at layer surface, we set $T_{\rm AMB} = 300$K and $\mu_{\rm AMB} = 0.6$. We also extend the computational domain to $\sim \pm 3z_{max}$ to add some volume between its borders and the layer surface. This extra volume is to decrease the flow velocity in the warm gas in directions $\mathbf{e}_x$ and $\mathbf{e}_y$, which results from redistribution of warm gas as the layer surface ripples. In Sections 5.3 to 5.5 we study layers confined thermal pressure from both sides; this setup is schematically shown on the right in Fig. 5.1.

The second kind of the external medium is an accreting gas imposing ram pressure on the layer surface. The gas of density $\rho_{\rm ACC}$, temperature $T_{\rm ACC}$ and sound speed $c_{\rm ACC}$ accretes supersonically at velocity $v_{\rm ACC}$ (Mach number is $=v_{\rm ACC}/c_s$) from the upper boundary forming a shock front at the upper layer surface. At densities in question, the cooling is rapid and we assume the shock to be isothermal, so we adopt $T_{\rm ACC} = T$ with $c_{\rm ACC} = c_s$.

Presented accreting models accrete from one surface, while the other (lower) surface is a contact discontinuity supported by thermal pressure from warm gas (see the scheme in the middle of Fig. 5.1), which is generated by the same way as for models confined with thermal pressure from both sides described above. To prevent the layer from vertical acceleration, the value of pressures acting on both surfaces are equal, i.e. $\rho_{\rm ACC}(v^2_{\rm ACC} + c^2_{\rm ACC}) = \rho_{\rm AMB}c^2_{\rm AMB}$. Although a self–gravitating layer compressed by shock fronts from both surfaces offers an interesting problem, we do not study it in the Thesis, because we focus on layers where at least one surface is a contact discontinuity.

Accretion causes large scale flows inside the layer, which mix the layer with the warm ambient medium. In nature, the mixed warm medium is shielded from ionising photons and cools to the layer temperature T. Although the mixed warm medium does not constitute a crucial contribution to the surface density in simulations, it would increase the layer temperature and the layer would thicken considerably if cooling were not implemented. We identify the mixed medium to be cooled down according to its column density σ calculated from the bottom side $z_{\rm BOT}$ of the computational domain

$$\sigma(z) = \int_{z_{\rm BOT}}^{z} \rho(z')\mathrm{d}z', \tag{5.3}$$

The maximum column density of the warm medium when the layer is plane parallel is $\simeq \rho_{\rm AMB}(z_{max} - |z_{\rm BOT}|)$. During simulations, the layer ripples, so some cells at $z > -z_{max}$ with $\sigma > \rho_{\rm AMB}(z_{max} - |z_{\rm BOT}|)$ happen to contain the warm ambient gas backing the layer. To enable the layer to freely ripple, the gas backing it must not be cooled down. Note that the column density of the mixed gas is significantly higher than $\rho_{\rm AMB}(z_{max} - |z_{\rm BOT}|)$ because the density of the layer is of two orders of magnitude higher than $\rho_{\rm AMB}$. Thus, we set the critical threshold in column density $\sigma_{\rm CRIT} = 2\rho_{\rm AMB}(z_{max} - |z_{\rm BOT}|)$ to activate cooling (i.e. any cell with $\sigma > \sigma_{\rm CRIT}$ is cooled to temperature T) to enable the layer to displace its surface by factor comparable to its thickness and to cool down the warm mixed gas inside the layer at the same time.

As the simulation proceeds, the warm gas is being consumed by intermixing and cooling in the layer, and would be exhausted without replenishment. We continuously add fresh warm gas from the bottom side of the computational domain so that the total mass of warm gas is kept constant during the simulation [1].

5.3 Testing dispersion relations

The dispersion relation of layers confined from low to medium values of the external pressure is studied by Dale et al. [2009], and Wünsch et al. [2010]. These authors find a discrepancy between V83 and the dispersion relation measured in their numerical models. This motivates their search for a better estimate of the dispersion relation, and they propose W10 (see Section 2.1.2) to account for the measured dispersion relation remarkably better than V83. However, in the range of the pressure confinement which was accessible to their study ($A \gtrsim 0.45$), they could not decide whether W10 is a better description than E78 (see upper row of Figure 2.4). Their model of three dimensional expanding shell with temporarily evolving surface density Σ also produces more noisy dispersion relation than the models of plane parallel layers presented in the Thesis (cf. fig. 7 in Wünsch et al. [2010] and our Figures 5.2 and 5.3 below).

Van Loo et al. [2014] simulate fragmentation of layers permeated by the magnetic field and they present a control run without the magnetic field with growth rate of selected modes. Although we cannot discern between the validity of E78 and W10 for their model because for their adopted self–gravity dominated case ($A = 0.96$), both dispersion relations are close to each other, their results again demonstrate deviations from V83.

---

[1] We experimented with heating the cold gas with $\sigma < \sigma_{\rm CRIT}$ to temperature $T_{\rm AMB}$, a process perhaps more natural to real H II regions. Since, in our computational domains with warm gas of very limited extend in comparison to H II regions, this approach resulted in sudden heating of descending dense fragments with a huge local increase in pressure and a drastic reduction of the time step, we resorted to the method described in the main text.

In this section, we measure the dispersion relation of layers confined by thermal pressure from both surfaces. Our setup of a plane parallel layer together with modified Ewald method for self–gravity enables us to explore layers with high pressure confinement ($A = 0.18$), where the difference between W10 and E78 is significant. Besides, we study layers with various degree of pressure confinement to detect possible smaller deviations from the analytical estimates.

To accomplish this aim, we use models with two kinds of initial perturbations: polychromatic with many perturbing wavenumbers simultaneously (P models), and monochromatic with perturbation of only one wavenumber (M models). While P models explore the whole branch of the dispersion relation, M models measures the growth rate of a selected mode with higher accuracy enabling to measure small differences from the analytical estimate of the dispersion relation. Initial conditions for perturbations are described in Section 5.3.1. The generic name of P models is in the form P<A>, where A represents the value of parameter A. The generic name of M models is in the form M<A>_<kH>, where A represents the value of parameter A and the numbers after the underscore the value of kH. Thus, for example, model M99_050 treats a layer with $A = 0.99$ seeded with a monochromatic perturbation of wavenumber $kH = 0.5$.

In Section 5.3.1, we compare the dispersion relation measured in our models with analytical estimates described in Chapter 2 and find that the solution proposed by Elmegreen and Elmegreen [1978] is the correct description. It raises the issue why the other two dispersion relations, W10 and V83 fail to predict the dispersion relation, and we offer the explanation in Section 5.3.3.

We recall that a dispersion relation can be applied only when the amplitude q_1 of perturbation for any quantity is smaller than its unperturbed value q_0. Therefore, we define the *linear regime of fragmentation* when the maximum of perturbed surface density Σ_1 is smaller than the unperturbed value Σ, and the *non–linear regime* otherwise. In this section, we focus on the linear regime.

5.3.1 Initial conditions for perturbations

Polychromatic perturbations

It appears that simulations with this kind of initial conditions provided us with the most interesting results presented in the Thesis. Therefore, it is essential to perform resolution tests with this kind of simulations, which means that the initial conditions must be independent on grid resolution. For this purpose, we generate amplitudes $\tilde{A}(k)$ of individual modes in the Fourier space, and map them on a grid by the inverse Fourier transform. Since we apriori do not know which of the proposed estimates of the dispersion relation is correct, we populate by wavenumbers the whole unstable branch for any of them. Thus, within a sphere of radius k_0, $k_0 > \max(k_{\mathrm{E78.MAX}}, k_{\mathrm{V83.MAX}}, k_{\mathrm{W10.MAX}})$, the mode amplitudes are generated as random variables from uniform distribution, and the amplitudes are zero for modes with $|k| > k_0$. The wavelength corresponding to k_0 is resolved by at least 4 grid cells to assure a reasonable resolution.

Apart from study the dispersion relation, we use the polychromatic models for determining the fragmenting time of the layer. To access the fragmenting time between models with different A, we set the mode amplitudes $\tilde{A}(k)$ to be

Run	A	$n_x \times n_y \times n_z$	H/dz	$N_{\rm J}$	$M_{\rm J}$ [$\mathrm{M}_\odot$]	$\bar{M}_{\rm CL}$ [$\mathrm{M}_\odot$]	$t^{\rm EFOLD}_{\rm E78.FAST}$ [Myr]	$t_{\rm FRG}$ [Myr]	$t_{\rm SINK}$ [Myr]	$t_{\rm NL}$ [Myr]
P18	0.18	1024 × 1024 × 64	4.0	8.8	2.3	1.1	0.15	2.01	2.15	0.42
P20	0.20	1024 × 1024 × 64	4.4	9.3	2.5	1.9	0.17	2.19	2.40	0.50
P22	0.22	1024 × 1024 × 64	4.4	12.8	2.8	1.7	0.18	2.11	2.23	0.58
P25	0.25	1024 × 1024 × 64	4.4	19.0	3.1	3.1	0.21	1.90	2.20	0.80
P30	0.30	512 × 512 × 64	3.9	9.8	3.6	2.1	0.25	2.20	2.40	0.99
P40	0.40	512 × 512 × 64	4.7	17.0	5.0	3.5	0.33	2.38	2.64	1.45
P60	0.60	512 × 512 × 64	6.6	29.7	7.4	10.0	0.47	3.00	3.35	2.22
P80	0.80	512 × 512 × 64	5.9	89.0	9.9	20.6	0.59	3.60	4.00	2.31
P99	0.99	512 × 512 × 64	9.1	71.0	12.5	32.0	0.66	4.15	4.90	2.90

Table 5.1: Parameters of P models. We provide the value of parameter A, number of cells at the highest refinement level n_x, n_y and n_z in directions $\mathbf{e}_x$, $\mathbf{e}_y$ and $\mathbf{e}_z$, the resolution of the layer half–thickness H/dz, number of Jeans masses in the computational domain $N_{\rm J}$ and the Jeans mass $M_{\rm J}$ for the density at the layer midplane. We further list the mean mass of gravitationally bound objects $\bar{M}_{\rm CL}$ at fragmenting time $t_{\rm FRG}$, the estimated e–folding time $t^{\rm EFOLD}_{\rm E78.FAST}$ according to E78 for the most unstable wavenumber $k_{\rm FAST}$, the time when sink particles in total consume 50% of the layer, and the transition time between linear and non–linear regime $t_{\rm NL}$.

comparable between all polychromatic models by requiring $\sqrt{\langle \tilde{A}^2(k) \rangle}/\tilde{A}(0) = c_A$, where c_A is a constant. Note that $\tilde{A}(0)$ is proportional to the unperturbed surface density. In order to simulate the linear regime, where the perturbations have small amplitudes, the value of c_A must be sufficiently small. On the other hand, there is a lower limit on c_A because the gravitational field generated by the perturbations must significantly exceed the artefacts due to the tree code algorithm. To pass both criteria, we set c_A so that $\Sigma_1 \simeq 0.1\Sigma$ at the beginning of each simulation.

Monochromatic perturbations

The initial conditions are eigenfunctions for an acoustic–surface–gravity mode of selected wavenumber k for a thick layer with free boundary conditions (i.e. the solution from eq. (2.32) to eq. (2.35) with eq. (2.39b)). The initial amplitude of the perturbed surface density is $\Sigma_1(0) \simeq 0.01\Sigma$. The computational domain accommodates one wavelength of the perturbation, i.e. its size in direction $\mathbf{e}_x$ is $2\pi/k$.

5.3.2 The numerical dispersion relation

Simulations with polychromatic perturbations (P models) are listed in Table 5.1. To measure the dispersion relation, we calculate the Fourier transform of the surface density for each frame, so we access the value of the amplitude $\tilde{A}(k,t)$ for each mode at time t. Then, we obtain the dispersion relation, i.e. ω as a function of wavenumber k, by linear fitting the time dependence of $\log_{10}(\sqrt{\tilde{A}(k,t)\overline{\tilde{A}(k,t)}})$ (bar denotes complex conjugation) over interval ($t^{fit}_{\rm O}$, t^{fit}_1). At the beginning, the

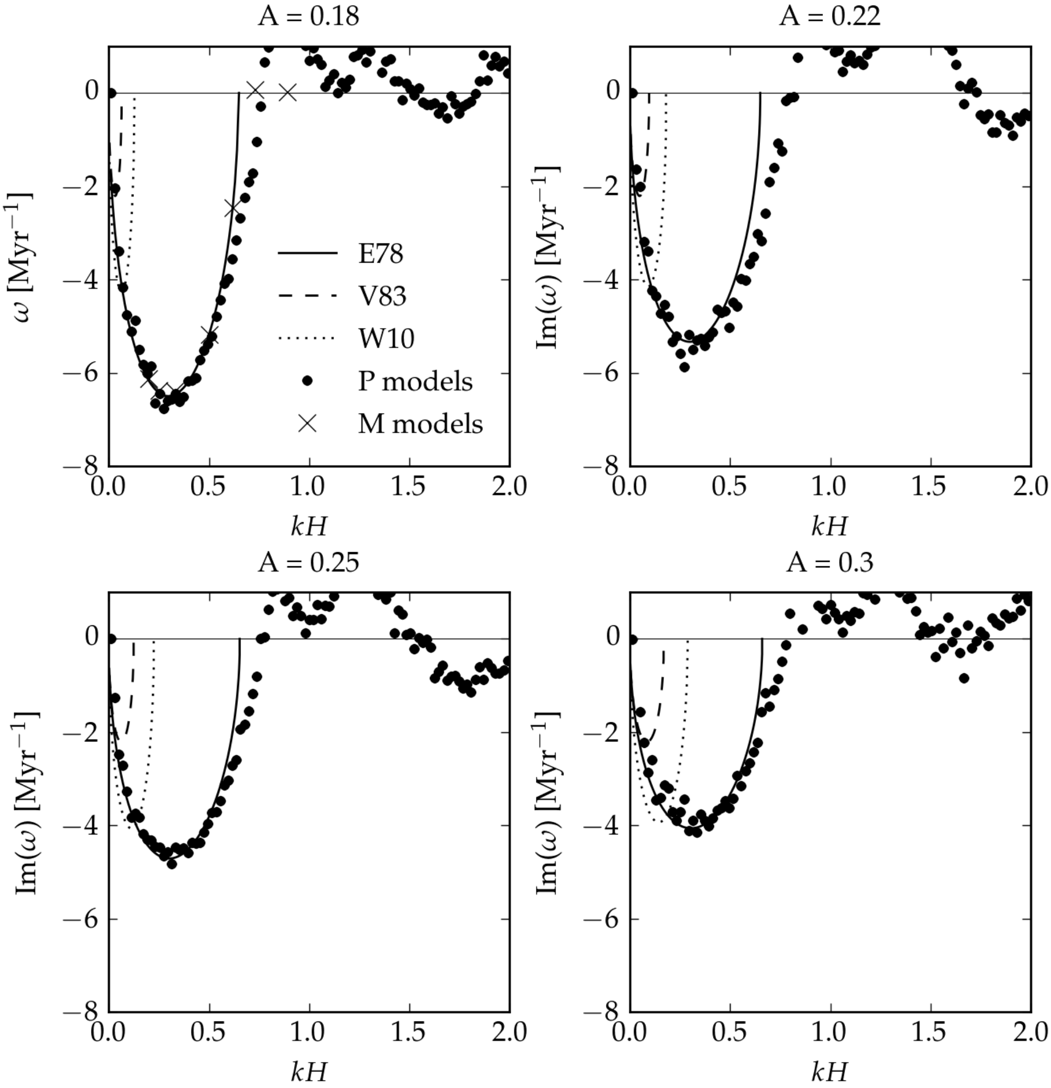

Figure 5.2: Comparison between the numerical dispersion relation and its analytical estimates for layers dominated by external pressure. Results from P models are shown by dots. For layer with $A = 0.18$, we calculate M models, the results of which are represented by crosses. The analytical estimates of E78 (with $\epsilon = 0.1$), V83 and W10 are plotted by solid, dashed and dotted lines, respectively.

modes relax, and it takes some time, t_{O}^{fit} when they start growing exponentially. The other endpoint of the interval, t_1^{fit}, is so constrained that the fragmentation is still in the linear regime. The timespan of the interval should be as large as possible to get more points for fitting. Inspecting the growth rates of individual modes, we find that $t_{\mathrm{O}}^{fit} = 1/\omega_{\mathrm{E78.FAST}}$ and $t_1^{fit} = 3/\omega_{\mathrm{E78.FAST}}$, where $\omega_{\mathrm{E78.FAST}}$ is the e–folding time for the wavenumber $k_{\mathrm{E78.FAST}}$ with the highest growth rate, fulfill these requirements reasonably good.

The numerical dispersion relation for layers with various degree of pressure confinement (from $A = 0.18$ to for $A = 0.99$) are shown in Figures 5.2 and 5.3. The data are binned to reduce the noise. For self–gravity dominated layers ($A \simeq 0.8$), we recover deviations from V83 in agreement with previous works. In this case, our results can be explained with E78 as well as with W10 and slightly altered parameter ϵ. For pressure dominated layers ($A \lesssim 0.5$), E78 again gives

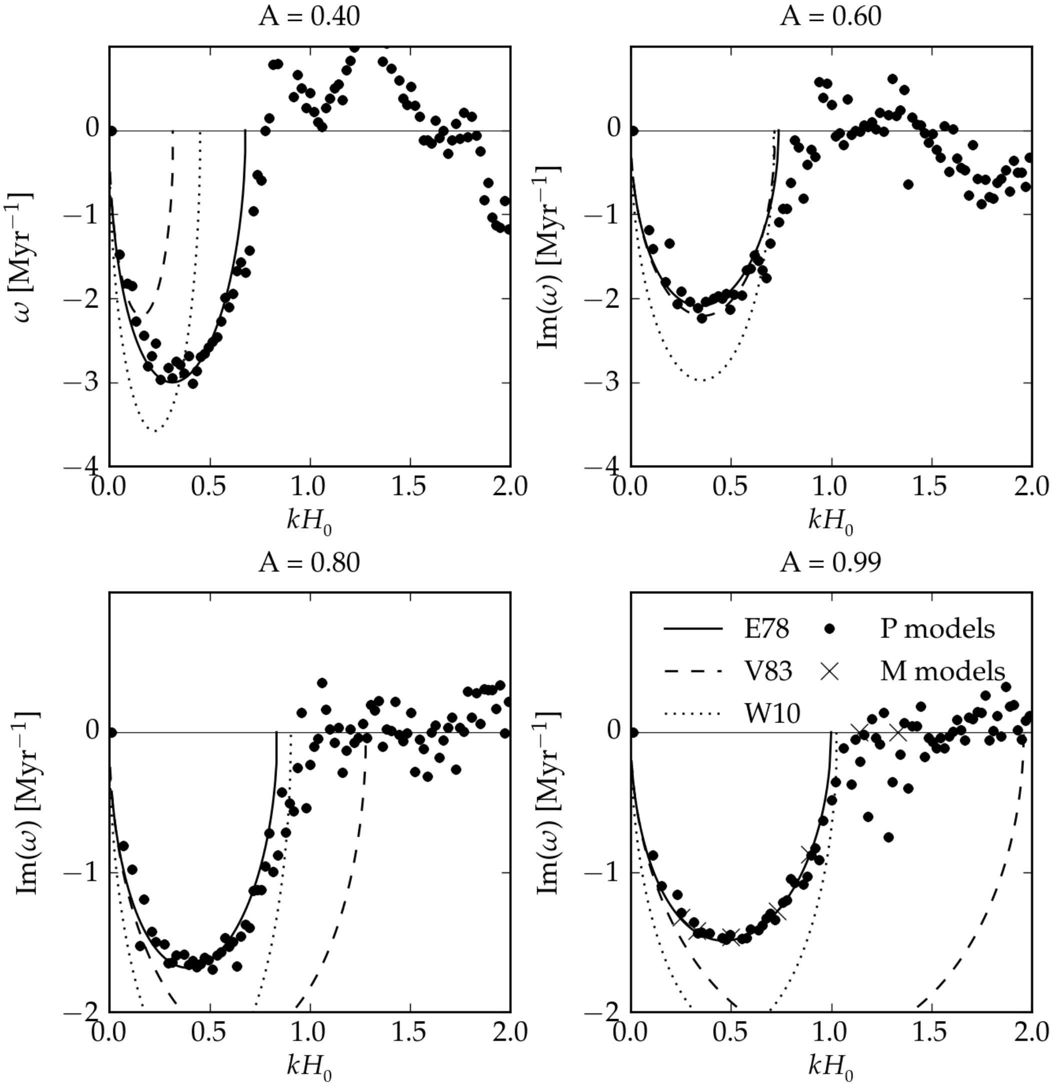

Figure 5.3: Comparison between the numerical dispersion relation and its analytical estimates for layers with medium and lower value of the external pressure. Results from P models are shown by dots. For layer with $A = 0.99$, we calculate M models, the results of which are represented by crosses. The analytical estimates of E78, V83 and W10 are plotted by solid, dashed and dotted lines, respectively.

Run	A	$n_x \times n_y \times n_z$	H/dz	kH	$t_{\mathrm{E78}}^{\mathrm{EFOLD}}$ [Myr]	t_{NUM} [Myr]
M18_020	0.18	640 × 128 × 128	20.2	0.20	0.16	0.16
M18_025	0.18	512 × 128 × 128	20.2	0.25	0.15	0.16
M18_033	0.18	384 × 128 × 128	20.2	0.33	0.15	0.16
M18_050	0.18	256 × 128 × 128	20.2	0.50	0.19	0.19
M18_062	0.18	208 × 128 × 128	20.2	0.62	0.41	0.41
M18_073	0.18	176 × 128 × 128	20.2	0.73	-	-
M18_089	0.18	144 × 128 × 128	20.2	0.89	-	-
M99_025	0.99	512 × 128 × 128	20.2	0.25	0.74	0.76
M99_033	0.99	384 × 128 × 128	20.2	0.33	0.69	0.70
M99_050	0.99	256 × 128 × 128	20.2	0.50	0.67	0.68
M99_073	0.99	176 × 128 × 128	20.2	0.73	0.77	0.78
M99_089	0.99	144 × 128 × 128	20.2	0.89	1.12	1.14
M99_114	0.99	112 × 128 × 128	20.2	1.14	-	-
M99_133	0.99	96 × 128 × 128	20.2	1.33	-	-

Table 5.2: Parameters of M models. The first five columns are as in Table 5.1. Then we list the perturbing wavenumber scaled to the layer half–thickness kH, the e–folding time $t_{\mathrm{E78}}^{\mathrm{EFOLD}}$ for the wavenumber as predicted by E78 and the e–folding time measured in the simulations t_{NUM}.

very accurate prediction for the growth rates of individual modes, the wavenumber with the highest growth rate k_{FAST} and the range of the unstable wavenumbers. There is only marginal difference in the range of unstable wavenumbers: the numerical dispersion relation appears to have slightly higher k_{MAX} than $k_{\mathrm{E78.MAX}}$. On the other hand, both V83 and W10 fail to predict the dispersion relation for pressure dominated layers.

Before drawing conclusion that E78 is the exact solution, we perform more accurate study of the growth rates for selected modes using M models (table 5.2). These models are calculated for layers with extreme values of parameter A, $A = 0.18$ and $A = 0.99$. Since the initial conditions for M modes are adopted from their eigenvectors, their initial growth rate is exactly that what E78 predicts from definition. Accordingly, we start measuring the dispersion relation at time t_{O}^{fit} after the initial conditions are significantly altered by evolution, which we estimate as the sound crossing time through one half of the perturbing wavelength, $t_{\mathrm{O}}^{fit} = \pi H/c_s$. Particular values are $t_{\mathrm{O}}^{fit} = 0.1$Myr for models M18 and $t_{\mathrm{O}}^{fit} = 1.4$Myr for models M99. The upper limit t_1^{fit} is set at the time when the perturbing amplitude terminates the linear regime, i.e. $\Sigma_1 \simeq \Sigma$. All models M18 are in the linear regime, so we set $t_1^{fit} = 0.6$Myr near the end of the simulations. The model M99_050 has the highest growth rate among M99 models and reaches the non–linear regime at the earliest time $t_1^{fit} = 2.8$Myr, we use this termination time for all M99 models.

Time evolution of the amplitudes for selected modes is shown in Figure 5.4. Nate that the instantaneous growth rate ω is the tangent to the plotted curves because $\Sigma_1(t) = \Sigma_1(0)e^{i\omega t}$. The instantaneous growth rate is very close to a constant in the linear regime with no sign of a change around time t_{O}^{fit}, which would indicate deviation from E78. There is a change in the growth rate later, but for

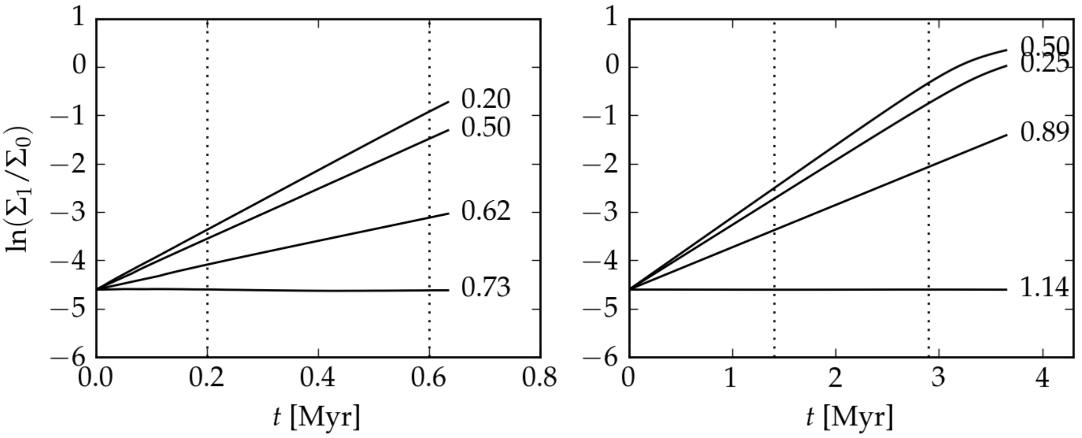

Figure 5.4: Time evolution of surface density perturbations for monochromatic models with $A = 0.18$ (left panel), and $A = 0.99$ (right panel). Vertical lines show the interval ($t_{\rm O}^{fit}$, t_1^{fit}) where e–folding time $t_{\rm E78}^{\rm EFOLD}$ of individual modes is calculated. Only selected models are plotted to avoid confusion.

the reason that the perturbing amplitude become so high that the linearised treatment no longer applies (right panel of Fig. 5.4). The value of $t_{\rm E78}^{\rm EFOLD}$ fitted in the interval ($t_{\rm O}^{fit}$, t_1^{fit}) is very close to E78 for both extreme values of parameter A (cf. Table 5.2 and top left panel of Fig. 5.2 and bottom right panel of Fig. 5.3). Since in models M18, we do not reproduce the slight difference between $k_{\rm E78.MAX}$ and $k_{\rm MAX}$ measured in model P18, we conclude that the difference is likely due to the approximative treatment in P models. We do not find any systematic difference between E78 and the numerical dispersion relation. Alternatively, this means that the numerical scheme we adopt accurately reproduces fragmentation in the linear regime, which adds some credence to results obtained for more complex models without known analytic solution presented in the following sections.

5.3.3 The cause of limitations to the thin shell approximation and PAGI

The failure of V83 and W10 to predict the dispersion relation of pressure dominated layers immediately prompts a question: which assumptions made in their derivation invalidates them in this case?

To answer this question, we investigate the cause of the different limiting behaviour for the highest unstable wavenumber $k_{\rm MAX}$ as predicted by E78 and V83 and W10 (top left panel of Figure 2.4). Let model the perturbation of wavenumber k by adding some gas into a circle of radius $R_C = \pi/k = \lambda/2$ located on the layer surface, so that the surface density decreases from $\Sigma_C = \Sigma_0 + \Sigma_1$ at the center of the circle (Σ_1 is the central excess in surface density) to Σ_0 at its edge. We assume that the perturbation is of small amplitude, so $\Sigma_1 \lesssim \Sigma_0$. On the vertical sound crossing timescale $t_{vsc} = H/c_s$, which is significantly shorter than $t_{\rm EFOLD}$ for layers with small A, so the perturbing amplitude does not increase substantially during t_{vsc}, the layer adjusts close to its hydrostatic equilibrium in the vertical direction. Note that the equilibrium state depends on coordinates (x, y) because its surface density is a function of (x, y). The density isocontours are close to an oblate spheroid because the perturbed solution is of the form

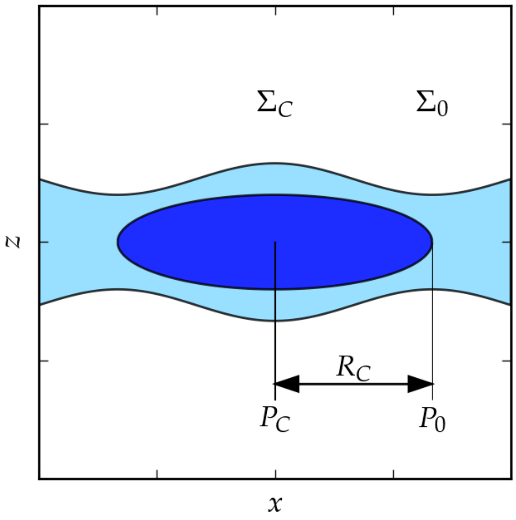

Figure 5.5: A scheme of a vertical slice through a perturbed pressure dominated layer. After the perturbation adjusts to the vertical hydrostatic equilibrium, its density isocontours are close to an oblate spheroid (dark blue). The semi–major axis of the spheroid is denoted R_C. The unperturbed pressure in the layer midplane is denoted P_0, and the midplane pressure at the centre of the overdensity perturbation is P_C. The layer surfaces corrugate to fulfill eq. (2.26) for local surface density, which increases from Σ_0 at the edge of the perturbation to Σ_C at the centre.

$\rho_1 = \rho_{10}(z)\cos(kx)$ (see Section 2.2.1) and $\rho_{10}(z)$ is only a weak function of z for pressure dominated layers. Figure 5.5 shows a vertical structure of the perturbed layer with overdensity depicted in dark blue.

Consider the acceleration experienced by a small gaseous parcel located at the edge of the perturbation R_C. The gravitational acceleration due to the overdensity is $\beta G\pi\Sigma_1$, where β takes into account that the perturbation is of non–uniform surface density, and that it generates non–spherical symmetric gravitational field. Factor β is of order unity. The force due to pressure gradient $\sim (P_1 - P_{\mathrm{O}})/(\rho_{00} R_C)$ acts in the opposite direction. P_1 and P_{O} is the pressure at the centre and at the margin of the perturbation (see Fig. 5.5), respectively, and ρ_{00} is the midplane density at the edge of the spheroid. There is a critical wavenumber k_{MAX} at which both forces balance. Substituting the total surface density at the spheroid centre and edge for Σ_0 in eq. (2.27), and exploiting eq. (2.29), the condition for the balance becomes

$$k_{\mathrm{MAX}} H \simeq \beta\pi/2. \tag{5.4}$$

Equation (5.4) has the correct limiting behaviour as the marginally stable wavenumber $k_{\mathrm{E78.MAX}}$ for E78 (cf. Figure 2.4). According to this equation, arbitrarily short wavelengths can be unstable provided that the external pressure compresses H sufficiently. Although this behaviour may seem counterintuitive, it is a consequence how the pressure dominated layer reacts when perturbed. Note that such a layer is of almost constant density, and that a perturbation in surface density results in a displacement of the layer surface with very little change in the midplane density. Consequently, the pressure gradient (which is proportional to the density gradient for an isothermal model) between the center and edge of the spheroid is unable to prevent the collapse because the majority of the material contained in the perturbation is displaced above the layer, so it does not contribute to the pressure gradient in the midplane. Yet, the material contributes to the gravitational force in direction $\mathbf{e}_x$ making the fragment unstable.

On the other hand, W10 predicts asymptotically different behaviour, $k_{\mathrm{W10.MAX}} H = 9\pi^2 A^2/20$ when $A \to 0$, which together with eq. (2.29) implies substantially larger wavelengths of marginally unstable fragments than in the case of E78. Recall that the density perturbation in W10 is approximated by an oblate spheroid. The wrong assumption in W10 is the constancy of the semi–minor axis of the spheroid. This implies that the spheroid cannot decrease its central pressure by displacing some material above its upper and lower surface. The high pressure gradient stabilises wavenumbers in the range $(9\pi^2 A^2/20, \beta\pi/2)$, which would be unstable in a real layer.

The same neglected assumption causes the failure of V83 for layers in the case of high external pressure. We can look at V83 as the limiting case in $A \to 0$ of the dispersion relation for a thick layer with rigid boundary conditions. From their definition, the boundary conditions disable any surface displacement leaving the pressure gradient too high for layers with freely moving surfaces.

Although the presented simulations manifest limitations of V83 and W10 for layers with a strong confinement of thermal pressure, we do not claim that V83 and W10 are of no astrophysical interest. Firstly, the layer at the interface between two colliding clouds is confined by ram pressure from both sides. Since ram pressure acts only in one direction, it tends to dissolve surface corrugations, so the simple model presented in this section may not apply in this case. It is possible, that models including rigid surface implicitly (i.e. V83 and W10) are more appropriate in this case. In addition, a layer accreting from both sides is also a subject of nonlinear thin shell instability (Section 2.3.4), which leads to redistribution of momentum not included in the model of perturbation presented above in this section. Secondly, V83 gives a rough and W10 approximate description of fragment mass for layers with lower pressure confinement ($A \gtrsim 0.5$; right panel of Fig. 2.5).

5.4 Evolution in the non–linear regime

In this section, we follow fragmentation of the layer to the non–linear regime, where the amplitudes of perturbations become large, fragments collapse forming gravitationally bound objects, the centers of which are traced by sink particles. Each layer is simulated to the stage when at least 1/2 of the total initial mass in the computational domain is accreted on sink particles. The simulations are unable to reproduce further evolution since they do not include protostellar feedback, which would be important after sink particles form. We use P models, which are described in Section 5.3.1 and listed in Table 5.1.

In this Section, we address two issues. Firstly, we investigate the course of fragmentation for layers with different degree of pressure confinement (Section 5.4.1). It turns out that the relative importance of the external pressure governs the course of fragmentation in the non–linear regime qualitatively. While self-gravity dominated layers form monolithically collapsing fragments, pressure–dominated layers fragment in two stages: they form gravitationally stable fragment, which gradually gain mass by mutual coalescence until they assemble enough mass to collapse and form gravitationally stable objects. Secondly, based on our simulations, we estimate the fragmenting time of the layer and the characteristic mass of fragments as a function of the properties of the layer (Section 5.4.2).

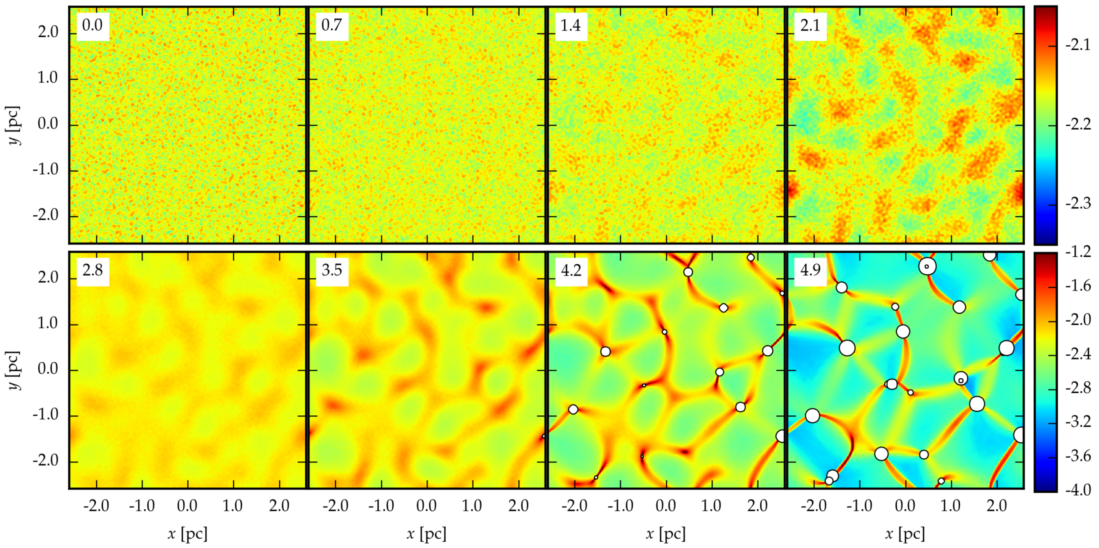

Figure 5.6: Evolution of surface density for a layer dominated by self–gravity ($A = 0.99$; model P99). The upper left corner shows time in Myr. Sink particles are plotted by white circles with mass of a particle corresponding to the area of a circle. Note that the upper row has a different colourscale than the lower row. The figure is adopted from [Dinnbier et al., 2017].

5.4.1 Monolithic and coalescence driven collapse

Figure 5.6 shows the evolution of surface density for self–gravity dominated layer ($A = 0.99$; model P99). In the linear regime (the transition to non–linear regime occurs at time $t_{\rm NL} = 2.9$Myr, see Table 5.1), the layer breaks into round fragments. As the collapse proceeds, the axis ratio of fragments increases, so they they become more and more slender (frames between 2.8Myr and 4.9Myr) and filamentary–like. This behaviour was predicted by the second order perturbation theory of Miyama et al. [1987a]. Sink particles form at the densest parts of filaments attracting and accreting their surrounding material, so they are located mostly at intersections of filaments (frames at 4.2Myr and 4.9Myr). After a fragment emerges, it collapse monolithically forming a gravitationally bound object with a sink particle in its centre.

Figure 5.7 represents fragmentation of pressure dominated layer ($A = 0.18$; model P18). The layer forms many fragments already at the end of the linear regime. Since the mass of the fragments is significantly lower than the mass for the critical Bonnor–Ebert sphere (which is not very different from the Jeans mass $M_{\rm J}$ [Bonnor, 1956]), the fragments are stable in respect to further collapse. However, the fragments gradually assemble mass by coalescence (frames between 0.7Myr and 2.0Myr). Eventually, some of the fragments exceed the critical mass, become gravitationally unstable and collapse (at 1.7Myr and 2.0Myr). As the coalescence often occurs at large impact parameter, the resulting cloud is spined up, which leads to a formation of a disc around the collapsed object (frame at 2.3Myr). After an object gravitationally collapses, its cross section for future coalescence is reduced and coalescence rate decreases.

The fragmenting process for a pressure dominated layer proceeding via coalescence of many objects followed by a collapse is very different from the continuous collapse of a single clump reported for a self–gravity dominated layer. Thus,

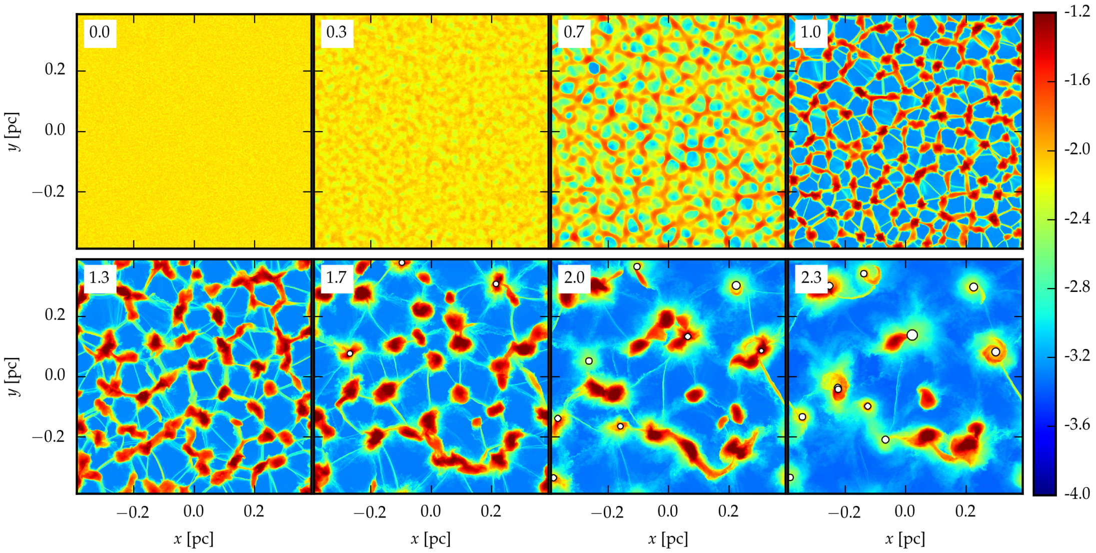

Figure 5.7: Evolution of surface density for a layer dominated by external pressure ($A = 0.18$; model P18). Caption is the same as in Fig. 5.6. The figure is adopted from [Dinnbier et al., 2017].

we refer to the former and latter as *coalescence driven collapse* and *monolithic collapse*, respectively.

5.4.2 Some properties of fragmenting layers

In Section 5.3.2, we demonstrate that E78 is the correct description for the dispersion relation of layers with a wide range of pressure confinement. The most unstable wavelength $\lambda_{\rm MAX}$ for layer with given Σ_0 sets the characteristic mass, and the highest growth rate $\omega_{\rm MAX}$ the characteristic timescale. These quantities have often been used as estimates for fragment mass and fragmenting timescale. In the linear regime, E78 gives these values correctly. However, as we have seen in previous section, the fragmenting process in the following non–linear regime is more complicated.

In this Section, we determine the fragmenting time $t_{\rm FRG}$ and the mean mass of gravitationally bound objects $\bar{M}_{\rm CL}$ from our simulations at the late stage of fragmentation when the layer is broken into well separated fragments, and compare $t_{\rm FRG}$ and $\bar{M}_{\rm CL}$ with the analytical estimates based on the dispersion relation.

To reach the aim, we begin by defining these quantities. We experimented with several definitions of fragmenting time. It appears that the instant when the total mass of gravitationally bound objects exceeds 1/2 of the total mass contained in the computational domain is a reasonable indicator, which we use as the definition of $t_{\rm FRG}$ because once gravitational collapse starts, the objects quickly accrete the majority of the available gas, so taking another fraction of the total mass than 1/2 would not lead to significantly different results. Moreover, even if the remaining of the layer formed some objects in more distant future, these objects could not constitute the most important star forming event because their total mass would be subordinate to the total mass of the objects formed previously. The mean mass of fragments $\bar{M}_{\rm CL}$ is calculated at time $t_{\rm FRG}$.

The fragmenting time $t_{\rm FRG}$ occurs at higher number $n_{\rm EFOLD}$, $n_{\rm EFOLD}$ =

$t_{\rm FRG}/t_{\rm E78.FAST}$ of e–folding time $t_{\rm E78.FAST}$ for pressure dominated layers than for self–gravity dominated layers (Table 5.1 and the left panel of Figure 5.8). Note that the dependence of $n_{\rm EFOLD}$ on A is not due to our choice of initial condition, as it would be the case if the initial perturbations for self–gravity dominated layers started with effectively higher amplitudes, so these models would reach the non–linear regime earlier and also fragment earlier. Instead, layers reach the transition to the non–linear regime $t_{\rm NL}$ after a comparable number of $t_{\rm E78.FAST}$ independently on the value of A (left panel of Fig. 5.8). We attribute the delayed fragmenting time for pressure dominated layers to the time during coalescence. Given the numerical values of $n_{\rm EFOLD}$, the assumption that a layer fragments at the constant number of e–folding time regardless of the value of parameter A would estimate the fragmenting time only within a factor of 2 for layers with A in interval $(0.18, 1.0)$.

The right panel of Fig. 5.8 and Table 5.1 show the mean mass of gravitationally bound objects condensing from layers with the same surface density Σ as a function of pressure confinement indicated by parameter A. The estimate of fragment mass ($M = \pi\Sigma(\lambda_{\rm FAST}/2)^2$ where $\lambda_{\rm FAST} = 2\pi/k_{\rm FAST}$) according to V83 and E78 (M_{V83} and M_{E78}, respectively) is shown by lines. We also plot the Jeans mass calculated for the midplane density (we use $M_{\rm J} = 4.26\ Ac_s^4/(G^2\Sigma_{\rm O})$ from eq. (13-33) in Spitzer [1978]). For self–gravity dominated layers, the mass of fragments is in a good agreement with E78. In this case, the fragment mass does not change substantially throughout the collapse, which proceeds monolithically. On the other hand, E78 underestimates the fragment mass for pressure dominated layers substantially, because it does not take into account that the fragment mass increases dramatically due to coalescence in the non–linear regime. V83 underestimates fragment mass for layers with $A \gtrsim 0.6$, and overestimates fragment mass when $A \lesssim 0.6$. The Jeans mass is a rough estimate for fragment mass in the pressure dominated case, because the corresponding density is near the threshold above which the coalescing fragments collapse. We use the Jeans mass as the proxy for $\bar{M}_{\rm CL}$ condensing out of pressure dominated shells in Chapter 6.

The limitations of E78 in predicting both $t_{\rm FRG}$ and $\bar{M}_{\rm CL}$ is a cautionary tale against using estimates, though appropriate for linearised systems for estimating quantities, which are set when the system behaves non–linearly.

5.5 Does interaction of modes lead to pattern formation?

Based on an analytic study, Fuchs [1996] proposes, that a triple of modes inclined at an angle 60° and of wavevectors $\|\vec{k}\| \simeq k_{\rm FAST}$ starts to interact when the fragmentation becomes non–linear. Consequently, the triple grow faster than the rest of modes forming a regular hexagonal pattern in surface density. Similar behaviour is reported by Wünsch and Palouš [2001], who study fragmentation of a shell including second order perturbations. Another result was obtained by Miyama et al. [1987a,b], who suggest that a layer naturally fragments into a network of filaments in the non–linear regime of fragmentation.

We search for regular patterns in surface density in our polychromatic simulations and find no evidence for them. We obtain the same result also in two

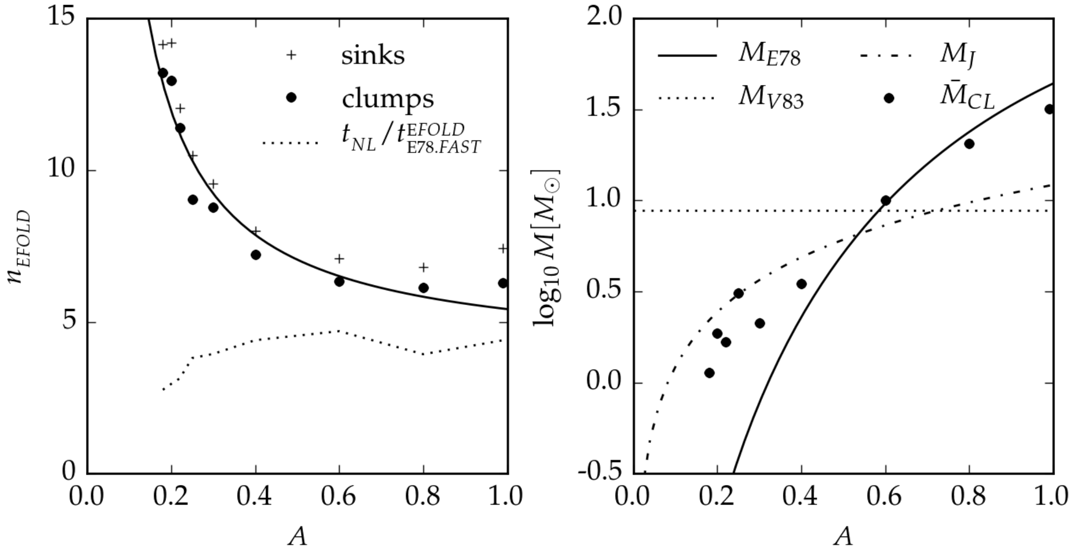

Figure 5.8: LEFT PANEL: The dependence of the number n_{EFOLD} of e–folding time $t_{\text{E78.FAST}}$ needed to reach time t_{FRG} (circles) and time t_{SINK} (pluses) on the parameter A. The dashed line shows the time t_{NL} of transition between the linear and the non–linear regime of fragmentation. The solid line shows the fit to t_{FRG} expressed by n_{EFOLD} as given by eq. (6.3). RIGHT PANEL: Average mass of a gravitationally bound object $\bar{M}_{\text{CL}}$ at time t_{FRG} (circles). Analytical estimates E78, V83, and the Jeans mass for midplane density are represented by solid, dotted and dashed lines, respectively.

dedicated simulations where the pattern should be more conspicuous than in polychromatic ones.

Name of the models dedicated to investigating possible pattern formation is in the form I<*A*>_<*dk*>, where the first two numbers after ”I” represent the parameter A and the numbers after the underscore the parameter dk described in Section 5.5.1.

5.5.1 Initial conditions for perturbations

Here, we describe the initial conditions for I models. The amplitudes $\tilde{A}(k)$ of the perturbing wavevectors are firstly generated by the same method as for the polychromatic models (see Section 5.3.1 for description). Then, we choose three modes $\vec{k}_i$ ($i = 1, 2, 3$) with $\|\vec{k}_i\| \simeq k_{\text{E78.FAST}}$ inclined at an angle around 60° and amplify amplitudes of all modes inside a circle at centre $\vec{k}_i$ of radius dk by a gaussian, so the amplitudes of perturbations $\tilde{A}_n$ are calculated by

$$\tilde{A}_n(k) = \begin{cases} A_{int}\tilde{A}(k)\exp(-\|\vec{k},\vec{k}_i\|_2/\sigma_A^2) & , \ \|\vec{k},\vec{k}_i\|_2 \leq \mathrm{d}k \\ \tilde{A}(k) & , \ \text{otherwise} \end{cases} \tag{5.5}$$

where $\|\vec{k},\vec{k}_i\|_2 = \sqrt{(k_x - k_{ix})^2 + (k_y - k_{iy})^2}$ and A_{int} and σ_A are parameters of the gasussian used in the particular model (Table 5.3). The only parameter which differs between the models is the radius dk. To include possible interaction of modes close to 60°, but not exactly the angle, we calculate two models. For model I99_00, we amplify only the amplitudes of the selected wavevectors $\vec{k}_i$, for model I99_14, we amplify wavepackets inside non–zero radius dk centered on $\vec{k}_i$.

Run	A	$n_x \times n_y \times n_z$	H/dz	A_{int}	σ_A [pc^{-1}]	dk [pc^{-1}]	$t^{\mathrm{EFOLD}}_{\mathrm{E78.FAST}}$ [Myr]
I99_14	0.99	512 × 512 × 32	5.1	10.0	28	14	0.66
I99_00	0.99	512 × 512 × 32	5.1	10.0	28	0	0.66

Table 5.3: Parameters of models I. First four columns have the same meaning as the columns in Table 5.2. Parameters A_{int}, σ_A and dk characterise properties of the mode amplifying function, eq. (5.5). Time $t^{\mathrm{EFOLD}}_{\mathrm{E78.FAST}}$ is as in Table 5.1.

5.5.2 Evolution of interacting modes

Evolution of the amplitude for the selected triple of modes for models I99_14 and I99_00 is plotted in the upper panel of Figure 5.9. We recall that the growth rate ω is time derivative of the plotted functions. The vertical lines mark the transition from the linear to non–linear regime of fragmentation. According to Fuchs [1996], the growth rate of the modes should increase in the non–linear regime. We report the opposite since the growth rate decreases for all three modes.

To investigate possible interaction of another than the selected modes, we proceed as follows. Let Fourier transform of the surface density be $B(k_x, k_y)$. A regular pattern in the surface density would manifest itself as an anisotropy of function B. We look at the plane (k_x, k_y) as it is given in polar coordinates specified by radius $\|\vec{k}\|$ and azimuthal angle α. To search for the anisotropy, we evaluate function B both on a circle with radius $\|\vec{k}\| = k_{\mathrm{E78.FAST}}$, i.e. $B_{rad}(\alpha) \equiv B(\|\vec{k}\| = k_{\mathrm{E78.FAST}}, \alpha)$ and on an annulus with $k_{\mathrm{E78.FAST}}/2 < \|\vec{k}\| < 3k_{\mathrm{E78.FAST}}/2$. If two modes inclined at an angle $\tilde{\alpha}$ have the highest amplitudes, function $B_{rad}(\alpha)$ has maxima separated by the angle $\tilde{\alpha}$. Therefore, the value of azimuthal autocorrelation of $B_{rad}(\alpha)$

$$c(\alpha) = \int_0^{\pi} B_{rad}(\alpha')B_{rad}(\alpha + \alpha')\mathrm{d}\alpha', \tag{5.6}$$

is proportional to the amplitudes of modes adjoined by α.

Time dependence of maximum c_{max} of function c normalised to its mean $\langle c\rangle$ for models I99_14 and I99_00 is shown in the middle panel of Figure 5.9. In the non–linear regime, $c_{max}/\langle c\rangle$ decreases, again indicating no formation of a regular pattern. This test is more stringent than the study of growth rate for individual modes since it can detect interaction of modes at any angle, not necessarily the ones at proposed 60°. We repeat the same procedure to both pressure and self–gravity dominated polychromatic models (i.e. P18 and P99) and again obtain negative results (bottom panel of Figure 5.9).

In order to explore the possibility of patter formation, we study mode interaction only in the azimuthal direction α in the Fourier space. We do not study mode interaction in radial direction $\|\vec{k}\|$, which apparently occurs in the non–linear regime. Our findings do not contradict the mechanism proposed by Miyama et al. [1987a,b], which leads to randomly oriented filaments.

5.6 Accreting layers

In this Section, we investigate fragmentation of layers accreting from the upper surface and backed by a contact discontinuity from their lower surface. As we

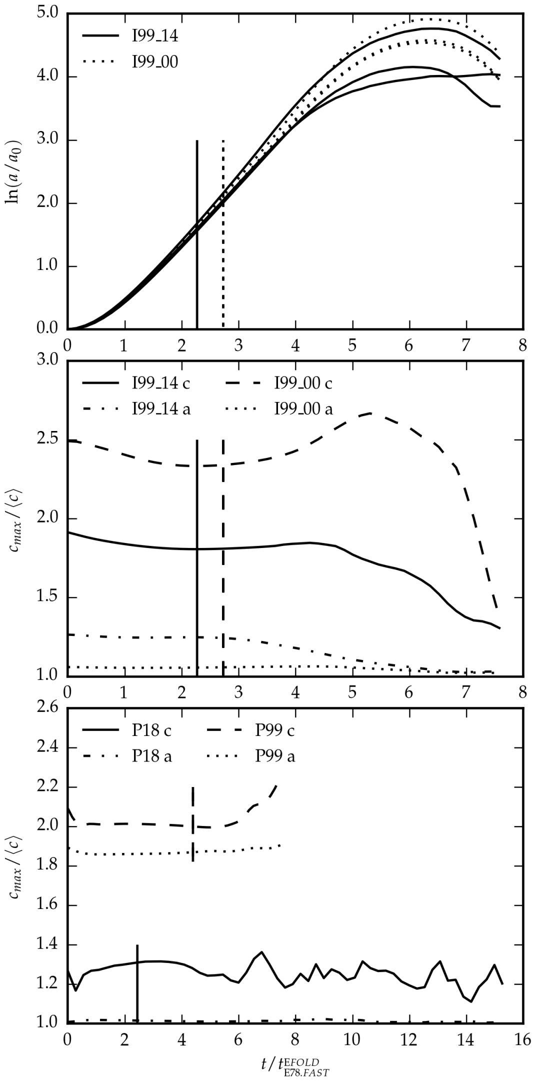

Figure 5.9: Upper panel: Amplitude evolution of the selected three modes at angle around 60° for model I99_14 (solid line) and I99_00 (dotted line). Vertical bars denote transition from linear to non–linear regime for model I99_14 (solid line) and I99_00 (dotted line). Middle: Evolution of azimuthal autocorrelation eq. (5.6) for models I99_14 and I99_00. Letter c and a refer to $\vec{k}$ evaluated on a circle and on an annulus in Fourier space, respectively. Vertical bars denote transition from linear to non–linear regime for particular model. Bottom: The same as in the middle but for polychromatic runs P18 and P99.

Run	A	$n_x \times n_y \times n_z$	$\frac{H}{\mathrm{d}z}$	$\mathscr{M}$	$\dot{\Sigma}$ $\frac{\mathrm{M}_\odot}{\mathrm{Myrpc}^2}$	M_J	$\bar{M}_\mathrm{CL}$ [$\mathrm{M}_\odot$]	$t^{\mathrm{EFOLD}}_{\mathrm{E78.FAST}}$ [Myr]	t_FRG [Myr]	A_FRG
A30_05	0.30	512 × 512 × 64	3.9	5	76	3.6	4.0	0.25	1.5	0.73
A30_10	0.30	512 × 512 × 64	3.9	10	39	3.6	3.5	0.25	1.7	0.59
A30_20	0.30	512 × 512 × 64	3.9	20	20	3.6	3.4	0.25	1.8	0.59

Table 5.4: Parameters of accreting simulations (models A). First four columns have the same meaning as the columns in Table 5.2 and quantities M_J, $\bar{M}_\mathrm{CL}$, $t_\mathrm{E78.FAST}$ and t_FRG are explained in Table 5.1. We further list the Mach number $\mathscr{M}$ of the accreting medium, accreting rate $\dot{\Sigma}$, and values of parameter A and surface density at the time t_FRG.

see in Section 5.4, for pressure dominated layers, the dispersion relation does not provide the correct estimate for fragmenting time and fragment masses. Thus, we focus mainly on fragmentation in the non–linear regime.

Generic name of accreting models is in the form A<A>_<$\mathscr{M}$>, where A represents the value of parameter A, and $\mathscr{M}$ the Mach number of accreting gas. Calculated models are listed in Table 5.4.

Since the ram pressure due to the shock equals to the thermal pressure at the contact discontinuity, the simulations with lower Mach number accretes at higher rate $\dot{\Sigma}$. Note that the external pressure is a temporary constant.

Evolution of surface density for simulation with the highest accreting rate, model A30_05 is shown in the top row of Figure 5.10. Time in Myr is indicated at the upper left corner of each frame, while the value of the parameter A is at the upper right corner. Due to its high accretion rate, the layer reaches the pressure dominated case early, so the major part of fragmentation is undergone in this case. After fragments appear (at t = 1Myr), they collapse to a sink particle. Accreting fragments arrange to a network of filaments. This kind of fragmentation is similar to the monolithic collapse for thermal pressure confined layers.

On the other hand, the model with the lowest accreting rate, A30_20 (low row of Fig. 5.10) spends a significant part of its fragmentation when confined with a higher value of the external pressure. The density inside the layer is approximately constant for the first 1Myr, and the excess in surface density is mainly due to surface corrugations. The density enhancements gradually coalesce, assembling mass, and eventually gravitationally collapse (frame at 2Myr). The fragmenting process for model A30_20 is similar to coalescence driven collapse for thermal pressure confined layers.

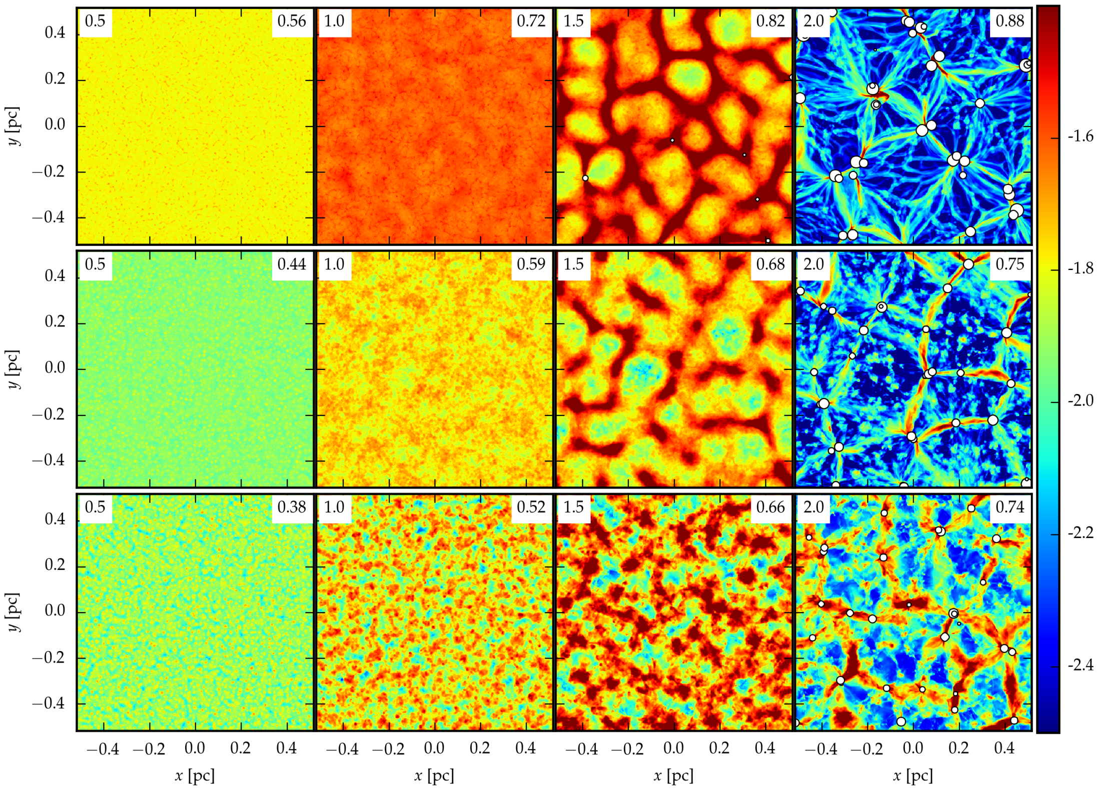

Figure 5.10: Surface density evolution for accreting layers. Time in Myr is shown in the upper left corner. Value of parameter A is indicated in the upper right corner. The figure is adopted from [Dinnbier et al., 2017].

6. Estimates for shell fragmentation

In this Chapter, we provide an estimate for properties of fragments condensing of a fragmenting shell powered by an H II region. The mass of fragments is of a particular interest, because it tells us about the possibility of propagating star formation.

Although this issue have been addressed in previous works, e.g. [Elmegreen, 1994, Whitworth et al., 1994a, Ehlerova et al., 1997, Iwasaki et al., 2011], we are motivated to revisit it for following reasons. Firstly, to access the typical fragment mass $M_{\rm FRG}$, majority of works use the thin shell dispersion relation (V83), which as we show in Section 5.3, is not the appropriate description for the dispersion relation of pressure confined layers. Since it appears that shells start fragmenting in the pressure dominated case (see eq. (6.6b) below or Whitworth et al. [1994b]), the dispersion relation for this situation, E78, predicts substantially different growth rates and ranges of unstable wavenumber resulting in different fragment masses than V83 (Figures 2.4 and 2.5).

Secondly, even though E78 is correct description of fragment masses forming out of a layer in the linear regime, the dispersion relation itself does not provide us with masses of *gravitationally bound fragments*, which form by a coalescence of stable fragments in pressure dominated layers. Likewise, E78 does not provide us with fragmenting timescale. We encountered this issue in Section 5.4.2.

Taking these considerations into account, we estimate the fragmenting timescale from dimensional analysis, where we use our simulations to calibrate the apriori unknown dimensionless functions rather than from the dispersion relations, which become unreliable in the non–linear regime.

6.1 Properties of fragmenting shells in context of propagating star formation

Consider an H II region powered by a massive star producing $\dot{N}$ ionising photons per second sitting in a homogeneous medium with density $\rho_{\rm ACC}$ (we use subscript ACC for the surrounding medium since the medium is accreted in the reference frame of the shell). We introduce $\dot{N}_{49} = [\dot{N}/10^{49}{\rm s}^{-1}]$, $c_{s2} = [c_{\rm S}/0.2{\rm km/s}]$, and $n_3 = [n_{\rm ACC}/10^3{\rm cm}^{-3}]$ where $c_{\rm S}$ is sound speed in the swept up shell, and $n_{\rm ACC}$ is the particle density in the surrounding medium. We further assume that fragmentation is accomplished in pressure dominated case, so the shell wall fragments by coalescence driven collapse. We show, at the end of this Section, that our results are consistent with this assumption.

As the shell expands, its surface density $\Sigma(t)$, and external pressure $P_{\rm EXT}(t)$ acting on its surfaces evolves with time. We assume that a small area in the shell wall fragments at any instant t with the same growth rate as a layer characterised by the same values of $\Sigma(t)$ and $P_{\rm EXT}(t)$. If fragmentation starts at time $t_{\rm O}$, it is accomplished at time t_1 given by

$$1 = \int_{t_{\mathrm{O}}}^{t_1} \frac{\omega_{\mathrm{E78.FAST}}(t)}{n_{\mathrm{EFOLD}}(A(t))}\mathrm{d}t = \int_{t_{\mathrm{O}}}^{t_1} \frac{\sqrt{0.276}\pi G\Sigma(A(t))}{c_{\mathrm{S}}A(t)n_{\mathrm{EFOLD}}(A(t))}\mathrm{d}t, \tag{6.1}$$

where we assume $A \to 0$, and exploit eq. (2.40). Before we use our accreting simulations with time dependent $\Sigma(t)$ to test validity of this assumption, we should determine the proxy for the fragmenting time t_{FRG} of a layer.

We argue in Section 5.4.2, that the number n_{EFOLD} of e–folding time $t_{\mathrm{E78.FAST}}$ depends on parameter A, which prevents us from using the $t_{\mathrm{E78.FAST}}$ as the proxy for t_{FRG}. However, since the model layers are characterised only by three parameters, P_{EXT}, Σ and c_s, any quantity with dimension of time describing the layer is expressed by

$$t = \frac{c_s f(A)}{G\Sigma}, \tag{6.2}$$

where $f(A)$ is an unknown dimensionless function of A. Parameter A is also the only dimensionless quantity which can be constructed from P_{EXT}, Σ and c_s. Thus, t_{FRG} and $t_{\mathrm{E78.FAST}}$ are given by eq. (6.2) (each timescale has presumably different form of $f(A)$). The ratio, $n_{\mathrm{EFOLD}} = t_{\mathrm{FRG}}/t_{\mathrm{E78.FAST}}$ can be also only a function of parameter A. After we obtain the dependence $n_{\mathrm{EFOLD}} = n_{\mathrm{EFOLD}}(A)$ from our simulations, we can determine the fragmenting time t_{FRG} for a layer with any P_{EXT}, Σ, c_s because $t_{\mathrm{E78.FAST}}$ can be calculated easily. We obtain

$$n_{\mathrm{EFOLD}} = 1.63/A + 3.79. \tag{6.3}$$

by fitting the data from Table 5.1.

Since the mass of fragments for our accreting simulations is almost independent on the Mach number, and the mass differs by less than factor 2 from the non–accreting simulation with the same value of pressure confinement (model P30), where the mass is comparable to the midplane Jeans mass M_J, we adopt the Jeans mass as the proxy for estimating the fragment mass.

To test the assumption that a layer with temporarily dependent parameters fragment at timescale provided by eq. (6.1), we compare the analytically calculated timescale with the fragmenting timescale measured in accreting models A30_05, A30_10 and A30_20. The models fragment at time 1.5 (1.36) Myr, 1.7 (1.64) Myr and 1.8 (1.85) Myr, respectively, where the first number is obtained from the simulation (Table 5.4) and the bracketed number is the solution of eq. (6.1) indicating a good agreement.

The radius R of a shell driven by an H II region evolves as $R = R_{\mathrm{ST}}(1 + 7c_{II}t/4R_{\mathrm{ST}})^{4/7}$ [Spitzer, 1978], where R_{ST} is the Strömgren radius, and c_{II} is speed of sound in the ionised gas inside the shell. The ram pressure and surface density evolve as $P_{\mathrm{RAM}} = \rho_{\mathrm{ACC}}(\mathrm{d}R/\mathrm{d}t)^2$ and $\Sigma = \rho_{\mathrm{ACC}}R(t)/3$. Thermal pressure P_{EXT} inside the shell is equal to P_{RAM}. Substituting these values to eq. (2.28), one yields the time dependence of parameter A of the shell

$$A = \left\{1 + \frac{18c_{II}^2}{\pi G\rho_{\mathrm{ACC}}(R_{\mathrm{ST}}(1 + 7c_{II}t/(4R_{\mathrm{ST}})))^2}\right\}^{-1/2}. \tag{6.4}$$

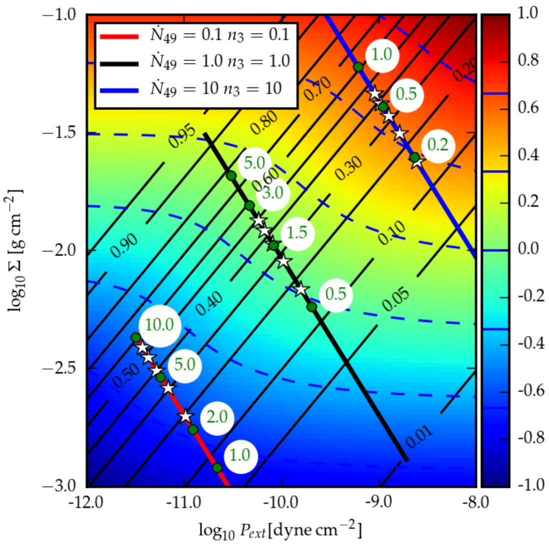

Figure 6.1: Evolution of surface density of a shell wall and pressure confining its surfaces for expansion around H II regions. H II regions with ($\dot{N}_{49}$, n_3) = (0.1, 0.1), ($\dot{N}_{49}$, n_3) = (1, 1) and ($\dot{N}_{49}$, n_3) = (10, 10) are shown by red, black and blue lines, respectively. Time in Myr from the start of the expansion is indicated by green numbers. The instants when the integral in eq. (6.1) equals 0, 0.25, 0.50, 0.75 and 1.0 are shown by white asterisks. The value of parameter A is shown by black labelled contours. Colourscale and dashed blue contours represent logarithm of the integrand in eq. (6.1) expressed in Myr^{-1}. The plot is constructed for $c_{s2} = 1$.

Substituting A from eq. (6.4) in eq. (6.1) for general configuration, one obtains the condition for the expansion around H II region as

$$\frac{0.81 c_{\mathrm{S}}}{\left\{(G\rho_{\mathrm{ACC}})^3 R_{\mathrm{ST}}^6 c_{II}^8\right\}^{1/14}} = \int_{A_{\mathrm{O}}}^{A_1} \frac{(1 - A^2)^{-25/14}}{n_{\mathrm{EFOLD}}(A) A^{3/7}} \mathrm{d}A, \tag{6.5}$$

where $A_{\mathrm{O}} = A(t_{\mathrm{O}})$ and $A_1 = A(t_1)$ is the value of parameter A at the beginning and end of fragmentation, respectively.

Following Whitworth et al. [1994a], we assume that fragmentation commences when self–gravity of a fragment containing one Jeans mass (its radius is $R_{\mathrm{J}} = \sqrt{M_{\mathrm{J}}/(\pi\Sigma)}$) is more important than stretching. This condition gives

$$t_{\mathrm{O}} = 0.76\ \mathrm{Myr}\ c_{s2}^{\frac{28}{37}}\ n_3^{-\frac{33}{74}}\ \dot{N}_{49}^{-\frac{4}{37}}, \tag{6.6a}$$

$$A_{\mathrm{O}} = 0.17\ \mathrm{Myr}\ c_{s2}^{\frac{28}{37}}\ n_3^{\frac{4}{74}}\ \dot{N}_{49}^{-\frac{4}{37}}, \tag{6.6b}$$

$$\tag{6.6c}$$

We neglect the role of the thermal pressure in supporting the fragment against lateral collapse since we assume that the layer already broke into gravitationally stable fragments because the shell is dominated by external pressure (see evolutionary paths in Figure 6.1). Note that the exact choice of t_{O} has only a weak dependence on the results (any numerical coefficient in eq. (6.7) would differ by less than 20 % if we used $t_{\mathrm{O}} = 0$ instead of eq. (6.6a)).

Figure 6.1 shows the evolution of P_{EXT}, Σ and A for walls of shells with typical values for galactic H II regions. Model with $\dot{N}_{49} = 0.1$ (approximately an O9V star [Martins et al., 2005]) expands into a homogeneous ambient medium of particle density $n_3 = 0.1$, model with $\dot{N}_{49} = 1$ (O6V star) expands in medium of $n_3 = 1$, and model with $\dot{N}_{49} = 10$ (two O3V stars) expands in medium of $n_3 = 10$. Any other model within a set $\dot{N}_{49} \times n_3$ in range $(0.1, 10) \times (0.1, 10)$ lies in between them.

Time $t_{\rm O}$ when the fragmentation starts (determined from eq. (6.6a)) is represented by the first white asterisk on the evolutionary path. The instants when the integral eq. (6.1) reaches values 0.25, 0.5, 0.75 and 1.0 are shown by following asterisks indicating that fragmentation is accomplished in the pressure dominated case.

For an H II region characterised by $(\dot{N}_{49}, n_3)$ we calculate $A(t_1)$ by integrating eq. (6.5), and from eq. (6.4) we find the fragmenting time t_1. ¿From known t_1, it is straightforward to calculate corresponding shell radius $R_{\rm FRG}$, and surface density $\Sigma_{\rm FRG}$. Taking Jeans mass in the shell wall as an estimate for fragment mass $M_{\rm FRG}$, the fragment radius is $r_{\rm FRG} = \sqrt{M_{\rm FRG}/(\pi G)}$. We present the results in the form of a polynomial fit of these quantities for $c_{\rm S} = 0.2$km/s over range $\dot{N}_{49} \times n_3 = (0.1, 10) \times (0.1, 10)$, which reads

$$t_{\rm FRG} = 2.4 \text{ Myr } n_3^{-0.43} \; \dot{N}_{49}^{-0.12} \tag{6.7a}$$
$$M_{\rm FRG} = 3.1 \text{ M}_\odot \; n_3^{-0.41} \; \dot{N}_{49}^{-0.16} \tag{6.7b}$$
$$r_{\rm FRG} = 0.12 \text{ pc } n_3^{-0.44} \; \dot{N}_{49}^{-0.11} \tag{6.7c}$$
$$A_{\rm FRG} = 0.51 \; n_3^{0.04} \; \dot{N}_{49}^{-0.08} \tag{6.7d}$$
$$\Sigma_{\rm FRG} = 63 \text{ M}_\odot \text{ pc}^{-2} \; n_3^{0.46} \; \dot{N}_{49}^{0.08} \tag{6.7e}$$
$$R_{\rm FRG} = 7.7 \text{ pc } n_3^{-0.53} \; \dot{N}_{49}^{0.08}. \tag{6.7f}$$

Unless n_3 is very high or $\dot{N}_{49}$ very low, equation eq. (6.7d) justifies the assumption made at the beginning of this study that the fragmentation is accomplished before the shell enters the self–gravity dominated case $A_{\rm FRG} \gtrsim 0.6$. We investigate fragmentation of pressure dominated shells only, because the proxy for the mass of fragments, the Jeans mass, does not change significantly during the fragmentation. Since the Jeans mass increases rapidly as the shell becomes dominated by self–gravity, it is not clear what is the estimate for fragment mass, and we defer this issue to possible further work. To fulfill the condition $A_{\rm FRG} \lesssim 0.6$, we also restrict our study to shells with $c_{\rm S} = 0.2$km/s (temperature around 10K) because with increasing temperature the end point of fragmentation $A_{\rm FRG}$ increases and moves to the self–gravity dominated case.

6.2 Discussion

The most important simplifications made when estimating properties of fragmenting shells are the following: expansion into homogeneous medium, absence of radiation penetrating the shell, no deceleration, and no complicated thermodynamics. On the other hand, stretching due to expansion has probably not essential as was shown by [Whitworth et al., 1994a]. These phenomena may alter the simple course of the fragmenting process as described in Chapter 5 to such an extent that the distinction on monolithic and coalescence driven collapse may not apply.

Despite the simplifications, our work presents more accurate estimate for fragment properties of idealised layers than works based on the linearised dispersion relations. In contrast to Whitworth et al. [1994a], who based on V83, obtained significantly higher fragment masses, their analog to our eq. (6.7b) reads,

$$M_{\rm FRG} = 23\ {\rm M}_{\odot}\ n_3^{-0.46}\ \dot{N}_{49}^{-0.09} a_2^{3.64}, \tag{6.8}$$

which would favour propagating star formation. Note that V83 overestimates fragment masses for pressure dominated layers (Fig. 2.5) because it does not take into account surface–gravity waves. Another estimate for fragment masses is investigated by [Iwasaki et al., 2011]. Based on three dimensional SPH simulations, they suggest much smaller fragment masses (the constant in 6.8 is $3.5{\rm M}_{\odot}$), a value very close to ours (cf. eq. (6.7b)).

Equation eq. (6.7b) predicts that massive stars can be easily formed in low density medium while high density medium would produce low mass stars, a situation which is hardly observed. This paradoxical situation casts doubts on the whole adopted approach and goes back to the Jeans mass, which raises the same issue [Bonnell et al., 2001]. Due to the maximum in dispersion relation for shells or layers as we encountered in Section 2.2.2, if fragmented according to this simple prescription, these structures would produce stars with a narrow mass range. However, mass functions of this shape are in disagreement with observations [Wünsch et al., 2010, Kroupa et al., 2013]. It implies, that either the number of stars formed in triggering events is small in comparison to the number of spontaneously formed stars, or that the number of triggered stars is high, but the shells or layers would form stars of approximately canonical IMF.

In view of these considerations, we conclude that isothermal models of shells expanding into homogeneous medium cannot provide us with definitive predictions about propagating star formation. Nevertheless, our results suggest, based on more sophisticated models than previous works, that a typical shell fragments into objects of too low mass to form massive stars and sustain self–propagating star formation.

Summary and conclusion

Massive stars are copious producers of ionising radiation and stellar winds. At the end of their existence, they explode as supernovae an they release an enormous amount of energy (10^{51}erg) in the form which interacts with matter. This strongly impacts the state of their surrounding interstellar medium, which is often swept up and compressed into a dense cold shell. Under favourable conditions, the shell may fragment and form new generation of stars. If the new stellar generation contains stars massive enough ($M \gtrsim 8\mathrm{M}_{\odot}$) to be able to sweep their own shells by their feedback, the shells would fragment, and form another stellar generation. By this process, star formation may propagate in a series of bursts.

Several studies have attempted to analytically or semi–analytically estimate the crucial parameter for the process to be maintained, the maximum mass of a star which the shell can form, from the wavenumber with the highest growth rate λ_{MAX} given by the dispersion relation of the shell. Since the wavenumber is significantly shorter than the shell radius, the shell curvature can be neglected, and a representative area in shell surface approximated by a plane parallel layer. Although this simplifies the problem, there are at least three different estimates for the dispersion relation depending on adopted assumptions. Each estimate predicts different fragment mass, and for some shell parameters the difference can be so large that while one estimate predicts very massive fragments able to form massive stars of powerful feedback with possible triggering star formation, another estimate predicts for the same shell parameters low mass fragments unable to trigger new star forming event.

We modify the standard Ewald method, which is derived for computational domains with periodic boundary conditions, to computational domains with boundary conditions periodic in two directions and isolated in the third direction. This modification enables us to calculate gravitational field for self–gravitating layers by a tree code accurately and efficiently. We also modified the Ewald method for computational domains with periodic boundary conditions in one direction, and with isolated boundary conditions in the other two directions. The second modification is suited for simulating objects with axial symmetry, e.g. filaments. We implement standard Ewald method and its two modifications to publicly available astrophysical hydrodynamical codes Flash and Gandalf. Derivation of the formulae for the modified Ewald method and tests of their implementation in the hydrodynamical codes is presented in Chapter 4 and forms a part of (Wünsch et al. in preparation).

We perform three dimensional simulations to study several aspects of the fragmenting process of isothermal layers. Obtained results are presented in Chapter 5 and in [Dinnbier et al., 2017]. The layers are immersed in hot rarefied gas imposing thermal pressure on both surfaces. We explore layers with various degree of pressure confinement. In the linear regime of fragmentation (i.e. when the perturbing amplitudes of a quantity are small in comparison to its unperturbed value), we find that the dispersion relation of a layer is in an excellent agreement with the dispersion relation proposed by Elmegreen and Elmegreen [1978] for layers from very high to very low degree of pressure confinement. On the other hand, we report a significant limitations to thin shell dispersion relation [Vishniac, 1983] and PAGI [Wünsch et al., 2010] in describing the dispersion relation for pressure confined layers ($A \lesssim 0.5$; see eq. (2.28) for definition of parameter A).

In the non–linear regime of fragmentation, when the perturbations are large, the degree of external pressure confinement distinguishes between two qualitatively different ways of fragmentation. Layers confined with low value of pressure break into gravitationally unstable fragments, which monolithically collapse. On the other hand, layers confined with high value of external pressure fragment in two steps. Firstly, the layers break into small gravitationally stable fragments, which subsequently grow by coalescence until they assemble enough mass that they gravitationally collapse. Although the dispersion relation proposed by Elmegreen and Elmegreen [1978] predicts correctly fragmentation in the linear regime, it underestimates fragment masses for layers with high pressure confinement since the dispersion relation does not take into account coalescence of fragments. It implies that even the appropriate dispersion relation is unable to predict the fragment mass.

We investigate the possibility suggested in some previous semi–analytic works, that in the non–linear regime, the layer self–organises forming a regular hexagonal pattern. Although our searching method is possible to detect any regular pattern, and we perform two dedicated simulations where the pattern formation should be enhanced, we do not find any support for this scenario.

Our simulations suggest that substituting the conditions at one layer surface from contact discontinuity to a shock front for pressure confined layers preserves the distinction between monolithic and coalescence driven collapse. As we keep the external pressure a constant during accretion and surface density increases, the degree of pressure confinement decreases. Thus the role of external pressure swiftly decreases for layers with high accreting rate, so their fragmentation resembles the monolithic collapse reported for non–accreting layers. Layers with low accretion rate remain confined by high degree of external pressure so long, that they undergo coalescence driven collapse before the pressure confinement decreases significantly.

We use the values of fragmenting time and mass of fragments obtained from our simulations in the non–linear regime to estimate fragment properties of a shell swept up by an expanding H II region. This model is described in Chapter 6 and in [Dinnbier et al., 2017]. For typical properties of the star forming ISM (particle density $\simeq 10^3 \mathrm{cm}^{-3}$, temperature $\simeq 10\mathrm{K}$), this model leads to masses of fragments $\simeq 3\mathrm{M}_\odot$. Stars formed in these fragments would not be able to ignite new H II regions to sustain propagating star formation. This is the opposite result than that of Whitworth et al. [1994a], who assume thin shell dispersion relation as the correct description for fragmentation. However, given the simplifications adopted for estimating the fragment mass in our model, we conclude that further work is needed to provide more reliable answer on propagating star formation in this configuration.

Acknowledgements

The author gratefully acknowledges support from grant GA ČR P209/12/1795, grant GA ČR č. 14-37086G and project MŠMT LG14013. Large simulations presented in this work were calculated on IT4I facilities supported by The Ministry of Education, Youth and Sports from the Large Infrastructures for Research, Experimental Development and Innovations project IT4Innovations National Supercomputing Center LM2015070. Matplotlib library of Python Hunter [2007] was an invaluable tool for preparing figures in this Thesis.

Bibliography

J. Alves, M. Lombardi, and C. J. Lada. The mass function of dense molecular cores and the origin of the IMF. A&A, 462:L17–L21, 2007.

S. J. Arthur. Wind-Blown Bubbles and HII Regions around Massive Stars. In *Revista Mexicana de Astronomia y Astrofisica Conference Series*, volume 30 of *Revista Mexicana de Astronomia y Astrofisica, vol. 27*, pages 64–71, 2007.

J. Ballesteros-Paredes and L. Hartmann. Remarks on Rapid vs. Slow Star Formation. Rev. Mexicana Astron. Astrofis., 43:123–136, 2007.

J. Barnes and P. Hut. A hierarchical O(N log N) force-calculation algorithm. Nature, 324:446–449, 1986.

N. Bastian, K. R. Covey, and M. R. Meyer. A Universal Stellar Initial Mass Function? A Critical Look at Variations. ARA&A, 48:339–389, 2010.

M. R. Bate, I. A. Bonnell, and N. M. Price. Modelling accretion in protobinary systems. MNRAS, 277:362–376, 1995.

T. G. Bisbas, R. Wünsch, A. P. Whitworth, and D. A. Hubber. Smoothed particle hydrodynamics simulations of expanding H II regions. I. Numerical method and applications. A&A, 497:649–659, 2009.

T. G. Bisbas, R. Wünsch, A. P. Whitworth, D. A. Hubber, and S. Walch. Radiation-driven Implosion and Triggered Star Formation. ApJ, 736:142, 2011.

A. Blaauw. The O Associations in the Solar Neighborhood. ARA&A, 2:213, 1964.

A. Blaauw. OB Associations and the Fossil Record of Star Formation. In C. J. Lada and N. D. Kylafis, editors, *NATO Advanced Science Institutes (ASI) Series C*, volume 342 of *NATO Advanced Science Institutes (ASI) Series C*, page 125, 1991.

L. Blitz. Star Forming Giant Molecular Clouds. In C. J. Lada and N. D. Kylafis, editors, *NATO Advanced Science Institutes (ASI) Series C*, volume 342 of *NATO Advanced Science Institutes (ASI) Series C*, page 3, 1991.

I. A. Bonnell, M. R. Bate, C. J. Clarke, and J. E. Pringle. Accretion and the stellar mass spectrum in small clusters. MNRAS, 285:201–208, 1997.

I. A. Bonnell, M. R. Bate, and H. Zinnecker. On the formation of massive stars. MNRAS, 298:93–102, 1998.

I. A. Bonnell, M. R. Bate, C. J. Clarke, and J. E. Pringle. Competitive accretion in embedded stellar clusters. MNRAS, 323:785–794, 2001.

I. A. Bonnell, M. R. Bate, and S. G. Vine. The hierarchical formation of a stellar cluster. MNRAS, 343:413–418, 2003.

W. B. Bonnor. Boyle's Law and gravitational instability. MNRAS, 116:351, 1956.

D. F. A. Boyd and A. P. Whitworth. The minimum mass for opacity-limited fragmentation in turbulent cloud cores. A&A, 430:1059–1066, 2005.

J. Brand, F. Massi, A. Zavagno, L. Deharveng, and B. Lefloch. Triggered star formation at the borders of the H ii region Sh 2-217. A&A, 527:A62, 2011.

A. Bressan, F. Fagotto, G. Bertelli, and C. Chiosi. Evolutionary sequences of stellar models with new radiative opacities. II - Z = 0.02. A&AS, 100:647–664, 1993.

A. Burkert and L. Hartmann. Collapse and Fragmentation in Finite Sheets. ApJ, 616:288–300, 2004.

J. Castor, R. McCray, and R. Weaver. Interstellar bubbles. ApJ, 200:L107–L110, 1975.

J. Cernicharo. The Physical Conditions of Low Mass Star Forming Regions. In C. J. Lada and N. D. Kylafis, editors, *NATO Advanced Science Institutes (ASI) Series C*, volume 342 of *NATO Advanced Science Institutes (ASI) Series C*, page 287, 1991.

G. Chabrier. Galactic Stellar and Substellar Initial Mass Function. PASP, 115: 763–795, 2003.

E. Churchwell, M. S. Povich, D. Allen, M. G. Taylor, M. R. Meade, B. L. Babler, R. Indebetouw, C. Watson, B. A. Whitney, M. G. Wolfire, T. M. Bania, R. A. Benjamin, D. P. Clemens, M. Cohen, C. J. Cyganowski, J. M. Jackson, H. A. Kobulnicky, J. S. Mathis, E. P. Mercer, S. R. Stolovy, B. Uzpen, D. F. Watson, and M. J. Wolff. The Bubbling Galactic Disk. ApJ, 649:759–778, 2006.

E. Churchwell, D. F. Watson, M. S. Povich, M. G. Taylor, B. L. Babler, M. R. Meade, R. A. Benjamin, R. Indebetouw, and B. A. Whitney. The Bubbling Galactic Disk. II. The Inner 20°. ApJ, 670:428–441, 2007.

P. C. Clark, I. A. Bonnell, H. Zinnecker, and M. R. Bate. Star formation in unbound giant molecular clouds: the origin of OB associations? MNRAS, 359: 809–818, 2005.

P. Colella and P. R. Woodward. The Piecewise Parabolic Method (PPM) for Gas-Dynamical Simulations. *Journal of Computational Physics*, 54:174–201, 1984.

R. M. Crutcher. Magnetic Fields in Molecular Clouds. ARA&A, 50:29–63, 2012.

S. E. Dahm. *The Young Cluster and Star Forming Region NGC 2264*, page 966. 2008.

J. E. Dale. The modelling of feedback in star formation simulations. New A Rev., 68:1–33, 2015.

J. E. Dale, R. Wünsch, A. Whitworth, and J. Palouš. The fragmentation of expanding shells - I. Limitations of the thin-shell approximation. MNRAS, 398:1537–1548, 2009.

J. E. Dale, B. Ercolano, and I. A. Bonnell. Ionizing feedback from massive stars in massive clusters - II. Disruption of bound clusters by photoionization. MNRAS, 424:377–392, 2012.

J. E. Dale, J. Ngoumou, B. Ercolano, and I. A. Bonnell. Massive stars in massive clusters - IV. Disruption of clouds by momentum-driven winds. MNRAS, 436: 3430–3445, 2013.

J. E. Dale, J. Ngoumou, B. Ercolano, and I. A. Bonnell. Before the first supernova: combined effects of H II regions and winds on molecular clouds. MNRAS, 442: 694–712, 2014.

J. E. Dale, T. J. Haworth, and E. Bressert. The dangers of being trigger-happy. MNRAS, 450:1199–1211, 2015.

J. R. Dawson, A. Kawamura, N. Mizuno, T. Onishi, and Y. Fukui. Catalogue of ^{12}CO(J = 1-0) and ^{13}CO(J = 1-0) Molecular Clouds in the Carina Flare Supershell. PASJ, 60:1297–1315, 2008a.

J. R. Dawson, N. Mizuno, T. Onishi, N. M. McClure-Griffiths, and Y. Fukui. The 'Carina Flare' supershell: probing the atomic and molecular ISM in a Galactic chimney. MNRAS, 387:31–44, 2008b.

J. R. Dawson, N. M. McClure-Griffiths, J. M. Dickey, and Y. Fukui. Molecular Clouds in Supershells: A Case Study of Three Objects in the Walls of GSH 287+04-17 and GSH 277+00+36. ApJ, 741:85, 2011a.

J. R. Dawson, N. M. McClure-Griffiths, A. Kawamura, N. Mizuno, T. Onishi, A. Mizuno, and Y. Fukui. Supershells as Molecular Cloud Factories: Parsec Resolution Observations of H I and ^{12}CO(J = 1-0) in GSH 287+04-17 and GSH 277+00+36. ApJ, 728:127, 2011b.

E. J. de Geus. Interactions of stars and interstellar matter in Scorpio Centaurus. A&A, 262:258–270, 1992.

L. Deharveng, B. Lefloch, A. Zavagno, J. Caplan, A. P. Whitworth, D. Nadeau, and S. Martín. Triggered massive-star formation at the border of the H II Region Sh 104. A&A, 408:L25–L28, 2003a.

L. Deharveng, A. Zavagno, L. Salas, A. Porras, J. Caplan, and I. Cruz-González. Sequential star formation at the periphery of the H II regions Sh 217 and Sh 219. A&A, 399:1135–1145, 2003b.

L. Deharveng, A. Zavagno, and J. Caplan. Triggered massive-star formation on the borders of Galactic H II regions. I. A search for "collect and collapse" candidates. A&A, 433:565–577, 2005.

L. Deharveng, F. Schuller, L. D. Anderson, A. Zavagno, F. Wyrowski, K. M. Menten, L. Bronfman, L. Testi, C. M. Walmsley, and M. Wienen. A gallery of bubbles. The nature of the bubbles observed by Spitzer and what ATLASGAL tells us about the surrounding neutral material. A&A, 523:A6, 2010.

L. Deharveng, A. Zavagno, M. R. Samal, L. D. Anderson, G. LeLeu, D. Brevot, A. Duarte-Cabral, S. Molinari, M. Pestalozzi, J. B. Foster, J. M. Rathborne, and J. M. Jackson. Bipolar H II regions - Morphology and star formation in their vicinity. I. G319.88+00.79 and G010.32-00.15. A&A, 582:A1, 2015.

R. I. Diaz-Miller, J. Franco, and S. N. Shore. Photoionized and Photodissociated Regions around Main-Sequence Stars. ApJ, 501:192–206, 1998.

F. Dinnbier, R. Wünsch, A. Whitworth, and J. Palouš. Fragmentation of vertically stratified gaseous layers: monolithic or coalescence-driven collapse. MNRAS, in press, 2017.

C. L. Dobbs and J. E. Pringle. The exciting lives of giant molecular clouds. MNRAS, 432:653–667, 2013.

C. L. Dobbs, M. R. Krumholz, J. Ballesteros-Paredes, A. D. Bolatto, Y. Fukui, M. Heyer, M.-M. M. Low, E. C. Ostriker, and E. Vázquez-Semadeni. Formation of Molecular Clouds and Global Conditions for Star Formation. *Protostars and Planets VI*, pages 3–26, 2014.

A. G. Doroshkevich. Fragmentation of a Primordial Flat Layer, and the Formation of Internal Cluster Structure. Soviet Ast., 24:152–157, 1980.

B. T. Draine. *Physics of the Interstellar and Intergalactic Medium.* 2011.

A. Dubey, R. Fisher, C. Graziani, G. C. Jordan, IV, D. Q. Lamb, L. B. Reid, P. Rich, D. Sheeler, D. Townsley, and K. Weide. Challenges of Extreme Computing using the FLASH code. In N. V. Pogorelov, E. Audit, and G. P. Zank, editors, *Numerical Modeling of Space Plasma Flows*, volume 385 of *Astronomical Society of the Pacific Conference Series*, page 145, 2008.

C. M. Dutra, E. Bica, J. Soares, and B. Barbuy. New infrared star clusters in the southern Milky Way with 2MASS. A&A, 400:533–539, 2003.

J. E. Dyson and D. A. Williams. *Physics of the interstellar medium.* 1980.

R. Ebert. Über die Verdichtung von H I-Gebieten. Mit 5 Textabbildungen. ZAp, 37:217, 1955.

S. Ehlerova, J. Palous, C. Theis, and G. Hensler. Fragmentation of expanding shells in spiral and irregular galaxies. A&A, 328:121–129, 1997.

B. G. Elmegreen. Quiescent formation of bound galactic clusters. MNRAS, 203: 1011–1020, 1983.

B. G. Elmegreen. A Q condition for long-range propagating star formation. ApJ, 427:384–387, 1994.

B. G. Elmegreen. Observations and Theory of Dynamical Triggers for Star Formation. In C. E. Woodward, J. M. Shull, and H. A. Thronson, Jr., editors, *Origins*, volume 148 of *Astronomical Society of the Pacific Conference Series*, page 150, 1998.

B. G. Elmegreen. On the Rapid Collapse and Evolution of Molecular Clouds. ApJ, 668:1064–1082, 2007.

B. G. Elmegreen and D. M. Elmegreen. Star formation in shock-compressed layers. ApJ, 220:1051–1062, 1978.

B. G. Elmegreen and C. J. Lada. Sequential formation of subgroups in OB associations. ApJ, 214:725–741, 1977.

N. J. Evans, II, M. M. Dunham, J. K. Jørgensen, M. L. Enoch, B. Merín, E. F. van Dishoeck, J. M. Alcalá, P. C. Myers, K. R. Stapelfeldt, T. L. Huard, L. E. Allen, P. M. Harvey, T. van Kempen, G. A. Blake, D. W. Koerner, L. G. Mundy, D. L. Padgett, and A. I. Sargent. The Spitzer c2d Legacy Results: Star-Formation Rates and Efficiencies; Evolution and Lifetimes. ApJS, 181: 321-350, 2009.

P. P. Ewald. Die Berechnung optischer und elektrostatischer Gitterpotentiale. *Annalen der Physik*, 369:253–287, 1921.

C. Federrath, R. Banerjee, P. C. Clark, and R. S. Klessen. Modeling Collapse and Accretion in Turbulent Gas Clouds: Implementation and Comparison of Sink Particles in AMR and SPH. ApJ, 713:269–290, 2010.

K. Foyle, H.-W. Rix, F. Walter, and A. K. Leroy. Arm and Interarm Star Formation in Spiral Galaxies. ApJ, 725:534–541, 2010.

J. Franco, G. Tenorio-Tagle, and P. Bodenheimer. On the formation and expansion of H II regions. ApJ, 349:126–140, 1990.

B. Fryxell, K. Olson, P. Ricker, F. X. Timmes, M. Zingale, D. Q. Lamb, P. MacNeice, R. Rosner, J. W. Truran, and H. Tufo. FLASH: An Adaptive Mesh Hydrodynamics Code for Modeling Astrophysical Thermonuclear Flashes. ApJS, 131:273–334, 2000.

B. Fuchs. The fragmentation of uniformly rotating self-gravitating discs. MNRAS, 278, 1996.

N. Fukuda and T. Hanawa. Sequential Star Formation Triggered by Expansion of an H II Region. ApJ, 533:911–923, 2000.

M. P. Geyer and A. Burkert. The effect of gas loss on the formation of bound stellar clusters. MNRAS, 323:988–994, 2001.

J. M. Girart, R. Rao, and D. P. Marrone. Magnetic Fields in the Formation of Sun-Like Stars. *Science*, 313:812–814, 2006.

P. Goldreich and D. Lynden-Bell. I. Gravitational stability of uniformly rotating disks. MNRAS, 130:97, 1965.

S. P. Goodwin, D. Nutter, P. Kroupa, D. Ward-Thompson, and A. P. Whitworth. The relationship between the prestellar core mass function and the stellar initial mass function. A&A, 477:823–827, 2008.

K. M. Górski, E. Hivon, A. J. Banday, B. D. Wandelt, F. K. Hansen, M. Reinecke, and M. Bartelmann. HEALPix: A Framework for High-Resolution Discretization and Fast Analysis of Data Distributed on the Sphere. ApJ, 622:759–771, 2005.

L. Hartmann, J. Ballesteros-Paredes, and E. A. Bergin. Rapid Formation of Molecular Clouds and Stars in the Solar Neighborhood. ApJ, 562:852–868, 2001.

L. Hernquist, F. R. Bouchet, and Y. Suto. Application of the Ewald method to cosmological N-body simulations. ApJS, 75:231–240, 1991.

M. Heyer, C. Krawczyk, J. Duval, and J. M. Jackson. Re-Examining Larson's Scaling Relationships in Galactic Molecular Clouds. ApJ, 699:1092–1103, 2009.

J. D. Hunter. Matplotlib: A 2d graphics environment. *Computing In Science & Engineering*, 9(3):90–95, 2007.

J. H. Hunter, Jr., M. T. Sandford, II, R. W. Whitaker, and R. I. Klein. Star formation in colliding gas flows. ApJ, 305:309–332, 1986.

O. Iffrig and P. Hennebelle. Mutual influence of supernovae and molecular clouds. A&A, 576:A95, 2015.

S.-I. Inutsuka and S. M. Miyama. Self-similar solutions and the stability of collapsing isothermal filaments. ApJ, 388:392–399, 1992.

K. Iwasaki, S.-i. Inutsuka, and T. Tsuribe. Gravitational Fragmentation of Expanding Shells. II. Three-dimensional Simulations. ApJ, 733:17, 2011.

A. Kawamura, Y. Mizuno, T. Minamidani, M. D. Filipović, L. Staveley-Smith, S. Kim, N. Mizuno, T. Onishi, A. Mizuno, and Y. Fukui. The Second Survey of the Molecular Clouds in the Large Magellanic Cloud by NANTEN. II. Star Formation. ApJS, 184:1–17, 2009.

J.-G. Kim, W.-T. Kim, Y. M. Seo, and S. S. Hong. Gravitational Instability of Rotating, Pressure-confined, Polytropic Gas Disks with Vertical Stratification. ApJ, 761:131, 2012.

R. Klessen. GRAPESPH with fully periodic boundary conditions - Fragmentation of molecular clouds. MNRAS, 292:11, 1997.

J. Koda, N. Scoville, T. Sawada, M. A. La Vigne, S. N. Vogel, A. E. Potts, J. M. Carpenter, S. A. Corder, M. C. H. Wright, S. M. White, B. A. Zauderer, J. Patience, A. I. Sargent, D. C. J. Bock, D. Hawkins, M. Hodges, A. Kemball, J. W. Lamb, R. L. Plambeck, M. W. Pound, S. L. Scott, P. Teuben, and D. P. Woody. Dynamically Driven Evolution of the Interstellar Medium in M51. ApJ, 700:L132–L136, 2009.

H. Koyama and S.-i. Inutsuka. An Origin of Supersonic Motions in Interstellar Clouds. ApJ, 564:L97–L100, 2002.

P. Kroupa. On the variation of the initial mass function. MNRAS, 322:231–246, 2001.

P. Kroupa. The Initial Mass Function of Stars: Evidence for Uniformity in Variable Systems. *Science*, 295:82–91, 2002.

P. Kroupa, S. Aarseth, and J. Hurley. The formation of a bound star cluster: from the Orion nebula cluster to the Pleiades. MNRAS, 321:699–712, 2001.

P. Kroupa, C. Weidner, J. Pflamm-Altenburg, I. Thies, J. Dabringhausen, M. Marks, and T. Maschberger. *The Stellar and Sub-Stellar Initial Mass Function of Simple and Composite Populations*, page 115. 2013.

M. R. Krumholz and C. D. Matzner. The Dynamics of Radiation-pressure-dominated H II Regions. ApJ, 703:1352–1362, 2009.

M. R. Krumholz, C. F. McKee, and R. I. Klein. Embedding Lagrangian Sink Particles in Eulerian Grids. ApJ, 611:399–412, 2004.

C. J. Lada and E. A. Lada. Embedded Clusters in Molecular Clouds. ARA&A, 41:57–115, 2003.

C. J. Lada, M. Margulis, and D. Dearborn. The formation and early dynamical evolution of bound stellar systems. ApJ, 285:141–152, 1984.

E. A. Lada, D. L. Depoy, N. J. Evans, II, and I. Gatley. A 2.2 micron survey in the L1630 molecular cloud. ApJ, 371:171–182, 1991.

L. D. Landau and E. M. Lifshitz. *Fluid mechanics*. 1959.

R. B. Larson. Turbulence and star formation in molecular clouds. MNRAS, 194: 809–826, 1981.

B. Lefloch and B. Lazareff. Cometary globules. 1: Formation, evolution and morphology. A&A, 289:559–578, 1994.

L. A. Lopez, M. R. Krumholz, A. D. Bolatto, J. X. Prochaska, and E. Ramirez-Ruiz. What Drives the Expansion of Giant H II Regions?: A Study of Stellar Feedback in 30 Doradus. ApJ, 731:91, 2011.

L. A. Lopez, M. R. Krumholz, A. D. Bolatto, J. X. Prochaska, E. Ramirez-Ruiz, and D. Castro. The Role of Stellar Feedback in the Dynamics of H II Regions. ApJ, 795:121, 2014.

M.-M. Mac Low and M. L. Norman. Nonlinear growth of dynamical overstabilities in blast waves. ApJ, 407:207–218, 1993.

P. MacNeice, K. M. Olson, C. Mobarry, R. de Fainchtein, and C. Packer. PARAMESH: A parallel adaptive mesh refinement community toolkit. *Computer Physics Communications*, 126:330–354, 2000.

F. Martins, D. Schaerer, and D. J. Hillier. A new calibration of stellar parameters of Galactic O stars. A&A, 436:1049–1065, 2005.

F. Martins, M. Pomarès, L. Deharveng, A. Zavagno, and J. C. Bouret. Near-IR integral field spectroscopy of ionizing stars and young stellar objects on the borders of H II regions. A&A, 510:A32, 2010.

P. Massey. The Initial Mass Function of Massive Stars in the Local Group. In G. Gilmore and D. Howell, editors, *The Stellar Initial Mass Function (38th Herstmonceux Conference)*, volume 142 of *Astronomical Society of the Pacific Conference Series*, page 17, 1998.

C. D. Matzner. On the Role of Massive Stars in the Support and Destruction of Giant Molecular Clouds. ApJ, 566:302–314, 2002.

R. McCray and M. Kafatos. Supershells and propagating star formation. ApJ, 317:190–196, 1987.

C. F. McKee and J. P. Williams. The Luminosity Function of OB Associations in the Galaxy. ApJ, 476:144–165, 1997.

S. M. Miyama, S. Narita, and C. Hayashi. Fragmentation of Isothermal Sheet-Like Clouds. I —Solutions of Linear and Second-Order Perturbation Equations—. *Progress of Theoretical Physics*, 78:1051–1064, 1987a.

S. M. Miyama, S. Narita, and C. Hayashi. Fragmentation of Isothermal Sheet-Like Clouds. II —Full Nonlinear Numerical Simulations—. *Progress of Theoretical Physics*, 78:1273–1287, 1987b.

R. Nishi. On the Instability of Decelerating Shock Waves. *Progress of Theoretical Physics*, 87:347–365, 1992.

S. S. R. Offner, R. I. Klein, C. F. McKee, and M. R. Krumholz. The Effects of Radiative Transfer on Low-Mass Star Formation. ApJ, 703:131–149, 2009.

J. H. Oort and L. Spitzer, Jr. Acceleration of Interstellar Clouds by O-Type Stars. ApJ, 121:6, 1955.

V. Ossenkopf and M.-M. Mac Low. Turbulent velocity structure in molecular clouds. A&A, 390:307–326, 2002.

J. Ostriker. The Equilibrium of Polytropic and Isothermal Cylinders. ApJ, 140:1056, 1964.

A. Pon, J. A. Toalá, D. Johnstone, E. Vázquez-Semadeni, F. Heitsch, and G. C. Gómez. Aspect Ratio Dependence of the Free-fall Time for Non-spherical Symmetries. ApJ, 756:145, 2012.

T. Preibisch and E. Mamajek. *The Nearest OB Association: Scorpius-Centaurus (Sco OB2)*, page 235. 2008.

T. Preibisch and H. Zinnecker. The History of Low-Mass Star Formation in the Upper Scorpius OB Association. AJ, 117:2381–2397, 1999.

T. Preibisch and H. Zinnecker. Sequentially triggered star formation in OB associations. In B. G. Elmegreen and J. Palous, editors, *Triggered Star Formation in a Turbulent ISM*, volume 237 of *IAU Symposium*, pages 270–277, 2007.

T. Preibisch, A. G. A. Brown, T. Bridges, E. Guenther, and H. Zinnecker. Exploring the Full Stellar Population of the Upper Scorpius OB Association. AJ, 124:404–416, 2002.

A. Rivera-Ingraham, P. G. Martin, D. Polychroni, F. Motte, N. Schneider, S. Bontemps, M. Hennemann, A. Men'shchikov, Q. Nguyen Luong, P. André, D. Arzoumanian, J.-P. Bernard, J. Di Francesco, D. Elia, C. Fallscheer, T. Hill, J. Z. Li, V. Minier, S. Pezzuto, A. Roy, K. L. J. Rygl, S. I. Sadavoy, L. Spinoglio, G. J. White, and C. D. Wilson. Herschel Observations of the W3 GMC: Clues to the Formation of Clusters of High-mass Stars. ApJ, 766:85, 2013.

H. Rogers and J. M. Pittard. Feedback from winds and supernovae in massive stellar clusters - I. Hydrodynamics. MNRAS, 431:1337–1351, 2013.

J. Roman-Duval, J. M. Jackson, M. Heyer, J. Rathborne, and R. Simon. Physical Properties and Galactic Distribution of Molecular Clouds Identified in the Galactic Ring Survey. ApJ, 723:492–507, 2010.

D. Ryu and E. T. Vishniac. The growth of linear perturbations of adiabatic shock waves. ApJ, 313:820–841, 1987.

J. K. Salmon and M. S. Warren. Skeletons from the treecode closet. *Journal of Computational Physics*, 111:136–155, 1994.

E. E. Salpeter. The Luminosity Function and Stellar Evolution. ApJ, 121:161, 1955.

J. Scalo. The IMF Revisited: A Case for Variations. In G. Gilmore and D. Howell, editors, *The Stellar Initial Mass Function (38th Herstmonceux Conference)*, volume 142 of *Astronomical Society of the Pacific Conference Series*, page 201, 1998.

N. Z. Scoville and D. B. Sanders. H2 in the Galaxy. In D. J. Hollenbach and H. A. Thronson, Jr., editors, *Interstellar Processes*, volume 134 of *Astrophysics and Space Science Library*, pages 21–50, 1987.

L. I. Sedov. *Similarity and Dimensional Methods in Mechanics*. 1959.

F. H. Shu, F. C. Adams, and S. Lizano. Star formation in molecular clouds - Observation and theory. ARA&A, 25:23–81, 1987.

R. Simon. Gravitational instability in the isothermal stratified nebula. *Annales d'Astrophysique*, 28:40, 1965.

R. J. Simpson, M. S. Povich, S. Kendrew, C. J. Lintott, E. Bressert, K. Arvidsson, C. Cyganowski, S. Maddison, K. Schawinski, R. Sherman, A. M. Smith, and G. Wolf-Chase. The Milky Way Project First Data Release: a bubblier Galactic disc. MNRAS, 424:2442–2460, 2012.

C. L. Slesnick, L. A. Hillenbrand, and J. M. Carpenter. A Large-Area Search for Low-Mass Objects in Upper Scorpius. II. Age and Mass Distributions. ApJ, 688:377-397, 2008.

N. Smith. A census of the Carina Nebula - I. Cumulative energy input from massive stars. MNRAS, 367:763–772, 2006.

P. M. Solomon, A. R. Rivolo, J. Barrett, and A. Yahil. Mass, luminosity, and line width relations of Galactic molecular clouds. ApJ, 319:730–741, 1987.

L. Spitzer. *Physical processes in the interstellar medium.* 1978.

L. Spitzer, Jr. The Dynamics of the Interstellar Medium. III. Galactic Distribution. ApJ, 95:329, 1942.

V. Springel. The cosmological simulation code GADGET-2. MNRAS, 364:1105–1134, 2005.

S. W. Stahler and F. Palla. *The Formation of Stars.* 2005.

G. Strang. On the Construction and Comparison of Difference Schemes. *SIAM Journal on Numerical Analysis*, 5:506–517, 1968.

J. C. Tan, M. T. Beltrán, P. Caselli, F. Fontani, A. Fuente, M. R. Krumholz, C. F. McKee, and A. Stolte. Massive Star Formation. *Protostars and Planets VI*, pages 149–172, 2014.

G. Tenorio-Tagle. The gas dynamics of H II regions. I - The champagne model. A&A, 71:59–65, 1979.

M. A. Thompson, J. S. Urquhart, T. J. T. Moore, and L. K. Morgan. The statistics of triggered star formation: an overdensity of massive young stellar objects around Spitzer bubbles. MNRAS, 421:408–418, 2012.

R. I. Thompson. Lyman and Balmer continuum ionization in zero-age main-sequence stas - Applications to the line excess phenomenon. ApJ, 283:165–168, 1984.

J. K. Truelove, R. I. Klein, C. F. McKee, J. H. Holliman, II, L. H. Howell, and J. A. Greenough. The Jeans Condition: A New Constraint on Spatial Resolution in Simulations of Isothermal Self-gravitational Hydrodynamics. ApJ, 489:L179–L183, 1997.

S. Van Loo, E. Keto, and Q. Zhang. Core and Filament Formation in Magnetized, Self-gravitating Isothermal Layers. ApJ, 789:37, 2014.

E. Vázquez-Semadeni, G. C. Gómez, A. K. Jappsen, J. Ballesteros-Paredes, R. F. González, and R. S. Klessen. Molecular Cloud Evolution. II. From Cloud Formation to the Early Stages of Star Formation in Decaying Conditions. ApJ, 657:870–883, 2007.

E. T. Vishniac. The dynamic and gravitational instabilities of spherical shocks. ApJ, 274:152–167, 1983.

E. T. Vishniac. Nonlinear instabilities in shock-bounded slabs. ApJ, 428:186–208, 1994.

E. T. Vishniac and D. Ryu. On the stability of decelerating shocks. ApJ, 337: 917–926, 1989.

S. Walch and T. Naab. The energy and momentum input of supernova explosions in structured and ionized molecular clouds. MNRAS, 451:2757–2771, 2015.

S. Walch, P. Girichidis, T. Naab, A. Gatto, S. C. O. Glover, R. Wünsch, R. S. Klessen, P. C. Clark, T. Peters, D. Derigs, and C. Baczynski. The SILCC (SImulating the LifeCycle of molecular Clouds) project - I. Chemical evolution of the supernova-driven ISM. MNRAS, 454:238–268, 2015a.

S. Walch, A. P. Whitworth, T. G. Bisbas, D. A. Hubber, and R. Wünsch. Comparing simulations of ionization triggered star formation and observations in RCW 120. MNRAS, 452:2794–2803, 2015b.

S. K. Walch, A. P. Whitworth, T. Bisbas, R. Wünsch, and D. Hubber. Dispersal of molecular clouds by ionizing radiation. MNRAS, 427:625–636, 2012.

D. Ward-Thompson and A. P. Whitworth. *An Introduction to Star Formation.* 2011.

R. Weaver, R. McCray, J. Castor, P. Shapiro, and R. Moore. Interstellar bubbles. II - Structure and evolution. ApJ, 218:377–395, 1977.

B. C. Whitmore, R. Chandar, and S. M. Fall. Star Cluster Demographics. I. A General Framework and Application to the Antennae Galaxies. AJ, 133: 1067–1084, 2007.

A. Whitworth. The erosion and dispersal of massive molecular clouds by young stars. MNRAS, 186:59–67, 1979.

A. P. Whitworth, A. S. Bhattal, S. J. Chapman, M. J. Disney, and J. A. Turner. The Preferential Formation of High-Mass Stars in Shocked Interstellar Gas Layers. MNRAS, 268:291, 1994a.

A. P. Whitworth, A. S. Bhattal, S. J. Chapman, M. J. Disney, and J. A. Turner. The Preferential Formation of High-Mass Stars in Shocked Interstellar Gas Layers. MNRAS, 268:291, 1994b.

D. O. S. Wood and E. Churchwell. The morphologies and physical properties of ultracompact H II regions. ApJS, 69:831–895, 1989.

P. Woodward and P. Colella. The numerical simulation of two-dimensional fluid flow with strong shocks. *Journal of Computational Physics*, 54:115–173, 1984.

R. Wünsch and J. Palouš. Gravitational instability of expanding shells. Solution with nonlinear terms. A&A, 374:746–755, 2001.

R. Wünsch, J. E. Dale, J. Palouš, and A. P. Whitworth. The fragmentation of expanding shells - II. Thickness matters. MNRAS, 407:1963–1971, 2010.

H. W. Yorke and C. Sonnhalter. On the Formation of Massive Stars. ApJ, 569: 846–862, 2002.

A. Zavagno, L. Deharveng, F. Comerón, J. Brand, F. Massi, J. Caplan, and D. Russeil. Triggered massive-star formation on the borders of Galactic H II regions. II. Evidence for the collect and collapse process around RCW 79. A&A, 446:171–184, 2006.

H. Zinnecker and H. W. Yorke. Toward Understanding Massive Star Formation. ARA&A, 45:481–563, 2007.

List of Figures

List of Tables

List of Abbreviations

BCs	boundary conditions
E78	dispersion relation proposed by Elmegreen & Elmegreen 1978
IMF	initial mass function
ISM	interstellar medium
MC	molecular cloud
PAGI	pressure assisted gravitational instability
SFE	star formation efficiency
V83	dispersion relation proposed by Vishniac 1983
W10	dispersion relation proposed by Wünsch et al. 2010

Attachments

Appendices

A Reprint of paper ”Fragmentation of vertically stratified gaseous layers: monolithic or coalescence-driven collapse”

The paper **Dinnbier, F.**, Wünsch, R., Whitworth, A. & Palouš: Fragmentation of vertically stratified gaseous layers: monolithic or coalescence-driven collapse. Accepted to MNRAS.

MNRAS Advance Access published December 23, 2016

Fragmentation of vertically stratified gaseous layers: monolithic or coalescence–driven collapse

František Dinnbier[1,2]⋆, Richard Wünsch[1], Anthony P. Whitworth[3] and Jan Palouš[1]
[1] *Astronomical Institute, Academy of Sciences of the Czech Republic, Boční II 1401, 141 00 Prague, Czech Republic*
[2] *Charles University in Prague, Faculty of Mathematics and Physics, V Holešovičkách 2, 180 00 Prague, Czech Republic*
[3] *School of Physics and Astronomy, Cardiff University, Cardiff CF24 3AA, Wales, UK*

Accepted 0000 December 15. Received 0000 December 14; in original form 0000 October 11

ABSTRACT

We investigate, using 3D hydrodynamic simulations, the fragmentation of pressure-confined, vertically stratified, self-gravitating gaseous layers. The confining pressure is either thermal pressure acting on both surfaces, or thermal pressure acting on one surface and ram-pressure on the other. In the linear regime of fragmentation, the dispersion relation we obtain agrees well with that derived by Elmegreen & Elmegreen (1978), and consequently deviates from the dispersion relations based on the thin shell approximation (Vishniac 1983) or pressure assisted gravitational instability (Wünsch et al. 2010). In the non-linear regime, the relative importance of the confining pressure to the self-gravity is a crucial parameter controlling the qualitative course of fragmentation. When confinement of the layer is dominated by external pressure, self-gravitating condensations are delivered by a two-stage process: first the layer fragments into gravitationally bound but stable clumps, and then these clumps coalesce until they assemble enough mass to collapse. In contrast, when external pressure makes a small contribution to confinement of the layer, the layer fragments monolithically into gravitationally unstable clumps and there is no coalescence. This dichotomy persists whether the external pressure is thermal or ram. We apply these results to fragments forming in a shell swept up by an expanding H II region, and find that, unless the swept up gas is quite hot or the surrounding medium has low density, the fragments have low-mass ($\lesssim 3\,\mathrm{M_\odot}$), and therefore they are unlikely to spawn stars that are sufficiently massive to promote sequential self-propagating star formation.

Key words: stars: formation – ISM: H II regions – ISM: kinematics and dynamics – Physical processes: instabilities – Physical processes: hydrodynamics – Physical processes: waves

1 INTRODUCTION

Massive stars ($M_\star \gtrsim 8\,\mathrm{M_\odot}$) strongly influence the interstellar medium (ISM) surrounding them, mainly via photoionisation, stellar winds and supernova explosions. Elmegreen & Lada (1977) propose a mechanism (*Collect and Collapse*) whereby an over-pressured H II region, driven by young massive stars, expands into dense molecular gas. The expansion induces a spherical shock, and the surrounding gas accumulates between the shock and the ionisation front. The resulting shell of cool gas increases in mass, and eventually fragments to form a new generation of stars. A crucial issue is the maximum mass of these newly formed stars. If some of them are sufficiently massive to excite a new H II region, the process can repeat recursively and star formation propagates itself sequentially. Otherwise, star formation is quenched. Various triggering mechanisms are discussed in Elmegreen (1998).

From an observational perspective, shells are common morphological structures in the ISM. Ehlerová & Palouš (2005) have detected more than 600 shells in H I . Churchwell et al. (2007) have identified 322 complete or partial rings in the infrared. Simpson et al. (2012) list more than 5000 infrared shells. Deharveng et al. (2010) find that at least 86% of the infrared shells identified by Churchwell et al. (2007) encircle H II regions ionised by O- and early B-type stars, suggesting that the shells are due to feedback from these stars. After a careful examination, Deharveng, Zavagno & Caplan (2005) find 17 infrared shells that are candidates for the *Collect and Collapse* mechanism. Evidence for propagating star formation has also been reported in significantly larger H I shells (Dawson et al. 2008, 2011; Egorov

---

⋆ E-mail:frantisek.dinnbier@asu.cas.cz

et al. 2014), indicating that feedback operates over a large range of scales. Further observational support for propagating star formation comes from age sequences of OB associations and star clusters in the vicinity of star forming regions e.g. (Blaauw 1964, 1991; Brown, de Geus & de Zeeuw 1994; Bik et al. 2010)

In order to estimate the properties of fragments condensing out of a swept up shell, Elmegreen & Elmegreen (1978, hereafter E78), Doroshkevich (1980) and Lubow & Pringle (1993) investigate the stability of a vertically resolved self–gravitating layer [1] , and derive a semi-analytical formula for the corresponding dispersion relation. Vishniac (1983, hereafter V83) derives the dispersion relation for a self–gravitating infinitesimally thin shell, and this has been used to estimate the properties of clumps condensing out of fragmenting shells. Whitworth et al. (1994a) and Elmegreen (1994) analyse the fragmentation of accreting shells, while Wünsch & Palouš (2001) consider non-accreting shells expanding into a vacuum.

These dispersion relations are based on linear perturbation theory, so they are relevant only as long as the perturbing amplitudes are small. Miyama, Narita & Hayashi (1987a,b) extend the linearised solution of Elmegreen & Elmegreen (1978) into the non-linear regime, by including second order terms. They find that a layer breaks into filaments that become increasingly slender with time. In contrast, Fuchs (1996) proposes that, in the non-linear regime, the fragments form a semi-regular hexagonal pattern on the surface of the layer.

In order to test the validity of these analytic derivations, Dale et al. (2009) obtain a dispersion relation, based on numerical simulations of expanding, non-accreting shells, confined by constant external pressure. They find significant differences between their dispersion relation and that of V83 (based on the thin shell approximation). In subsequent work, Wünsch et al. (2010, hereafter W10) explain the difference by modifying V83 to include the effect of pressure confinement. They call the mechanism underlying their dispersion relation *Pressure Assisted Gravitational Instability* (PAGI Wünsch et al. 2010). Since Dale et al. (2009) simulate fragmentation of a whole shell, and the shell gets thinner with increasing external pressure, they are only able to resolve shells which are confined by low to moderate values of the external pressure, and therefore the W10 dispersion relation is unverified in the case of high external pressure. However, it is in the limit of high external pressure that W10 differs substantially from E78. Van Loo, Keto & Zhang (2014) investigate self-gravitating layers permeated by magnetic fields and present a non-magnetic control run. Although their results differ from V83, they are in agreement with both E78 and W10, because their layer is confined by a very low external pressure. Iwasaki, Inutsuka & Tsuribe (2011b) also derive a numerical dispersion relation that differs significantly from that of V83.

Our main aims are to simulate the fragmentation of gaseous layers, in both the low and high ambient pressure cases, and to compare the results with the analytic or semi-analytic estimates derived in previous studies. This comparison addresses three issues: (i) dispersion relations in the linear regime of fragmentation; (ii) the elapsed time before the layer forms gravitationally bound fragments, and the resulting fragment masses; and (iii) the possibility that mode interaction leads to fragments distributed on a regular periodically repeating pattern. We study only a small square patch on the layer, so that we can attain good resolution in directions perpendicular to the layer, even when the layer is significantly compressed. In addition to layers confined from both sides by thermal pressure, we also simulate layers accreting onto one surface. We use these results to investigate the fragmentation of a shell driven by an expanding H II region — using an analytic solution to account for the expansion of the H II region — and contrast our results with those obtained analytically by Whitworth et al. (1994a), and by Iwasaki, Inutsuka & Tsuribe (2011b) who performed simulations with small perturbing amplitudes.

The paper is organised as follows. Section 2 reviews the most important properties of self–gravitating layers and the analytical estimates (E78, V83, W10) of the dispersion relations. These estimates are used for comparison with the numerical results. Section 3 describes applied numerical methods and initial conditions. Section 4 describes simulations of layers confined on both sides by thermal pressure (due to a very hot rarefied gas), and seeded with monochromatic perturbations. Section 5 describes simulations of layers confined on both sides by thermal pressure, and seeded with polychromatic perturbations. Section 6 describes simulations in which we explore whether fragments forming in layers tend to be arranged into regular patterns. Section 7 describes simulations of layers in which one side is confined by thermal pressure and the other by the ram pressure of a homogeneous plane-parallel inflow. Section 8 considers an H II region expanding into a homogeneous medium, and estimates the time at which the swept up shell fragments, and the properties of the fragments. Section 9 discusses the results, and Section 10 summarises our main conclusions. Appendix A describes our algorithm developed for finding gravitationally bound fragments.

2 LINEARISED THEORY OF LAYER FRAGMENTATION

2.1 The unperturbed state

Before introducing the dispersion relations describing the growth rate of perturbations in the self-gravitating presure-confined layer, we review the unperturbed configuration. The model is also used to generate the initial conditions for our simulations.

We assume that the layer is initially in plane-parallel stratified hydrostatic equilibrium, i.e. it is infinite in the x and y directions, its normal points in the z direction, and all quantities are functions of z only. The layer is isothermal with sound speed $c_{\rm S}$, so the density distribution is as derived

---

[1] We distinguish a *layer*, which ideally is plane-parallel stratified, from a *shell*, which ideally is part, or the whole, of a hollow spherically symmetric structure. Although most of the observations motivating this work concern shells, the configurations we simulate in this paper are layers. Then we apply results derived for layers in the analysis of star formation triggered by expanding H II regions — so in that analysis we also use the term shell, because the spatial curvature and velocity divergence of the shell can be neglected.

by Spitzer (1942) and Goldreich & Lynden-Bell (1965), i.e.

$$\rho(z) = \frac{\rho_{\mathrm{O}}}{\cosh^2(z/H_{\mathrm{O}})}, \tag{1}$$

where ρ_{O} is the density on the midplane ($z\!=\!0$),

$$H_{\mathrm{O}} = \frac{c_{\mathrm{S}}}{\sqrt{2\pi G\rho_{\mathrm{O}}}}, \tag{2}$$

is the vertical scale height, and G is the gravitational constant. The surfaces of the layer are at $z\!=\!\pm z_{\mathrm{MAX}}$, and outside this ($|z| > z_{\mathrm{MAX}}$) there is a hot gas with negligible density which exerts an external pressure P_{EXT}.

The layer is fully characterised by P_{EXT}, c_{S} and its surface density Σ_{O}. A dimensionless parameter constructed from these quantities (Elmegreen & Elmegreen 1978),

$$A = \frac{1}{\sqrt{1+\left(2P_{\mathrm{EXT}}/\pi G\Sigma_{\mathrm{O}}^2\right)}}\,, \tag{3}$$

reflects the relative importance of self-gravity and external pressure in holding the layer together. Parameter A increases monotonically from nearly 0 (external pressure dominated; $P_{\mathrm{EXT}} \gg G\Sigma_{\mathrm{O}}^2$) to 1 (self–gravity dominated).

From pressure equilibrium at the surfaces, $P_{\mathrm{EXT}} = \rho(z_{\mathrm{MAX}})c_{\mathrm{S}}^2$, it follows

$$z_{\mathrm{MAX}} = H_{\mathrm{O}}\mathrm{arcosh}^{-1}\left(\frac{\rho_{\mathrm{O}}c_{\mathrm{S}}^2}{P_{\mathrm{EXT}}}\right) = H_{\mathrm{O}}\mathrm{arcosh}^{-1}\left(\frac{1}{\sqrt{1-A^2}}\right). \tag{4}$$

Half–thickness of a stratified layer is defined by $H_{\mathrm{HT}} \equiv \Sigma_{\mathrm{O}}/(2\rho_{\mathrm{O}})$. Equations (3), (1) and (2) then yield

$$H_{\mathrm{HT}} = \frac{\Sigma_{\mathrm{O}}c_{\mathrm{S}}^2}{2P_{\mathrm{EXT}}+\pi G\Sigma_{\mathrm{O}}^2} = \frac{c_{\mathrm{S}}^2A^2}{\pi G\Sigma_{\mathrm{O}}}\,, \tag{5}$$

and the midplane density, ρ_{O}, depends on Σ_{O} as

$$\rho_{\mathrm{O}} = \frac{2P_{\mathrm{EXT}}+\pi G\Sigma_{\mathrm{O}}^2}{2c_{\mathrm{S}}^2} = \frac{\pi G\Sigma_{\mathrm{O}}^2}{2c_{\mathrm{S}}^2A^2}. \tag{6}$$

Pressure dominated layers are of almost uniform density ($z_{\mathrm{MAX}} \simeq H_{\mathrm{HT}}$), while self–gravity dominated layers have a pronounced density maximum on the midplane ($z_{\mathrm{MAX}} \gg H_{\mathrm{HT}}$).

2.2 Analytical estimates of the dispersion relation

In this section, we review and compare the assumptions underlying the dispersion relations derived by E78, V83 and W10. To simplify the discussion, we neglect the effects of shell curvature and velocity divergence, by setting the shell radius to infinity. The results are therefore applicable to a plane–parallel layer, and can also be applied to a shell, as long as the unstable wavelengths are much shorter than the radius of the shell.

The dispersion relation gives the perturbation growth rate $\boldsymbol{\omega}$ as a function of wavenumber k. In planar geometry, and for the dispersion relations in question, $\boldsymbol{\omega}$ is either purely real or purely imaginary. In this paper, we adopt the convention that growing instability is described by the positive real part of $\boldsymbol{\omega}$, which we denote for simplicity ω, and we omit the oscillating imaginary part. The characteristic timescale of perturbation growth, its e–folding time, is defined as $t_{\mathrm{EFOLD}} = 1/\omega$.

For all the dispersion relations in question, there is a finite range of unstable wavenumbers $(0, k_{\mathrm{MAX}})$, where k_{MAX} is the highest unstable wavenumber. The maximum growth rate ω_{FAST} is attained for wavenumber k_{FAST} which is always approximately $k_{\mathrm{MAX}}/2$. The wavelengths corresponding to k_{MAX} and k_{FAST} are denoted λ_{MAX} and λ_{FAST}, respectively. When describing a particular analytical estimate of the dispersion relation, the subscript begins with its name, e.g. $k_{\mathrm{E78.FAST}}$ is the wavelength k_{FAST} for E78. The abbreviations E78, V83 and W10 refer to the particular dispersion relation, not to the paper where they are firstly described. The unstable branches of the dispersion relations for both self–gravity ($A = 0.99$) and external pressure dominated ($A = 0.18$) layers are shown in the right column of Fig. 2.

2.2.1 Dispersion relation for the thin shell approximation

To estimate the dispersion relation of an expanding shell, Vishniac (1983) reduce the problem to two dimensions by integrating the continuity, Euler, and Poisson's equation through the thickness of the shell. In planar geometry, the thin shell dispersion relation becomes

$$\boldsymbol{\omega}_{\mathrm{V83}}^2(k) = 2\pi G\Sigma_{\mathrm{O}}k - c_{\mathrm{S}}^2k^2. \tag{7}$$

The stability of modes is determined by the imbalance between self-gravity and internal pressure gradient, and there is no contribution from external pressure.

2.2.2 Dispersion relation for pressure assisted gravitational instability

In order to evaluate the influence of external pressure, Wünsch et al. (2010) investigate perturbations with the form of an oblate spheroid, embedded in a layer. The spheroid is homogeneous and confined by external pressure P_{EXT}. Its semi-major axis is r, its semi-minor axis is the layer's half-thickness, H_{HT}, and its total mass is M. Radial excursion of an element on the equator of the spheroid is regulated by the equation of motion

$$\begin{aligned}\ddot{r} \;\; = \;\; & -\frac{3GM}{2r^2}\left\{\frac{\cos^{-1}(H_{\mathrm{HT}}/r)}{(1-(H_{\mathrm{HT}}/r)^2)^{3/2}} - \frac{H_{\mathrm{HT}}/r}{1-(H_{\mathrm{HT}}/r)^2}\right\} \\ & -\frac{20\pi r H_{\mathrm{HT}}P_{\mathrm{EXT}}}{3M} + \frac{5c_{\mathrm{S}}^2}{r}\end{aligned} \tag{8}$$

(Boyd & Whitworth 2005).

Wünsch et al. (2010) equate the instability growth rate to the radial contraction rate of the spheroid. Collapse from radius r_{O}, by a small factor ϵ to radius $(1-\epsilon)r_{\mathrm{O}}$, in time t_ϵ, fulfils $(\epsilon-1)r_{\mathrm{O}} = \dot{r}_{\mathrm{O}}t_\epsilon + \frac{1}{2}\ddot{r}_{\mathrm{O}}t_\epsilon^2$. Using $\boldsymbol{\omega} = 1/t_\epsilon$ and $r = \lambda/2 = \pi/k$, this yields

$$\begin{aligned}\boldsymbol{\omega}_{\mathrm{W10}}^2(k) \;\; & = \;\; -\frac{\ddot{r}_{\mathrm{O}}}{2\epsilon r_{\mathrm{O}}} \\ & = \;\; \frac{1}{\epsilon}\Bigg\{-\frac{5c_{\mathrm{S}}^2k^2}{2\pi^2} \\ & \quad +\frac{3G\Sigma_{\mathrm{O}}k}{4}\left(\frac{\cos^{-1}(kH_{\mathrm{HT}}/\pi)-\sqrt{k^2H_{\mathrm{HT}}^2/\pi^2-1}}{(1-k^2H_{\mathrm{HT}}^2/\pi^2)^{3/2}}\right) \\ & \quad +\frac{10P_{\mathrm{EXT}}c_{\mathrm{S}}^2k^2}{3\pi^2(2P_{\mathrm{EXT}}+\pi G\Sigma_{\mathrm{O}}^2)}\Bigg\}.\end{aligned} \tag{9}$$

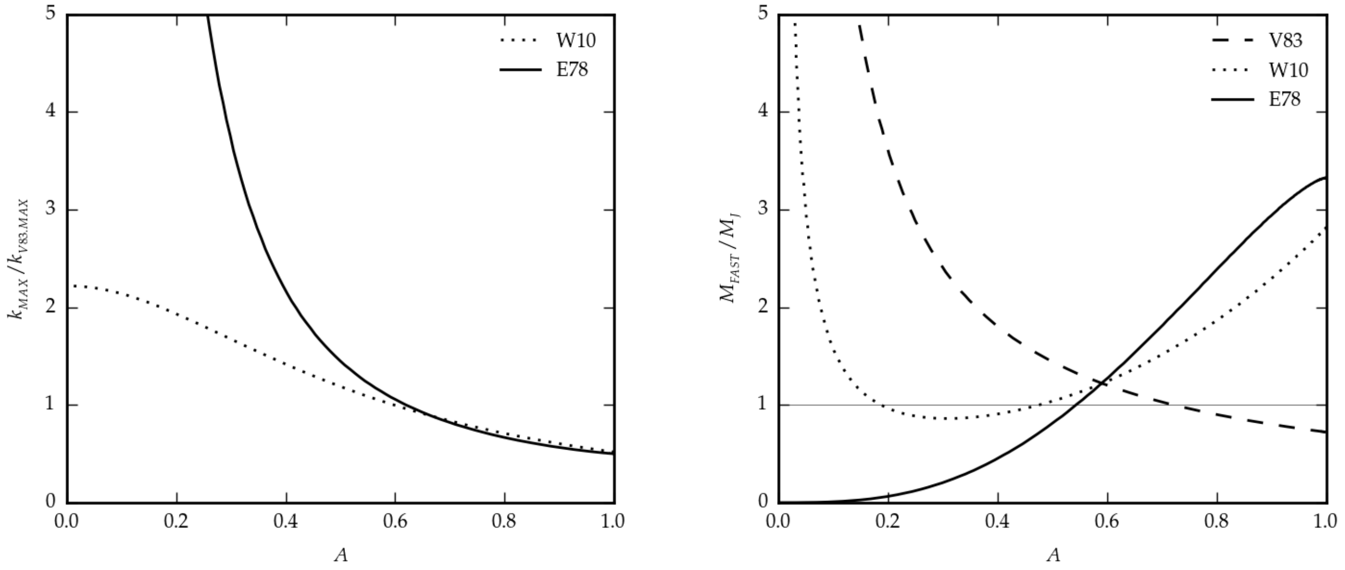

Figure 1. Comparison between the dispersion relations derived by E78, V83 and W10, as a function of A. LEFT PANEL: the marginally stable wavenumber $k_{\rm MAX}$, for E78 and W10, normalised to $k_{\rm V83.MAX}$. RIGHT PANEL: Mass of the fragment with the highest growth rate, $M_{\rm FAST}$, normalised to the midplane Jeans mass, $M_{\rm J}$. Fragments formed with mass below $\sim M_{\rm J}$ (thin line) are gravitationally stable.

The terms on the right hand side of Eq. (9) represent the gradient of internal pressure (second line), self-gravity (third line), and confinement by external pressure (fourth line). Wünsch et al. (2010) suggest setting $\epsilon \sim 0.1$, but, although ϵ affects the magnitude of $\boldsymbol{\omega}_{\rm W10}$, it does not influence the range of unstable wave-numbers.

2.2.3 Dispersion relation for a vertically stratified layer

Elmegreen & Elmegreen (1978) obtain the dispersion relation for a self-gravitating, pressure confined, semi-inifinite layer in hydrostatic equilibrium by solving the system of perturbed continuity, Euler and Poisson equations. Kim et al. (2012) revisit their study and offer an additional insight. According to Kim et al. (2012), the dispersion relation can be written

$$\boldsymbol{\omega}_{\rm E78}^2 = 2\pi G\Sigma_{\rm O} k(\eta F_{\rm J} + (1-\eta)F_{\rm D}) - c_{\rm EFF}^2 k^2 \,. \tag{10}$$

Here $c_{\rm EFF}$ is the effective sound speed. $F_{\rm J}$ and $F_{\rm D}$ are reduction factors for self-gravity. Parameter η is the fraction of the perturbed surface density that is attributable to compression of material near the centre of a proto-fragment (and hence near the mid-plane of the layer). The rest of the perturbed surface density is due to corrugations on the surface of the layer. Thus η controls the relative importance of compressional and surface-gravity waves. The former are important in self–gravity dominated layers, while the latter are important in pressure dominated layers. $c_{\rm EFF}$, η, $F_{\rm J}$ and $F_{\rm D}$ are complicated functions of k, which can not generally be expressed in closed form.

The growth rate $\omega_{\rm E78.FAST}$ of the most unstable wavenumber $k_{\rm E78.FAST}$ in the limit $A \to 0$ (layers dominated by external pressure) is (eq. (47) in Kim et al. (2012))

$$\omega_{\rm E78.FAST}^2 = 0.276 \times 2\pi G\rho_{\rm O} = 0.276 \left(\frac{\pi G\Sigma_{\rm O}}{c_{\rm S} A}\right)^2 . \tag{11}$$

2.2.4 Comparison between the analytical estimates of the dispersion relation

The left panel of Figure 1 shows the dependence of $k_{\rm MAX}$ normalised to $k_{\rm V83.MAX}$ on parameter A for different dispersion relations. For self–gravity dominated layers, both W10 and E78 predict almost identical ranges of unstable wavenumbers ($k_{\rm E78.MAX}/k_{\rm W10.MAX} \to 0.966$ as $A \to 1$), but V83 predicts a broader range with $k_{\rm W10.MAX}/k_{\rm V83.MAX} \to 0.518$. With increasing external pressure (decreasing A), the difference between E78 and V83 diminishes. However, when $A \lesssim 0.5$, E78 extends to much higher wavenumbers, indicating that shorter wavelengths are unstable. And, as $A \to 0$, W10 and E78 have different limiting behaviour: $k_{\rm W10.MAX}$ tends to a constant ($k_{\rm W10.MAX}/k_{\rm V83.MAX} \to 2.216$), whereas $k_{\rm E78.MAX} \propto H_{\rm HT}^{-1} \propto A^{-2}$.

Since the wavelength $\lambda_{\rm FAST}$ has the highest growth rate, we assume that the fragment mass $M_{\rm FAST}$ is approximately the mass confined inside a circle of radius $\lambda_{\rm FAST}/2$, i.e. $M_{\rm FAST} = \pi\Sigma_{\rm O}(\lambda_{\rm FAST}/2)^2 = \pi\Sigma_{\rm O}(\pi/k_{\rm FAST})^2$. Masses $M_{\rm FAST}$ normalised to the midplane Jeans mass $M_{\rm J}$ are plotted in the right panel of Fig. 1. V83 and W10 predict that when formed, the fragments are already gravitationally unstable ($M_{\rm FAST}/M_{\rm J} \gtrsim 1$) for any A. On the other hand, E78 predicts gravitationally unstable fragments only when $A \gtrsim 0.5$. According to E78, the layer breaks into gravitationally stable fragments for lower values of A, thus predicting qualitatively different scenario than V83 and W10. We simulate and discuss evolution of pressure dominated layers (low A) in Sections 5.3 and 9.1.

3 METHODS AND INITIAL CONDITIONS

3.1 Numerics

All the hydrodynamic simulations presented in the paper are performed with the MPI-parallelised FLASH4.0 code (Fryxell et al. 2000). FLASH is an AMR code based on the PARAMESH library (MacNeice et al. 2000). The hydrodynamic equations are solved by the piecewise parabolic method (Colella & Woodward 1984).

Self-gravity is calculated using an octal tree code (Wünsch et al. in preparation) which offers three acceptance criteria for interaction between the target point (where the acceleration is evaluated) and a node (the source of the gravitational force):

(i) The algorithm invented by Barnes & Hut (1986), which accepts nodes seen from the target point at an angle smaller than a specified value. This algorithm is purely geometric since it does not take into account distribution of mass inside nodes, or their relative contribution to the net gravitational force.

(ii) A set of criteria using the node size, mass and optionally higher multipole moments of the mass distribution within the node. They either estimate the upper limit on the acceleration error of the cell-node interaction $\Delta a^{\max}$ from Equation 9 of Salmon & Warren (1994), or they use the approximation by Springel (2005),

$$\Delta a^{\max}_{(\mathrm{p})} = \frac{GM}{d^2}\left(\frac{h}{d}\right)^{p+1}, \tag{12}$$

where M and h are the node mass and size, respectively, d is the distance between the cell and the node mass centre, and p is the order of the multipole expansion.

(iii) An experimental implementation of the "sumsquare" criterion of Salmon & Warren (1994), which controls the sum of all errors origination from all individual node contributions.

We invoke the criterion (ii) with Equation (12) and $p = 1$ in all our simulations because our tests show that it provides the best compromise between the code performance and accuracy.

We convert dense gaseous condensations into sink particles according to conditions described in Federrath et al. (2010). To create a sink particle inside a particular cell, all following conditions must be fulfilled:

(i) the cell is at the highest refinement level,
(ii) the cell contains minimum of gravitational potential,
(iii) all the gas inside a sphere of accretion radius r_{ACC} centered at the cell is above a specified density threshold,
(iv) the gas inside the sphere is gravitationally bound, Jeans-unstable and converging,
(v) radius r_{ACC} of the sink particle would not overlap with accretion radius of an already existing sink particle.

Following (Federrath et al. 2010), we set the accretion radius to 2.5 grid cell size at the highest refinement level.

All the simulations have mixed boundary conditions (BCs) for self-gravity, i.e. periodic in the two directions x, y parallel to the layer, and isolated in the third direction z perpendicular to the layer. In order to calculate the gravitational field in this configuration, it is natural to seek for a modification of the standard Ewald method (Ewald 1921; Klessen 1997). By computing the appropriate limit of the standard Ewald method, we find formulae for the gravitational acceleration and potential in closed form for a configuration with mixed BCs; the derivation is described in (Wünsch et al. in preparation). The modification is used to calculate the gravitational field in the simulations presented here.

The hydrodynamic BCs are periodic in the x and y directions, and reflecting in the z direction for all but accreting simulations. For accreting simulations, the BCs are inflow from the top of the computational domain, and diode from the bottom to prevent reflections of waves.

The column density needed for cooling the warm ambient gas intermixed with the cold layer during accreting runs (see Section 3.3 for details) is calculated using module `TreeRay/OpticalDepth` of the tree code.

The grid cells are cubic in all the simulations. The half-thickness of the layer (H_{HT}; see Eqn. 5 below), is always at least four grid cells (see Tables 1 to 5). Consequently, the Jeans length is always resolved by more than four grid cells, and the simulations satisfy the criterion for avoiding artificial gravitational fragmentation, as given by Truelove et al. (1997). We have performed successful convergence tests throughout the range of conditions simulated. We have also checked that the portion of the layer inside the computational domain is sufficiently large, i.e. that the periodic copies in the x and y directions do not significantly influence the properties of fragments.

3.2 Initial conditions for the layer

Each model starts with a layer with properties described in Section 2.1 seeded with a perturbation. The perturbation is either a single mode given by the eigenfunction for acoustic-surface-gravity modes or white noise. The exact form of the perturbation is described at the beginning of a corresponding Section (4 to 7).

Particular values for the layer parameters are adopted from Iwasaki, Inutsuka & Tsuribe (2011b) who investigate an H II region excited by a $41\,\mathrm{M}_{\odot}$ star, expanding into a medium with number density $n = 10^3\,\mathrm{cm}^{-3}$. At time $t = 0.81\,\mathrm{Myr}$, the shell has radius $R = 3.86\,\mathrm{pc}$, and surface density $\Sigma_{\mathrm{O}} = 0.0068\,\mathrm{g\,cm}^{-2}$. We use this value of Σ_{O} for the initial conditions of all the simulations presented here, and vary A by changing P_{EXT}. However, we note that the model is sufficiently simple that its physical parameters, $(\Sigma_{\mathrm{O}}, c_{\mathrm{S}}, P_{\mathrm{EXT}})$, can be rescaled arbitrarily, as long as A is unchanged, i.e. $P_{\mathrm{EXT}} \propto \Sigma_{\mathrm{O}}^2$.

The sound velocity, c_{S}, is related to the temperature T by the ideal gas law $c_{\mathrm{S}}^2 = \gamma R_{gas} T/\mu$, where γ is the effective barotropic exponent, R_{gas} is the ideal gas constant, and μ is the mean molecular weight. Inside the layer, we set $\gamma = 1.0001$ (effectively isothermal, $\gamma = 1.0$ is excluded with the adopted numerical scheme) $\mu = 2$ (pure molecular hydrogen), and $T = 10\,\mathrm{K}$.

3.3 The external medium

We use two different kinds of the layer confinement: in Sections 4, 5 and 6, we investigate layers confined with thermal pressure from both surfaces; in Section 7, we investigate layers confined with the ram pressure from one surface, and with thermal pressure from the other.

The medium imposing the thermal pressure is implemented as follows. In order to compare our simulations with the analytic theory, it is necessary that the ambient medium has no dynamical influence on the layer, apart from exerting the thermal pressure. By means of convergence tests we establish that this can be achieved by setting $\rho_{\rm AMB}(z_{\rm MAX}) \lesssim 10^{-2}\rho_{\rm O}$. In addition, to diminish the influence of sound waves reflection from borders of the computational domain, we extend the computational domain to $\sim \pm 3z_{\rm MAX}$. Therefore, we set the ambient medium to be isothermal with temperature $T_{\rm AMB} = 300\,{\rm K}$ and mean molecular weight $\mu_{\rm AMB} = 0.6$. To prevent the ambient medium from falling on the layer, we set its density profile close to the hydrostatic equilibrium, i.e.

$$\begin{aligned}\rho_{\rm AMB}(z) &= \rho_{\rm AMB}(z_{\rm MAX}) \times \\ &\exp\left(-\frac{2\pi G\Sigma_0\mu_{\rm AMB}(|z| - z_{\rm MAX})}{R_{gas}T_{\rm AMB}}\right). \end{aligned} \tag{13}$$

In the case of accreting layers, ram pressure is realised by supersonic accretion of gas with uniform density $\rho_{\rm ACC}$, temperature $T_{\rm ACC}$ and sound velocity $c_{\rm ACC}$. The gas impacts at velocity $v_{\rm ACC}$ (and hence Mach number $\mathscr{M} = v_{\rm ACC}/c_{\rm S}$) onto the upper surface of the layer at $z \simeq z_{\rm MAX}$. The accreted gas is cold and molecular and the shock is isothermal, i.e. $T_{\rm ACC} = T$ and $c_{\rm ACC} = c_{\rm S}$. The bottom surface at $z \simeq -z_{\rm MAX}$ is confined by the ambient medium at temperature $T_{\rm AMB}$, $T_{\rm AMB} \gg T$ exerting the thermal pressure on the layer. To prevent the layer from bulk acceleration, we set the pressures acting on both surfaces to be equal, i.e. $\rho_{\rm ACC}(v_{\rm ACC}^2 + c_{\rm ACC}^2) = \rho_{\rm AMB}c_{\rm AMB}^2$.

The accretion leads to large scale flows inside the layer (see Section 7.2 and Fig. 9), which mix the layer with the warmer ambient medium. Consequently, if cooling were not implemented, the temperature of the layer would increase and the layer would thicken. This is a spurious behaviour which we suppress because a real layer would quickly cool to temperature T.

To keep the layer at constant temperature, we need to distinguish it from the warm ambient medium. We detect the layer according to the surface density σ calculated from the bottom side $z_{\rm BOT}$ of the computational domain

$$\sigma(z) = \int\limits_{z_{\rm BOT}}^{z} \rho(z')\,dz'\,. \tag{14}$$

We cool to temperature T any cell with the column density above threshold $\sigma_{\rm CRIT}$. We set $\sigma_{\rm CRIT} = 2\int\limits_{z_{\rm BOT}}^{-z_{\rm MAX}} \rho_{\rm AMB}(z')\,dz'$ to enable the layer to freely ripple. The layer detection is sensitive because the total column density of the ambient medium is of the order of the column density of one cell inside the layer, so $\sigma(z)$ rises steeply once z enters the layer.

Although most of the mass delivered to the layer comes from the accreted medium, the intermixing consumes a significant amount of the warm ambient medium. To prevent the ambient medium from being exhausted in the course of a simulation, we continuously replenish gas at temperature $T_{\rm AMB}$ through the bottom boundary of the computational domain, so that the total mass of ambient gas remains constant. The fresh ambient gas moves towards the layer and induces two artificial effects: a small ram pressure acting on the contact discontinuity and an increase of layer surface density Σ. We discuss the influence of the ram pressure at the end of Section 7.3 and show that it is not important.

4 LAYERS CONFINED BY THERMAL PRESSURE WITH MONOCHROMATIC PERTURBATIONS

In this section, we test the dispersion relations by comparing them to simulations. We study two extreme cases of pressure confinement: self–gravity dominated with $A = 0.99$ and external pressure dominated with $A = 0.18$. The applied perturbation is of a single wavelength (monochromatic).

Since the analytical estimates are based on linearised equations, they are valid only as long as the perturbing amplitude q_1 of any quantity is smaller than its unperturbed value $q_{\rm O}$. Accordingly, we define the linear regime of fragmentation if the maximum of the perturbed surface density Σ_1 is smaller than $\Sigma_{\rm O}$ and the non–linear regime otherwise. The dispersion relation can be determined only in the linear part of the fragmenting process.

The generic name of a monochromatic simulation is in the form M<A>_<$kH_{\rm HT}$>, where the first two numbers after "M" represent the value of parameter A and the numbers after the underscore the perturbing wavenumber in the dimensionless form $kH_{\rm HT}$. Thus, for example, simulation M18_020 treats a layer with $A = 0.18$, and initial monochromatic perturbation $kH_{\rm HT} = 0.20$.

4.1 Initial conditions for perturbations

The initial monochromatic perturbation for a layer confined by thermal pressure corresponds to the eigenfunction for acoustic–surface–gravity modes of a thick layer with freely moving surfaces (see eqs. (20) – (23) in Kim et al. (2012)). The initial amplitude of perturbed surface density is $\Sigma_1(0) = 0.01\Sigma_{\rm O}$. The length of the computational domain in direction x is equal to one perturbing wavelength.

4.2 The dispersion relation

Simulations for the external pressure dominated layer ($A = 0.18$, models M18) are listed in Table 1. Upper left panel of Figure 2 shows evolution of surface density perturbations for selected modes. Since a small perturbing amplitude in the surface density behaves as $\Sigma_1(t) = \Sigma_1(0)e^{i\omega t}$, the instantaneous growth rate ω equals to the slope of the curves shown in the upper left panel of Fig. 2. ω is almost time independent throughout the simulations. Modes with $kH_{\rm HT} \lesssim 0.65$ are unstable and grow, modes with $kH_{\rm HT} \gtrsim 0.65$ are stable. We measure ω by linear fit to $\ln(\Sigma_1/\Sigma_1(0))$ over time interval $t_{\rm O}^{fit}$, t_1^{fit}. The starting time $t_{\rm O}^{fit}$ is determined so as to suppress the influence of the initial conditions (which are exactly that of E78 eigenvectors). We suppose that the initial growth rate should be significantly altered at the timescale of sound crossing time through one half of the wavelength, i.e. $\simeq \pi H_{\rm HT}/c_{\rm S}$ (we use $t_{\rm O}^{fit} = 0.1\,{\rm Myr}$). The upper bound t_1^{fit} is constrained by the condition for the perturbation to

Run	A	$n_x \times n_y \times n_z$	H_{HT}/dz	kH_{HT}	$t_{\mathrm{E78}}^{\mathrm{EFOLD}}$ [Myr]	t_{NUM} [Myr]
M18_020	0.18	640 × 128 × 128	20.2	0.20	0.16	0.16
M18_025	0.18	512 × 128 × 128	20.2	0.25	0.15	0.16
M18_033	0.18	384 × 128 × 128	20.2	0.33	0.15	0.16
M18_050	0.18	256 × 128 × 128	20.2	0.50	0.19	0.19
M18_062	0.18	208 × 128 × 128	20.2	0.62	0.41	0.41
M18_073	0.18	176 × 128 × 128	20.2	0.73	-	-
M18_089	0.18	144 × 128 × 128	20.2	0.89	-	-
M99_025	0.99	512 × 128 × 128	20.2	0.25	0.74	0.76
M99_033	0.99	384 × 128 × 128	20.2	0.33	0.69	0.70
M99_050	0.99	256 × 128 × 128	20.2	0.50	0.67	0.68
M99_073	0.99	176 × 128 × 128	20.2	0.73	0.77	0.78
M99_089	0.99	144 × 128 × 128	20.2	0.89	1.12	1.14
M99_114	0.99	112 × 128 × 128	20.2	1.14	-	-
M99_133	0.99	96 × 128 × 128	20.2	1.33	-	-

Table 1. Parameters for simulations of layers confined by thermal pressure with monochromatic perturbations (models M). We list parameter A, number of cells at the highest refinement level n_x, n_y and n_z, resolution in the vertical direction H_{HT}/dz, parameter kH_{HT} where k is the selected wavenumber, $t_{\mathrm{E78}}^{\mathrm{EFOLD}}$ is the analytical e–folding time according to E78 for given k, and t_{NUM} ($t_{\mathrm{NUM}} = 1/\omega$) is the e–folding time measured in our simulations.

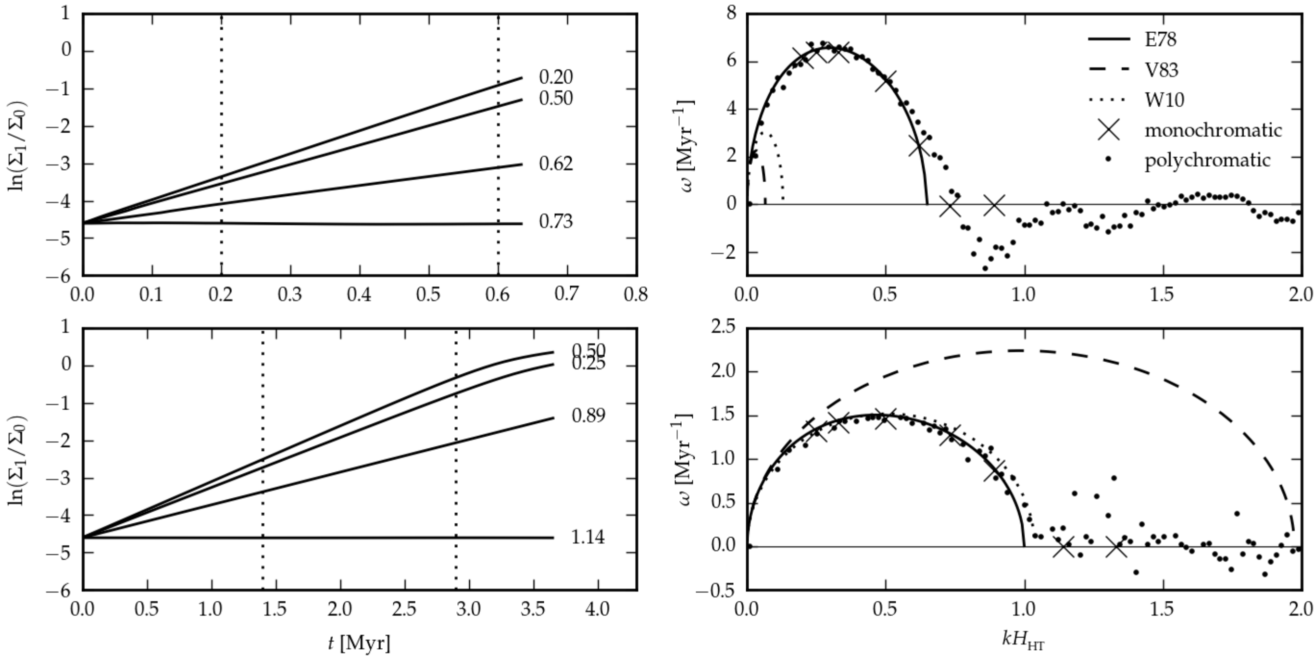

Figure 2. The dispersion relation for a self–gravity dominated ($A = 0.99$; top row) and external–pressure dominated ($A = 0.18$; bottom row) layer. Left panels: Time evolution of the surface density perturbations for monochromatic models. Only selected models are plotted to avoid confusion. The value of parameter kH_{HT} for a particular model is on right from the curve. The growth rate is calculated in the interval marked by the vertical dotted lines. Right panels: Comparison between analytical (E78, V83 and W10) and numerically obtained dispersion relations. The growth rate obtained from monochromatic and polychromatic simulations is plotted by crosses and dots, respectively. Data for polychromatic simulations is binned to reduce noise. See Sections 4.2 and 5.2 for a detailed description.

be small, i.e. $\Sigma_1 < \Sigma_{\mathrm{O}}$. Since model M18 terminates before this condition is fulfilled, we set t_1^{fit} near the end of the simulation. We compare measured ω with the analytical dispersion relations Eq. (7), Eq. (9) and Eq. (10) in the upper right panel of Figure 2 and list measured e–folding time $t_{\mathrm{NUM}} = 1.0/\omega$ alongside the E78 analytical estimate $t_{\mathrm{E78}}^{\mathrm{EFOLD}}$ in Table 1. Our results are very close to E78 (solid line) and are inconsistent with both W10 (dotted line) and V83 (dashed line).

Monochromatic simulations for the self–gravity dominated layer ($A = 0.99$, models M99) also show nearly time independent ω (lower left panel of Figure 2) with deviations towards the end only when the perturbing amplitude becomes large $\Sigma_1 \gtrsim \Sigma_{\mathrm{O}}$. Measured ω ($t_{\mathrm{O}}^{fit} = 1.4\,\mathrm{Myr}$, $t_1^{fit} = 3.0\,\mathrm{Myr}$) is in a good agreement with E78 dispersion relation and inconsistent with V83 (lower right panel of Fig. 2). Since W10 and E78 are similar, our data could not distinguish between them for self–gravity dominated layers.

5 LAYERS CONFINED BY THERMAL PRESSURE WITH POLYCHROMATIC PERTURBATIONS

In this Section, we investigate fragmentation of self–gravitating pressure confined layers both in linear and non–linear regime. Initial perturbations contain many wavelengths simultaneously (polychromatic). In the linear regime of fragmentation, we measure the dispersion relation. We also study the fragmenting process qualitatively as a function of parameter A, and compare the fragment masses and fragmenting timescales with analytical estimates.

The generic name of a polychromatic simulation consists of letter "P" followed by two numbers indicating the value of the parameter A. For example, simulation P18 treats a layer with $A = 0.18$.

5.1 Initial conditions for perturbations

To initiate simulations of layers confined by thermal pressure with polychromatic perturbations, we perturb the layer with many wavevectors pointing in all three spatial directions. In order to be able to perform resolution tests, we generate their amplitudes in the Fourier space and then map them by the inverse Fourier transform on a grid, so their spectrum does not depend on grid resolution. The amplitudes $\tilde{A}(k)$ are drawn as random variables from the uniform distribution for $\|\vec{k}\| < k_{\mathrm{O}}$ and are zero otherwise, so the amplitudes occupy a sphere in the Fourier space. To assure reasonable resolution, the highest wavenumber k_{O} corresponds to the size of at least 4 grid cells. The whole unstable range of wavenumbers predicted by any of the discussed estimate to the dispersion relation is always included inside the sphere, i.e. $\max(k_{\mathrm{E78.MAX}}, k_{\mathrm{V83.MAX}}, k_{\mathrm{W10.MAX}}) < k_{\mathrm{O}}$.

In order to compare fragmenting timescales between layers with different values of parameter A, it is necessary to choose comparable amplitudes of their initial perturbation. To reach the aim, we normalise all the perturbing amplitudes $\tilde{A}(k)$ to satisfy $\sqrt{\langle \tilde{A}(k)^2 \rangle} / \tilde{A}(0) = const.$ To be able to calculate the dispersion relation in the simulations, the initial perturbing amplitudes must be small. This imposes an upper limit on the normalisation constant. The lower limit is constrained by accuracy of the tree code. To fulfill these requirements, we set $\Sigma_1 \simeq 0.1 \Sigma_{\mathrm{O}}$.

5.2 The dispersion relation

To measure the dispersion relation, we compute Fourier transform of surface density for any frame of the simulation and then fit growth rate of each individual mode in time interval $(t^{fit}_{\mathrm{O}}, t^{fit}_{1})$. As the initial conditions do not correspond to the eigenfunctions, the modes relax at the beginning, and need some time before start growing at a temporarily constant growth rate. The choice of t^{fit}_{O} is constrained so as the modes with the longest wavelengths present in the computational domain already grow at a constant rate. t^{fit}_{1} is constrained so as the modes with the highest growth rate have not reached the nonlinear regime yet. We find that $t^{fit}_{\mathrm{O}} = 1/\omega_{\mathrm{E78.FAST}}$ and $t^{fit}_{1} = 3/\omega_{\mathrm{E78.FAST}}$ fulfill at best the requirements for our parameter choice.

We calculate the dispersion relation for the same values of parameter A (models P18 and P99 in Table 2; right panels of Figure 2) as for the monochromatic models presented in Section 4. The data are binned to reduce noise. The critical wavenumber k_{MAX} as well as the growth rate of wavenumbers $k < k_{\mathrm{MAX}}$ are again in a very good agreement with E78 both in self–gravity and external pressure dominated cases. Wavenumbers with $k > k_{\mathrm{MAX}}$ are stable. We do not detect any significant deviation between our results and E78.

5.3 Evolution in non–linear regime

Evolution of surface density for self–gravity dominated model P99 is shown in Figure 3. The fragmentation begins with emergence of round objects (at time from 0.7Myr to 2.1Myr). These objects then gradually grow and become slender as was predicted by the second order perturbation theory by Miyama, Narita & Hayashi (1987b). The transformation of objects from roundish to filamentary–like is apparent between plots at 2.8Myr to 4.9Myr. Sink particles form in the densest parts of the filaments and accrete material from surrounding filaments. Comparing the last plot at 4.9Myr with a plot at the early stage of fragmentation (e.g. 2.1Myr), we see that when a clump appears, it monolithically collapses to a gravitationally unstable object.

Fragmentation in pressure–dominated case is represented by model P18 (Fig. 4). At the beginning of fragmentation, the layer swiftly breaks into small objects (plots from 0.3Myr to 1.0Myr) with masses smaller than the Jeans mass M_J. The subjeans masses are a direct consequence of fragmentation according to E78 for layers with low A (right panel of Fig. 1). For confinement of the objects, external pressure is more important than self–gravity, so apart from being immersed in an external gravitational field of the layer, the objects are equivalents to gravitationally stable Bonnor–Ebert spheres. The stable objects then gradually merge until enough mass for a gravitationally bound clump is assembled (see plots from 1.0Myr to 2.3Myr). Merging often leads to non–radial accretion resulting in spinning–up the fragments and disc formation around them (plot at time 2.3Myr). As a bound clump is formed, it collapses and its cross section for possible following mergers is reduced and merging rate decreases. Therefore the fragmenting process in the pressure dominated case, which proceeds via coalescence of many small clumps, is qualitatively different from the continuous collapse in the self–gravity dominated case. We refer to the former and latter as *coalescence driven collapse* and *monolithic collapse*, respectively.

Since the analytical dispersion relations are often used for estimating fragmenting time–scales and mass of fragments, it is interesting to compare these quantities with those found in our simulations. We identify gravitationally bound fragments with the algorithm described in Appendix A. We experiment with several definitions of fragmenting time t_{FRG}, and conclude that taking t_{FRG} to be an instant when the total mass of gravitationally bound objects exceeds 1/2 of the total mass of the layer is a reasonable estimate for following reasons. As formation of bound objects starts, their total mass increases rapidly, so taking another fraction of the total mass than 1/2 would not lead to a significantly different time scale. Time t_{FRG} is also close to the time t_{SINK} when sink particles in total contain 1/2 of the total mass of the layer (see Table 2 and left panel of Fig. 5).

Comparison between t_{FRG} and E78 estimate $t^{\mathrm{EFOLD}}_{\mathrm{E78.FAST}} =$

Run	A	$n_x \times n_y \times n_z$	H_{HT}/dz	N_{J}	M_{J} [$\mathrm{M}_\odot$]	$\bar{M}_{\mathrm{CL}}$ [$\mathrm{M}_\odot$]	$t^{\mathrm{EFOLD}}_{\mathrm{E78.FAST}}$ [Myr]	t_{FRG} [Myr]	t_{SINK} [Myr]	t_{NL} [Myr]
P18	0.18	1024 × 1024 × 64	4.0	8.8	2.3	1.1	0.15	2.01	2.15	0.42
P20	0.20	1024 × 1024 × 64	4.4	9.3	2.5	1.9	0.17	2.19	2.40	0.50
P22	0.22	1024 × 1024 × 64	4.4	12.8	2.8	1.7	0.18	2.11	2.23	0.58
P25	0.25	1024 × 1024 × 64	4.4	19.0	3.1	3.1	0.21	1.90	2.20	0.80
P30	0.30	512 × 512 × 64	3.9	9.8	3.6	2.1	0.25	2.20	2.40	0.99
P40	0.40	512 × 512 × 64	4.7	17.0	5.0	3.5	0.33	2.38	2.64	1.45
P60	0.60	512 × 512 × 64	6.6	29.7	7.4	10.0	0.47	3.00	3.35	2.22
P80	0.80	512 × 512 × 64	5.9	89.0	9.9	20.6	0.59	3.60	4.00	2.31
P99	0.99	512 × 512 × 64	9.1	71.0	12.5	32.0	0.66	4.15	4.90	2.90

Table 2. Parameters for simulations of layers confined by thermal pressure with polychromatic perturbations (models P). First four columns have the same meaning as the columns in Table 1. Further, we provide number of Jeans masses in the computational domain N_{J}, Jeans mass M_{J}, mean mass of gravitationally bound objects $\bar{M}_{\mathrm{CL}}$ at fragmenting time t_{FRG}, time t_{SINK}, analytical e–folding time $t^{\mathrm{EFOLD}}_{\mathrm{E78.FAST}}$ for the most unstable wavenumber k_{FAST} and transition time between linear and non–linear regime t_{NL}.

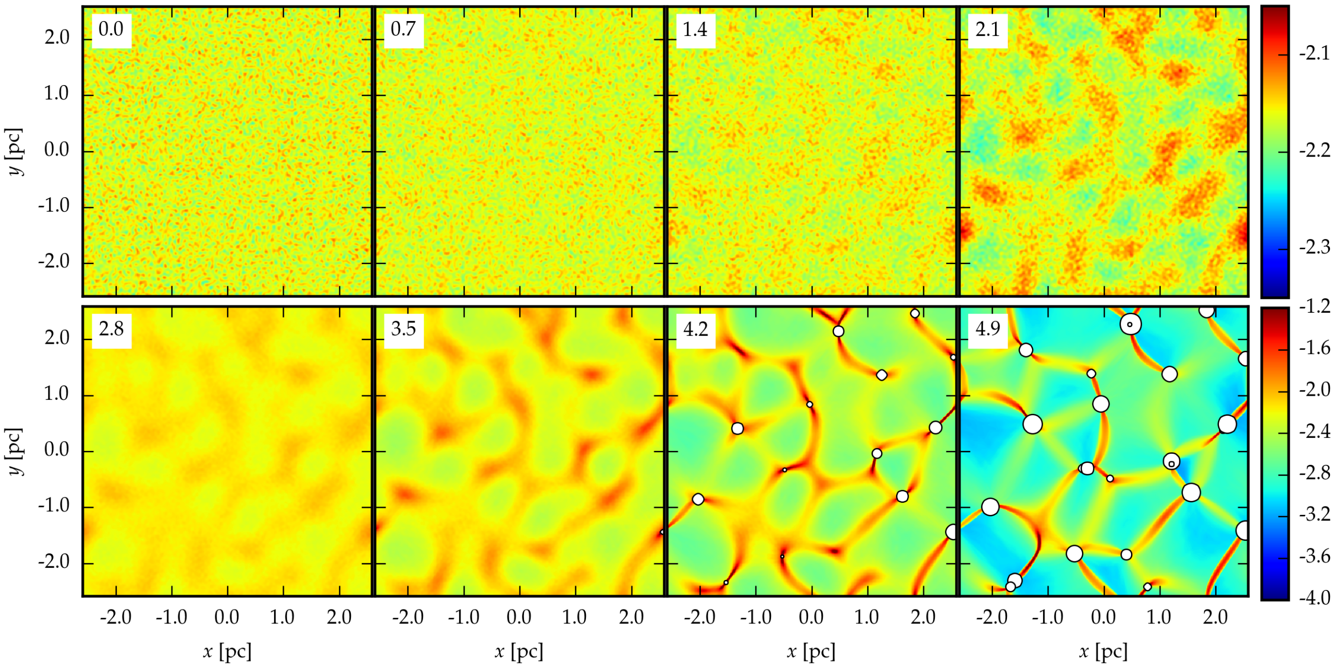

Figure 3. Evolution of surface density for the self–gravity dominated layer (model P99). Number at the upper left corner is the time in Myr. Sink particles are plotted as white circles. Area of a particular circle corresponds to the sink particle mass. Note that the colourscale for upper and bottom row is different.

$1/\omega_{\mathrm{E78.FAST}}$ (Eq. (11)) as a function of parameter A is plotted in the left panel of Fig. 5. We test the commonly adopted assumption that the fragmentation occurs at a constant number of analytic e–folding times $t^{\mathrm{EFOLD}}_{\mathrm{E78.FAST}}$ regardless of A, so we multiply $t^{\mathrm{EFOLD}}_{\mathrm{E78.FAST}}$ by a constant to match the data point for run P99. The assumption of constant number of e–folding times holds in self–gravity dominated case, but it underestimates the collapse time when external pressure dominates.

The parameters describing the layer are Σ_{O}, c_{S} and P_{EXT}. From dimensional analysis it follows that any quantity with the dimension of time is given by

$$t = \frac{c_{\mathrm{S}} f(A)}{G\Sigma_{\mathrm{O}}}, \qquad (15)$$

where $f(A)$ is an unknown function of the parameter A. Since both $t^{\mathrm{EFOLD}}_{\mathrm{E78.FAST}}$ and t_{FRG} are given by Eq. (15) (with presumably different description of $f(A)$), the number of e–folding times when fragmentation happens $n_{\mathrm{EFOLD}} = t_{\mathrm{FRG}}/t^{\mathrm{EFOLD}}_{\mathrm{E78.FAST}}$ is only a function of A for any layer. If we obtain $n_{\mathrm{EFOLD}}(A)$ from our simulations, we can estimate t_{FRG} for any layer because $t^{\mathrm{EFOLD}}_{\mathrm{E78.FAST}}$ is already known from Eq. (11).

The dependence of n_{EFOLD} on A is shown in the middle panel of Fig. 5 (solid line). Whereas n_{EFOLD} is nearly constant in the self–gravity dominated case, it strongly increases as the external pressure increases. Before drawing conclusions from this result, we should verify that it is not simply caused by the fact that self–gravity dominated models already start with effectively higher initial perturbations. For any model, the transition to the non–linear regime at time t_{NL} (when $\Sigma_1 = \Sigma_{\mathrm{O}}$) occurs at almost constant number of $t^{\mathrm{EFOLD}}_{\mathrm{E78.FAST}}$ (Table 2 and middle panel of Fig. 5), so the initial perturbations are in this sense comparable among models with different A. Taking t_{NL} instead of $t = 0$ as the time

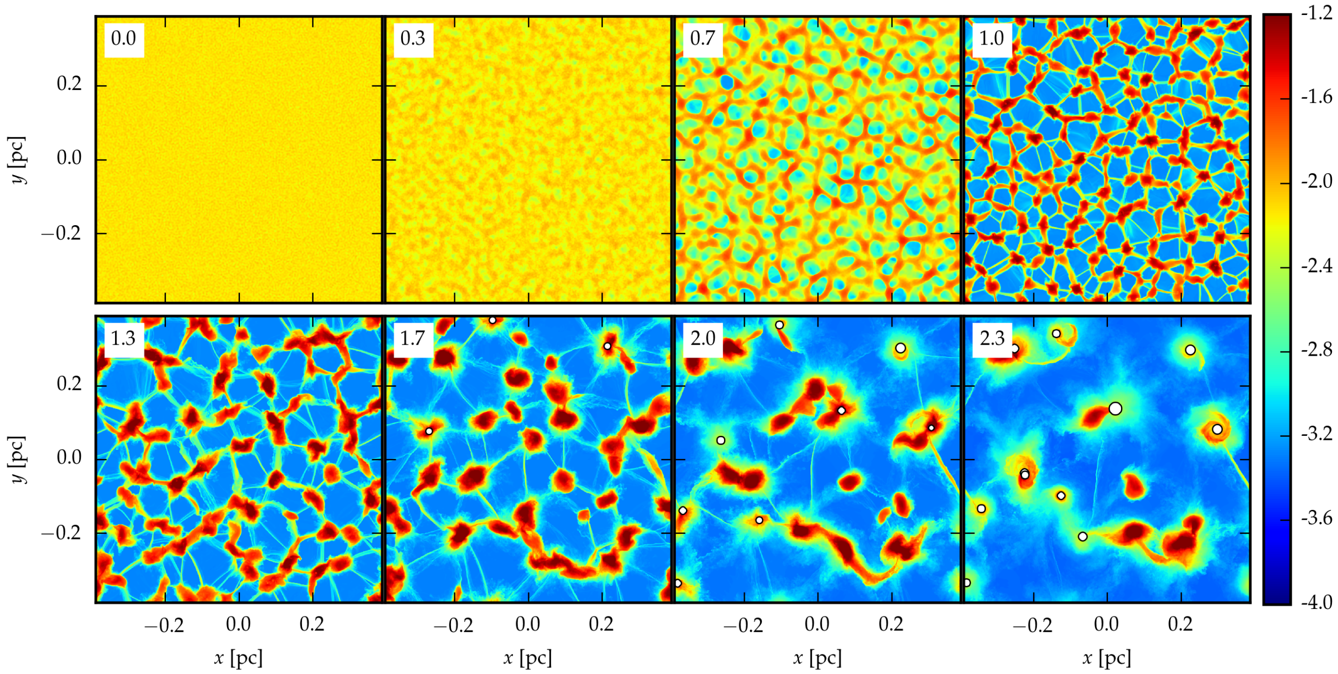

Figure 4. Evolution of surface density for the external pressure dominated layer (model P18). Caption is the same as in Fig. 3.

when the perturbing amplitudes are comparable would even emphasize the dependence of the number of $t^{\mathrm{EFOLD}}_{\mathrm{E78.FAST}}$ on A; when A is near unity, the fragmentation occurs soon after t_{NL}, when A is small, it takes many e–folding times to reach t_{FRG}. This behaviour reflects the two different fragmenting scenarios; when A is near unity, the clumps continue collapsing, when A is small, the clumps are stable and gradually merge, which causes the delay in fragmentation time. We conclude that neither E78 describes fragmenting time correctly because fragmentation does not occur at a constant number of e–folding times for various A.

The mean mass of bound objects $\bar{M}_{\mathrm{CL}}$ at the fragmenting time as a function of A is listed in Table 2 and shown in the right panel of Figure 5. Analytical estimates for V83 and E78 (M_{V83} and M_{E78}, respectively) and the Jeans mass M_{J} for the midplane density (we use $M_{\mathrm{J}} = 4.26\ Ac_s^4/(G^2\Sigma_{\mathrm{O}})$ from eq. (13-33) in Spitzer (1978)) are plotted by lines. The fragment masses for E78 and V83 are estimated from the wavelength with the highest growth rate (i.e. $M = \pi\Sigma_{\mathrm{O}}(\lambda_{\mathrm{FAST}}/2)^2$ where $\lambda_{\mathrm{FAST}} = 2\pi/k_{\mathrm{FAST}}$). In the self–gravity dominated case, the mass of fragments is in a good agreement with the E78 prediction. This result is a natural consequence of the monolithic collapse since the mass of fragments formed in the linear regime does not significantly change later on, during the non–linear collapse. The thin–shell approximation systematically underestimates the fragment masses for $A \gtrsim 0.6$.

In the external pressure dominated case, the mass of fragments is of the order of the Jeans mass. It is a result of their formation process, since the fragments are initially subjeans and stable until they assembled approximately the Jeans mass and then collapse. Therefore, the estimate based on E78 leads to too small fragment mass. In contrast, V83 overestimates fragment mass as it does not take into account the decrease of the Jeans mass with increasing external pressure.

6 LAYERS CONFINED BY THERMAL PRESSURE AND POSSIBLE PATTERN FORMATION IN SURFACE DENSITY

Fuchs (1996) proposes that when fragmentation of an infinitely thin disc becomes non–linear, a triple of modes with wavevectors $\|\vec{k}\| \simeq k_{\mathrm{FAST}}$ inclined at angles around 60° (i.e. in the Fourier space forming an equilateral triangle) has the highest growth rate due to interaction. Wünsch & Palouš (2001) semi–analytically find similar behaviour for the surface of a shell assuming V83. As a result, the modes create a hexagonal pattern in surface density. On the other hand, applying second–order perturbation theory, Miyama, Narita & Hayashi (1987a) show that a fragmenting layer breaks into gradually slendering filaments with no signs of the hexagonal pattern.

In this section, we test the Fuchs' proposition by searching regular patterns in surface density in our polychromatic simulations. Since we find no evidence for any pattern, we perform three dedicated models to test whether pattern formation arises at all under very idealised circumstances.

Name of the special models exploring possible pattern formation is in the form I<A>_<N_w>_[S|D], where the first two numbers after "I" represent the parameter A and the number after underscore the number N_w of amplified wavepackets. For models with suffix S, the wavepackets are amplified by a smooth function (wavepackets and the function are described in Section 6.1), while for models with suffix D, the wavepackets are degenerated to single modes.

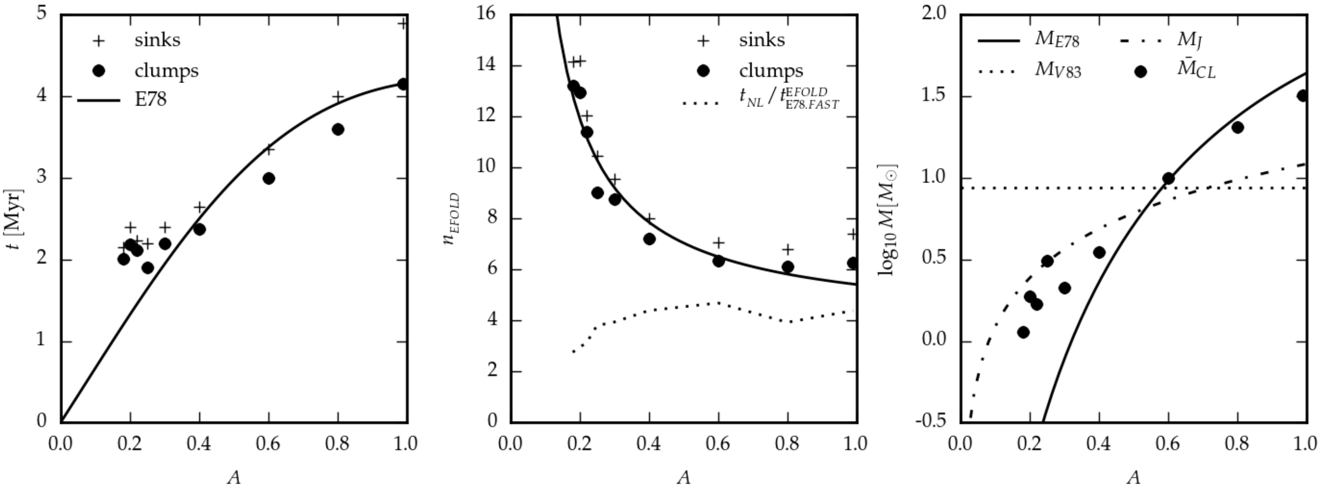

Figure 5. Fragmenting time and fragment mass of P models. Left panel: Time when 50% of the total mass is in the form of sink particles (pluses) and gravitationally bound objects (circles). The solid line is the analytical estimate for E78, with e–folding time $t^{\mathrm{EFOLD}}_{\mathrm{E78.FAST}}$ scaled so as to match t_{FRG} for model P99. Middle panel: Number n_{EFOLD} of e–folding times $t^{\mathrm{EFOLD}}_{\mathrm{E78.FAST}}$ needed to reach time t_{FRG}. Solid line shows the fit Eq. (19), dotted line shows the transition between linear and non–linear regime $t_{\mathrm{NL}}/t^{\mathrm{EFOLD}}_{\mathrm{E78.FAST}}$. Right panel: Average mass of gravitationally bound objects at time t_{FRG} (circles). Analytical estimates for E78, V83 and the Jeans mass for the midplane density are shown with solid, dotted and dashed lines, respectively.

6.1 Initial conditions for perturbations

For the dedicated I models, the amplitudes $\tilde{A}(k)$ of the perturbing wavevectors are firstly generated by the same method as for the polychromatic models (see Section 5.1 for description). Then, for models I99_3_S and I99_3_D, we choose three modes $\vec{k}_i$ $(i = 1, 2, 3)$ with $\|\vec{k}_i\| \simeq k_{\mathrm{E78.FAST}}$ inclined at an angle around 60° and amplify amplitudes of all modes inside a circle at centre $\vec{k}_i$ of radius dk by a bell shaped curve. Thus the perturbing amplitudes $\tilde{A}_n$ are calculated as

$$\tilde{A}_n(k) = \begin{cases} A_{int}\tilde{A}(k)\exp(-\|\vec{k},\vec{k}_i\|_2^2/\sigma_A^2) & , \|\vec{k},\vec{k}_i\|_2 \le \mathrm{d}k \\ \tilde{A}(k) & , \text{otherwise} \end{cases} \tag{16}$$

where $\|\vec{k},\vec{k}_i\|_2 = \sqrt{(k_x - k_{ix})^2 + (k_y - k_{iy})^2}$ and A_{int} and σ_A are parameters of the multiplying curve used in the particular model (Table 3). The only parameter differentiating models I99_3_D and I99_3_S is the radius dk. We experimented with amplifying amplitudes of only the selected wavevectors $\vec{k}_i$ (model I99_3_D) and wavepackets inside non–zero radius dk centered on $\vec{k}_i$ (model I99_3_S). The initial conditions for model I99_1_D are identical to that of model I99_3_D except that only one mode, $\vec{k}_1$ is amplified.

6.2 Evolution of interacting modes

Polychromatic models P18 and P99 (i.e. the ones with extreme values of parameter A in our sample) enter non–linear regime at time 0.42 Myr and 2.90 Myr, respectively (Table 2). Inspecting corresponding plots in Figs. 3 and 4 by eye, we do not see pattern formation at any stage of fragmenting process.

We perform more rigorous analysis to find a firmer support for this statement. Let Fourier transform of the surface density be $B(k_x, k_y)$. A regular pattern in the surface density would manifest itself as an anisotropy of function B. We look at the plane (k_x, k_y) as it is given in polar coordinates specified by radius $\|\vec{k}\|$ and azimuthal angle α. To search for the anisotropy, we analyse function B evaluated on two different radially-averaged subsets in the (k_x, k_y) plane. In the first case, B is evaluated on a thin annulus with radius $\|\vec{k}\| = k_{\mathrm{E78.FAST}}$, i.e. $B_{\mathrm{RAD.1}}(\alpha) \equiv B(\|\vec{k}\| = k_{\mathrm{E78.FAST}}, \alpha)$. In the second case, the annulus is wider so it includes more modes around radius $k_{\mathrm{E78.FAST}}$, i.e. $B_{\mathrm{RAD.2}}(\alpha) \equiv B(k_{\mathrm{E78.FAST}}/2 \le \|\vec{k}\| \le 3k_{\mathrm{E78.FAST}}/2, \alpha)$. If two modes inclined at an angle $\tilde{\alpha}$ have the highest amplitudes, function $B_{\mathrm{RAD.J}}(\alpha)$ (letter J stands for 1 or 2) has maxima separated by the angle $\tilde{\alpha}$. Thus the amplitudes of modes adjoined by the angle α are proportional to the value of azimuthal autocorrelation of $B_{\mathrm{RAD.J}}(\alpha)$, i.e.

$$c_J(\alpha) = \int_0^\pi B_{\mathrm{RAD.J}}(\alpha')B_{\mathrm{RAD.J}}(\alpha + \alpha')\mathrm{d}\alpha'. \tag{17}$$

Function $c_J(\alpha)$ detects interaction of modes inclined by any angle, not necessarily 60°.

When analysing the data, it is important to note that the autocorrelation function always attains its maximum at zero. The maxima due to two modes adjoined by an angle are local maxima of function c_J. We denote $c_{\mathrm{MAX.J}}$ the highest local maximum of function c_J after its global maximum $c_J(0)$. During the simulations, the value of c_J increases as amplitudes of modes increase. Since the interacting modes are predicted to grow faster than the rest of modes, we normalise $c_{\mathrm{MAX.J}}$ with the mean $\langle c_J \rangle$.

Time dependence of $c_{\mathrm{MAX.1}}/\langle c_J \rangle$ and $c_{\mathrm{MAX.2}}/\langle c_2 \rangle$ for models P18, P60 and P99 is shown in the upper panel of Figure 6. Vertical bars indicate the transition to the non–linear regime. We detect no significant growth of $c_{\mathrm{MAX.J}}/\langle c_J \rangle$ after the models enter the non–linear regime indicating isotropy in the plane $B(k_x, k_y)$ and thus no formation of a regular pattern.

The bottom panel of Fig. 6 shows the angle α at which

Run	A	$n_x \times n_y \times n_z$	H_{HT}/dz	A_{int}	σ_A [pc^{-1}]	dk [pc^{-1}]	i	$t^{\mathrm{EFOLD}}_{\mathrm{E78.FAST}}$ [Myr]
I99_3_S	0.99	512 × 512 × 32	5.1	10.0	28	14	1,2,3	0.66
I99_3_D	0.99	512 × 512 × 32	5.1	10.0	28	0	1,2,3	0.66
I99_1_D	0.99	512 × 512 × 32	5.1	10.0	28	0	1	0.66

Table 3. Parameters for simulations designed to study mode interaction (models I). First four columns have the same meaning as the columns in Table 1. Parameters A_{int}, σ_A and dk characterise properties of the mode amplifying function, Eq. (16). Further, we list indices i of amplified modes $\vec{k}_i$. Time $t^{\mathrm{EFOLD}}_{\mathrm{E78.FAST}}$ is as in Table 2.

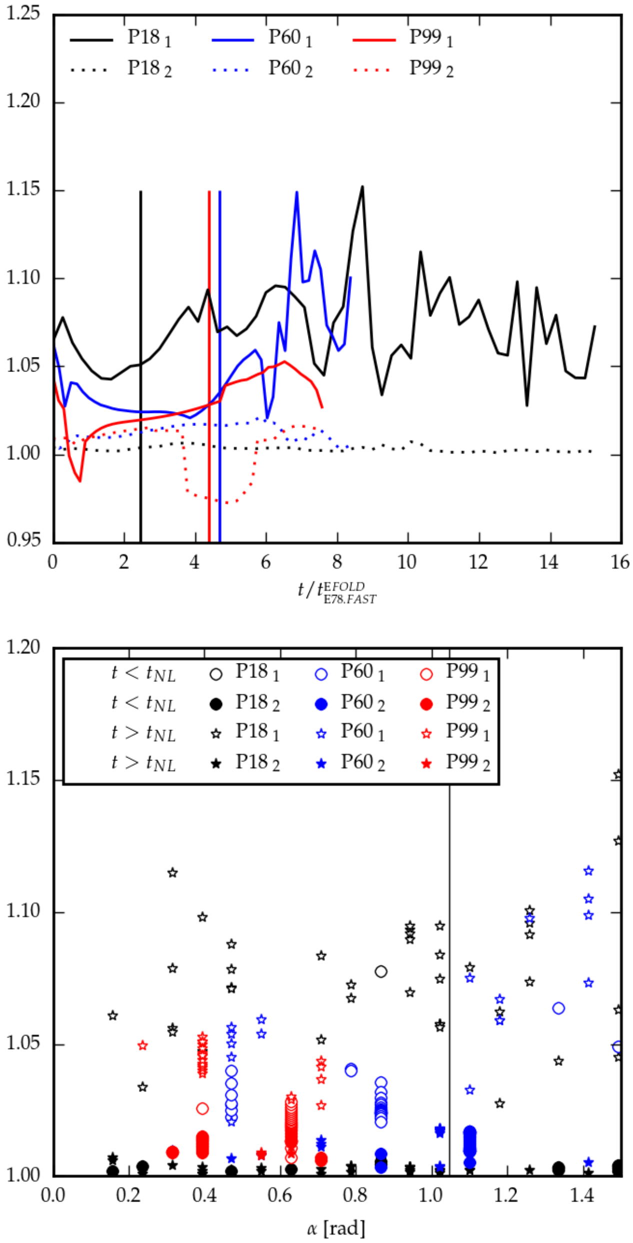

Figure 6. Upper panel: Evolution of azimuthal autocorrelation, Eq. (17), for models P18 (black line), P60 (blue line) and P99 (red line). Subscript characters 1 and 2 refer to two versions of function $B_{\mathrm{RAD.}}$; $B_{\mathrm{RAD.1}}$ and $B_{\mathrm{RAD.2}}$. Vertical bars denote transition from linear to non–linear regime for particular model as represented by its colour. Bottom panel: Angular separation α between modes with $c_{\mathrm{MAX.J}}/\langle c_J \rangle$ at given time for models P18 (black symbols), P60 (blue symbols) and P99 (red symbols). The symbols are circles and asterisks in linear and non–linear regime of fragmentation for each model, respectively. Open and filled symbols represent analysis with $B_{\mathrm{RAD.1}}$ and $B_{\mathrm{RAD.2}}$, respectively. The angle 60°, which is expected to be adjoined by the triple of the highest growing modes in scenario proposed by Fuchs (1996), is denoted by the vertical solid line.

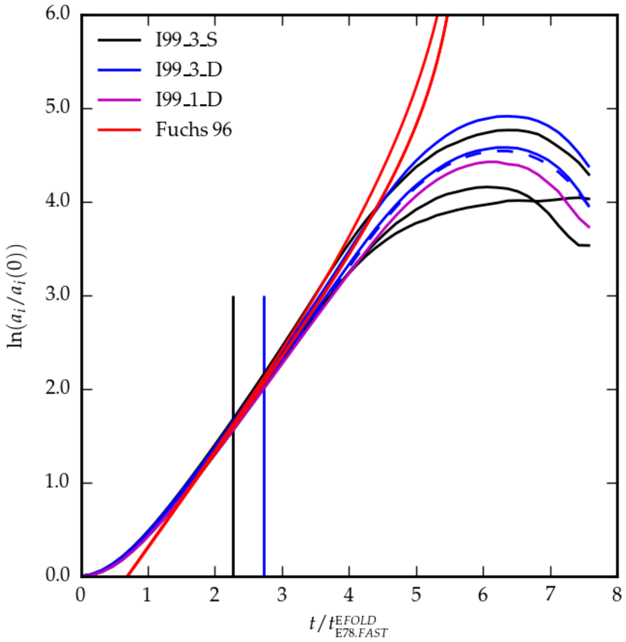

Figure 7. Amplitude evolution of the three amplified modes for models I99_3_S (black line) and I99_3_D (blue line), and for the single amplified mode for model I99_1_D (magenta line). The mode of model I99_3_D which is identical to the amplified mode of model I99_1_D is shown by the dashed blue line. Numerical solution to the second order perturbation equations proposed by Fuchs (1996) is plotted by red lines. The transition from the linear to non–linear regime is shown by vertical bars.

$c_{\rm MAX.J}/\langle c_J\rangle$ is attained. Data points representing linear and non–linear regime are distinguished by circles and asterisks, respectively. In the linear regime, there is no preferred angle adjoined by modes with the highest growth rate. This result is not surprising since the modes are predicted to grow independently on one another in the linear regime. If modes started interacting in the non–linear regime, asterisks would be clustered around a particular angle ($\alpha = 60^\circ$ is represented by a vertical line) with concomitant increase of $c_{\rm MAX.J}/\langle c_J\rangle$. Instead, the symbols show neither preferential clustering nor a rapid increase of $c_{\rm MAX.J}/\langle c_J\rangle$. The absence of both signposts strongly disfavours the possibility of regular pattern formation.

Models I enable us to study the evolution of amplitudes a_i of the individual modes $\vec{k}_i$; this is plotted in Fig. 7. Models I99_3_S (black lines) and I99_3_D (blue lines) contain the triple of modes, which according to Fuchs (1996), should have an increased growth rate in the non–linear regime. Red lines show numerical solution to the second order perturbation equations for the thin shell approximation (cf. eqs. (28) in (Fuchs 1996)) with the initial mode amplitudes of model I99_3_D [2] .The vertical bars mark the transition from the linear to non–linear regime. Recall that the growth rate ω is the time derivative of the plotted functions. The growth rate obtained from our simulations does not follow the increased growth rate predicted by Fuchs. In contrast, the simulated growth rate even decreases in the non–linear regime.

In the previous paragraph, we demonstrate that the possible interaction between the triple of modes does not increase their growth rate above $\omega_{\rm E78.FAST}$. Do the triple of modes interact at least to some degree? To assess this question, we use the same initial conditions as for model I99_3_D, but we amplify only one mode, $\vec{k}_1$ (model I99_1_D). Amplitude of this mode (magenta line in Fig. 7) evolves very close to that of the corresponding mode in model I99_3_D (blue dashed line). Moreover, the similar shape between these two curves suggests that the non–linear terms due to the two other modes are not important.

Note that to study pattern formation, we investigate mode interaction only in the azimuthal direction α of the Fourier space. We do not investigate mode interaction in radial direction $\|\vec{k}\|$, which apparently arises in the non–linear regime. Our findings do not contradict the mechanism proposed by Miyama, Narita & Hayashi (1987a,b), which leads to randomly oriented filaments.

7 LAYERS ACCRETING FROM ONE SIDE, AND CONTAINED BY THERMAL PRESSURE ON THE OTHER

In this section, we study layers accreting homogeneous medium from the upper surface and bounded by thermal pressure from the lower surface. We investigate their dispersion relation and subsequent evolution in the non–linear regime. These models approximate a part of a shell sweeping up the ambient medium on one surface and backed by thermal pressure on the other. As we show in Section 8 that shells around H II regions fragment in the pressure dominated case, we start the simulations in this case, setting $A = 0.3$ at the beginning of a simulation.

---

[2] Since the initial conditions for models I are not eigenfunctions, they do not exhibit the constant growth rate from the beginning. Eqs. (28) in (Fuchs 1996) are derived for eigenfunctions, so they already starts with the constant growth rate. To compensate for the offset, we divide the latter by a constant so that their amplitudes equal to that of the former at the end of the linear regime.

The generic name of accreting models is in the form A<A>_<$\mathscr{M}$>_<T_{AMB}>_[$N|L$]. First number after letter A represents the value of the parameter A at the beginning, followed by the Mach number $\mathscr{M}$ of the accreting medium and the temperature T_{AMB} of the ambient medium imposing the thermal pressure. The suffix L or N indicates whether the simulation terminates in linear or non–linear regime, respectively. For example, simulation A30_08_10_L treats a layer with $A = 0.30$, which accretes at velocity $\mathscr{M} = 8$, and which is backed with an ambient medium of temperature 10 000 K.

We use two kinds of models to address two different issues. Models with suffix L are used for studying evolution in the linear regime (the dispersion relation and flows inside the layer). For this purpose, it is sufficient to use computational domain in xy directions significantly (8×) smaller than in corresponding non–accreting model P30. Consequently, we can afford to use two times higher resolution $H_{\mathrm{HT}}/\mathrm{d}z$, even though a number of grid cells in x and y directions are 4 times smaller. Models with suffix N focus on evolution in the non–linear regime, where the priority is to include many Jeans masses inside the computational domain. For this purpose, we use the same size of the computational domain and the resolution as for model P30.

7.1 Initial conditions for perturbations

Initial perturbations are generated by the same method as for the polychromatic models (Section 5.1).

7.2 Evolution in linear regime

Numerically obtained dispersion relations in time interval $(t_{\mathrm{O}}^{fit}, t_1^{fit}) = (1/\omega_{\mathrm{E78.FAST}}, 2/\omega_{\mathrm{E78.FAST}})$ for models with $T_{\mathrm{AMB}} = 300\mathrm{K}$, i.e. A30_08_03_L, A30_20_03_L and A30_50_03_L (Table 4) are plotted in the upper panel of Figure 8. As the layer accretes, its surface density and parameter A increase, we list these quantities at t_{O}^{fit} and t_1^{fit} in the last four columns of Table 4. We compare the results with E78 for two extreme values of parameter A attained in the simulations; one corresponds to $t = 0$, i.e. $A = 0.30$, the other to the model with the highest A at t_1^{fit}, i.e. $A = 0.48$. If the dispersion relation for the accreting layer were the same as for the thermal–pressure confined layer, all models would fit between these curves. However, the range of unstable wavenumbers extends to significantly higher values of kH_{HT}. The highest growth rate is around factor 2 higher than that of E78. To study possible influence of the temperature in the ambient medium, we calculate the same models with temperature $T_{\mathrm{AMB}} = 10^4\mathrm{K}$ (lower panel of Fig. 8). Both kinds of models reproduce similar features indicating that the dispersion relation depends only weakly on the temperature of the ambient medium. Note that these features are unlikely to be caused by resolution, which is here higher (7.8 cells per H_{HT}; Table 4) than that for polychromatic models ($\simeq 4H_{\mathrm{HT}}$; Table 2), which reproduce their analytic dispersion relation very well.

Evolution of density and velocity field inside the accreting layer (model A30_08_10_L) is shown in Figure 9. As the upper part of the layer is mildly corrugated, the different directions of incidence between the ram pressure and thermal pressure lead to a dynamical instability similar to the one described by Vishniac (1983), and it results in gas motions towards the convex parts (panel (a)). The gas then moves through the layer and protrudes from contact discontinuity until it is eventually stopped by gravitational attraction of the layer (panels (b) and (c)). Formation of the protrusions at the contact discontinuity broadens the unstable range of the dispersion relation towards higher kH_{HT} as is apparent from Fig. 8. At the same time, the corrugations of the bottom surface of the layer shield the hot gas in concave regions, leading to a pressure drop and thus cause flows of hot gas toward the concave regions. Upward flows of hot gas cause upward motions of cold gas inside the layer (panels (b) and (c)). However, the different nature of boundary conditions leads to different behaviour of the flows when they reach the surface. Whereas the upper flows are eroded by a shock, the downward flows can significantly corrugate the contact discontinuity (panel (d)) because this surface is pliable. The self–gravity then pulls the protruding gas, while it is still replenished from the original direction, resulting in circular motions (panel (d)). At this time ($\omega_{\mathrm{E78.FAST}}t \simeq 4$), the growth of perturbations with $kH_{\mathrm{HT}} \gtrsim 0.7$ is saturated, so the range of unstable wavenumbers is comparable to that of the thermal–pressure confined layer.

7.3 Evolution in non–linear regime

The subsequent non–linear fragmentation is investigated by models A30_05_03_N, A30_10_03_N and A30_20_03_N (Table 5). Evolution of surface density is shown in Figure 10. Model A30_05_03_N accretes at the highest rate (cf. the 6th column in Table 5) and substantial part of fragmentation occurs in self–gravity dominated case ($A \gtrsim 0.6$; value of A is at the upper right corner of each frame of Fig. 10). Fragments emerge at $t = 1\mathrm{Myr}$ and subsequently collapse, forming filaments and then sink particles at their junctions ($t = 1.5\mathrm{Myr}$ and $t = 2\mathrm{Myr}$). Although the boundary conditions at the upper surface are different from that of purely thermal pressure confined layers, we see a similar evolutionary pattern as for the monolithic collapse (model P99 described in Section 5.3).

In contrast, the amount of gas accreted in model A30_20_03_N is substantially smaller and the main part of fragmentation is accomplished still in pressure–dominated case. At the beginning of the fragmentation ($t \lesssim 1.0\mathrm{Myr}$), the density inside the layer is approximately constant and the overdensities seen in panels at $t = 0.5\mathrm{Myr}$ and $t = 1.0\mathrm{Myr}$ are corrugations of the contact discontinuity. The corrugations then gradually merge until they become gravitationally unstable and collapse (panel at $t = 2.0\mathrm{Myr}$). Note that the values of A seen in Fig. 10 are slightly higher than due to the accretion since cooling of hot gas at the contact discontinuity also contributes to the surface density, which increases A. The gradual merging forms less defined and more fluffy filaments than the direct collapse at smaller Mach numbers. Thus the fragmenting process of model A30_20_03_N is very similar to the coalescence driven collapse seen in model P18.

The mean clump mass $\bar{M}_{\mathrm{CL}}$ for models A30_05_03_N, A30_10_03_N and A30_20_03_N ($3.4\,\mathrm{M}_\odot$ to $4.0\,\mathrm{M}_\odot$, Table 5) is close to the Jeans mass ($3.6\,\mathrm{M}_\odot$ for $A = 0.3$). We interpret values of $\bar{M}_{\mathrm{CL}}$ as follows: As the layer starts accreting in pressure dominated case, its density (according to Eq. (6)) and therefore the Jeans mass M_{J} is only a weak function of

Run	A	$n_x \times n_y \times n_z$	$H_{\rm HT}/dz$	$\mathscr{M}$	$\rho_{\rm ACC}$ $[10^{-21}{\rm g.cm}^{-3}]$	$T_{\rm AMB}$ [K]	$t^{\rm EFOLD}_{\rm E78.FAST}$	A_{T1}	A_{T2}	$\Sigma_{T1}/\Sigma_{\rm O}$	$\Sigma_{T2}/\Sigma_{\rm O}$
A30_08_10_L	0.30	128 × 128 × 64	7.8	8	1.660	10000	0.25	0.39	0.47	1.37	1.76
A30_20_10_L	0.30	128 × 128 × 64	7.8	20	0.320	10000	0.25	0.33	0.38	1.16	1.35
A30_50_10_L	0.30	128 × 128 × 64	7.8	50	0.052	10000	0.25	0.31	0.33	1.06	1.15
A30_08_03_L	0.30	128 × 128 × 64	7.8	8	1.660	300	0.25	0.39	0.48	1.39	1.78
A30_20_03_L	0.30	128 × 128 × 64	7.8	20	0.320	300	0.25	0.34	0.41	1.17	1.48
A30_50_03_L	0.30	128 × 128 × 64	7.8	50	0.052	300	0.25	0.31	0.39	1.07	1.39

Table 4. Parameters of accreting simulations intended to study evolution in the linear regime (models A). First four columns have the same meaning as the columns in Table 1 (parameter A is taken at time zero). Further we list Mach number $\mathscr{M}$ and density $\rho_{\rm ACC}$ of the accreting medium, temperature of the ambient medium $T_{\rm AMB}$, and surface density and the value of parameter A at time $t^{\rm EFOLD}_{\rm E78.FAST}$ and $2t^{\rm EFOLD}_{\rm E78.FAST}$. Surface density at the beginning is denoted $\Sigma_{\rm O}$.

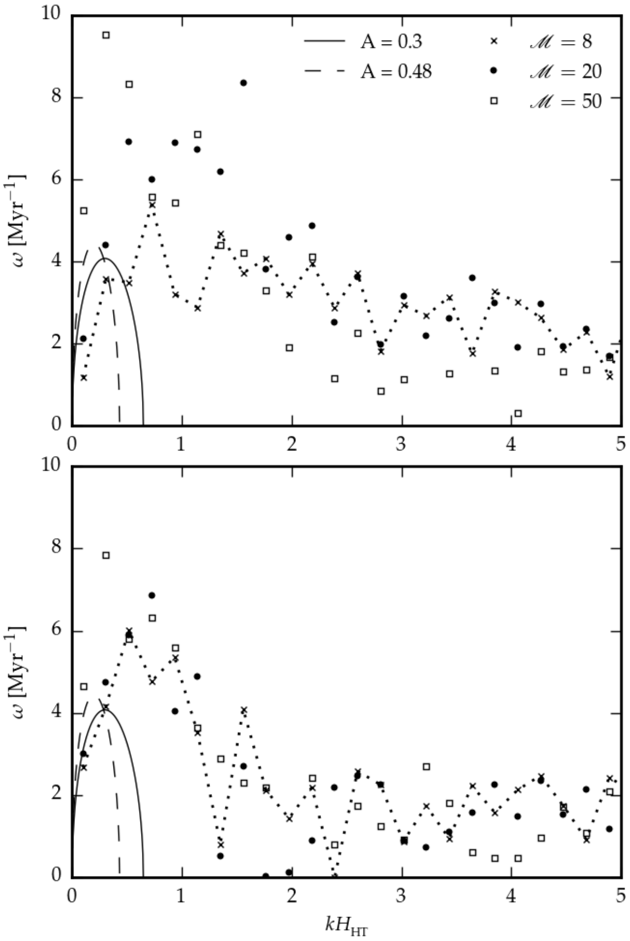

Figure 8. Dispersion relations for layers with $A = 0.3$ accreting homogeneous medium at Mach numbers 8, 20 and 50 (markers). Solid and dashed lines show E78 dispersion relation for two extreme values of A; $A = 0.3$ and $A = 0.48$, respectively. UPPER PANEL: temperature of the ambient medium is 300K (models A30_08_03_L, A30_20_03_L and A30_50_03_L). The dotted line is to guide the eye for $\mathscr{M} = 8$ model. BOTTOM PANEL: temperature of the ambient medium is 10^4K (models A30_08_10_L, A30_20_10_L and A30_50_10_L).

Run	A	$n_x \times n_y \times n_z$	$\frac{H_{\rm HT}}{\rm dz}$	$\mathscr{M}$	$\rho_{\rm ACC}$ $[10^{-21}{\rm g.cm}^{-3}]$	$\dot{\Sigma}$ $\frac{\rm M_\odot}{\rm Myr\,pc^2}$	$N_{\rm J}$	$M_{\rm J}$ $[\rm M_\odot]$	$\bar{M}_{\rm CL}$ $[\rm M_\odot]$	$t^{\rm EFOLD}_{\rm E78.FAST}$ [Myr]	$t_{\rm FRG}$ [Myr]	$A_{\rm FRG}$	$\frac{\Sigma_{\rm FRG}}{\Sigma_{\rm O}}$
A30_05_03_N	0.30	512 × 512 × 64	3.9	5	4.94	76	9.8	3.6	4.0	0.25	1.5	0.73	3.5
A30_10_03_N	0.30	512 × 512 × 64	3.9	10	1.27	39	9.8	3.6	3.5	0.25	1.7	0.59	2.4
A30_20_03_N	0.30	512 × 512 × 64	3.9	20	0.32	20	9.8	3.6	3.4	0.25	1.8	0.59	2.4

Table 5. Parameters of accreting simulations intended for the non–linear regime of fragmentation (models A). First four columns have the same meaning as the columns in Table 1 and quantities $N_{\rm J}$, $M_{\rm J}$, $\bar{M}_{\rm CL}$, $t_{\rm E78.FAST}$ and $t_{\rm FRG}$ are explained in Table 2. We further list the Mach number $\mathscr{M}$ and density $\rho_{\rm ACC}$ of the accreting medium, accreting rate $\dot{\Sigma}$, and values of parameter A and surface density at the time $t_{\rm FRG}$ ($\Sigma_{\rm O}$ is the surface density at the beginning).

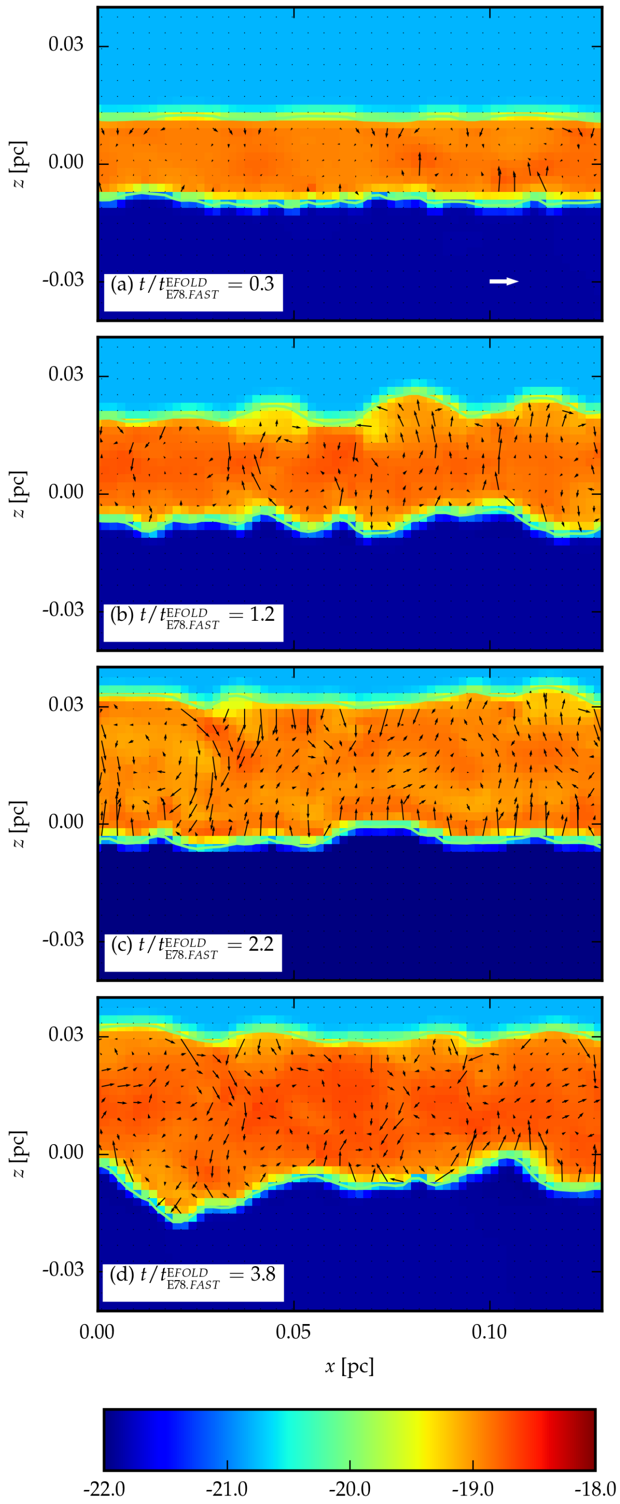

Figure 9. Density profile and velocity field on cross sections for model A30_08_10_L. The gas is accreted from the top. The velocity vectors are plotted only for the gas inside the layer to avoid confusion The length of the thick white arrow in panel (a) corresponds to velocity 1 Mach number inside the layer.

A. The highest change of $M_{\rm J}$ is for the model with the highest accreting rate, i.e. A30_05_03_N; $M_{\rm J}$ decreases only by factor 1.7× from beginning to the fragmenting time. Compared to non–accreting model P99, where $\bar{M}_{\rm CL} = 2.1\,{\rm M}_{\odot}$ (Table 2), the accreting simulations have at most by factor 2 higher $\bar{M}_{\rm CL}$. Therefore the Jeans mass at $t = 0$ is a relatively good estimate for fragment mass also for accreting layers, so we can use it as a proxy when estimating fragments properties for an accreting shell in Section 8.

Finally, we discuss the influence of our cooling method (described in Section 3.3) on the boundary conditions. Recall that intermixing the warm gas into the layer and its imminent cooling deplete the warm gas on the lower side of the layer. The depleted gas is compensated by warm gas inflow, which causes ram pressure on the contact discontinuity. If the ram pressure is strong enough, it would change the contact discontinuity to a shock front which is an artificial and unwanted behaviour (e.g. surface gravity waves would be suppressed), so we should check that this does not occur. From the beginning to the fragmenting time, the highest ratio between the ram and thermal pressure at the contact discontinuity is 0.03, 0.12 and 0.5 for models A30_05_03_N, A30_10_03_N and A30_20_03_N, respectively. Thus the ram pressure is negligible when compared to the thermal pressure for models A30_05_03_N, A30_10_03_N and it is not dominant for model A30_20_03_N so that the contact discontinuity is preserved in all simulations.

8 FRAGMENTATION OF A SHELL SWEPT UP BY AN EXPANDING H II REGION

We use results of previous sections to estimate properties of a fragmenting shell (e.g. fragmenting time, mass) swept up around an H II region. The H II region is powered by a massive star emitting $\dot{N}$ ionising photons per second situated in a homogeneous medium with density $\rho_{\rm ACC}$ (we use subscript ACC for the surrounding medium since it is accreted in the reference frame of the shell). For convenience, we define $\dot{N}_{49} = [\dot{N}/10^{49}{\rm s}^{-1}]$, $c_{s2} = [c_{\rm S}/0.2{\rm km/s}]$, and $n_3 = [n_{\rm ACC}/10^3{\rm cm}^{-3}]$ where $c_{\rm S}$ is sound velocity in the swept up shell, and $n_{\rm ACC}$ is the number density in the surrounding medium. Following Whitworth et al. (1994b), we assume that fragmentation is accomplished in pressure dominated case, which means that the shell fragments by coalescence driven collapse. At the end we show that our results are consistent with this assumption.

8.1 An analytic estimate for fragmentation of a shell swept up by an expanding H II region

The remarkable property of our accreting simulations is that their fragmenting time depends very weakly on the Mach number (Table 5) and differs at most by factor 1.5 from their non–accreting counterpart (model P30). Mass of the fragments also differs at most by factor two from the non–accreting model. This behaviour suggests that fragmenting time and mass of fragments of a non–accreting layer can be used to estimate corresponding quantities for an accreting layer.

Further we assume that a thermal pressure–confined layer with time dependent surface density $\Sigma(t)$ and external pressure $P_{\rm EXT}(t)$ fragments at any instant as the same layer with constant $\Sigma_{\rm O}$ and $P_{\rm EXT}$. Thus, when fragmentation starts at time $t_{\rm O}$, it is accomplished at time t_1 fulfilling

$$1 = \int_{t_{\rm O}}^{t_1} \frac{\omega_{\rm E78.FAST}(t)}{n_{\rm EFOLD}(A(t))}{\rm d}t = \int_{t_{\rm O}}^{t_1} \frac{\sqrt{0.276}\pi G\Sigma(A(t))}{c_{\rm S}A(t)n_{\rm EFOLD}(A(t))}{\rm d}t, \tag{18}$$

where the second equality follows from Eq. (11). Fitting measured data (Table 2 and middle panel in Fig. 5), we obtain

$$n_{\rm EFOLD} = 1.63/A + 3.79. \tag{19}$$

We use our accreting models (with time dependent Σ) to test the assumption made in the previous paragraph. Models A30_05_03_N, A30_10_03_N and A30_20_03_N fragment at time 1.5 (1.36) Myr, 1.7 (1.64) Myr and 1.8 (1.85) Myr, respectively, where the first number is obtained from the simulation and the bracketed number is from Eq. (18) showing a good agreement.

The radius R of a shell around an H II region expands according to $R = R_{\rm ST}(1 + 7c_{II}t/4R_{\rm ST})^{4/7}$ (Spitzer 1978), where $R_{\rm ST}$ and c_{II} is Strömgren radius and sound velocity in the ionised gas, respectively. Surface density of the shell and ram pressure due to swept up gas evolve as $\Sigma = \rho_{\rm ACC}R(t)/3$ and $P_{\rm RAM} = \rho_{\rm ACC}({\rm d}R/{\rm d}t)^2$. Thermal pressure $P_{\rm EXT}$ inside the H II region is equal to $P_{\rm RAM}$. Thus approximating a small patch on the shell wall as a layer, its parameter A (Eq. (3)) evolves as

$$A = \left\{1 + \frac{18c_{II}^2}{\pi G\rho_{\rm ACC}(R_{\rm ST}(1 + 7c_{II}t/(4R_{\rm ST})))^2}\right\}^{-1/2}. \tag{20}$$

Evolution of $P_{\rm EXT}$, Σ and A for walls of shells powered by sources with $\dot{N}_{49} = 0.1$ (approximately an O9V star (Martins, Schaerer & Hillier 2005)), $\dot{N}_{49} = 1$ (O6V star) and $\dot{N}_{49} = 10$ (two O3V stars) expanding into a homogeneous ambient medium of particle density $n_3 = 0.1$, $n_3 = 1$ and $n_3 = 10$, respectively, is shown in Figure 11. Plotted models are extremes in the sense that any evolutionary path for a shell within a set $\dot{N}_{49} \times n_3$ in range $(0.1, 10) \times (0.1, 10)$ lies in between them. The mentioned set $\dot{N}_{49} \times n_3$ covers typical values for galactic H II regions. Time $t_{\rm O}$ as determined from Eq. (22) below is plotted as the first asterisk on the evolutionary path. Following asterisks represent instants when integral in Eq. (18) reaches 0.25, 0.5, 0.75 and 1.0. They show that fragmentation proceeds in pressure dominated case.

Substituting A from Eq. (20) for t in Eq. (18) gives

$$\frac{0.81c_{\rm S}}{\left\{(G\rho_{\rm ACC})^3R_{\rm ST}^6c_{II}^8\right\}^{1/14}} = \int_{A_{\rm O}}^{A_1} \frac{(1 - A^2)^{-25/14}}{n_{\rm EFOLD}(A)A^{3/7}}{\rm d}A, \tag{21}$$

where $A_{\rm O} = A(t_{\rm O})$ and $A_1 = A(t_1)$ denote the value of parameter A at the beginning and end of fragmentation, respectively.

We adopt $t_{\rm O}$ as the earliest time when self–gravity of a fragment containing one Jeans mass (its radius is $R_{\rm J} = \sqrt{M_{\rm J}/(\pi\Sigma)}$) dominates stretching, i.e. $G\Sigma = R_{\rm J}(4/(7t_{\rm O}))^2$ (see appendix A in Whitworth et al. (1994b)) [3] . We neglect

---

[3] Our choice of $t_{\rm O}$ is an approximation since for smaller fragments with $\lambda_{\rm MAX}$, $\lambda_{\rm MAX} < R_{\rm J}$ self–gravity dominates stretching earlier

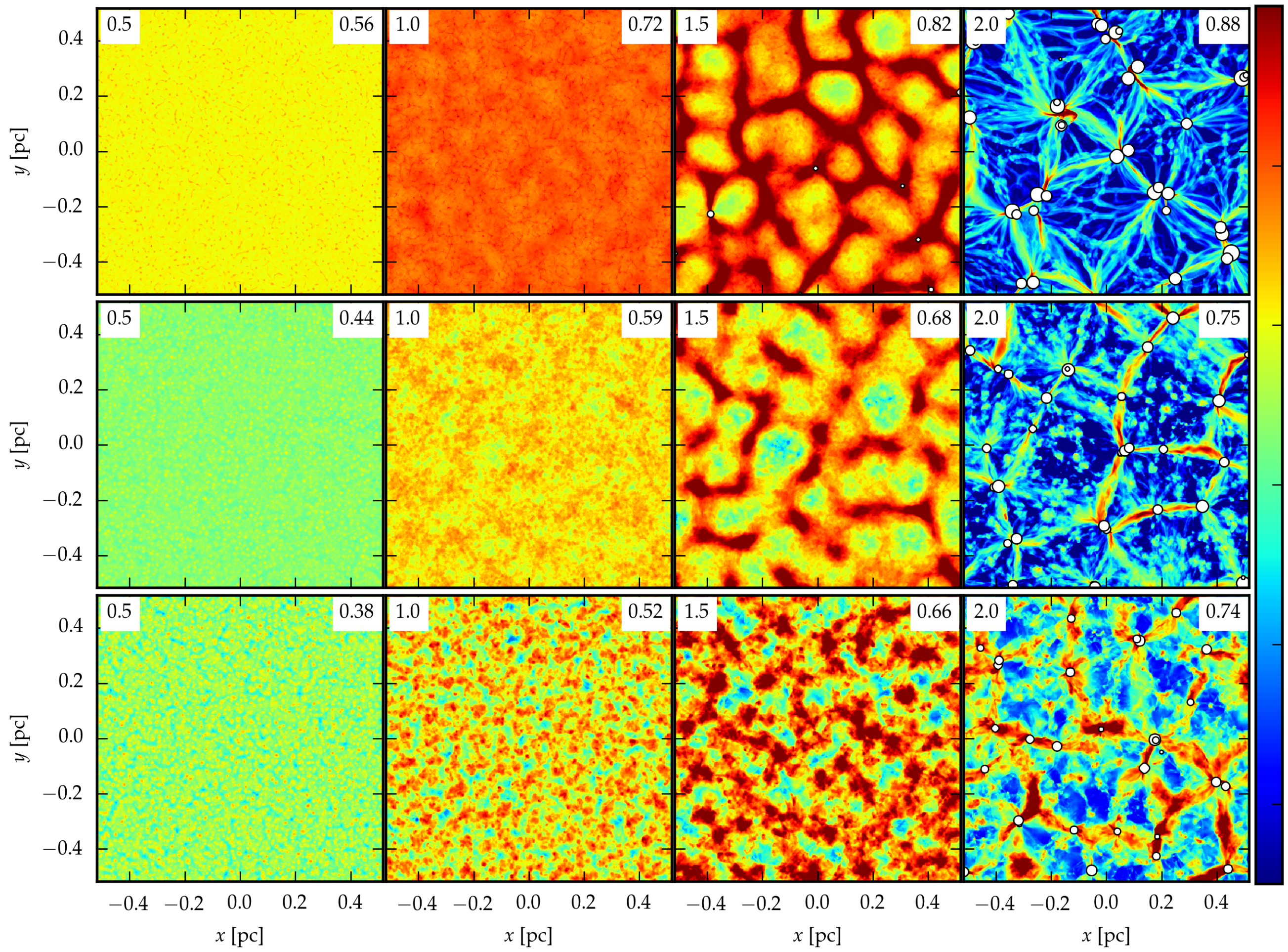

Figure 10. Evolution of surface density for accreting simulations. TOP ROW: $\mathscr{M} = 5$ (model A30_05_03_N), MIDDLE: $\mathscr{M} = 10$ (A30_10_03_N), BOTTOM: $\mathscr{M} = 20$ (A30_20_03_N). Time in Myr is in the upper left corner, the value of parameter A in the upper right corner.

the pressure gradient term since the unstable objects form via coalescence when the role of pressure support is already lost. Thus,

$$t_{\rm O} = 0.76\ {\rm Myr}\ c_{s2}^{\frac{28}{37}}\ n_3^{-\frac{33}{74}}\ \dot{N}_{49}^{-\frac{4}{37}}. \qquad (22)$$

8.2 The properties of fragments formed in a shell swept up by an expanding H II region

Integrating Eq. (21) we find $A(t_1)$ and from Eq. (20) fragmenting time t_1. We evaluate integral Eq. (21) for $c_{\rm S} = 0.2$km/s on a set of $\dot{N}_{49} \times n_3$ in range $(0.1, 10) \times (0.1, 10)$,

than at $t_{\rm O}$. However, the results (Eq. (23)) are weakly dependent on $t_{\rm O}$; Any numerical coefficients in Eq. (23) would differ by less than 20 % if we used $t_{\rm O} = 0$ instead of Eq. (22).

and by polynomial fitting we find

$$t_{\rm FRG} = 2.4\ {\rm Myr}\ n_3^{-0.43}\ \dot{N}_{49}^{-0.12} \qquad (23a)$$

$$M_{\rm FRG} = 3.1\ {\rm M}_\odot\ n_3^{-0.41}\ \dot{N}_{49}^{-0.16} \qquad (23b)$$

$$r_{\rm FRG} = 0.12\ {\rm pc}\ n_3^{-0.44}\ \dot{N}_{49}^{-0.11} \qquad (23c)$$

$$A_{\rm FRG} = 0.51\ n_3^{0.04}\ \dot{N}_{49}^{-0.08} \qquad (23d)$$

$$\Sigma_{\rm FRG} = 63\ \ {\rm M}_\odot\ {\rm pc}^{-2}\ n_3^{0.46}\ \dot{N}_{49}^{0.08} \qquad (23e)$$

$$R_{\rm FRG} = 7.7\ {\rm pc}\ n_3^{-0.53}\ \dot{N}_{49}^{0.08}, \qquad (23f)$$

where $M_{\rm FRG}$ is fragment mass, $r_{\rm FRG}$ fragment radius, and $A_{\rm FRG}$, $R_{\rm FRG}$ and $\Sigma_{\rm FRG}$ are parameter A, shell radius and surface density at time $t_{\rm FRG}$, respectively. Since we show in Sections 5.3 and 7 that fragment mass of a pressure confined layer is comparable to the Jeans mass, we use the Jeans mass as the estimate of fragment mass in Eq. (23b). We compare Eq. (23) with results of previous studies in Section 9.3.

Throughout this section, we have assumed that the shell fragments in external pressure dominated case. The highest value attained by A in Eq. (23d) justifies this assumption ($A_{\rm FRG} \lesssim 0.6$) unless n_3 is either very high or $\dot{N}_{49}$ very low.

We restrict our study to sound velocity $c_{s2} = 1$ (i.e. shell temperature 10 K) to fulfill the condition $A_{\rm FRG} \lesssim 0.6$ for re-

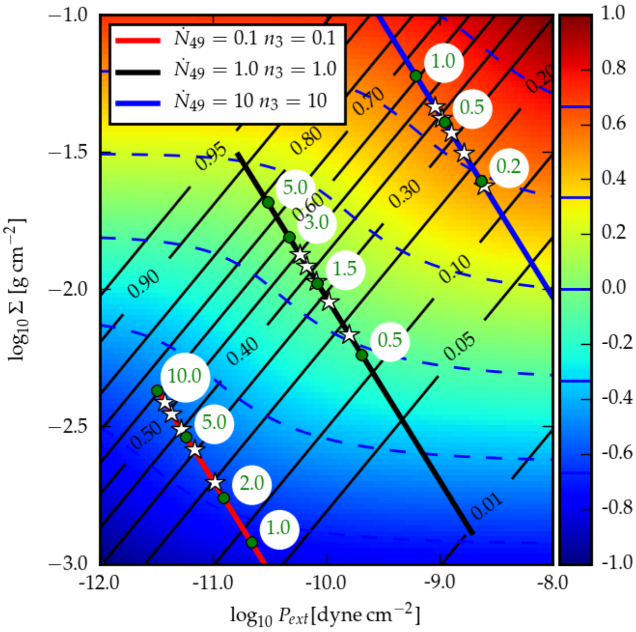

Figure 11. Evolutionary paths for shell walls around expanding H II regions. The paths with $(\dot{N}_{49},\, n_3) = (0.1,\, 0.1)$, $(\dot{N}_{49},\, n_3) = (1,\, 1)$ and $(\dot{N}_{49},\, n_3) = (10,\, 10)$ are shown by red, black and blue lines, respectively. Green circles with numbers give time in Myr since the expansion started. White asterisks represent the instants when the integral in Eq. (18) equals 0, 0.25, 0.50, 0.75 and 1.0. Parameter A is shown by black labelled contours. Colourscale and dashed blue contours represent logarithm of the integrand in Eq. (18) expressed in Myr^{-1}. The plot is constructed for $c_{s2} = 1$.

alistic values of $\dot{N}_{49}$ and n_3 because the area in $(\dot{N}_{49}, n_3)$ plane where the condition is met decreases as c_{S} increases. Since fragmentation of self–gravity dominated shells is more complicated (time dependent ρ_0, gravitational focusing on emerging fragments, …), it is not clear what is the proxy for fragment mass in this case and we do not study it here.

9 DISCUSSION

9.1 Comparison of numerical with analytic dispersion relations

The simulations in linear regime (when perturbed surface density Σ_1 is smaller than unperturbed Σ_{O}) clearly reproduce the semi–analytical estimate E78 in both self–gravity ($A = 0.99$) and pressure dominated ($A = 0.18$) cases (Fig. 2). We do not detect any systematic difference from E78 confirming correctness of the derivation done by Elmegreen & Elmegreen (1978). Although W10 provides a good approximation to the range of unstable wavenumbers in the self–gravity dominated case, it underestimates the highest unstable wavenumber k_{MAX} for $A \lesssim 0.5$ (Fig. 1). V83 overestimates k_{MAX} by a factor 2 for $A = 1$, predicts correct k_{MAX} for $A \simeq 0.6$ and underestimates k_{MAX} for lower A.

Comparing to work of Dale et al. (2009) and Wünsch et al. (2010), our non–accreting models are more suitable for testing dispersion relations of a layer since they have time independent Σ_{O} and no stretching. They are also completely free of Vishniac and Rayleigh–Taylor instabilities. The lowest value of A that Wünsch et al. (2010) reach is 0.42 (bottom right panel in their fig. 7). Although their results favour W10 to V83, they can hardly distinguish W10 from E78. We recover a less noisy dispersion relation and also reach lower value of A where we can detect the differences between W10 and E78.

Since W10 was proposed to include the influence of the external pressure, it may be surprising why W10 differs from our results (and therefore E78) when $A \lesssim 0.5$. We illustrate the limitation of W10 on a simple model where the layer is perturbed by an overdensity in a form of a circular patch of radius R_C and central surface density Σ_1. The perturbed surface density decreases to zero from the centre to the edge at R_C. We estimate its stability against lateral collapse by comparing self–gravity with pressure gradient between the centre and the edge of the perturbation taken in the mid-plane. Then the condition for a lateral collapse is

$$G\beta\pi\Sigma_1 \gtrsim \frac{P_1 - P_{\mathrm{O}}}{\rho_{\mathrm{O}} R_C}, \tag{24}$$

where P_1 and P_{O} is the pressure in the centre and the edge of the perturbation, respectively. Factor β takes into account that the perturbation generates non–spherically symmetric gravitational field. Factor β is of order unity. Substituting $\Sigma_1 + \Sigma_{\mathrm{O}}$ and Σ_{O} into Eq. (6) and using Eq. (5), Eq. (24) becomes $R_C\beta \gtrsim 2H_{\mathrm{HT}}$. Assuming $R_C = \lambda/2$, Eq. (24) takes the form

$$\beta\pi/2 \gtrsim kH_{\mathrm{HT}}. \tag{25}$$

Therefore the model explains why the range of unstable wavelengths is of the order of the layer thickness for any A as proposed by E78 and found in our simulations.

The limit of W10 (Eq. (9)) in $A \to 0$ predicts a significantly narrower range of unstable wavelengths, $kH_{\mathrm{HT}} \leq 9\pi^2 A^2/20$. The difference is due to how a perturbation is treated in the models. Imposing a perturbation with positive surface density Σ_1 when A is small, the layer thickens locally, so the majority of perturbed mass is deposited above the surface with very little density enhancement in the midplane. The layer is almost of constant density where variations in surface density are dominated by corrugations of the surface. The weak dependence of P_1 on Σ_1 when $2P_{\mathrm{EXT}}/(\pi G\Sigma_{\mathrm{O}}^2) \gg 1$ is apparent from Eq. (6). The density (pressure) gradient is much smaller than it would be if the perturbation were placed in the midplane, so the pressure gradient is easily overcame by self–gravity and substantially shorter wavelengths are unstable. In contrast, this mechanism is absent in W10 where the perturbed mass is in the form of a homogeneous spheroid with no possibility to place the excess mass outside its surfaces. This assumption in W10 results in much higher difference between pressures P_{O} and P_1, which needs a more massive fragment (with longer λ_{MAX}) to be overcame with its self–gravity.

In Section 8, assuming that shells swept up by H II regions are at temperature 10K, we conclude that the shells fragment in pressure dominated case. In this case, the significant difference between E78 and the other two dispersion relations leads to a substantially different prediction for fragment masses. On the other hand, V83 or W10 may still provide rough estimates for fragment masses of large H I shells, which are self–gravity dominated. Also note that E78 cannot be applied to layers forming at the interface between two colliding streams because such layers lack a surface with a contact discontinuity.

9.2 The effect of pre-existing density structure in the accretion flow

We assume that the perturbing amplitudes for both polychromatic and accreting simulations do not depend on k (see Section 5.1 for details), and that the accreting simulations accrete homogeneous medium. These assumptions significantly constrain the possible spectrum of perturbations. This simple model was adopted in order to reduce the number of free parameters. The real interstellar medium is highly inhomogeneous and when accreted, the resulting surface density enhancements have presumably different spectrum of perturbations. Since our fit giving the dependence of the number of e–folding times n_{EFOLD} on A is done for the spectrum we adopt, the form of $n_{\mathrm{EFOLD}} = n_{\mathrm{EFOLD}}(A)$ is presumably a function of the spectrum shape. In other words, the spectrum introduces another dimensionless parameters into Eq. (15). The parameters may further alter the properties of the fragmenting shell (Eq. (23)).

Accretion of even a single cloud could modify properties of final fragments substantially. For illustration, consider a spherically symmetric cloud. When accreted on a homogeneous layer, the ensuing structure would be a superposition of the layer and a circular overdensity. We further assume that the circular cloud contains many Jeans masses. This configuration is presumably prone to the edge effect (Burkert & Hartmann 2004; Pon et al. 2012), so it would tend to collapse laterally on its own timescale t_{GC} proportional to its radius r_{AC} and overdensity Σ_1 as $t_{GC} \simeq \sqrt{r_{AC}/(\pi G\Sigma_1)}$. Given that the layer contains pre-existing perturbations of small amplitudes, the globally collapsing circular cloud would also fragment as a part of a layer and would break into pieces as we saw in Section 5.3.

We suggest that external pressure could influence the result of fragmentation also in these circumstances if the circular cloud breaks into pieces before it collapsed globally. If the cloud is dominated by self–gravity, the fragments undergo an imminent collapse, so their radii shrink significantly diminishing probability of further coalescence. Consequently, the fragments would form a cluster in the center. If the cloud is dominated by external pressure, the fragments are still stable against gravitational collapse, so their radii are comparable to their distances, and they can coalesce. However, the coalescence rate would be significantly enhanced in comparison to the scenario we saw in Section 5.3, since the fragments would be attracted to the centre or swept up by the passing edge of the cloud. This probably leads to objects substantially more massive than the Jeans mass. This issue may be an objective for future work.

9.3 Fragmenting shells in other works

When estimating properties of fragments forming in the shell, we use significantly simplified models. The most important simplifications are the following: no deceleration, no ionising radiation penetrating into the shell, no complicated thermodynamics, and homogeneous medium into which the shell expands. Vertical acceleration of the unperturbed layer has reflective symmetry relative to the midplane; this assumption is violated in decelerating shells where it changes the dispersion relation as is shown by Iwasaki, Inutsuka & Tsuribe (2011a). The role of stretching is probably not crucial as estimated by Whitworth et al. (1994a). These phenomena may influence the course of fragmentation significantly and possibly modify or even suppress coalescence driven collapse in real shells.

Nevertheless, our work improves the model proposed by Whitworth et al. (1994a), which adopts the same simplified assumptions, since we use more appropriate estimates for mass of fragments and relevant timescales. Taking into account approximations we made, we emphasize that Eq. (23) is rather an application of our results for layers than the definite answer to the problem of propagating star formation due to photoionising feedback. Assuming temperature of 10K in the shells, Eq. (23) predicts that shell fragmentation tends to form objects of too low mass for star formation to propagate.

The dependence of our estimate Eq. (23) on $\dot{N}_{49}$ and n_3 is very close to the results provided by Whitworth et al. (1994a) and Iwasaki, Inutsuka & Tsuribe (2011b) (with sound velocity $c_{s2} = 1$). Compared to Whitworth et al. (1994a), Eq. (23a) predicts a slightly later fragmenting time ensuing in a larger shell radius (numerical constants they provide are 1.56 Myr and 5.8 pc). However, our model predicts much smaller fragment masses ($3.1\,\mathrm{M}_\odot$ vs. $23\,\mathrm{M}_\odot$) and smaller fragment radii (0.12 pc vs. 0.41 pc). This result is the consequence of taking as a proxy for fragment mass the Jeans mass for a significantly compressed layer instead of the Jeans mass for not compressed layer as done by Whitworth et al. (1994a).

In order to test the numerical constants in formulae derived by Whitworth et al. (1994a), Dale, Bonnell & Whitworth (2007) select one point in $\dot{N}_{49}, n_3$ plane, $(\dot{N}_{49}, n_3) = (1.0, 0.2)$ and follow its evolution by an SPH simulation. They find an approximate agreement with the work of Whitworth et al. (1994a). However, comparing density of their shell $\sim 10^{-21}\mathrm{g\,cm^{-3}}$ with the analytic value which is approx. 50× higher, we suspect that their resolution is not enough to resolve the shell vertically. The low–density in the shell leads to fragments of artificially high mass.

On the other hand, our mass estimate in Eq. (23b) is close to the value $3.5\,\mathrm{M_\odot}$ found by Iwasaki, Inutsuka & Tsuribe (2011b) based on monochromatic SPH simulations. We cannot compare fragmenting time since they use a different definition of the quantity.

10 CONCLUSIONS

We perform 3D hydrodynamic simulations of self–gravitating isothermal layers in order to investigate their dispersion relations and subsequent fragmentation. We apply the results of fragmenting and accreting layers to estimate typical masses and fragmenting time for a shell swept up around an H II region.

We find that if the perturbations are small, thermal pressure confined layers fragment in an excellent agreement with the dispersion relation proposed by Elmegreen & Elmegreen (1978) both in the self–gravity and pressure dominated case. PAGI (Wünsch et al. 2010) is a good approximation and thin shell (Vishniac 1983) a rough approximation in the self–gravity dominated case. However, the latter two are inappropriate for the pressure dominated case ($A \lesssim 0.5$; Eq. (3)) because they do not take into account surface corrugations. Since the shells around H II regions presumably fragment in the pressure dominated case, we suggest that both PAGI and thin shell dispersion relations are not appropriate for their description.

Fragmentation in the non–linear regime proceeds in two qualitatively different ways depending on parameter A. When the layer is dominated by self–gravity, fragments form by a monolithic collapse. When the layer is dominated by external pressure, it fragments in two steps; firstly it breaks into small gravitationally stable objects. It is an interesting feature because purely gravitational instability in planar geometry can form objects which are themselves stable against gravitational collapse. Then, the fragments continuously merge until they form an unstable object which eventually collapses (coalescence driven collapse). Neither of the dispersion relations presented can predict correctly properties of gravitationally bound fragments for a pressure dominated layer. However, a rough estimate for their mass is the Jeans mass in the midplane of the layer.

In the non–linear regime, we investigate the possibility that the layer self–organises and forms a regular pattern on its surface. We seek our standard models covering various degree of external pressure confinement ($A = 0.18$, $A = 0.60$, $A = 0.99$), and find no evidence for this scenario. In addition, we obtain the same result with two models designed to enhance pattern formation. We note that our method is able to find any regular pattern, not only a hexagonal pattern as is suggested to form by analytic work of Fuchs (1996). Instead of regular patterns, we observe formation of randomly oriented filamentary–like structures in agreement with Miyama, Narita & Hayashi (1987a,b).

For pressure dominated layers, we substitute boundary conditions on one surface from thermal pressure for an accreting homogeneous medium. The dispersion relation for accreting layers has the range of unstable wavenumbers extended towards higher values of k in comparison to the dispersion relation for thermal pressure confined layers. The highest growth rate is by factor $\simeq 2$ higher. In the non–linear regime of fragmentation, accreting layers also undergo monolithic or coalescence driven collapse depending on the importance of confining pressure during the major part of fragmentation. Layers with high accreting rate become earlier dominated by self–gravity and collapse monolithically, while layers with lower accreting rate remain dominated by external pressure and fragment via coalescence driven collapse. Fragmentation occurs at time comparable to thermal pressure confined layers with the same instantaneous surface density and ambient pressure. The mass of gravitationally bound fragments is again comparable to the Jeans mass.

We use our results from accreting layers to estimate fragment properties of a shell swept–up around an expanding H II region. For typical density ($10^3\,\mathrm{cm^{-3}}$) and temperature (10 K) in molecular clouds, the fragmentation is accomplished while the shell is still dominated by the external pressure. This leads to fragment masses $\simeq 3\,\mathrm{M_\odot}$. Stars formed of fragments of this mass are not able to ignite new H II regions. This indicates that for star formation to propagate, either higher temperature in shells or a different scenario (e.g. geometry) is required.

ACKNOWLEDGMENTS

The authors like to thank the referee, Sven Van Loo for constructive comments which helped to significantly improve the paper. FD, RW and JP acknowledge support from the Czech Science Foundation grant P209/12/1795 and by the project RVO:67985815. The presented simulations were performed on IT4I facilities supported by The Ministry of Education, Youth and Sports from the Large Infrastructures for Research, Experimental Development and Innovations project IT4Innovations National Supercomputing Center LM2015070.

REFERENCES

Barnes J., Hut P., 1986, Nat, 324, 446
Bik A. et al., 2010, ApJ, 713, 883
Blaauw A., 1964, ARA&A, 2, 213
Blaauw A., 1991, in NATO Advanced Science Institutes (ASI) Series C, Vol. 342, NATO Advanced Science Institutes (ASI) Series C, Lada C. J., Kylafis N. D., eds., p. 125
Boyd D. F. A., Whitworth A. P., 2005, A&A, 430, 1059
Brown A. G. A., de Geus E. J., de Zeeuw P. T., 1994, A&A, 289, 101
Burkert A., Hartmann L., 2004, ApJ, 616, 288
Churchwell E. et al., 2007, ApJ, 670, 428
Colella P., Woodward P. R., 1984, Journal of Computational Physics, 54, 174
Dale J. E., Bonnell I. A., Whitworth A. P., 2007, MNRAS, 375, 1291
Dale J. E., Wünsch R., Whitworth A., Palouš J., 2009, MNRAS, 398, 1537

Dawson J. R., McClure-Griffiths N. M., Kawamura A., Mizuno N., Onishi T., Mizuno A., Fukui Y., 2011, ApJ, 728, 127

Dawson J. R., Mizuno N., Onishi T., McClure-Griffiths N. M., Fukui Y., 2008, MNRAS, 387, 31

Deharveng L. et al., 2010, A&A, 523, A6

Deharveng L., Zavagno A., Caplan J., 2005, A&A, 433, 565

Doroshkevich A. G., 1980, Soviet Ast., 24, 152

Egorov O. V., Lozinskaya T. A., Moiseev A. V., Smirnov-Pinchukov G. V., 2014, MNRAS, 444, 376

Ehlerová S., Palouš J., 2005, A&A, 437, 101

Elmegreen B. G., 1994, ApJ, 427, 384

Elmegreen B. G., 1998, in Astronomical Society of the Pacific Conference Series, Vol. 148, Origins, Woodward C. E., Shull J. M., Thronson Jr. H. A., eds., p. 150

Elmegreen B. G., Elmegreen D. M., 1978, ApJ, 220, 1051

Elmegreen B. G., Lada C. J., 1977, ApJ, 214, 725

Ewald P. P., 1921, Annalen der Physik, 369, 253

Federrath C., Banerjee R., Clark P. C., Klessen R. S., 2010, ApJ, 713, 269

Fryxell B. et al., 2000, ApJS, 131, 273

Fuchs B., 1996, MNRAS, 278, 985

Goldreich P., Lynden-Bell D., 1965, MNRAS, 130, 97

Iwasaki K., Inutsuka S.-i., Tsuribe T., 2011a, ApJ, 733, 16

Iwasaki K., Inutsuka S.-i., Tsuribe T., 2011b, ApJ, 733, 17

Kim J.-G., Kim W.-T., Seo Y. M., Hong S. S., 2012, ApJ, 761, 131

Klessen R., 1997, MNRAS, 292, 11

Lubow S. H., Pringle J. E., 1993, MNRAS, 263, 701

MacNeice P., Olson K. M., Mobarry C., de Fainchtein R., Packer C., 2000, Computer Physics Communications, 126, 330

Martins F., Schaerer D., Hillier D. J., 2005, A&A, 436, 1049

Miyama S. M., Narita S., Hayashi C., 1987a, Progress of Theoretical Physics, 78, 1051

Miyama S. M., Narita S., Hayashi C., 1987b, Progress of Theoretical Physics, 78, 1273

Pon A., Toalá J. A., Johnstone D., Vázquez-Semadeni E., Heitsch F., Gómez G. C., 2012, ApJ, 756, 145

Salmon J. K., Warren M. S., 1994, Journal of Computational Physics, 111, 136

Simpson R. J. et al., 2012, MNRAS, 424, 2442

Spitzer L., 1978, Physical processes in the interstellar medium

Spitzer, Jr. L., 1942, ApJ, 95, 329

Springel V., 2005, MNRAS, 364, 1105

Truelove J. K., Klein R. I., McKee C. F., Holliman, II J. H., Howell L. H., Greenough J. A., 1997, ApJ, 489, L179

Van Loo S., Keto E., Zhang Q., 2014, ApJ, 789, 37

Vishniac E. T., 1983, ApJ, 274, 152

Whitworth A. P., Bhattal A. S., Chapman S. J., Disney M. J., Turner J. A., 1994a, A&A, 290

Whitworth A. P., Bhattal A. S., Chapman S. J., Disney M. J., Turner J. A., 1994b, MNRAS, 268, 291

Wünsch R., Dale J. E., Palouš J., Whitworth A. P., 2010, MNRAS, 407, 1963

Wünsch R., Palouš J., 2001, A&A, 374, 746

APPENDIX A: CLUMP FINDING ALGORITHM

In order to determine the fragmenting time and mass of emerging bound objects, we need to identify gravitationally bound entities. We search for a gravitationally bound object around each minimum in gravitational potential in the computational domain. The gravitational potential is a sum of the gaseous potential as determined by FLASH code and the potential due to sink particles. When investigating a particular minimum i at potential ϕ_i (Figure A1), we draw a sphere of the sink particle radius $r_{\rm SINK}$ with centre at the potential minimum, and check whether the sphere contains at least one grid cell with negative binding energy $e_{\rm CELL}$. The binding energy of a cell is

$$\begin{aligned} e_{\rm CELL} &= \frac{1}{2} m_{\rm CELL} (v_{\rm CELL} - v_{\rm CL})^2 + \frac{3 m_{\rm CELL} cs^2_{\rm CELL}}{2} + \\ & \frac{1}{2} m_{\rm CELL} (\phi_{\rm CELL} - \phi^{ij}), \qquad \text{(A1)} \end{aligned}$$

where $m_{\rm CELL}$, $\phi_{\rm CELL}$, $v_{\rm CELL}$ and $cs_{\rm CELL}$ are mass, potential, bulk velocity and sound velocity of the cell. The kinetic energy is corrected by velocity of the mass centre $v_{\rm CL}$ of the bound object, which is composed of all bound grid cells.

The gravitational binding energy is related to the potential at the saddle point ϕ^{ij} (the second letter in the superscript denotes the deeper minimum, i.e. $\phi_j < \phi_i$). The saddle for minimum i is a pair of two neighbouring cells at the lowest potential $\phi_{\rm CELL}$ where a path in potential from one cell monotonically descends to minimum i and a path from the other cell monotonically descends to another, deeper minimum j (see Fig. A1). Mixed boundary conditions are taken into account, so the path can lead through a periodic boundary. No cell with $\phi_{\rm CELL} > \phi^{ij}$ can be bound to the minimum i.

If at least one bound cell is found, the radius of the sphere is increased by one grid cell size and condition Eq. (A1) is applied to any cell in the spherical shell between the new and previous searching radius. The procedure is repeated until the sphere exceeds the saddle point, or until it exceeds the cloud boundary, i.e. all cells in the spherical shell are unbound. If sink particles are present, they are very close to local potential minima and their mass is added to the mass budget of the bound object identified around the minimum.

The computational domain typically contains many objects. Considerable number of the objects are interacting and overlapping. The algorithm firstly sorts the minima in ordering of decreasing potential and starts searching around the minimum with the highest value of potential and continues in direction of decreasing potential. This searching direction assures that the objects with minima at higher potential levels, which are usually situated close to more massive objects with minima at lower potential levels, are investigated before so that their mass is properly assigned to the lower mass objects. Any cell identified as bound is marked, and can not be accessed later when investigating a deeper minimum.

We illustrate some of the features of the algorithm on Fig. A1. Note that the ordering of potential minima ($\phi_m > \phi_l > \phi_i > \phi_j > \phi_k$) is not reflected by ordering of saddles $\phi^{lk} > \phi^{jk} > \phi^{mj} > \phi^{ij}$. Only cells around i with $\phi < \phi^{ij}$ can be assigned to minimum i. Since the saddle ϕ^{jk} for object j is at a higher equipotential surface then previ-

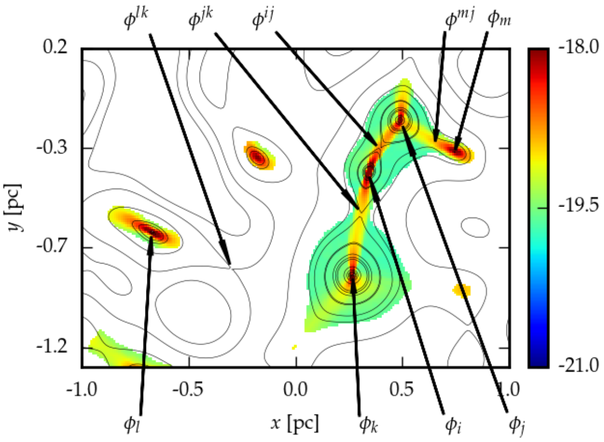

Figure A1. Position of saddles and potential minima to illustrate our clump finding algorithm. Potential minima and saddle points are marked by subscripts and superscripts, respectively. Equipotential curves are plotted by thin solid lines, cells identified as bound are plotted by colour corresponding to their density. Note that only selected minima and saddles are marked.

ous saddle ϕ^{ij}, many cells situated close to i, which were not previously assigned to minimum i are now identified as gravitationally bound and assigned to j. Cells situated around a shallow minimum at m, where no bound object was found previously, are checked if they are bound to j. The algorithm is able to find objects both filling and underfilling their critical equipotentials (e.g. i and l) and also identify highly non–spherically symmetric objects (e.g. j).

B Formulae for Ewald method implementation

We provide the functional forms of $\mathbf{A}^{Ewald}$, $A_i^{Ewald} \equiv -\partial P^{Ewald}/\partial r_i$ and spatial derivatives of $\mathbf{A}^{Ewald}$, $C_{ij}^{Ewald} \equiv \partial A_i^{Ewald}/\partial r_j$ for all the configurations studied in Chapter 4. These formulae may be useful for an implementation of the Ewald method into a hydrodynamic code.

B.1 Configuration 3P

The boundary conditions are periodic in all three directions $\mathbf{e}_x$, $\mathbf{e}_y$ and $\mathbf{e}_z$. To simplify the formulae, we introduce

$$u_{i_1,i_2,i_3} = (x - x_a - i_1 L_x)^2 + (y - y_a - i_2 b L_x)^2 + (z - z_a - i_3 c L_x)^2, \tag{B.9}$$

$$v_{l_1,l_2,l_3} = \frac{2\pi l_1 (x - x_a)}{L_x} + \frac{2\pi l_2 (y - y_a)}{b L_x} + \frac{2\pi l_3 (z - z_a)}{c L_x}. \tag{B.10}$$

From eq. (4.2), one obtains the components of function $\mathbf{A}^{Ewald}$ as

$$\begin{aligned} A_x^{Ewald} = & \sum_{\substack{i_1,i_2,i_3 \\ i_1^2+(bi_2)^2+(ci_3)^2 \le 10}} \left\{ \frac{2\alpha}{\sqrt{\pi}} \frac{\exp(-\alpha^2 u_{i_1,i_2,i_3})}{u_{i_1,i_2,i_3}} + \frac{\mathrm{erfc}(\alpha\sqrt{u_{i_1,i_2,i_3}})}{u_{i_1,i_2,i_3}^{3/2}} \right\} (x - x_a - i_1 L_x) \\ & + \frac{2}{bcL_x^2} \sum_{\substack{l_1,l_2,l_3 \\ l_1^2+(l_2/b)^2+(l_3/c)^2 \le 10}} l_1 \frac{\exp\left(-\zeta(l_1^2 + (l_1/b)^2 + (l_3/c)^2)\right)}{l_1^2 + (l_1/b)^2 + (l_3/c)^2} \sin\left(v_{l_1,l_2,l_3}\right), \end{aligned} \tag{B.11}$$

$$\begin{aligned} A_y^{Ewald} = & \sum_{\substack{i_1,i_2,i_3 \\ i_1^2+(bi_2)^2+(ci_3)^2 \le 10}} \left\{ \frac{2\alpha}{\sqrt{\pi}} \frac{\exp(-\alpha^2 u_{i_1,i_2,i_3})}{u_{i_1,i_2,i_3}} + \frac{\mathrm{erfc}(\alpha\sqrt{u_{i_1,i_2,i_3}})}{u_{i_1,i_2,i_3}^{3/2}} \right\} (y - y_a - i_2 b L_x) \\ & + \frac{2}{b^2 c L_x^2} \sum_{\substack{l_1,l_2,l_3 \\ l_1^2+(l_2/b)^2+(l_3/c)^2 \le 10}} l_2 \frac{\exp\left(-\zeta(l_1^2 + (l_1/b)^2 + (l_3/c)^2)\right)}{l_1^2 + (l_1/b)^2 + (l_3/c)^2} \sin\left(v_{l_1,l_2,l_3}\right), \end{aligned} \tag{B.12}$$

$$\begin{aligned} A_z^{Ewald} = & \sum_{\substack{i_1,i_2,i_3 \\ i_1^2+(bi_2)^2+(ci_3)^2 \le 10}} \left\{ \frac{2\alpha}{\sqrt{\pi}} \frac{\exp(-\alpha^2 u_{i_1,i_2,i_3})}{u_{i_1,i_2,i_3}} + \frac{\mathrm{erfc}(\alpha\sqrt{u_{i_1,i_2,i_3}})}{u_{i_1,i_2,i_3}^{3/2}} \right\} (z - z_a - i_3 c L_x) \\ & + \frac{2}{bc^2 L_x^2} \sum_{\substack{l_1,l_2,l_3 \\ l_1^2+(l_2/b)^2+(l_3/c)^2 \le 10}} l_3 \frac{\exp\left(-\zeta(l_1^2 + (l_1/b)^2 + (l_3/c)^2)\right)}{l_1^2 + (l_1/b)^2 + (l_3/c)^2} \sin\left(v_{l_1,l_2,l_3}\right). \end{aligned} \tag{B.13}$$

Calculating spatial derivatives of eq. (B.11) to eq. (B.13), we obtain

$$\begin{aligned} C_{xx}^{Ewald} = & - \sum_{\substack{i_1,i_2,i_3 \\ i_1^2+(bi_2)^2+(ci_3)^2 \le 10}} \frac{2\alpha}{\sqrt{\pi}} \frac{\exp(-\alpha^2 u_{i_1,i_2,i_3})}{u_{i_1,i_2,i_3}} + \frac{\mathrm{erfc}(\alpha\sqrt{u_{i_1,i_2,i_3}})}{u_{i_1,i_2,i_3}^{3/2}} + \\ & \left\{ \frac{3\mathrm{erfc}(\alpha\sqrt{u_{i_1,i_2,i_3}})}{u_{i_1,i_2,i_3}^{5/2}} + \frac{2\alpha \exp\left(-\alpha^2 u_{i_1,i_2,i_3}\right)}{\sqrt{\pi} u_{i_1,i_2,i_3}} \left(2\alpha^2 + 3/u_{i_1,i_2,i_3}\right) \right\} (x - x_a - i_1 L_x)^2 \\ & + \frac{4\pi}{bcL_x^2} \sum_{\substack{l_1,l_2,l_3 \\ l_1^2+(l_2/b)^2+(l_3/c)^2 \le 10}} l_1^2 \frac{\exp\left(-\zeta(l_1^2 + (l_1/b)^2 + (l_3/c)^2)\right)}{l_1^2 + (l_1/b)^2 + (l_3/c)^2} \cos\left(v_{l_1,l_2,l_3}\right), \end{aligned} \tag{B.14}$$

$$
\begin{aligned}
C_{xy}^{Ewald} &= -\sum_{\substack{i_1,i_2,i_3\\ i_1^2+(bi_2)^2+(ci_3)^2\le 10}} \left\{ \frac{2\alpha\exp\left(-\alpha^2 u_{i_1,i_2,i_3}\right)}{\sqrt{\pi}u_{i_1,i_2,i_3}}\left(2\alpha^2+3/u_{i_1,i_2,i_3}\right)\right.\\
&\left. +\frac{3\mathrm{erfc}(\alpha\sqrt{u_{i_1,i_2,i_3}})}{u_{i_1,i_2,i_3}^{5/2}}\right\}(x-x_a-i_1L_x)(y-y_a-i_2bL_x)\\
&+\frac{4\pi}{b^2cL_x^2}\sum_{\substack{l_1,l_2,l_3\\ l_1^2+(l_2/b)^2+(l_3/c)^2\le 10}} l_1l_2\,\frac{\exp\left(-\zeta(l_1^2+(l_1/b)^2+(l_3/c)^2)\right)}{l_1^2+(l_1/b)^2+(l_3/c)^2}\cos\left(v_{l_1,l_2,l_3}\right), \quad \text{(B.15)}
\end{aligned}
$$

$$
\begin{aligned}
C_{xz}^{Ewald} &= -\sum_{\substack{i_1,i_2,i_3\\ i_1^2+(bi_2)^2+(ci_3)^2\le 10}} \left\{ \frac{2\alpha\exp\left(-\alpha^2 u_{i_1,i_2,i_3}\right)}{\sqrt{\pi}u_{i_1,i_2,i_3}}\left(2\alpha^2+3/u_{i_1,i_2,i_3}\right)\right.\\
&\left. +\frac{3\mathrm{erfc}(\alpha\sqrt{u_{i_1,i_2,i_3}})}{u_{i_1,i_2,i_3}^{5/2}}\right\}(x-x_a-i_1L_x)(z-z_a-i_3cL_x)\\
&+\frac{4\pi}{bc^2L_x^2}\sum_{\substack{l_1,l_2,l_3\\ l_1^2+(l_2/b)^2+(l_3/c)^2\le 10}} l_1l_3\,\frac{\exp\left(-\zeta(l_1^2+(l_1/b)^2+(l_3/c)^2)\right)}{l_1^2+(l_1/b)^2+(l_3/c)^2}\cos\left(v_{l_1,l_2,l_3}\right), \quad \text{(B.16)}
\end{aligned}
$$

$$
\begin{aligned}
C_{yy}^{Ewald} &= -\sum_{\substack{i_1,i_2,i_3\\ i_1^2+(bi_2)^2+(ci_3)^2\le 10}} \frac{2\alpha}{\sqrt{\pi}}\frac{\exp(-\alpha^2 u_{i_1,i_2,i_3})}{u_{i_1,i_2,i_3}}+\frac{\mathrm{erfc}(\alpha\sqrt{u_{i_1,i_2,i_3}})}{u_{i_1,i_2,i_3}^{3/2}}+\\
&\left\{\frac{3\mathrm{erfc}(\alpha\sqrt{u_{i_1,i_2,i_3}})}{u_{i_1,i_2,i_3}^{5/2}}+\frac{2\alpha\exp\left(-\alpha^2 u_{i_1,i_2,i_3}\right)}{\sqrt{\pi}u_{i_1,i_2,i_3}}\left(2\alpha^2+3/u_{i_1,i_2,i_3}\right)\right\}(y-y_a-i_2bL_x)^2\\
&+\frac{4\pi}{b^3cL_x^2}\sum_{\substack{l_1,l_2,l_3\\ l_1^2+(l_2/b)^2+(l_3/c)^2\le 10}} l_2^2\,\frac{\exp\left(-\zeta(l_1^2+(l_1/b)^2+(l_3/c)^2)\right)}{l_1^2+(l_1/b)^2+(l_3/c)^2}\cos\left(v_{l_1,l_2,l_3}\right), \quad \text{(B.17)}
\end{aligned}
$$

$$
\begin{aligned}
C_{yz}^{Ewald} &= -\sum_{\substack{i_1,i_2,i_3\\ i_1^2+(bi_2)^2+(ci_3)^2\le 10}} \left\{ \frac{2\alpha\exp\left(-\alpha^2 u_{i_1,i_2,i_3}\right)}{\sqrt{\pi}u_{i_1,i_2,i_3}}\left(2\alpha^2+3/u_{i_1,i_2,i_3}\right)\right.\\
&\left. +\frac{3\mathrm{erfc}(\alpha\sqrt{u_{i_1,i_2,i_3}})}{u_{i_1,i_2,i_3}^{5/2}}\right\}(y-y_a-i_2bL_x)(z-z_a-i_3cL_x)\\
&+\frac{4\pi}{b^2c^2L_x^2}\sum_{\substack{l_1,l_2,l_3\\ l_1^2+(l_2/b)^2+(l_3/c)^2\le 10}} l_2l_3\,\frac{\exp\left(-\zeta(l_1^2+(l_1/b)^2+(l_3/c)^2)\right)}{l_1^2+(l_1/b)^2+(l_3/c)^2}\cos\left(v_{l_1,l_2,l_3}\right), \quad \text{(B.18)}
\end{aligned}
$$

$$
\begin{aligned}
C_{zz}^{Ewald} &= - \sum_{\substack{i_1,i_2,i_3 \\ i_1^2+(bi_2)^2+(ci_3)^2\le 10}} \frac{2\alpha}{\sqrt{\pi}} \frac{\exp(-\alpha^2 u_{i_1,i_2,i_3})}{u_{i_1,i_2,i_3}} + \frac{\mathrm{erfc}(\alpha\sqrt{u_{i_1,i_2,i_3}})}{u_{i_1,i_2,i_3}^{3/2}} + \\
& \left\{ \frac{3\mathrm{erfc}(\alpha\sqrt{u_{i_1,i_2,i_3}})}{u_{i_1,i_2,i_3}^{5/2}} + \frac{2\alpha\exp\left(-\alpha^2 u_{i_1,i_2,i_3}\right)}{\sqrt{\pi}u_{i_1,i_2,i_3}} \left(2\alpha^2 + 3/u_{i_1,i_2,i_3}\right) \right\} (z - z_a - i_3 c L_x)^2 \\
& + \frac{4\pi}{bc^3 L_x^2} \sum_{\substack{l_1,l_2,l_3 \\ l_1^2+(l_2/b)^2+(l_3/c)^2\le 10}} l_3^2 \frac{\exp\left(-\zeta(l_1^2+(l_1/b)^2+(l_3/c)^2)\right)}{l_1^2+(l_1/b)^2+(l_3/c)^2} \cos\left(v_{l_1,l_2,l_3}\right). \qquad \text{(B.19)}
\end{aligned}
$$

B.2 Configuration 2P1I

The boundary conditions are periodic in directions $\mathbf{e}_x$ and $\mathbf{e}_y$ and isolated in direction $\mathbf{e}_z$. We define

$$
u_{i_1,i_2} = (x - x_a - i_1 L_x)^2 + (y - y_a - i_2 b L_x)^2 + (z - z_a)^2, \qquad \text{(B.20)}
$$

$$
v_{l_1,l_2} = \frac{2\pi l_1(x - x_a)}{L_x} + \frac{2\pi l_2(y - y_a)}{bL_x}, \qquad \text{(B.21)}
$$

to simplify the formulae below. In Section 4.2, the derivation of the equation for the potential led to eq. (4.16) with function I expressed by eq. (4.13) for $|l_1| + |l_2| \neq 0$. However, for practical work, it is necessary to rewrite the equation to overcome problems with numerical overflows and underflows in the long–range term P_L for computational domains elongated in the direction z (maximum value of γ is $2\pi L_z/L_x$, which causes problems in terms $\exp(2\gamma\sqrt{l_1^2 + (l_2/b)^2})$ and $\mathrm{erfc}((\zeta\sqrt{l_1^2 + (l_2/b)^2} + \gamma/2)/\sqrt{\zeta}))$. Thus, we express the long–range term for the potential as

$$
P_L(\vec{r}, \vec{r_a}) = \frac{1}{\pi L_x b} \sum_{\substack{l_1,l_2 \\ l_1^2+(l_1/b)^2\le 10}} \cos(v_{l_1,l_2}) \widetilde{I}(l_1, l_2, z - z_a), \qquad \text{(B.22)}
$$

where

$$
\begin{aligned}
\widetilde{I}(l_1, l_2, z - z_a) &= \frac{\pi}{2\sqrt{l_1^2 + (l_2/b)^2}} \left\{ \exp(-\frac{\gamma^2}{4\zeta}) \exp(-\zeta(l_1^2 + (l_2/b)^2)) \right. \\
& \times \mathrm{erfcx}\left(\frac{\zeta\sqrt{l_1^2 + (l_2/b)^2} + \gamma/2}{\sqrt{\zeta}} \right) \\
& \left. + \exp(-\gamma\sqrt{l_1^2 + (l_2/b)^2}) \times \mathrm{erfc}\left(\frac{\zeta\sqrt{l_1^2 + (l_2/b)^2} - \gamma/2}{\sqrt{\zeta}} \right) \right\}, \qquad \text{(B.23)}
\end{aligned}
$$

for $|l_1| + |l_2| \neq 0$. Function $\mathrm{erfcx}(x) \equiv \mathrm{erfc}(x)\exp(x^2)$ is the exponentially scaled complementary error function. For $l_1 = l_2 = 0$, $\widetilde{I}(0, 0, z - z_a) = I(0, 0, z - z_a)$ as given by eq. (4.15).

The components of function $\mathbf{A}^{Ewald}$ are

$$
\begin{aligned}
A_x^{Ewald} \quad &= \sum_{\substack{i_1,i_2 \\ i_1^2+(bi_2)^2\le 10}} \left\{ \frac{2\alpha}{\sqrt{\pi}} \frac{\exp(-\alpha^2 u_{i_1,i_2})}{u_{i_1,i_2}} + \frac{\operatorname{erfc}(\alpha\sqrt{u_{i_1,i_2}})}{u_{i_1,i_2}^{3/2}} \right\} (x - x_a - i_1 L_x) \\
&+ \frac{2}{bL_x^2} \sum_{\substack{l_1,l_2 \\ l_1^2+(l_2/b)^2\le 10}} l_1 \sin(v_{l_1,l_2}) \widetilde{I}(l_1, l_2, z - z_a), \qquad \text{(B.24)}
\end{aligned}
$$

$$
\begin{aligned}
A_y^{Ewald} \quad &= \sum_{\substack{i_1,i_2 \\ i_1^2+(bi_2)^2\le 10}} \left\{ \frac{2\alpha}{\sqrt{\pi}} \frac{\exp(-\alpha^2 u_{i_1,i_2})}{u_{i_1,i_2}} + \frac{\operatorname{erfc}(\alpha\sqrt{u_{i_1,i_2}})}{u_{i_1,i_2}^{3/2}} \right\} (y - y_a - i_2 b L_x) \\
&+ \frac{2}{b^2 L_x^2} \sum_{\substack{l_1,l_2 \\ l_1^2+(l_2/b)^2\le 10}} l_2 \sin(v_{l_1,l_2}) \widetilde{I}(l_1, l_2, z - z_a), \qquad \text{(B.25)}
\end{aligned}
$$

$$
\begin{aligned}
A_z^{Ewald} \quad &= \sum_{\substack{i_1,i_2 \\ i_1^2+(bi_2)^2\le 10}} \left\{ \frac{2\alpha}{\sqrt{\pi}} \frac{\exp(-\alpha^2 u_{i_1,i_2})}{u_{i_1,i_2}} + \frac{\operatorname{erfc}(\alpha\sqrt{u_{i_1,i_2}})}{u_{i_1,i_2}^{3/2}} \right\} (z - z_a) \\
&- \frac{2}{bL_x^2} \sum_{\substack{l_1,l_2 \\ l_1^2+(l_2/b)^2\le 10}} \cos(v_{l_1,l_2}) I'(l_1, l_2, z - z_a), \qquad \text{(B.26)}
\end{aligned}
$$

where

$$
\begin{aligned}
I'(l_1, l_2, z - z_a) \;&\equiv\; \mathrm{d}I(l_1, l_2, \gamma)/\mathrm{d}\gamma \\
&= \pi \Bigg\{ \exp(-\frac{\gamma^2}{4\zeta}) \exp(-\zeta(l_1^2 + (l_2/b)^2)) \\
&\quad \times \operatorname{erfcx}\left(\frac{\zeta\sqrt{l_1^2 + (l_2/b)^2} + \gamma/2}{\sqrt{\zeta}} \right) \\
&\quad - \exp(-\gamma\sqrt{l_1^2 + (l_2/b)^2}) \times \operatorname{erfc}\left(\frac{\zeta\sqrt{l_1^2 + (l_2/b)^2} - \gamma/2}{\sqrt{\zeta}} \right) \Bigg\} \qquad \text{(B.27)}
\end{aligned}
$$

The coefficients C_{ij}^{Ewald} are

$$
\begin{aligned}
C_{xx}^{Ewald} \quad &= - \sum_{\substack{i_1,i_2 \\ i_1^2+(bi_2)^2\le 10}} \frac{2\alpha}{\sqrt{\pi}} \frac{\exp(-\alpha^2 u_{i_1,i_2})}{u_{i_1,i_2}} + \frac{\operatorname{erfc}(\alpha\sqrt{u_{i_1,i_2}})}{u_{i_1,i_2}^{3/2}} + \\
&\left\{ \frac{3\operatorname{erfc}(\alpha\sqrt{u_{i_1,i_2}})}{u_{i_1,i_2}^{5/2}} + \frac{2\alpha \exp\left(-\alpha^2 u_{i_1,i_2}\right)}{\sqrt{\pi} u_{i_1,i_2}} \left(2\alpha^2 + 3/u_{i_1,i_2}\right) \right\} (x - x_a - i_1 L_x)^2 \\
&+ \frac{4\pi}{bL_x^3} \sum_{\substack{l_1,l_2 \\ l_1^2+(l_2/b)^2\le 10}} l_1^2 \cos\left(v_{l_1,l_2}\right) \widetilde{I}(l_1, l_2, z - z_a), \qquad \text{(B.28)}
\end{aligned}
$$

$$
\begin{aligned}
C_{xy}^{Ewald} \;=\; & -\sum_{\substack{i_1,i_2\\ i_1^2+(bi_2)^2\leq 10}} \left\{ \frac{2\alpha\exp\left(-\alpha^2 u_{i_1,i_2}\right)}{\sqrt{\pi}u_{i_1,i_2}}\left(2\alpha^2+3/u_{i_1,i_2}\right)\right.\\
& \left. +\frac{3\mathrm{erfc}(\alpha\sqrt{u_{i_1,i_2}})}{u_{i_1,i_2}^{5/2}}\right\}(x-x_a-i_1L_x)(y-y_a-i_2bL_x)\\
& +\frac{4\pi}{b^2L_x^3}\sum_{\substack{l_1,l_2\\ l_1^2+(l_2/b)^2\leq 10}} l_1 l_2\,\cos\left(v_{l_1,l_2}\right)\widetilde{I}(l_1,l_2,z-z_a),
\end{aligned}
\tag{B.29}
$$

$$
\begin{aligned}
C_{xz}^{Ewald} \;=\; & -\sum_{\substack{i_1,i_2\\ i_1^2+(bi_2)^2\leq 10}} \left\{ \frac{2\alpha\exp\left(-\alpha^2 u_{i_1,i_2}\right)}{\sqrt{\pi}u_{i_1,i_2}}\left(2\alpha^2+3/u_{i_1,i_2}\right)\right.\\
& \left. +\frac{3\mathrm{erfc}(\alpha\sqrt{u_{i_1,i_2}})}{u_{i_1,i_2}^{5/2}}\right\}(z-z_a)(x-x_a-i_1L_x)\\
& +\frac{2\pi}{bL_x^3}\sum_{\substack{l_1,l_2\\ l_1^2+(l_2/b)^2\leq 10}} l_1\,\sin\left(v_{l_1,l_2}\right)I'(l_1,l_2,z-z_a),
\end{aligned}
\tag{B.30}
$$

$$
\begin{aligned}
C_{yy}^{Ewald} \;=\; & -\sum_{\substack{i_1,i_2\\ i_1^2+(bi_2)^2\leq 10}} \frac{2\alpha}{\sqrt{\pi}}\frac{\exp(-\alpha^2 u_{i_1,i_2})}{u_{i_1,i_2}}+\frac{\mathrm{erfc}(\alpha\sqrt{u_{i_1,i_2}})}{u_{i_1,i_2}^{3/2}}+\\
& \left\{\frac{3\mathrm{erfc}(\alpha\sqrt{u_{i_1,i_2}})}{u_{i_1,i_2}^{5/2}}+\frac{2\alpha\exp\left(-\alpha^2 u_{i_1,i_2}\right)}{\sqrt{\pi}u_{i_1,i_2}}\left(2\alpha^2+3/u_{i_1,i_2}\right)\right\}(y-y_a-i_2bL_x)^2\\
& +\frac{4\pi}{b^3L_x^3}\sum_{\substack{l_1,l_2\\ l_1^2+(l_2/b)^2\leq 10}} l_1^2\,\cos\left(v_{l_1,l_2}\right)\widetilde{I}(l_1,l_2,z-z_a),
\end{aligned}
\tag{B.31}
$$

$$
\begin{aligned}
C_{yz}^{Ewald} \;=\; & -\sum_{\substack{i_1,i_2\\ i_1^2+(bi_2)^2\leq 10}} \left\{ \frac{2\alpha\exp\left(-\alpha^2 u_{i_1,i_2}\right)}{\sqrt{\pi}u_{i_1,i_2}}\left(2\alpha^2+3/u_{i_1,i_2}\right)\right.\\
& \left. +\frac{3\mathrm{erfc}(\alpha\sqrt{u_{i_1,i_2}})}{u_{i_1,i_2}^{5/2}}\right\}(z-z_a)(y-y_a-i_2bL_x)\\
& +\frac{2\pi}{b^2L_x^3}\sum_{\substack{l_1,l_2\\ l_1^2+(l_2/b)^2\leq 10}} l_2\,\sin\left(v_{l_1,l_2}\right)I'(l_1,l_2,z-z_a),
\end{aligned}
\tag{B.32}
$$

$$
\begin{aligned}
C_{zz}^{Ewald} \;=\; & -\sum_{\substack{i_1,i_2\\ i_1^2+(bi_2)^2\leq 10}} \frac{2\alpha}{\sqrt{\pi}}\frac{\exp(-\alpha^2 u_{i_1,i_2})}{u_{i_1,i_2}}+\frac{\mathrm{erfc}(\alpha\sqrt{u_{i_1,i_2}})}{u_{i_1,i_2}^{3/2}}+\\
& \left\{\frac{3\mathrm{erfc}(\alpha\sqrt{u_{i_1,i_2}})}{u_{i_1,i_2}^{5/2}}+\frac{2\alpha\exp\left(-\alpha^2 u_{i_1,i_2}\right)}{\sqrt{\pi}u_{i_1,i_2}}\left(2\alpha^2+3/u_{i_1,i_2}\right)\right\}(z-z_a)^2\\
& +\frac{1}{bL_x^2}\sum_{\substack{l_1,l_2\\ l_1^2+(l_2/b)^2\leq 10}} \cos\left(v_{l_1,l_2}\right)I''(l_1,l_2,z-z_a),
\end{aligned}
\tag{B.33}
$$

where

$$\begin{aligned}
I''(l_1,l_2,z-z_a) &\equiv \mathrm{d}I'(l_1,l_2,\gamma)/\mathrm{d}\gamma \\
&= \frac{2\pi^2}{\sqrt{\zeta}L_x}\Bigg\{\exp(-\frac{\gamma^2}{4\zeta})\exp(-\zeta(l_1^2+(l_2/b)^2))\times \\
&\quad \left[\frac{2}{\sqrt{\pi}}-\sqrt{\zeta(l_1^2+(l_2/b)^2)}\mathrm{erfcx}\left(\frac{\zeta\sqrt{l_1^2+(l_2/b)^2}+\gamma/2}{\sqrt{\zeta}}\right)\right] \\
&\quad -\sqrt{\zeta(l_1^2+(l_2/b)^2)}\exp(-\gamma\sqrt{l_1^2+(l_2/b)^2})\mathrm{erfc}\left(\frac{\zeta\sqrt{l_1^2+(l_2/b)^2}-\gamma/2}{\sqrt{\zeta}}\right)\Bigg\}
\end{aligned} \tag{B.34}$$

B.3 Configuration 1P2I

The boundary conditions are periodic in direction $\mathbf{e}_x$ and isolated in directions $\mathbf{e}_y$ and $\mathbf{e}_z$. We define

$$u_{i_1} = (x-x_a-i_1L_x)^2+(y-y_a)^2+(z-z_a)^2, \tag{B.35}$$

$$v_{l_1} = \frac{2\pi l_1(x-x_a)}{L_x}, \tag{B.36}$$

to simplify the formulae below. Differencing eq. (4.28), we find

$$\begin{aligned}
A_x^{Ewald} &= \sum_{i_1,i_1^2\leq 10}\left\{\frac{2\alpha}{\sqrt{\pi}}\frac{\exp(-\alpha^2u_{i_1})}{u_{i_1}}+\frac{\mathrm{erfc}(\alpha\sqrt{u_{i_1}})}{u_{i_1}^{3/2}}\right\}(x-x_a-i_1L_x) \\
&\quad +\frac{4\pi}{L_x^2}\sum_{l_1,l_1^2\leq 10} l_1\exp(-\zeta l_1^2)\sin(v_{l_1})K(l_1,y-y_a,z-z_a),
\end{aligned} \tag{B.37}$$

$$\begin{aligned}
A_y^{Ewald} &= \sum_{i_1,i_1^2\leq 10}\left\{\frac{2\alpha}{\sqrt{\pi}}\frac{\exp(-\alpha^2u_{i_1})}{u_{i_1}}+\frac{\mathrm{erfc}(\alpha\sqrt{u_{i_1}})}{u_{i_1}^{3/2}}\right\}(y-y_a) \\
&\quad +\frac{4\pi}{L_x^2}\frac{y-y_a}{\sqrt{(y-y_a)^2+(z-z_a)^2}}\sum_{l_1,l_1^2\leq 10}\exp(-\zeta l_1^2)\sin(v_{l_1})M(l_1,y-y_a,z-z_a),
\end{aligned} \tag{B.38}$$

$$\begin{aligned}
A_z^{Ewald} &= \sum_{i_1,i_1^2\leq 10}\left\{\frac{2\alpha}{\sqrt{\pi}}\frac{\exp(-\alpha^2u_{i_1})}{u_{i_1}}+\frac{\mathrm{erfc}(\alpha\sqrt{u_{i_1}})}{u_{i_1}^{3/2}}\right\}(z-z_a) \\
&\quad +\frac{4\pi}{L_x^2}\frac{z-z_a}{\sqrt{(y-y_a)^2+(z-z_a)^2}}\sum_{l_1,l_1^2\leq 10}\exp(-\zeta l_1^2)\cos(v_{l_1})M(l_1,y-y_a,z-z_a),
\end{aligned} \tag{B.39}$$

where $K(l_1,y-y_a,z-z_a)$ is given by eq. (4.26) for $l_1=0$, and by eq. (4.27) otherwise, and function $M(l_1,y-y_a,z-z_a)$ is

$$M(l_1,y-y_a,z-z_a)=\int_0^\infty\frac{J_1(\eta q)\exp(-\zeta q^2)q^2}{l_1^2+q^2}\mathrm{dq}. \tag{B.40}$$

The coefficients C_{ij}^{Ewald} are

$$\begin{aligned}
C_{xx}^{Ewald} = & -\sum_{i_1, i_1^2 \leq 10} \frac{2\alpha}{\sqrt{\pi}} \frac{\exp(-\alpha^2 u_{i_1})}{u_{i_1}} + \frac{\mathrm{erfc}(\alpha\sqrt{u_{i_1}})}{u_{i_1}^{3/2}} + \\
& \left\{ \frac{3\mathrm{erfc}(\alpha\sqrt{u_{i_1}})}{u_{i_1}^{5/2}} + \frac{2\alpha \exp\left(-\alpha^2 u_{i_1}\right)}{\sqrt{\pi} u_{i_1}} \left(2\alpha^2 + 3/u_{i_1}\right) \right\} (x - x_a - i_1 L_x)^2 \\
& + \frac{8\pi^2}{L_x^3} \sum_{l_1, l_1^2 \leq 10} l_1^2 \, \exp\left(-\zeta l_1^2\right) \cos\left(v_{l_1}\right) K(l_1, y - y_a, z - z_a),
\end{aligned} \tag{B.41}$$

$$\begin{aligned}
C_{xy}^{Ewald} = & -\sum_{i_1, i_1^2 \leq 10} \left\{ \frac{2\alpha \exp\left(-\alpha^2 u_{i_1}\right)}{\sqrt{\pi} u_{i_1}} \left(2\alpha^2 + 3/u_{i_1}\right) \right. \\
& \left. + \frac{3\mathrm{erfc}(\alpha\sqrt{u_{i_1}})}{u_{i_1}^{5/2}} \right\} (x - x_a - i_1 L_x)(y - y_a) - \frac{y - y_a}{\sqrt{(y - y_a)^2 + (z - z_a)^2}} \frac{8\pi^2}{L_x^3} \\
& \times \sum_{l_1, l_1^2 \leq 10} l_1 \, \exp\left(-\zeta l_1^2\right) \sin\left(v_{l_1}\right) M(l_1, y - y_a, z - z_a),
\end{aligned} \tag{B.42}$$

$$\begin{aligned}
C_{xz}^{Ewald} = & -\sum_{i_1, i_1^2 \leq 10} \left\{ \frac{2\alpha \exp\left(-\alpha^2 u_{i_1}\right)}{\sqrt{\pi} u_{i_1}} \left(2\alpha^2 + 3/u_{i_1}\right) + \frac{3\mathrm{erfc}(\alpha\sqrt{u_{i_1}})}{u_{i_1}^{5/2}} \right\} \times \\
& (x - x_a - i_1 L_x)(z - z_a) - \frac{z - z_a}{\sqrt{(y - y_a)^2 + (z - z_a)^2}} \frac{8\pi^2}{L_x^3} \times \\
& \sum_{l_1, l_1^2 \leq 10} l_1 \, \exp\left(-\zeta l_1^2\right) \sin\left(v_{l_1}\right) M(l_1, y - y_a, z - z_a),
\end{aligned} \tag{B.43}$$

$$\begin{aligned}
C_{yy}^{Ewald} = & -\sum_{i_1, i_1^2 \leq 10} \frac{2\alpha}{\sqrt{\pi}} \frac{\exp(-\alpha^2 u_{i_1})}{u_{i_1}} + \frac{\mathrm{erfc}(\alpha\sqrt{u_{i_1}})}{u_{i_1}^{3/2}} + \\
& \left\{ \frac{3\mathrm{erfc}(\alpha\sqrt{u_{i_1}})}{u_{i_1}^{5/2}} + \frac{2\alpha \exp\left(-\alpha^2 u_{i_1}\right)}{\sqrt{\pi} u_{i_1}} \left(2\alpha^2 + 3/u_{i_1}\right) \right\} (y - y_a)^2 + \\
& + (z - z_a)^2 \, \frac{4\pi}{L_x^2} \sum_{l_1, l_1^2 \leq 10} \frac{\exp\left(-\zeta l_1^2\right) \cos\left(v_{l_1}\right) M(l_1, y - y_a, z - z_a)}{((y - y_a)^2 + (z - z_a)^2)^{3/2}} + \\
& (y - y_a)^2 \, \frac{8\pi^2}{L_x^3} \sum_{l_1, l_1^2 \leq 10} \frac{\exp\left(-\zeta l_1^2\right) \cos\left(v_{l_1}\right) N(l_1, y - y_a, z - z_a)}{(y - y_a)^2 + (z - z_a)^2},
\end{aligned} \tag{B.44}$$

$$\begin{aligned}
C_{yz}^{Ewald} = & -\sum_{i_1, i_1^2 \leq 10} \left\{ \frac{2\alpha \exp\left(-\alpha^2 u_{i_1}\right)}{\sqrt{\pi} u_{i_1}} \left(2\alpha^2 + 3/u_{i_1}\right) + \frac{3\mathrm{erfc}(\alpha\sqrt{u_{i_1}})}{u_{i_1}^{5/2}} \right\} (y - y_a)(z - z_a) \\
& - (y - y_a)(z - z_a) \, \frac{4\pi}{L_x^2} \sum_{l_1, l_1^2 \leq 10} \frac{\exp\left(-\zeta l_1^2\right) \cos\left(v_{l_1}\right) M(l_1, y - y_a, z - z_a)}{((y - y_a)^2 + (z - z_a)^2)^{3/2}} \\
& + (y - y_a)(z - z_a) \, \frac{8\pi^2}{L_x^3} \sum_{l_1, l_1^2 \leq 10} \frac{\exp\left(-\zeta l_1^2\right) \cos\left(v_{l_1}\right) N(l_1, y - y_a, z - z_a)}{(y - y_a)^2 + (z - z_a)^2},
\end{aligned} \tag{B.45}$$

$$
\begin{aligned}
C_{zz}^{Ewald} \;=\; & -\sum_{i_1, i_1^2 \le 10} \frac{2\alpha}{\sqrt{\pi}} \frac{\exp(-\alpha^2 u_{i_1})}{u_{i_1}} + \frac{\mathrm{erfc}(\alpha\sqrt{u_{i_1}})}{u_{i_1}^{3/2}} + \\
& \left\{ \frac{3\mathrm{erfc}(\alpha\sqrt{u_{i_1}})}{u_{i_1}^{5/2}} + \frac{2\alpha \exp\left(-\alpha^2 u_{i_1}\right)}{\sqrt{\pi} u_{i_1}} \left(2\alpha^2 + 3/u_{i_1}\right) \right\} (z - z_a)^2 + \\
& + (y - y_a)^2 \frac{4\pi}{L_x^2} \sum_{l_1, l_1^2 \le 10} \frac{\exp\left(-\zeta l_1^2\right) \cos\left(v_{l_1}\right) M(l_1, y - y_a, z - z_a)}{((y - y_a)^2 + (z - z_a)^2)^{3/2}} + \\
& (z - z_a)^2 \frac{8\pi^2}{L_x^3} \sum_{l_1, l_1^2 \le 10} \frac{\exp\left(-\zeta l_1^2\right) \cos\left(v_{l_1}\right) N(l_1, y - y_a, z - z_a)}{(y - y_a)^2 + (z - z_a)^2}, \qquad \text{(B.46)}
\end{aligned}
$$

where

$$
N(l_1, y - y_a, z - z_a) = \int_0^\infty \frac{(J_0(\eta q) - J_1(\eta q)/(\eta q)) \exp(-\zeta q^2) q^3}{l_1^2 + q^2} \mathrm{dq}. \qquad \text{(B.47)}
$$